MITOCHONDRIAL RELATIONSHIPS AND CONTRIBUTIONS TO MUSCLE WEAKNESS AND WASTING DURING CANCER CACHEXIA

LUCA J DELFINIS

A DISSERTATION SUBMITTED TO THE FACULTY OF GRADUATE STUDIES IN PARTIAL FULFILLMENT OF THE REQUIREMENTS FOR THE DEGREE OF DOCTOR OF PHILOSOPHY

GRADUATE PROGRAM IN Kinesiology and Health Sciences
YORK UNIVERSITY
TORONTO, ONTARIO

August 2024

Abstract

Cancer-induced cachexia is the on-going loss of skeletal muscle mass and function throughout cancer progression. 20%-80% of cancer patients are predicted to develop cachexia depending on the type and stage of cancer, of which, there is currently no treatment. Current literature on the mechanisms of muscle loss and weakness in cancer have been limiting, especially as it relates to mitochondrial function. Moreover, several experts have suggested the use of cancer cachexia models which replicate the human disease more accurately would be of large utility towards mechanism elucidation and therapy development within this disease.

The focus of this dissertation was to first determine the precise muscle-specific and time-dependent cancer-induced muscle myopathy through two different preclinical models of cancer cachexia. We first used the well-established Colon-26 (C26)-ectopic model of cancer cachexia to characterize skeletal muscle weakness, atrophy and mitochondrial function across time and muscle types. We then used a novel metastatic and orthotopic model of epithelial ovarian cancer (EOC) cachexia to further identify precise cancer-induced skeletal muscle myopathy, once again across time and different muscle types. Finally, to both establish the efficacy of a novel treatment and establish a direct link between cancer-induced skeletal muscle myopathy and mitochondrial function, we administered the mitochondrial-targeted therapeutic SkQ1 to EOC tumour bearing mice.

Our findings reveal that cancer-induced skeletal muscle weakness precedes the development of skeletal muscle atrophy in both the C26-ectopic and EOC-orthotopic models of cancer cachexia. Thus, this dissertation identifies muscle atrophy-independent contributions to skeletal muscle weakness exist in cancer-induced myopathy, a phenomenon yet to be explored. Our findings also demonstrate decreases in mitochondrial respiration and increases in mitochondrial reactive oxygen species are associated with skeletal muscle weakness and atrophy across two preclinical models.

Last, treatment with SkQ1 establishes a direct link between mitochondrial function and skeletal muscle weakness independent of atrophy as this mitochondrial-enhancing drug improved force production across various muscles and time. In conclusion, this dissertation identifies a direct relationship between mitochondrial function and cancer-induced weakness. This work supports the future investigation of mitochondrial targeted therapy in cancer cachexia.

Acknowledgments

There are far too many people to acknowledge for the completion of this dissertation. First, and foremost, I am forever grateful for the supervision, guidance, support and mentorship from Dr. Christopher Perry. It goes without saying that this work would not be possible without your unique and exceptional scientific literacy, curiosity, passion and – most importantly – your trust in me. There is a debt that can never be repaid for your time and commitment and to that, "thank you" will never be enough. The best I could do is carry on with the "Dad Jokes" although I will never be able to tell them as well as you (re: pineapple joke).

I would also like to thank Dr. Jim Petrik for enabling us to study such an amazing model of ovarian cancer. Without Dr. Petrik, this work would have simply not been possible. As such, I would also like to thank Dr. Arthur Cheng who has been more than just a committee member to this dissertation but also a consistent collaborator and mentor along the way. Thank you for fielding my scientific questions and always providing an expert perspective on our work.

While this document only exemplifies my doctoral work, the people who brought me in a position to be able to complete this work date far back from the inception of the degree. First, I would like to acknowledge my undergraduate supervisor Dr. Jayne Kalmar. Jayne set the foundation of my research skills that enabled me to excel and grow past my undergraduate studies. While laboratory techniques may have been different from undergraduate-graduate school, my ability to think critically was perhaps the most important transferable skill I learned early on. Second, I would like to thank all of the Perry Lab members. Thank you all for being so helpful at every step of the way and laughing at every terrible joke I could come up with. To Shar, seeing you develop from an undergrad thesis student to a MSc thesis student has been a fulfilling experience - I'm glad you found a passion in this work as I did. Thank you for all the help. To my family and friends, thank you all for acting like you understood the work I did and for being so supportive when times were tough.

Finally, to Sara, no one truly knows how much you know about cancer cachexia and mitochondria. You listened to me ramble about experiments, get excited about new studies and watched all my presentations before anyone else. Thank you, for all your support. It's made all the difference.

Table of Contents

List of Tables

Chapter 2

Chapter 4

Chapter 5

Chapter

List of Figures

Chapter 2

Chapter 4

Chapter 5

Chapter 6

Chapter 7

List of Supplemental Figures

Chapter 4

Chapter 5

Chapter 6

List of Abbreviations

-Creatine: Without creatine
+Creatine: With creatine
1RM: one-repetition max
4HNE: 2-hydroxy-4-noneal
40SkQ: Early-Stage SkQ1 treated mice
40Veh: Early-Stage Veh treated mice
80SkQ: Late-Stage SkQ1 treated mice
80Veh: Late-Stage Veh treated mice
ACD: accidental cell death
ADP: Adenosine diphosphate
AH130: Yoshida ascites hepatoma
ANT: Adenine nucleotide translocators
Apc: adenomatous polyposis coli
ASCO: American Society of Clinical Oncology
ATP: Adenosine triphosphate
BAT: brown adipose tissue
BLEB: Blebbistatin
BW: Body weight
C26: Colon-26
Cr: Creatine
CSA: Cross sectional area
CT: Computed tomography
CTRL: control PBS injected mice
DEG: Differentially expressed gene
DHPR: Dihydropyridine receptors
DNA: Deoxyribonucleic acid
ECC: Stimulated eccentric contractions
eMHC: Embryonic myosin heavy chain
EOC: Epithelial ovarian cancer
ETC: Electron transport chain
Extensor digitorum longus
$FADH_2$: Flavin adenine dinucleotide
FDA: Food and drug administration
FDB: Flexor digitorum brevis
GA: Gastrocnemius
Gadd45a: growth arrest and DNA damage-inducible 45α
GDF15: Growth differentiation factor 15
GDH: Glutamate dehydrogenase
GO: Gene ontology
GSH: reduced glutathione
GSSG: oxidized glutathione
H_2O_2: Hydrogen peroxide
ICB: immune checkpoint therapy
IFN-γ: Interferon gamma

IL-1: Interleuikin-1
IL-6: Interleukin 6
IM: inner membrane
IMS: intermembrane space
KPC: murine pancreatic cancer
LLC: Lewis lung carcinoma
L_o: Optimal Resting Length
MAC16: colon adenocarcinoma
MENAC: multimodal-exercise, nutrition and anti-inflammatory medication for cachexia
mH_2O_2: Mitochondrial hydrogen peroxide
MHC: Myosin Heavy Chain
MitoQ: MiroguinoneQ
MPT: mitochondrial permeability transition
mtCK: Mitochondrial creatine kinase
mTORC1: mammalian target of rapamycin complex I
MURF-1: Muscle RING-finger protein-1
NADH: Nicotinamide adenine dinucleotide
NF-κβ: nuclear factor κβ
NSAID: non-steroidal anti-inflammatory drug
OCT: Optimal cutting temperature
OM: outer membrane
OXPHOS: Oxidative phosphorylation
PARP: poly ADP-ribose polymerase
PBS: Phosphate buffered saline
PCr: Phosphocreatine
PDA: pancreatic ductal adenocarcinoma
PDAC: Pancreatic ductal adenocarcinoma
PDH: Pyruvate dehydrogenase
PDK: pyruvate dehydrogenase kinase
PDX: patient-derived pancreatic cells
PIF: Proteolysis-inducing factor
PLT: Plantaris
PmFB: Permeabilized Fiber bundles
PUFA: poly unsaturated fatty acid
Quad: Quadriceps
RCD: regulated cell death
RCR: respiratory control ratio
RCT: randomized control trial
RET: Reverse electron transfer
RNASeq: RNA sequencing
RNS: Reactive nitrogen species
ROS: reactive oxygen species
Rt-PCR: Reverse transcription- polymerase chain reaction
RyR1: Ryanodine receptor
SERCA: Sarcoendoplasmic reticulum calcium ATPase
SOD: superoxide dismutase

Sol: Soleus
SR: sarcoplasmic reticulum
TA: Tibialis anterior
TCA: tricarboxylic acid
TEM: Transmission electron microscopy
TLR: Toll-like receptors
TNFα: Tumour necrosis factor alpha
UBC: ubiquitin C
UCP: Uncoupling proteins
VDAC: Voltage gated anion channel
VWR: volutional wheel running
WO: weeks old

1 INTRODUCTION

Cancer is fundamentally understood as continual, unregulated cell proliferation that occurs due to mutations from single cells[1]. Unregulated cell proliferation can generate tumours which cause a myriad of complications to the host[2]. One understudied secondary complication of cancer is its ability to impact skeletal muscle inducing muscle loss and weakness. This phenomenon is termed cancer cachexia. The international consensus on the definition of cancer cachexia is "a multifactorial syndrome characterized by an ongoing loss of muscle mass (with or without fat mass) that cannot be fully reversed by conventional nutritional support and leads to progressive functional impairment"[3]. It is estimated that 20%-80% of cancer patients will develop cachexia depending on the type and stage of cancer[4]. Dozens of therapeutic clinical investigations have been conducted for this disease, but none have produced sufficiently positive results to yield an approved therapy[5]. Thus, there is currently no licensed treatment or standard-of-care for cancer cachexia patients.

Leading dogmas hypothesize that muscle loss during cancer is induced by circulating factors which trigger protein degradation and loss of myofibrillar proteins through various mechanisms[6–8]. However, recent literature also suggests skeletal muscle mitochondria are subject to damage during cancer cachexia[9–11] and may be direct contributors to muscle wasting. Indeed, oxidative phosphorylation is impaired in the soleus, gastrocnemius and plantaris muscles of tumour-bearing mice, while reactive oxygen species (ROS) – in the form of mitochondrial H_2O_2 emission (mH_2O_2) – can be increased or decreased depending on the muscle and duration of cancer[10–12]. Moreover, in the Lewis lung carcinoma (LLC) ectopic xenograft model, certain indices of skeletal muscle mitochondrial dysfunction preceded the onset of muscle atrophy suggesting mitochondria may be a potential therapeutic target[12]. Yet, given the multifactorial contributions to cachexia during

cancer, the relationship between mitochondria and myopathy may differ between muscle types and cancer progression. In this light, the available literature does not provide sufficient information to predict the extent to which cancer will affect individual muscles, particularly in relation to their underlying mitochondrial responses to the systemic stress of the disease.

Moreover, much criticism has been given towards conventional models of cancer cachexia[13]. Indeed, popularly used models either require injections of cancer cells under the skin that grow ectopically (outside host organ), usage of immunocompromised mice, usage of mice with genetic mutations that develop tumours at birth, or last usage of mice that grow tumours spontaneously in adulthood which can require large animal colonies and expenses. While these models have set the foundation of mechanism and therapy elucidation in cancer cachexia, the utility of these models is under criticism due to the lack of success in clinical investigations[13]. It is for this reason, models that grow tumours in the host organ (orthotopic) that can be induced at any age in immunocompetent mice, which also demonstrate metastasis - have been suggested to be important for improving the predictive power of *in vivo* models of cancer cachexia[13–15]. The available literature does not provide sufficient information to predict the mitochondrial contributions to cachexia in an orthotopic, metastatic context especially in multiple muscles and across time.

Last, majority of research has investigated the mechanisms governing muscle loss in cancer, while less attention has been given to the mechanisms governing muscle weakness in this disease. Indeed, while muscle loss is an obvious contributor to weakness, there is little investigation on the mechanisms governing weakness independent of muscle loss, if any even exist. Understanding the relationship between cancer and muscle weakness is critical for cachexia therapy development as targeting weakness in conjunction with atrophy could lead to more successful therapeutic investigations. For example, improving muscle weakness could theoretically help cancer patients

adhere to exercise interventions which is significant considering exercise has already been shown to improve patient health-related quality of life[16], as well as have positive benefits in skeletal muscle health within preclinical models[17,18], and even potential anti-tumorigenic effects[19]. Therefore, the two main purposes of this dissertation were to 1) determine the time-course and muscle-specific relationship of ectopic-non-metastatic and orthotopic-metastatic cancer growth and mitochondrial function in relation to weakness and atrophy and 2) target mitochondria pharmacologically to elucidate the role of mitochondria in muscle weakness and atrophy in cancer cachexia while also evaluating its effectiveness as a cancer cachexia therapeutic.

2 LITERATURE REVIEW

2.1 Introduction to Cancer Cachexia

2.1.1 Overview of Cancer Cachexia

Cancer is a devastating disease that leads to millions of deaths each year around the globe. While understanding cancer biology and developing oncological therapeutics is an exceedingly important endeavour, the secondary complications of cancer can go undiscussed. In particular, cancer's ability to impact skeletal muscle – a condition known as cancer cachexia – has received little attention even though it has a significant impact on quality of life for cancer patients. As Rochelle - a cancer patient with cachexia - expressed in a series called "Dear Scientist" with the Boston Globe "cancer cachexia has made life as I knew it unrecognizable"[20].

Cancer cachexia is a debilitating condition that severely damages the fragment of life for cancer patients. In advanced stages of cancer, individuals often experience extreme muscle loss[21]. This is termed "cachexia" originating from the Greek, *kakos* and *hexis*, meaning "bad condition." The international consensus of the definition for cancer cachexia is "a multifactorial syndrome characterized by an ongoing loss of muscle mass (with or without fat mass) that cannot be fully reversed by conventional nutritional support and leads to progressive functional impairment"[3]. Cancer patients are considered cachectic if (i) patients exhibit greater than 5% body weight loss over 6 months, (ii) patient has a body mass index (BMI) of less than 20 or, (iii) patients have low muscle mass consistent with sarcopenia and weight loss of more than 2% [3].

It is predicted that 20%-80% of cancer patients develop cachexia depending on the type and stage of cancer[4]. For example, foundational literature predicts that patients with pancreatic or gastric cancer have the highest frequency of weight loss (83%-87%), while patients with colon, prostate

or lung cancer develop cachexia less frequently (48%-61%) and patients with non-Hodgkin lymphoma, breast cancer and sarcomas are among the least frequent (31%-40%)[4]. While the precise mechanisms that govern cachexia remain incompletely identified, it is well-accepted that the mechanisms facilitating muscle loss in cachexia is likely multifactorial in nature encompassing inflammation, autophagy, proteolysis, cell death, malnutrition, muscle disuse, chemotherapy toxicity and energy homeostasis[8]. Section 2.1.3 will review the current proposed mechanisms of muscle loss in cancer-induced cachexia.

2.1.2 Cancer Cachexia on Morbidity and Mortality

Cancer severely worsens quality of life and is associated with several physical, emotional and cognitive dysfunctions. One study identified "lack of energy" or "fatigue" as the most frequent patient-rated symptom or concern among 11 different advanced cancer types[22]. Studies have even identified that cancer patients perceive fatigue as the symptom with the highest impact on their daily social, leisure and self-care activities[23]. While the cause of fatigue is likely due to a myriad of reasons (chemotherapy toxicity, poor physical health, poor emotional health, etc.), it is clear that cancer patients exhibit a worsened quality of life. In addition, while these studies do not identify skeletal muscle-specific dysfunctions as the facilitators of worsened quality of life, skeletal muscle mass is one of the most powerful prognostic factors of cancer survival[24]. Indeed, in a cohort of approximately 1400 solid tumour cancer patients in Alberta, Canada; patients with cancer who presented with extreme muscle loss (>5%; evaluated with computed tomography (CT)) exhibit a poor prognosis regardless of overall body weight[24]. This suggests that protecting muscle mass could be key to improving survivability in cancer cachexia.

Developing cachexia during cancer makes matters significantly worse for cancer patients as cachectic patients exhibit reduced physical function and tolerance to anticancer therapies[25–27]. This also impacts the quality of life of cancer patients in conjunction with self-reports of fatigue. Moreover, cachectic cancer patients tend to have longer post-operative hospital stays compared to non-cachectic cancer patients. In one study, the length of stay of 98 gastrointestinal cancer patients over the age of 60 was analyzed post-surgery and revealed cachectic gastrointestinal cancer patients exhibit longer postoperative length of stay compared to non-cachectic gastrointestinal cancer patients[28]. Moreover, sarcopenia (age-induced muscle loss) is described to be associated with major chemotherapy toxicities resulting in dose reduction, dose delay or termination of chemotherapy for patients treated with fluoro-pyrimidines, anthracyclines, and tyrosine kinase inhibitors[29,30]. This further supports the need to protect muscle mass throughout cancer progression. Last, and perhaps most importantly, cancer patients with cachexia exhibit decreased survival. In one study, the 6-month survival in 835 different cancer patients above the age of 70 demonstrate that cancer patients with cachexia exhibit decreased survivability compared to non-cachectic cancer patients[31].

It is thus clear that maintaining healthy skeletal muscle mass is crucial for quality of life, tolerance to anticancer therapies and overall survivability for cancer patients. Currently there is no licensed treatment options for cancer cachectic patients and thus more mechanism elucidation and experimental therapy development needs to be completed. Nevertheless, clinical therapeutic investigations have been conducted rigorously and will be covered in section 2.1.4 in this literature review.

2.1.3 Proposed Mechanisms of Cancer Cachexia

There are several proposed mechanisms of myopathy in cancer-induced cachexia. The following section will review the proposed theories including inflammation, proteolysis, cell death, autophagy, malnutrition/muscle disuse and impaired energy homeostasis. While these mechanisms are written separately, these pathways are not functionally independent. Meaning, these pathways are connected and can occur in unison with similar signal transduction pathways. The overall sum of all of these mechanisms is believed to lead to myopathy in cancer cachexia.

2.1.3.1 Inflammation/Tumour Specific Factors as a Mechanism of Cancer Cachexia

Loss of muscle in cancer cachexia is frequently associated with increased production of factors known as tumour necrosis factor alpha (TNF-α), interleukin – 1 (IL-1), - 6 (IL-6) and interferon gamma (IFN-γ) [32]. These factors are termed "proinflammatory cytokines" which facilitate the growth and activity of other cell targets. This section will focus on the impact of cytokines on skeletal muscle for the purpose of understanding the role of inflammation in cancer cachexia. However, in order to understand the effects of cytokines on skeletal muscle, it is first important to understand how the immune system regulates cytokine production.

Immunity can be divided under two broad categories: innate immunity and adaptive immunity. Briefly, innate immunity is a non-specific, short-lasting initial response from myeloid (monocytes, macrophages, neutrophils) and lymphoid (natural killer cells) cells [33]; while adaptive immunity is a delayed response that induces a long-lasting, specific immune response mediated by $CD4^+$ T-helper cells, cytotoxic $CD8^+$ T cells and B cells[34]. Innate immune cells express Toll-like receptors (TLR) which recognize a myriad of antigens and lead to the activation of nuclear factor κβ (NF-κβ) and resulting cytokine production which mediates the magnitude of the inflammatory

response[35]. During the innate immune response, macrophages can form a continuum between an M1 (pro-inflammatory) and M2 (anti-inflammatory) profile[36]. The tumour microenvironment is rich in cytokines and other inflammatory mediators that influence immunosuppression, growth of cancer cells, tissue remodeling and angiogenesis[37].

It is well established in cancer cachectic patients that circulating levels of pro-inflammatory cytokines (most commonly TNFα and IL-6) are upregulated in several different types of cancers[38]. However, tumours are also believed to release specific factors that can induce similar downstream signaling cascades. Indeed, proteolysis-inducing factor (PIF) was originally characterized from tumours of MAC16 tumour bearing mice and urine of cachectic cancer patients[39]. PIF was first identified as a proteoglycan distinguished from cytokines by its structure and ability to accelerate breakdown of skeletal muscle both in vitro and in vivo by a process that does not involve anorexia[39]. PIF is thought to act through NF-κβ (similar to inflammatory cytokines)[40] and has been shown to activate the ubiquitin proteasome pathway in preclinical and cell culture models of cancer cachexia[41]. However, the precise role of PIF remains incompletely understood.

Proinflammatory cytokines and tumour specific factors induce a complex signalling cascade that results in inhibition of anabolic and/or anticatabolic signals in favour of skeletal muscle proteolysis[32]. Thus, in cancer cachexia, systemic inflammation is associated with reduced rates of protein synthesis paralleled with enhanced protein breakdown resulting in overall muscle loss. The downstream signalling cascade as it pertains to proteolysis, autophagy and cell death are discussed is sections below.

2.1.3.2 Proteolysis as a Mechanism of Cancer Cachexia

Skeletal muscle is in a constant balance of protein synthesis and degradation to maintain muscle mass. In cachexia, muscle loss is due to increased protein breakdown, decreased protein synthesis or a combination of the two[42]. The extent of protein synthesis vs protein breakdown is variable between studies and models, but dysregulation in protein homeostasis is considered the leading theory of muscle mass loss in cancer cachexia.

Proteolysis is the breakdown of proteins into polypeptides and amino acids. There are three major proteolytic pathways for the degradation of proteins in skeletal muscle: (i) the ubiquitin-proteasome pathway, (ii) calpains and (iii) the autophagy-lysosomal system[43]. While these degradation pathways will be discussed separately, it should be noted that overlap exists between all three. These are written separately in an attempt to simplify the current literature on cancer cachexia and proteolysis.

Original literature from the late 1990s and early 2000s demonstrates that the ubiquitin-proteasome pathway plays a critical role in protein breakdown in human cancer patients and preclinical rodent models[44–47]. This has since been reproduced in several models of cancer cachexia over the last two decades[48]. The ubiquitin-proteasome pathway is a complex, yet specific system used by the cell to execute protein degradation. Briefly, this pathway degrades proteins using four main enzymes: E1- ubiquitin carrier protein, E2 – ubiquitin-conjugating enzyme, E3 – ubiquitin-protein ligase and 26S proteasome complex[49]. The pathway can be summarized in two main steps (i) substrate tagging by covalent attachment of ubiquitin molecules, and (ii) degradation of tagged substrates through the 26S proteasome complex[49]. E1 enzymes activate ubiquitin using ATP, generating thiol-ester intermediates; enabling E2 enzymes to transfer activated ubiquitin moieties from E1 to the protein substrate through another thiol-ester intermediate[49]. At this point, protein substrates

can now bind E3 enzymes through a recognition motif and be degraded by the 26S proteasome with energy from ATP[49]. Muscle RING finger 1 (MURF-1) and Atrogin-1 (also referred to as Muscle Atrophy F-box MAFbx) are both E3 ubiquitin ligases expressed in skeletal muscle that are consistently upregulated in various models of cancer cachexia[48]. These E3 ligases can be activated through several catabolic pathways including NF-κβ activation, FOXO1/FOXO3 transcription factor activation through mammalian target of rapamycin complex I (mTORC1) inhibition and oxidative stress [50]. Interestingly, in the murine pancreatic cancer (KPC) model, injecting KPC cells into MURF-1$^{-/-}$ mice blunted muscle wasting and interestingly also slowed tumour growth[51]. Not only does this highlight the integral role of E3 ligases in cancer cachexia muscle myopathy within preclinical models, but this also demonstrates that cancer cachexia therapies could also aid in the pursuit of cancer treatment. Discussion about current cancer cachexia therapies will be further discussed in section 2.1.4. While activation of proteolysis through the ubiquitin-proteasome pathway is the current leading theory for muscle loss in cancer cachexia, there is also evidence that calpains and the autophagy-lysosome system can also contribute to proteolysis in this disease. Calpains are a group of calcium-activated cysteine proteases that include two ubiquitously expressed members (caplain-1 and calpain-2) and one muscle-specific member (calpain-3)[52]. While the role of calpains in cancer cachexia is less researched compared to the ubiquitin-proteasome pathway, the calpain system is also believed to be activated in some models of cancer cachexia. Indeed, in the AH-130 hepatoma and C26 colorectal model, calpains protein content is increased suggesting calpain activity could be increased[53]. Interestingly, administration of dantrolene or overexpression of calpastatin (calpain inhibitors) does not attenuate protein degradation or muscle mass loss in the AH-130 or C26 models[53]. This suggests that that while the calpain system may be activated in cancer cachexia, it likely does not regulate muscle proteolysis

to the same effect as the ubiquitin proteasome pathway. While two preclinical cancer cachexia models have been described, a recent review analysis evaluating all models of cancer cachexia demonstrate that the activation of calpains is sparce and requires further research[48].

The autophagy-lysosome system has also been proposed to contribute to muscle loss exhibited in cancer cachexia. Autophagy plays a vital role in the turnover of cell components to maintain healthy cell homeostasis[54]. Three main mechanisms exist in mammals for the transport of autophagic cargo to lysosomes: macroautophagy, chaperone-mediated autophagy and microautophagy[54]. Briefly, macroautophagy is triggered by the activation of a regulatory complex (contains Vps34, Beclin1, Vps15, Abra1 and Atg14) that induces LC3 recruitment to the autophagosome (double-membrane structure that engulfs proteins and substrates to be degraded)[54]. Proteins that are destined for degradation are then polyubiquitinated to the autophagosome by the p62 scaffold[54]. p62 is constantly removed by autophagy, therefore accumulation in this scaffold can indicate disturbances in autophagosome turnover. Understanding the role of autophagy in cancer cachexia becomes increasingly complicated since autophagy is necessary to maintain healthy muscle homeostasis. Therefore, it becomes challenging to delineate if changes in p62 are necessary to maintain healthy muscle mass or contributes to total net loss in mass. It is for this reason, “excessive autophagy” is believed to occur in cancer cachexia to contribute to muscle loss within the disease. It is thus an oversimplification to state autophagy is “increased” in cancer cachexia considering the complexity of this system. Indeed, different results exist across cancer cachexia models regarding the induction of autophagy. Beclin1 and LC3B, the initial steps of autophagy, appear to be increased to some effect across human and mouse models of cancer cachexia[55–58]. However, there are also reported increases in accumulation of p62 in cancer cachectic muscle in animals suggesting a disequilibrium between autophagosome formation and

clearance[57–59]. Data on autophagy-lysosomal induced muscle loss in cancer cachexia requires further investigation to understand the complex relationship between the initiation of autophagy, the degradation of cellular debris and the resulting impact on skeletal muscle mass.

Cancer can also induce muscle loss through the inhibition of protein synthesis. Indeed, while activation of various proteolytic pathways gains most attention, it is also important to note that skeletal muscle also cannot regulate protein synthesis effectively. Foundational literature in human cancer cachectic patients demonstrates that muscle protein synthesis is decreased relative to non-cachectic cancer patients using a tracer infusion of leucine labelled with a stable isotope[60]. Moreover, vast majority of animal models report a reduction in rate of protein synthesis with only a few studies demonstrating no change[48]. It's important to note that animal models induce cachexia more rapidly than human models. Thus, in the context of protein balance, protein breakdown may contribute to muscle loss more so in animal models than humans due to the rate at which muscle loss occurs. Nevertheless, decreases in protein synthesis also contribute to net muscle loss in cancer cachexia.

2.1.3.3 Cell Death as a Mechanism of Cancer Cachexia

Cell death can be both programmed and orchestrated by multiple networked cellular processes or occur suddenly. Thus, cell death can be termed regulated cell death (RCD) or accidental cell death (ACD)[61]. Indeed, RCD is a tightly coordinated process carried out by the cell whereas ACD can occur instantaneously because of physical (temperature, osmotic forces, high pressures), mechanical (shear force), or chemical (pH variations) changes[61]. There are numerous theoretical cell death pathways, and all pathways exhibits overlap regarding enzymes and targets involved[61].

Reviewing all pathways would fall outside the scope of this literature review, however, the following section will highlight relevant cell death pathways explored in cancer cachexia.

The current literature on cell death and cancer cachexia is sparce. However, of all cell death pathways, apoptosis – a form of RCD has been shown to potentially be upregulated in cancer cachexia. Briefly, apoptosis can be activated via an extrinsic-death receptor pathway and/or an intrinsic-mitochondrial pathway[62]. In the extrinsic pathway, apoptosis is initiated via transmembrane receptor-mediated signal transduction mechanisms from members of the tumor necrosis factor gene superfamily[62]. In the intrinsic pathway, opening of the mitochondrial permeability transition (MPT) due to calcium overload within the organelle induces the release of cytochrome *c*, which binds to Apaf-1 and procaspase-9 forming an "apoptosome"[62]. Both pathways converge on the same terminal or execution pathway – caspase-3 activation[62]. This results in DNA fragmentation, degradation of cytoskeletal and nuclear proteins, cross-linking of proteins and formation of apoptotic bodies, ultimately inducing programmed cell death[62].

In cancer cachexia, mixed results are observed across models. In a small cohort of human gastrointestinal cancer patients, there is a three-fold increase in DNA fragmentation and an increase in poly ADP-ribose polymerase (PARP) cleavage (index of apoptosis)[63]. In another small human cohort of stomach/colorectal cancer patients, caspase -8 and -9 is significantly increased compared to non-cachectic stomach/colorectal cancer patients[55]. Interestingly, however, in a small study of 16 gastric cancer patients, rectus abdominus muscle did not exhibit increases in markers of apoptosis compared to non-cachectic gastric cancer patients[64]. Indeed, no changes in caspase 1, -3, PARP cleavage, or percentages of apoptotic myonuclei were observed within this study, suggesting apoptosis was not initiated[64]. Authors did note that muscle loss in these cachectic patients were "moderate (6% body weight loss)," ultimately suggesting apoptosis may only occur

in severe cancer cachexia. In the rat model of AH-130 hepatoma and mouse model of Lewis lung carcinoma (LLC), there is reported increases in caspase-3 activity and DNA fragmentation[65]. Moreover, in the MAC16 (colon adenocarcinoma) murine model of cancer cachexia, gastrocnemius muscle caspase -1, -8, -3, -6 and -9 activity is increased along with PARP fragmentation and cytochrome *c* release into the cytosol[66]. These data suggest that apoptosis in both human and rodent models are contributors to muscle loss in cancer cachexia. Future research could explore other cell death pathways in conjunction with apoptosis to elucidate if other mechanisms of cell death contribute to muscle loss in cancer cachexia.

2.1.3.4 Malnutrition/Muscle Disuse as a Mechanism of Cancer Cachexia

It is predicted up to 85% of cancer patients are malnourished with the most prevalence in gastric, pancreatic, lung, prostate and colon cancer patients[67]. Several factors can contribute to the incidence of malnutrition in cancer patients including age, gender, anticancer treatments and type/location/grade of cancer[68]. Cancer-associated malnutrition occurs due to an imbalance between patient nutritional needs, tumour nutritional demand and availability of nutrients in the body[68]. Prolonged malnutrition can accelerate cachexia and induce complications. Foundational literature demonstrates how malnourished cancer patients compared to patients maintaining normal body weight can exhibit impaired response to anti-cancer treatment[27], susceptibility to chemo-induced toxicity [69,70] and higher incidence of post-operative complications[71].

It has been proposed that cancer development and malnutrition are closely linked and can develop into a “vicious circle” whereby, illness causes decreased food intake, malabsorption, loss of nutrients, and eventually results in increases susceptibility to complications[68]. These complications can further worsen illness by exacerbating fatigue, decrease mobility and worsening

responses to therapy[68]. While the very definition of cancer cachexia implies that nutrition is not the mechanism of cachexia ("muscle loss that cannot be fully reversed by conventional nutritional support" [3]), it is still important to bring attention to the role of malnutrition in the development of cachexia. In fact, recent opinions even suggest that while nutritional support cannot fully reverse cancer cachexia, partial reversal is possible with conventional nutritional therapy[72,73]. Indeed, while nutritional interventions may not be able to reverse muscle loss once cachexia has manifested, it is important to note that nutrition can still have some positive impact throughout disease development. Current clinical data on nutritional interventions to treat cancer cachexia are covered in section 2.4.1.

While advanced cancer patients are likely to be bedridden due to the severity of the disease, there is little evidence available to support the theory that muscle inactivity or disuse is a direct mechanism of muscle loss in cancer cachexia. However, reductions in food intake and physical inactivity are thought to contribute at least partially to cachexia throughout cancer progression[74,75]. The exact degree to which malnutrition and disuse contributes to cachexia could be investigated using "muscle disuse" controls whereby cancer patients could be compared to bed-rest healthy participants. Similarly, in preclinical studies, hindlimb suspension could be used as a model of disease-free muscle inactivity. Delineating the precise mechanisms by which disuse and malnutrition contribute to cachexia could guide therapy development, especially in the context of exercise and nutritional intervention in cancer patients.

2.1.3.5 Energy Homeostasis as a Mechanism of Cancer Cachexia

Well-balanced and controlled energy homeostasis is crucial to maintain healthy skeletal muscle. Cachexia is an energy balance disorder such that energy intake is decreased and/or energy

expenditure is increased[8]. When energy expenditure exceeds energy intake, the net result is loss in total body weight. In cancer, the contributions to energy intake or expenditure can vary based off cancer type and stage of cancer development[8]. However, although decreases in energy intake are often associated with cachexia, it is understood that this alone is not the cause of cachexia. Indeed, in one study, 119 small cell lung cancer patients on total parenteral nutrition (IV-administered nutrition) - and thus with perfectly controlled nutrient intake - still lose weight and suffer from cachexia symptoms[76]. It is thus believed that increases in energy expenditure, more specifically, resting energy expenditure is a possible mechanism of skeletal muscle wasting in cancer cachexia. There are several proposed mechanisms of increased resting energy expenditure in cancer cachexia. First, increased futile cycle activity is proposed to contribute to energetic inefficiency[8]. Futile cycles refer to the increased cycling of metabolic intermediates that utilize ATP to generate heat[77]. One example is the lactate recycling that is associated with the Cori cycle between the liver and tumour. The Cori Cycle (or lactic acid cycle) is the metabolic process whereby lactic acid produced in the muscle is converted to glucose by the liver and shuttled back to the muscle to be utilized again[78]. In the context of cancer cachexia, energetic inefficiency can induce futile cycling between the tumour and liver. Indeed, the gluconeogenic utilization of tumour-generated lactate is energetically inefficient but is necessary to compensate for tumour-induced acidosis[77]. Foundational literature in cultured myocytes demonstrate that Cachectin/TNF-mediated lactate production is linked to futile cycling specifically through activation of both phosphofructokinase and fructose bisphosphate phosphatase in glycolysis[79]. While this experiment was completed in the absence of a cancer stimulus, inflammatory markers are well-understood to be upregulated in cancer cachexia and thus could lead to a similar futile cycle within the human condition.

Second, mitochondrial energy uncoupling is also thought to lead to reduced energy efficiency in cancer cachexia[77]. Glycolysis produces 2 net adenosine triphosphate (ATP) molecules per glucose molecule while 36 additional ATP are produced from glucose as a result of the tricarboxylic acid (TCA) cycle and electron transport chain[80]. However, due to oxidative uncoupling, energetic inefficiencies can exist that do not yield ATP molecules from glucose but rather generate heat[77]. While skeletal muscle oxidative phosphorylation will be further discussed in section 2.3, the point remains – in cancer cachexia, substrates can be metabolized and not directly result in the generation of ATP molecules. This process is called uncoupled respiration and is completed by uncoupling proteins (UCPs)[81]. UCPs are expressed in skeletal muscle, brown adipose tissue (BAT) and heart[82]. While the function of UCPs is still not fully understood, UCPs in skeletal muscle is believed to be involved in the regulation of the production of reactive oxygen species through decreased membrane potential, mitochondrial fatty acid transport and regulation of glucose metabolism[83]. Interestingly, in the AH-130 hepatoma, MAC16 adenocarcinoma and LLC preclinical models of cancer cachexia, expression of UCPs genes is increased in skeletal muscle or BAT of cancer cachectic animals[84–86]. Moreover, increases in UCP gene expression has also been shown in skeletal muscle of human gastrointestinal adenocarcinoma patients and was associated with weight loss within this small cohort[87]. This suggests that uncoupling proteins are a likely source of energetic inefficiency in cancer cachexia.

Third, the sarcoendoplasmic reticulum Ca^{2+}-ATPase (SERCA) has also been thought to contribute to energetic inefficiency in cancer cachexia. SERCA is a key regulator of calcium homeostasis, translocating calcium from the cytosol to the sarcoplasmic reticulum (SR). Since translocation of calcium from the cytosol to the SR goes against a concentration gradient, this process requires ATP. Interestingly, however, some of the energy associated with SERCA activity does not result

in calcium translocation and has been identified to release heat as a mechanism of non-shivering thermogenesis[88,89]. In the Yoshida AH-130 hepatoma model, cancer cachectic rats exhibit increased SERCA protein content and gene expression concurrent with less ATP content[90]. While there is no indication of increased SERCA activity reported within the literature and thus is challenging to interpret SERCA function, this data is suggestive that increased SERCA protein content supports energetic inefficiencies in cancer cachexia. Last, decreased mitochondrial oxidative capacity has been commonly observed in several cancer cachexia preclinical models. As this is a specific focus of this dissertation, this will be covered in detail in section 2.4.1.

2.1.3.6 Chemotherapy as a Mechanism of Cancer Cachexia

Chemotherapy is a standard first-line drug treatment for nearly all cancers. It is estimated that the proportion of cancer patients that need chemotherapy was 63% in 2018 and projected to be 67% by 2040 in low- or middle-income countries[91]. However, chemotherapy is not cancer-specific, meaning healthy and normal cells are also subject to damage from treatment. While most cancer patients are treated with chemotherapy, data from cancer patient populations can be challenging to comprehend because it is unclear if cachexia occurs because of the tumour itself or a combination of the tumour and chemotherapy treatment. Preclinical models of cancer cachexia have shown very clearly that tumours themselves can cause cachexia, however, interestingly, this is also true for chemotherapy treatment alone. Indeed, while chemotherapy is a treatment for cancer, recent literature has shown that chemotherapy can induce muscle wasting without a tumour present. There are several types of chemotherapy treatment. Treatment and dosage typically depend on the type and stage of cancer. While reviewing all chemotherapy treatments falls outside

the scope of this literature review, the focus will be on chemotherapies with reported impact on skeletal muscle.

Anthracyclines based therapies are perhaps the most popularly used antitumour treatment which exhibit an extremely wide spectrum of activity in human cancer with only few cancers being unresponsive to their administration[92]. There are several analogues of anthracycline therapy including daunorubicin, doxorubicin, epirubicin, etoposide, idarubicin, irinotecan, mixtoxantrone and topotecan[93]. Interestingly, doxorubicin administration at a treatment cycle and dosage that replicates humans has been shown to induce body weight loss, muscle wasting and muscle weakness in mice without the presence of a tumour[94]. Moreover, muscle weakness and muscle mass loss also occur in rats with doxorubicin administered daily at low doses for 15 days [95]. The mechanisms that govern muscle loss with doxorubicin treatment are thought to parallel cancer with ubiquitin-proteasome activation, autophagy and oxidative stress suggested to play key roles as outlined in a meta-analysis of 20 studies[96], albeit variability in chemotherapy dosage and administration strategies make these mechanisms challenging to elucidate.

Platinum-based chemotherapies are also popularly used chemotherapies that are commonly used for breast, ovarian, and colorectal cancers[97]. This class of chemotherapies include cisplatin, carboplatin and oxaliplatin. Cisplatin was the first developed platinum-based chemotherapy and it's mechanism of action is believed to be cell death induced through inhibition of DNA transcription[98]. However, cisplatin can cause systemic toxicity and undesirable side effects[97]. Skeletal muscle is well documented to be subject to extensive damage with cisplatin administration[99]. Indeed, administration of cisplatin to mice without tumours have shown to decrease body weight, muscle mass and muscle atrophy with varying administration dosages (1 – 5mg/kg body weight) and durations (3-4 injections)[100–102]. This cachectic phenotype has been

reported to occur concurrently with up-regulation of atrogin-1, MURF1 and FOXO3 genes[100,101]. Interestingly, cisplatin administration was also coupled to intracellular calcium concentrations dysregulation, a mechanism of dysfunction yet to be explored in cancer cachexia[101].

The mechanisms of muscle wasting and weakness in cancer cachexia are multifactorial and can be exacerbated by chemotherapy. While several mechanisms of muscle loss and weakness were discussed in this section, a summary figure is provided in **Figure 2-1** of all the proposed mechanism to try and simplify this complex relationship. While there is currently no licensed treatment for cancer cachexia, an effective treatment likely requires a multi-factorial approach to halt or delay the loss of muscle mass throughout cancer progression.

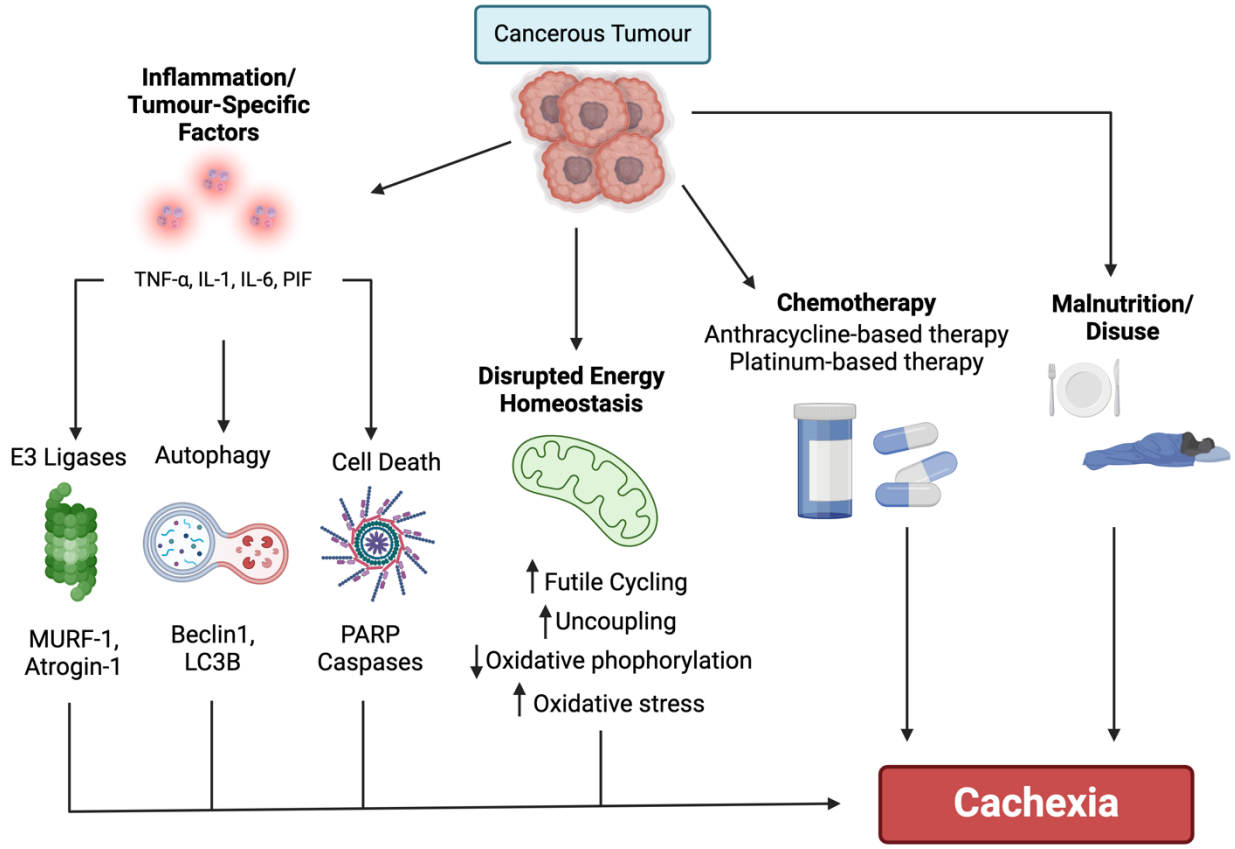

Figure 2-1. Proposed mechanisms of cachexia throughout cancer progression. Tumours release factors and induce the activation of several inflammatory cytokines that activate E3 ligases, autophagy and cell death mechanisms. Tumours also disrupt energy homeostasis by inducing increased futile cycling, uncoupling, oxidative stress and decreased oxidative phosphorylation. Anticancer treatment toxicity along with malnutrition and muscle inactivity are also thought to contribute to cachexia throughout cancer progression. This figure was partially adapted from *Argilés et al* 2014 [8].

2.1.4 Current Therapies in Cancer Cachexia

There are currently no treatments that have been approved by the US Food and Drug Administration (FDA) for cancer cachexia[103]. While cachexia is estimated to occur in 20-80% of cancer patients depending on the type and stage of cancer [4], identifying an effective treatment plan for this disease is an urgent matter. The following section will highlight the three commonly

researched interventions: nutrition, pharmacology, and exercise. A schematic summary is provided in **Figure 2-2**.

2.1.4.1 Nutrition as a Treatment for Cancer Cachexia

It is well understood in the international consensus of the definition of cancer cachexia that this disease cannot be reversed by nutritional support alone[3]. However, nutritional treatment has been extensively evaluated throughout the literature and has shown to have marginal benefits. While the American Society of Clinical Oncology (ASCO) recommendations regarding nutritional interventions are to consume high-protein, high-calorie, nutrient-dense foods and to use parenteral nutrition sparingly to selected groups[103], the overall evidence quality remains low highlighting the need for more clinical studies.

One meta-analysis conducted in 2018 which analyzed nine randomized control trials (RCTs) with cancer patients undergoing chemo(radio) therapy with no restriction on stage of cancer or nutritional status demonstrated overall dietary counselling and/or oral nutritional supplements were associated with improved body weight[104]. However, within this metanalysis, there was considerable heterogeneity due to low compliance with the nutritional intervention[104]. Indeed, the reported achieved calory intake fell between 1700-2000kcal while the target intake goal was 2100-2800[104]. Thus, a subgroup analysis was conducted to achieve this outcome of improved body weight due to nutritional intervention[104]. A second subgroup meta-analysis of data on body weight response showed that dietary intervention with protein, n-3 poly unsaturated fatty acid (PUFA)-enriched oral nutritional supplements led to significant improvements in body weight compared to isocaloric controls[104]. A subset analysis of the four RCT within this meta-analysis that evaluated

PUFA-enriched oral nutritional supplements on body weight changes in cancer demonstrate that body weigh was improved by approximately 2 kg[104].

Considering nutritional compliance can be challenging in cancer cachexia, parenteral nutrition has been explored. A meta-analysis completed in 1990 discovered that parenteral nutrition administration was actually associated with reduced survival and increased infectious complications[105]. The risk of infection persisted when catheter-related septicemia was excluded, suggesting that parenteral nutrition itself can increase susceptibility to infection and thus was strongly discouraged by authors[105]. Considering administration, dosing and composition of parenteral nutrition has changed since 1990, a systematic review completed in 2019 has also been completed to re-assess the viability of parenteral nutrition. Interestingly, this systemic review yielded similar results, such that parenteral nutrition was overall not beneficial[106]. While some RCTs within the analysis still reported occurrences of infection; an improvement in fat-free mass was seen after 12 weeks of parenteral nutrition but not 6, 18 or 24 weeks after suggesting the benefits are marginal[106]. However, there are specific situations in which a patient may have multifocal bowel obstructions and thus may benefit from a time-limited trial of home parenteral nutrition as recommended by the ASCO[103]. Thus, usage of parenteral nutrition is used sparingly in a situation-specific manner. It should be noted the overall level of evidence provided within these RCTs has been deemed “weak” by the ASCO and thus more clinical trials would be necessary[103]. Nevertheless, nutritional interventions seem to have some positive impact to combat cancer cachexia, particularly with consumption of PUFA through oral nutritional supplements.

2.1.4.2 Pharmacological Interventions as a Treatment for Cancer Cachexia

The current evidence is insufficient to endorse any pharmacologic agent to improve cancer cachexia outcomes according to the ASCO and thus, no FDA-approved medications currently exist with the exception of anamorelin which was approved in Japan[103]. Some of the pharmacological agents tested clinically in cancer cachexia include progesterone analogs, corticosteroids, anamorelin, cannabinoids, androgens, non- steroidal anti-inflammatory drugs (NSAIDS) and thalidomide. While these drugs do not produce sufficiently positive results to be a licensed treatment option in this disease, their marginal benefits to cancer patients are worth discussion and investigation.

Progesterone is an endogenous steroid and sex hormone involved in the menstrual cycle, pregnancy and embryogenesis. In the most recent meta-analysis done on megestrol acetate in anorexia-cachexia syndrome, in 23 RCTs with cancer patients, those who took megestrol acetate were more likely than those who took placebo to exhibit improved appetite, weight and quality of life[107]. While these results are positive outcomes for cancer cachectic patients, megestrol acetate was associated with increased risk of death, thromboembolic events and edema[107].

Corticosteroids are anti-inflammatory drugs used to treat conditions like rheumatoid arthritis or lupus. There has been limited exploration of corticosteroids in cancer cachexia except for a trial completed in 1974 using dexamethasone on 116 advanced gastrointestinal cancer patients[108]. Patients reported marginal improvements in appetite and sense of well-being but there was no benefit to survival and there were no reports of body weight or changes in muscle mass[108].

Anamorelin is a ghrelin receptor agonist, with appetite-enhancing and anabolic effects. Anamorelin is perhaps the most clinically assessed cancer cachexia therapy to date with the agent advancing as far as phase III RCTs in cancer patients with non-small-cell lung cancer and

cachexia[109,110]. A meta-analysis completed in 2017 evaluating four RCTs that used various doses of anamorelin across 12 weeks yielded positive results but with high heterogeneity[111]. In the two-part Phase III clinical trial, 979 patients with advanced non-small-cell lung cancer and cachexia were split into a placebo group and 100mg daily oral administration of anamorelin[109,110]. This trial demonstrated that anamorelin increased lean body mass but did not improve hand grip strength [109,110]. Interestingly, anamorelin did not receive approval from the FDA or any other national drug agency, perhaps due to limited reporting of safety data[112].

Given the ubiquitous reporting of increased inflammation in cancer cachexia, NSAIDS are a popular pharmacological agent in the pursuit for a cancer cachexia treatment. A meta-analysis evaluated four studies that used a range of NSAIDS (aspirin, celecoxib, indomethacin, prednisolone and ibuprofen with megestrol), across a range of cancer types (gastro-intestinal, head and neck, and advanced small cell lung cancer)[113]. These four studies reported some positive therapeutic effect on quality of life, performance status, inflammatory markers, weight gain and survival but these patient cohorts lacked uniformity of inclusion criteria and had limited sample sizes[113]. Future trials should include higher patient numbers, establish standardized NSAID treatment and intervene at an early point in cachexia development[113].

Last, both anti-myostatin and anti-GDF15 therapy interventions have shown some promise in treating cancer-induced muscle wasting. Indeed, myostatin levels in cancer cachexia have been shown to be elevated in both preclinical models [114] and humans with cancer cachexia[115]. Likewise, GDF15 is a recently identified cachectic regulator in cancer cachexia[116]. In colorectal and prostate preclinical models of cancer cachexia, *in-vivo* administration of myostatin neutralizing antibodies have been shown to preserve muscle mass and mouse grip strength without modulating tumour size [117]. Similarly, *in-vivo* administration of GDF15 neutralizing antibodies have also been shown

to preserve muscle mass and function in an ovarian cancer cachexia model [118]. Thus, it would be interesting to see if GDF15 or myostatin-targeted therapies progress from preclinical investigations to clinical trials.

2.1.4.3 Exercise as a Treatment for Cancer Cachexia

While there is currently no clinical trial completed with positive results reported in exercise as a therapy for cancer cachexia, the ASCO thus does not recommend exercise for treatment[103]. A phase II clinical trial using a multimodal approach, examining the feasibility and safety of using PUFA supplements, exercise and anti-inflammatory medication (celecoxib) in cancer patients with lung or pancreatic cancer under chemotherapy yielded no statistical difference on physical activity, muscle mass, survivability or Serious Adverse Events[119]. This was expected with the low sample size of 41 and is currently moved to phase III clinical trials[119].

Current clinical trials evaluating exercise as a therapy in cancer cachexia yield no sufficiently positive impact of exercise on disease outcomes, but these trials are considered very low quality and thus higher quality conducted studies are necessary[120]. While the phase III RCT discussed above may better identify if exercise is beneficial to maintaining skeletal muscle mass throughout cancer cachexia in a clinical context, preclinical models have already demonstrated promising results in several cancer types[17].

For extensive review on the effects of exercise on cancer cachexia outcome measures in preclinical models, the reader is directed towards *Tsitkanou et al.* 2022[17]. Briefly, exercise has shown to increase protein synthesis, increase mitochondrial health, decrease markers of inflammation and markers of protein degradation. Indeed, in the $Apc^{Min/+}$ model repeated stimulated eccentric contractions (ECC; 100Hz, 10 contractions, 6 sets) over 2 weeks increases muscle protein

synthesis and oxidative capacity[121]. In the C26 model, unstructured, volitional exercise improves mouse survival, muscle fiber size and decreases expression of canonical markers of the ubiquitin-proteasome pathway (Atrogin-1 and MURF-1) and autophagy (LC3B and p62)[122]. Even in a model of breast cancer, after 6 weeks of endurance exercise 5 times a week in mice with MC4L2 breast cancer cells injected ectopically, markers of inflammation (IL-6) were decreased along with tumour volume[123].

There are also positive effects of exercise on tumour growth. Indeed, in the pancreatic ductal adenocarcinoma model (PDA), mice that underwent aerobic exercise training five times per week at 30 minutes per day exhibited decreased tumour growth through an immune axis mechanism (IL-15/IL-15Rα)[19]. Moreover, exercise seemed to enhance the anti-tumour effects of immune checkpoint therapy (ICB) within this model[19]. It must be noted that these mice are not cachectic at the time of exercise and thus this does not support exercise for cancer cachexia treatment *per se*, however, it still demonstrates proof of principal that exercise – in this case aerobic – can have beneficial impact on tumour biology as well as muscle. Considering exercise has beneficial impact in several preclinical models on skeletal muscle health and some evidence of antitumorigenic effects in the PDA model, it will be interesting to see the results from the multimodal Phase III RCT discussed above. While there is no current therapy for cancer cachexia, there seems to be encouraging data in preclinical models to suggest exercise - especially in combination with PUFA oral administration and NSAIDS – may have great utility in cachexia treatment.

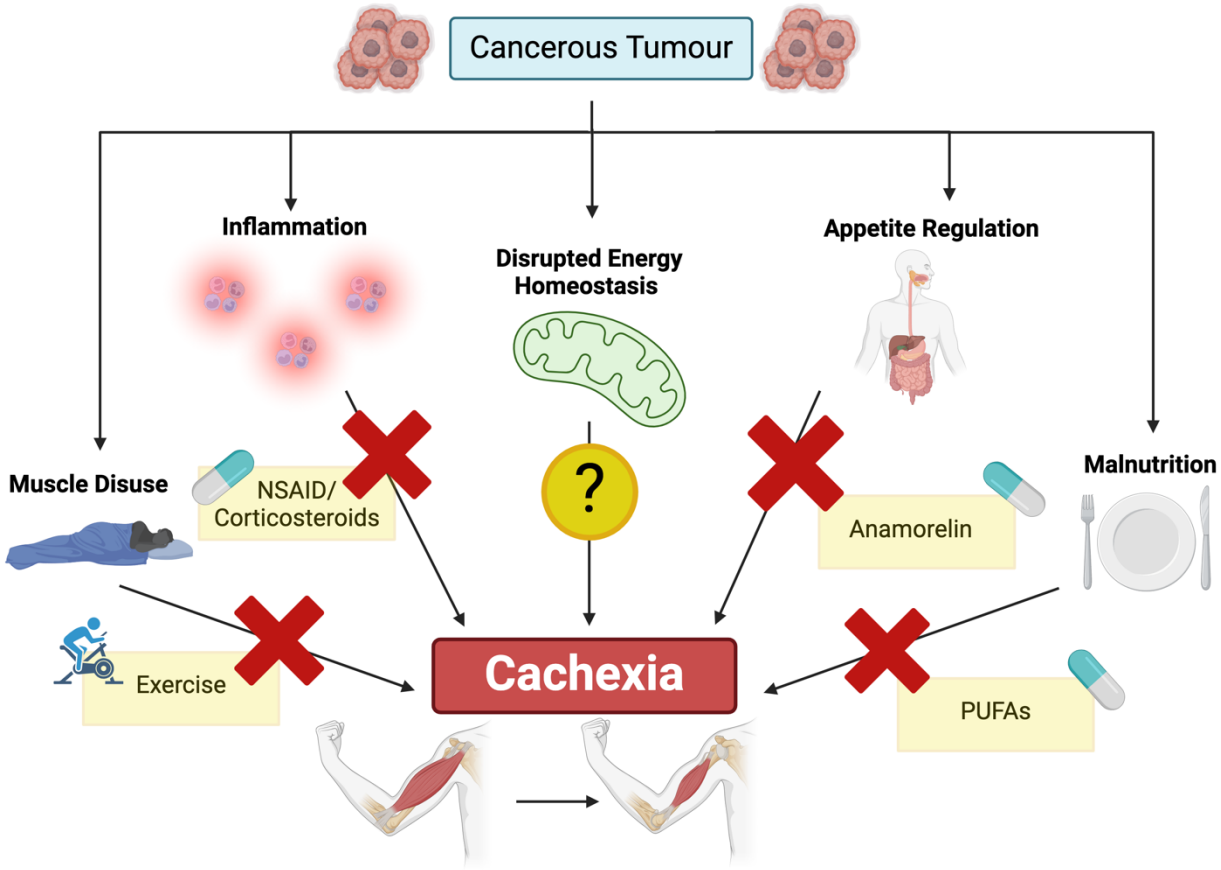

Figure 2-2. Schematic representation of cancer cachexia mechanisms with corresponding therapeutic interventions, Several clinical investigations have been conducted but none have yielded sufficiently positive results to be a licensed treatment. No clinical investigation has directly targeted mitochondria pharmacologically to date.

2.1.5 Preclinical Models for Researching Cancer Cachexia

Several models of cancer cachexia exist, each with their respective pros and cons. While generating the "perfect" model for cancer cachexia is likely impossible given the complexity of the disease for a myriad of reasons, there are some models that are "superior" to others due to their inoculation technique, species immunocompetency and even human disease replication. The following section will review the existing preclinical models of cancer cachexia. There will be no emphases on human cancer cachexia as this section will focus on experimental models that aim to recapitulate the human disease. As there are several cancer cachexia models, a non-comprehensive summary

of only the most commonly used cancer cachexia models is provided in **Table 2-1** to aid in the reader in understanding the literature review. Extra detail is provided in colorectal and ovarian cancer models as this dissertation uses these two models to evaluate the muscle specific and time dependent relationships of mitochondrial stress, force production and atrophy in cancer cachexia.

First, researchers can use cell culture techniques to evaluate cancer cachexia. While these models lack a living organism to replicate the crucial *in-vivo* aspects of cancer, these models still help elucidate disease mechanisms. C2C12 myoblasts are immortalized myoblast cells originating from adult mouse satellite cells. Researchers can co-culture C2C12s with cancer cells, blood serum from cancer cachectic mice, blood serum from cancer patients, ascites fluid from cancer patients and even extracellular vesicles from tumour cells or serum of cancer patients[124–127]. With these techniques, researchers can understand the effect of cancer-related factors on skeletal muscle atrophy and/or proliferation without the introduction of a host organism. These models also hold great utility in testing pharmacological therapeutics for treating cancer-induced cachexia[126]. Indeed, without the usage of a host organism, *in-vitro* results must be supplemented with the usage of a preclinical model to determine the promise of any therapy identified through cell culture. Nevertheless, utilization of cell culture techniques is invaluable to identify precise mechanisms of cancer-induced cachexia.

In-vivo preclinical experimental models of cancer cachexia can vary widely on host organism, species strain, species immunocompetency, inoculation technique, cancer cell type, tumour development time and even metastasis. While a great review is provided on animal models for cancer cachexia by *Ballarò et al. 2016* [128], the cancer cachexia field is evolving rapidly with several new models developing since the publication of this review[118,129–131]. Briefly, models vary widely on the inoculation technique. Inoculations can be performed ectopically (cancer injection occurs

anywhere peripheral to where the cancer cells originate), orthotopically (cancer injection occurs in the matching organ of which the cancer cells originated) or even grow spontaneously within the host organism due to genetic mutations.

Ectopic subcutaneous techniques are arguably most popular technique, likely due to experimental simplicity[128]. However, other ectopic injection methods also exist like intraperitoneal and intramuscular injections[128]. These models are beneficial for their logistical and expertise simplicity to study cancer cachexia. However, these models are also subject to criticism due to the rapid onset of cachexia (14-30 days), artificially large ectopic tumours (up to 30% of host organism body weight), and absence of metastasis which poorly recapitulates the human disease[128]. Foundational cancer cachexia preclinical work conducted in the 1990s utilized Yoshida ascites hepatoma (AH130) in Wistar rats that developed cachexia in as little as 14 days [44,45]. However as of recently, arguably the most used ectopic cancer cachexia models are the LLC and C26 cells subcutaneously inoculated in C57BL6 or CD2F1 mice[128]. While these models provide great value and set the foundation of cancer cachexia literature, experts argue that more orthotopic and metastatic models of cancer cachexia would help with mechanism elucidation and therapy development[13].

Orthotopic models are less popular among the literature, likely due to the complexity of cancer inoculation. Indeed, orthotopic inoculations require surgical expertise that can be difficult for lab groups to conduct. One recent report orthotopically injected patient-derived pancreatic cells (PDX) into the pancreas of NOD.Cg-prkdc II2rg/SzJ mice[132,133]. This model induces muscle wasting similar to that of human cachexia generating small primary tumours and recapitulating metastasis to the liver and lungs[132,133]. While this type of model can be seen as “superior” for its ability to replicate the human disease in mice, these mice still exhibit experimental concerns. Indeed, while this model recapitulates the human disease well, these mice are immunodeficient and thus

mechanism elucidation or therapy development that requires an intact immune system cannot be accurately completed[134]. While all models have advantageous and disadvantageous, it's important to use the model which best pertains to the researcher purpose and hypothesis. While in the pursuit of cancer cachexia mechanism elucidation and therapy development it has been advised to use metastatic orthotopic models[13], however, this isn't possible in all research groups and thus ectopic or cell culture techniques should be utilized.

2.1.5.1 Colon Cancer Models of Cancer Cachexia

In a cross-sectional survey conducted by *Poisson et al*. up to ~70% of colon cancer patients are predicted to develop cachexia throughout cancer progression[31]. Colon cancer cachexia is a popularly researched type of cancer-induced cachexia potentially due to its high prevalence. The two extensively researched models of colon cancer cachexia include the ectopic, subcutaneous C26 model and spontaneous tumour growing $Apc^{Min/+}$ model.

The C26 model has been used extensively throughout the literature summing to 225 original research articles indexed in PubMed when searching "C26" or "Colon-26" and "cancer cachexia" in the last decade. The $Apc^{Min/+}$ model is less popular but extensively used by some research groups. Both models are different in their ability to induce cachexia, however both have shown reproducibility and consistency across the literature when identical model implementation is used (i.e same mouse strain, age, sex, number of cells injected, injection site, tumour development time, etc). Indeed, within the C26 model, 1 million cancer cells are injected into the hindlimb of ~8-week-old CD2F1 mice and generate skeletal muscle wasting and weakness 4 weeks post tumour inoculation[10,11,135,136]. This has been repeated extensively throughout the literature and this model has also been used extensively in preclinical therapy development [137–141]. Thus, while the model

has drawbacks due to its relevance towards the human condition, is has still provided foundational understanding of mechanisms and therapy elucidation. In the *Apc*$^{Min/+}$ model, however, the onset of cachexia is different and more challenging to identify. Indeed, when cancer cells are inoculated, it is simple to define the amount of time cancer has been introduced into the organism as it was manufactured by the experimenter. In the In the *Apc*$^{Min/+}$ model, a nonsense mutation in the adenomatous polyposis coli (*Apc)* gene exists[142]. In the *Apc*$^{Min/+}$ model, mice are characterized by the formation of spontaneous intestinal adenomas beginning at approximately 12 weeks of age[143]. Thus, in this spontaneous tumour growing model, it can be challenging to estimate when cancer has truly initiated as the precise time can vary. In this model, mice tend to generate cachexia at ~20 weeks of age, while some *Apc*$^{Min/+}$ mice will remain weight stable[144]. Mice can then be sub-divided into a "cachectic" and "weight-stable" group to best assess cancer cachexia [144]. With this methodology, cachectic *Apc*$^{Min/+}$ mice exhibit increased markers of inflammation within the skeletal muscle along with decreased muscle mass and force production[144]. This model has also been used to test some preclinical therapies for cancer cachexia, albeit less extensively compared to the C26 model [145,146].

2.1.5.2 Ovarian Cancer Models of Cancer Cachexia

In the same cross-sectional study by *Poisson et al*., up to ~50% of ovarian cancer patients are predicted to develop cachexia throughout cancer progression [31]. However, ovarian cancer is much less studied with limited models available, despite being the most lethal gynecological cancer in women[147]. Indeed, at the inception of this dissertation, there was one preclinical ovarian cancer cachexia model available that requires the usage of a human cancer cell line[148]. Since then, three other models have been published to study ovarian cancer cachexia. Two models each use different

ectopic cancer inoculation and ovarian cell types [118,149]. One model even utilizes a Cre-inducible knock-in allele for *Pik3ca** crossed with heterozygous *Gdf9-iCre*$^{+/-}$ that forces the overgrowth of ovarian follicles generating ovaries that can be up to 250 times larger than healthy ovaries[130]. While this model utilizes a genetic manipulation to induce ovarian tumours, this model does not recapitulate the metastasis that would occur in humans and utilizes a genetic mutation that develops cancer from birth[130]. Nevertheless, this is the only ovarian cancer cachexia model with ovarian cancer growing within the ovaries.

These ovarian cancer cachexia models have been used seldomly throughout the literature, therefore providing limited insight in cancer cachexia pathology. However, these models still accurately demonstrate the body weight loss, muscle loss and muscle atrophy that occur in other cancer cachexia models [118,130,148,149]. Future research is needed to develop more models of ovarian cancer cachexia that best recapitulate the human disease.

Cancer Type	Model	Tumour injection	Species	Time until onset of cachexia
Colon	Colorectal-26 Carcinoma (C26) ---------- *Apc*$^{Min/+}$	Ectopic (subcutaneous) ---------- Genetic mutation: *Apc* gene in colon	Mouse --------- Mouse	~ 4 weeks ---------- ~ 8 weeks
Lung	Lewis lung Carcinoma (LLC)	Ectopic (subcutaneous)	Mouse	~ 4 weeks
Liver	Yoshida Ascites Hepatoma (AH130)	Ectopic (Intraperitoneal)	Rat	~ 2 weeks
Ovarian	PiK3CA* Mouse ---------- TOV21G	Genetic mutation: expression of *Gdf9-iCre* transgene in oocyte ---------- Ectopic (subcutaneous)	Mouse --------- Mouse	~ 11 weeks ---------- ~ 6 weeks
Pancreas	Pancreatic ductal adenocarcinoma (PDAC)	Subcutaneous/ intraperitoneal/ orthotopic	Mouse	~1-2 weeks

Table 2-1. List of commonly used models of cancer cachexia. Partially adapted from *Ballarò et al. 2016* [128].

2.2 Cancer Cachexia Muscle Pathology

Cancer cachexia is multifactorial; therefore, several complications exist in skeletal muscle. However, the primary pathology includes both skeletal muscle wasting and skeletal muscle weakness. While inflammation, autophagy and metabolic stress are well documented skeletal muscle within this disease, these factors are potential mechanisms for primary muscle pathology and were explained in detail in section 2.1.3. The following subsections will focus on the clinical and preclinical studies exemplifying this primary skeletal muscle pathology in cancer cachexia.

2.2.1 Skeletal Muscle Wasting in Cancer Cachexia

The consensus of the definition of cancer cachexia is defined as "a progressive loss of skeletal muscle mass"[3]. Clinical studies have shown extensively that muscle atrophy occurs in cancer cachexia by measuring cross sectional area of fibers from rectus abdominus and quadriceps skeletal muscle biopsies. Indeed, this has been shown in upper gastrointestinal/pancreatic cancer patients[150], stomach cancer patients[151] and non-small cell lung cancer patients[152] (See [153] for a detailed review). There is no evidence to suggest a fiber type shift occurs in gastrointestinal cancer patients[150] or lung cancer patients[154] that exhibit cachexia. However, skeletal muscle atrophy is not the only pathology exhibited in cancer cachexia. In pancreatic cancer patients, there is also evidence of increased fibrotic tissue and collagen content within the rectus abdominus which is positively correlated with percentage of weight loss[155]. Therefore, while skeletal muscle mass loss occurs in cancer patients, the "quality" of muscle also presents as a clinical concern. Last, some clinical cancer cachexia studies also demonstrate that rectus abdominus skeletal muscle presents with increased intramyocellular lipid droplets in a heterogenous cohort of oesophageal, gastric and pancreatic cancer patients[156], and pancreatic cancer patients alone[155]. While the definition of cancer cachexia is the ongoing loss of skeletal muscle mass, these clinical studies demonstrate how skeletal muscle of cancer cachectic patients exhibit other pathology highlighting how skeletal muscle "quality" is also impaired within this myopathy.

Similar but not identical relationships are also seen in preclinical models of cancer cachexia. Skeletal muscle atrophy at late stages of cancer cachexia is a ubiquitous phenomenon that is extensively published across ectopic and/or orthotopic models in ovarian, pancreatic, colon and lung cancer cachexia[12,130,132,136,144]. Interestingly, some reports suggest that fast-twitch type II fibers are subject to atrophy more so than slow twitch fibers, suggesting there is a fiber type shift

towards slow fibers in the C26 model[157]. However, this is not a ubiquitous phenomenon given several preclinical models (including the C26 model) do not demonstrate a fiber type shift[158–160]. This could suggest that this relationship is muscle-specific, or a result of several different fibre typing techniques used. Indeed, studies use different histological techniques such as ATPase stains, succinate dehydrogenase stains and myosin heavy chain (MHC) immunofluorescence. Skeletal muscle collagen content has also been shown to increase in the tibialis anterior of male mice four weeks after LLC inoculation[161]. Interestingly, in this same design but in female mice, the plantaris muscle does not exhibit increased collagen [161]. While it is unclear if this represents a sex difference or muscle-specific response of cancer, it nevertheless demonstrates the heterogeneity in preclinical models regarding muscle "quality." Indeed, fibrosis is well reported in human cancers[155,162], while this seems to be seldomly reported in preclinical models. This could once again represent muscle-specific differences considering most cancer cachexia data in humans seems to come from rectus abdominus biopsies[153], whereas preclinical models tend to use muscles from the hindlimb. Of course, this could also be representative of differing myopathy across different cancer types. The same argument can be made about fat infiltration in preclinical models of cancer cachexia. Indeed, several clinical studies have identified increased fat accumulation in skeletal muscle of cancer patients[155,156], but no preclinical models to date have clearly shown increased fat accumulation in skeletal muscle of tumour bearing animals. This could suggest a drawback in preclinical cancer cachexia models vs clinical patient data that can challenge mechanism elucidation and therapy development. Indeed, this divergence in muscle "quality" parameters could delineate clinical vs preclinical investigations of cancer cachexia. Albeit no preclinical model can replicate the human disease perfectly – especially in the context of cancer – it's worth mentioning that muscle atrophy

appears to be a ubiquitous phenomenon between clinical and preclinical cancer cachexia investigation but not measures of muscle "quality."

2.2.2 Skeletal Muscle Weakness in Cancer Cachexia

In addition to "a progressive loss of muscle mass," the international consensus on the definition of cancer cachexia also includes that the loss in muscle mass (with or without fat mass) leads to "gradual functional impairment" [3]. While "functional impairment" is a broad description, skeletal muscle weakness falls under this definition. Indeed, "functional impairment" is likely primarily meant to define completing tasks of daily living (walking, carrying groceries, going up and down stairs, etc) but could still include more direct measure of skeletal muscle function like isolated muscle contraction. Therefore, this section will first describe the mechanisms that regulate force production, then focus on cancer cachexia-induced muscle weakness in clinical and preclinical studies. While clinical studies typically measure muscle weakness through functional assessments (hand grip strength, stair climb power, short physical performance battery, etc), preclinical models evaluate cancer-induced muscle weakness through more direct measures (*in-situ*/*in-vitro* muscle stimulation in several muscles), thus these models will be discussed differently.

The regulation of force production is coordinated by two main processes: transmission of an action potential and calcium release that induces actin myosin cross-bridge formation[163]. First, an action potential propagates along the sarcolemma and eventually down the T-tubules, where the dihydropyridine receptors (DHPR) sense the changes in membrane potential and allosterically react with the SR ryanodine receptors (RyR1) to release calcium[164]. At this point, calcium binds to troponin C, moving tropomyosin and exposing myosin-binding sites on actin, permitting actin-

myosin crossbridge formation[165]. When myosin is bound to actin, this is known as the "rigor state" where the cross-bridge is kept at a 45-degree angle relative to the filaments[163]. Once ATP binds myosin, myosin dissociates from actin. Hydrolysis of ATP weakly binds myosin at 90 degrees relative to actin filaments and generates ADP and P_i which remain temporarily bound to myosin[163]. Then, the release of P_i from myosin initiates the power stroke, pushing the actin filament and forcing filament "sliding"[163]. At the end of the power stroke, ADP is released from myosin and the myosin head assumes the "rigor state" once again [163]. Cross-bridge formation and filament sliding across numerous sarcomeres generates whole muscle force production. Once an action potential no longer exists, the cell repolarizes, and calcium is actively pumped from the cytosol to the SR via SERCA[163]. Mitochondria are linked to skeletal muscle contraction as SERCA and myosin both require ATP to function and initiate skeletal muscle contraction/relaxation. Moreover, there are several potential redox sensitive proteins involved in contraction[166]. Thus, there are several potential research directions to examine how changes in mitochondrial ATP synthesis or ROS production can cause muscle weakness by modulating a variety of ATP-dependent or redox sensitive pathways that govern contraction.

[163][163]One study compares men with solid tumours who are cachectic vs non-cancer cachectic patients based off weight loss greater than or equal to 5%, and non-cancer controls[167]. Within this study, cancer cachectic patients exhibit deceased hand grip strength, stair climb power and upper body one-repetition maximum (1RM) in the chest press, latissimus pull-down and upper back seated row compared to control (non-cancer patients)[167] Interestingly, however, only stair climb power and chest press 1RM was significantly lower in the cancer cachectic group compared to the non-cancer cachectic patients and controls[167]. Moreover, there was no reported weakness in lower body 1RM exercises like hip extension, knee flexion or knee extension in cancer cachectic

patients[167]. In a longitudinal study evaluating thoracic and gastrointestinal cancer patients with cachexia (also defined by a recorded body weight loss of greater than 5%), patients were assessed at baseline, 4 weeks and 8 weeks evaluating isometric quadriceps and hamstrings strength, hand grip strength, standing balance and 10-minute walk time[168]. This investigation interestingly revealed no differences in functional assessments of cancer patients which is a likely result of a low sample size due to high dropout rate of participants[168]. Interestingly, in a recent investigation completed over 41 medical institutions in China, 14,682 cancer patients were studied to compare hand grip strength to prognosis in cancer cachexia to produce a potential predictor of cancer survivability[169]. This investigation revealed that hand grip strength was a strong predictor of survival in cancer patients suggesting that using hand grip strength could be a very useful and efficient tool to predict cancer patient prognosis[169].

In preclinical models of cancer cachexia, skeletal muscle weakness is popularly measured via limb grip strength and in-*situ*/*in-vitro* muscle stimulation. In the C26 model of cancer cachexia, there are clear decreases in mouse forelimb grip strength in tumour bearing mice[136]. This is also observed in a pancreatic cancer (KPC) and LLC mouse models of cancer induced cachexia[170]. The C26 model also exhibits muscle weakness evaluated through the force-frequency relationship in the tibialis anterior[136], diaphragm[158] soleus and extensor digitorum longus muscles [171]. Tibialis anterior skeletal muscle weakness is also observed in within the $Apc^{Min/+}$ model of cancer cachexia[144]. Interestingly, recent reports suggest that that there is a loss of motor unit connectivity (compound muscle action potentials and motor unit number estimation) in the C26 model and with chemotherapy-induced muscle weakness[172]. This suggests that there could be central nervous system contributors to muscle weakness in cancer in addition to peripheral muscular-mechanisms of weakness. Interestingly, however, all of these reports of skeletal muscle weakness occur at end

stage of tumour development and the onset of cachexia. It would be valuable to understand the time at which muscle weakness occurs within these models to best understand the time-course development of muscle weakness and atrophy in cancer cachexia muscle pathology.

2.3 Introduction to Mitochondrial Bioenergetics

Bioenergetics is the quantitative study of energy transductions that occurs in living cells. Mitochondria are double membraned organelles that harness energy from macronutrients (carbohydrates, fats and amino acids) through several redox reactions to generate adenosine triphosphate (ATP). ATP is considered the "energy currency" of the cell as it is used as the primary source of energy for numerous physiological reactions. Thus, mitochondrial bioenergetics can be understood as the study of energy transduction.

Briefly, mitochondria harness energy by utilizing a series of electron carriers and enzymes to force protons to translocate into the intermembrane space, which then use the proton motive force generated by this concentration gradient to drive ATP generation. A natural by-product of this energy transduction is the formation of reactive oxygen species (ROS). ROS is an essential cell signaling molecule for numerous physiological processes. The following section in this literature review will discuss the precise mechanisms that regulate ATP generation from macronutrients, ROS formation as a natural consequence of this process and the mechanisms that regulate high-energy phosphate shuttling in and out of the mitochondria to drive ATPases.

2.3.1 Oxidative Phosphorylation

Mitochondria are double membraned organelles with an outer membrane (OM), inner membrane (IM) and intermembrane space (IMS) in between both membranes. Embedded within the IM are

the five proteins of the electron transport chain [80]. The two electron carriers – nicotinamide adenine dinucleotide (NADH) and flavin adenine dinucleotide ($FADH_2$) – regulate and catalyze the electron transfer of electrons through several redox reactions within the electron transport chain (ETC) to generate free energy[80]. The use of free energy to produce ATP was first proposed by Peter Mitchell in 1961 and is now well accepted as the chemiosmotic theory[173]. Indeed, the chemiosmotic theory of oxidative phosphorylation defines the series of redox reactions coupled to H^+ ions crossing the IM and eventually passing through the OM, down the concentration gradient, back into the mitochondrial matrix to harvest ATP from free energy [173]. Within the ETC there are the five protein complexes are known as: NADH ubiquinone oxidoreductase (complex I), succinate dehydrogenase (Complex II), cytochrome bc_1 complex (Complex III), cytochrome oxidase (complex IV) and ATP synthase (complex V) and two electron acceptors in the IM known as ubiquinone and cytochrome *c*[174]. Through a series of redox reactions, this complex process begins when NADH or $FADH_2$ transfer electrons to Complex I or Complex II respectively[80]. These electrons are then transferred across to ubiquinone, Complex III, cytochrome *c* and finally Complex V where these electrons meet O_2 – the final electron acceptor[80]. At the same time, while these electrons shuttle through the ETC, hydrogen ions (H^+) translocate from the mitochondrial matrix (negatively charged) into the IMS (positively charged), generating a proton motive force (ΔP)[80]. This ΔP pushes H^+ back through to the mitochondrial matrix through Complex V to synthesize ATP from adenosine diphosphate (ADP) and inorganic phosphate (P_i), powered by the flow of protons against the electrochemical gradient[80]. The coupling of energy produced from the oxidation and phosphorylation of ADP is termed oxidative phosphorylation (OXPHOS) and is predicted to contribute to 95% of the ATP produced in the cell under basal conditions[80]. See **Figure 2-3** for a schematic representation of this process.

OXPHOS is tightly regulated through cellular energy demand. As the cell requires energy, the cell can upregulate OXPHOS to drive the generation of ATP. Moreover, OXPHOS is largely regulated by the availability of ADP and Pi as a substrate for phosphorylation[174]. ATP and ADP turnover can control both the rates of electron transfer, citric acid cycle and glycolysis[174]. Therefore, intracellular ADP concentrations or the mass action ratio of ATP/ (ADP + P_i) is a key index of a cell's energy status[174]. It is thus important to indicate the importance of mitochondrial ADP sensitivity especially in the context in disease and myopathy.

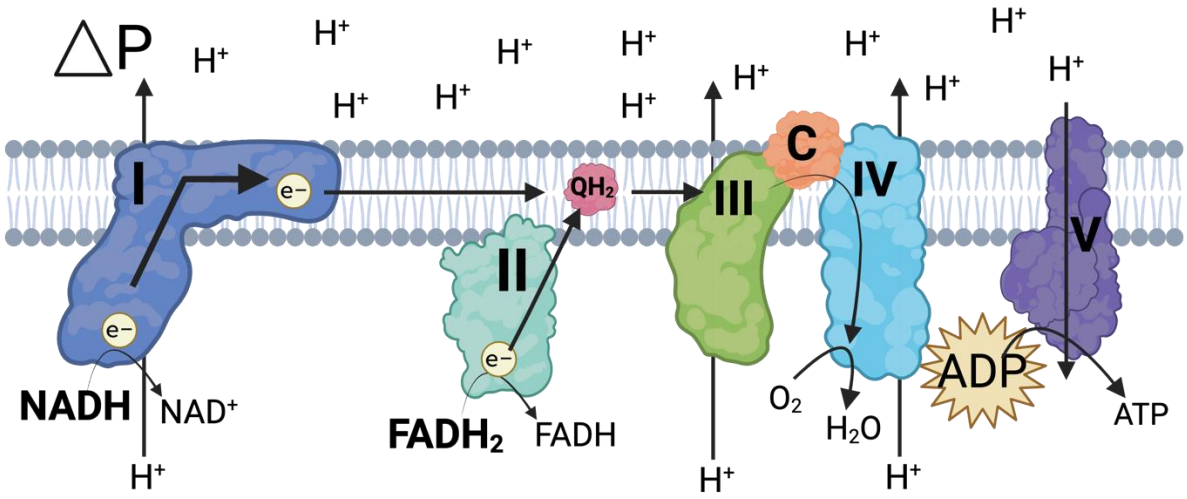

Figure 2-3. Schematic Representation of the ETC. Within the IM lies the five complexes and two electron carriers (NADH and $FADH_2$). These electron carriers can transfer electrons through redox reactions that release free energy. This process promotes complexes I, III and IV to pump protons from the matrix to the from the matrix into the IMS, against the concentration gradient. This energy an electrochemical gradient in the IMS that can be used to power the phosphorylation of ADP to produce ATP.

2.3.2 ROS Formation

During OXPHOS, there are several steps along the ETC at which mitochondria can produce ROS. This is a natural by-product of OXPHOS and at low concentrations is beneficial for the cell as

ROS acts as a second messenger to regulate various physiological processes[175]. At high concentrations, however, ROS can initiate cell growth arrest and cell death which can compromise cell survival[176].

As discussed above, electrons pass through the ETC to form water at Complex IV once electrons meet O_2, the final electron acceptor. However, sometimes, electrons can slip prematurely before they reach O_2 at Complex IV. When this occurs, the primary ROS superoxide anion ($O_2^{\bullet-}$) is generated by the one electron reduction of O_2[80]. This can occur when there is a high ΔP because of increased H^+ ions within the intermembrane space. During state II mitochondrial respiration (an artificial cellular state that does not occur *in-vivo*), there is no ADP present within the cell but maximal levels of reducing equivalence NADH or $FADH_2$. In this context, there are maximal levels of premature electron slip and thus ROS formation due to an artificially high ΔP. Under state III mitochondrial respiration, ADP is present within the cell and thus premature electron slip is less likely, albeit still occurs due to a more physiologically relevant ΔP. This concept of high ΔP and premature electron slip is depicted in one experimental example at Complex I in **Figure 2-4** within the context of forward electron flow and maximal NADH reducing equivalence.

Premature electron slip can occur at multiple locations along the ETC including Complex I, II, II oxoacid dehydrogenase complex, electron-transferring flavoprotein-ubiquinone oxidoreductase, dihydroorotate dehydrogenase and glycerol-3-phophate dehydrogenase[177,178]. At this point the superoxide anion can dismutate to from oxygen and hydrogen peroxide (H_2O_2) catalyzed by superoxide dismutase (SOD). In most cases, H_2O_2 produced is rendered inactive by glutathione peroxidases where reduced glutathione peptide reduces an H_2O_2 molecule generating O_2 and H_2O[80]. While ROS can generally be perceived as “harmful” to a cell, ROS is essential for cell signaling. Oxidative stress occurs when an imbalance exists between the generation and removal

of ROS within a cell. Oxidative stress can result in irreversible changes to a cell like the initiation of apoptosis, autophagy and hypoxia[178].

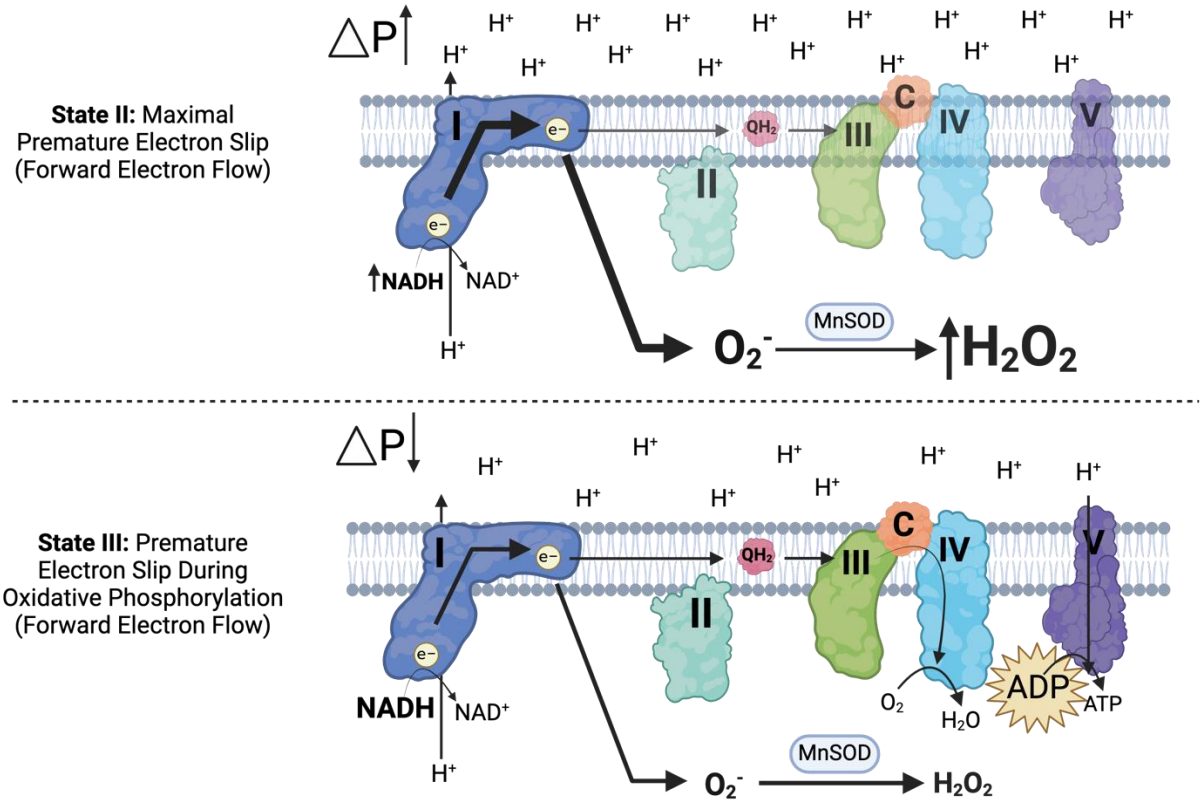

Figure 2-4. State II and State III premature electron slip. In an experimental context, mitochondrial H_2O_2 emissions can be assessed by supporting mitochondria with maximal amounts of pyruvate and malate to generate maximal NADH reducing equivalence (not shown). In state II (top) with maximal NADH reducing equivalence generates a high ΔP which forces premature electron slip. In state III (bottom), ADP can catalyze Complex V and lower ΔP, resulting in less premature electron slip.

2.3.3 High Energy Phosphate Shuttling

The mitochondrial OM, IMS and IM contain several transmembrane proteins that permit energy (in the form of high energy phosphates) to leave and enter the mitochondria. On the OM, the voltage-gated anion channel (VDAC) facilitates the translocation for metabolite transportation between the mitochondria and IMS. VDAC is responsible for the translocation of ATP out of the

mitochondria from the mitochondrial matrix and ADP into the mitochondria from the cytoplasm[179]. Adenine nucleotide translocators (ANT) is embedded within the IM and facilitates the transport of ATP and ADP between the IMS and mitochondrial matrix. Also, within the IMS, the enzyme mitochondrial creatine kinase (mtCK) binds directly to VDAC on the OM and cardiolipin on the IM. mtCK catalyzes the high energy phosphate transfer from ATP to creatine to generate phosphocreatine (PCr)[180]. PCr is then translocated out of the mitochondria through VDAC where it can provide high energy phosphate to several ATPases[181].

High energy phosphate can be shuttled in and out of the mitochondria through two channels: the creatine dependent phosphate shuttling system and the creatine independent phosphate shuttling system, as depicted in **Figure 2-5**. As ATP is produced through OXPHOS, ATP can exit the mitochondrial matrix one of two ways. First, in the absence of creatine, ATP can translocate through ANT in the IM and VDAC in the OM where it then diffuses within the cytosol to be utilized by myosin ATPase, sarco/endoplasmic reticulum Ca^{2+} ATPase and NA^{+}/K^{+} ATPase, a variety of kinases and other ATP-dependent pathways[182]. The ADP produced as a result of ATP hydrolysis for the purpose of harvesting energy can then re-enter the mitochondrial matrix through ANT and VDAC and catalyze the generation of new ATP at Complex V. This process is then repeated cyclically. It is predicted that ~20% of ATP produced by mitochondria is translocated through this creatine independent pathway, at least in cardiomyocytes[183]. In the presence of creatine ATP exits through ANT and binds to mtCK which transfers the high energy phosphate from ATP to creatine to generate PCr and ADP [180]. At this point, ADP can re-enter the mitochondria providing ATP synthase with new substrate for more ATP synthesis. At the same time, PCr exits the mitochondria though VDAC and reacts with cytosolic creatine kinase to generate ATP[180]. This creatine dependent system is believed to be responsible for ~80% of the

ATP exiting the cell[183]. This is likely a result of the ability of Cr/PCr to shuttle through the mitochondria faster than ATP/ADP. Indeed, spermatozoa's single mitochondrial structure reveal that PCr and Cr possess different diffusion rate compared to ADP and ATP[184], specifically; ADP diffusion is 2000 times slower compared with creatine and ATP is 7 times slower than PCr[184].

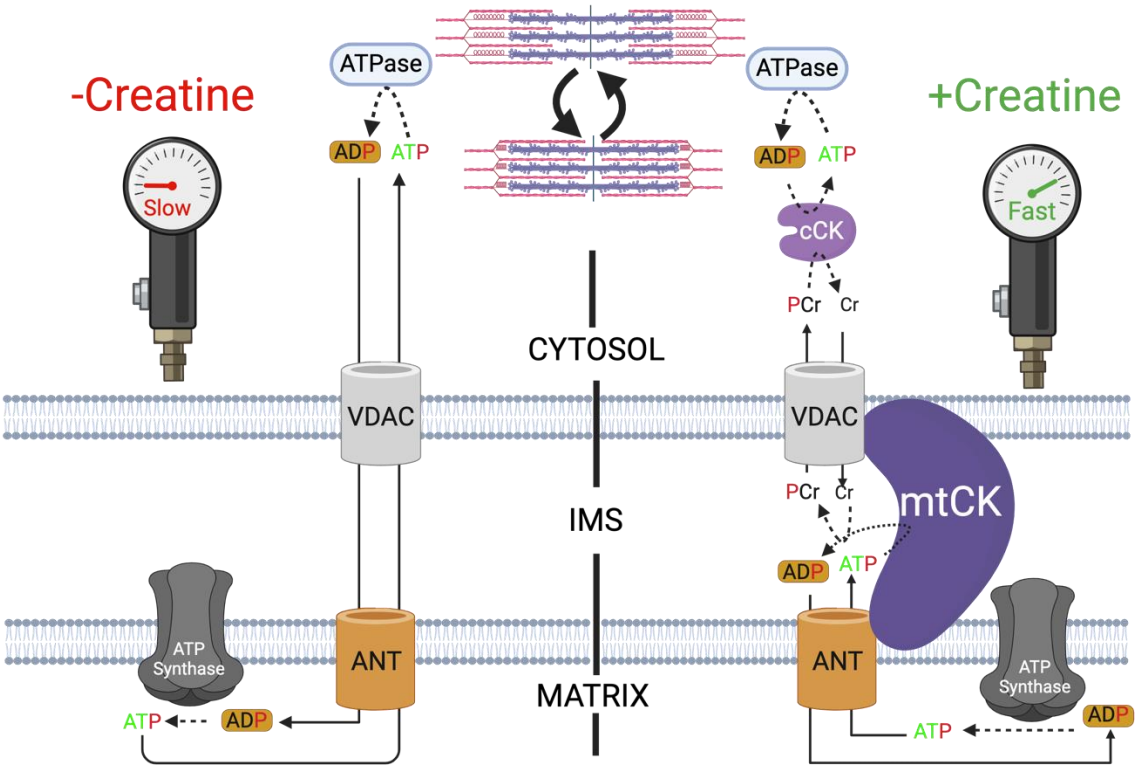

Figure 2-5. Model of Creatine Dependent and Creatine Independent High Energy Phosphate Shuttling. The creatine independent phosphate shuttling system (depicted on the left) demonstrates how ADP and ATP rely on diffusion to shuttle in and out of the mitochondria. The creatine dependent system (right) uses mtCK to catalyze the transfer of a high energy phosphate from ATP to Cr to create PCr. PCr can then diffuse to several kinases and ATPases. This figure was partially adapted from previous work [180,183–185].

2.3.4 Mitochondrial Therapeutics

Growing literature has gone into developing mitochondrial targeted antioxidants given the important role mitochondria play in the regulation of energy homeostasis and cell survival. Sometimes mitochondrial therapeutics can be loosely termed as "antioxidants." However, the term antioxidant is best defined as "any substance that, when present at low concentrations compared to those of an oxidizable substrate, significantly delays or prevents oxidation of that substrate" [186]. Several oxidizable substrates exist in the cell like proteins, lipids, carbohydrates and DNA, therefore, an "antioxidant" must function to prevent the formation of free radicals, scavenge ROS or their precursors. Several types of antioxidants exist including vitamins, inorganic antioxidants, synthetic antioxidants, butylated hydroxytoluene and a range of plant-derived polyphenols[187]. However, while the mechanisms of these antioxidants are well understood, these antioxidants do not accumulate preferentially in the mitochondria, the major site of ROS generation.

A predominant mechanism antioxidant drugs can target mitochondria is through mitochondrial biophysical properties (e.g. highly negative mitochondrial matrix)[187]. Several mitochondrial targeted antioxidant drugs have been developed through conjugation with the lipophilic cation triphenylphosphonium (TPP). Lipophilic cations can pass easily through lipid bilayers because their charge is dispersed over a large surface area and the charge gradient drives their accumulation into the mitochondrial matrix[188]. MitoQ is an extensively used mitochondrial-targeted antioxidant with Coenzyme Q conjugated to TPP which has been shown to scavenge superoxide, peroxynitrite as well as prevent lipid peroxidation[187,188]. Sk compounds with SkQ1 being among the most commonly used - is another example of a mitochondrial-targeted antioxidant conjugated to TPP

but instead of Coenzyme Q, SkQ1 is comprised of plastoquinone – a compound equivalent to ubiquinone and found to be a stronger antioxidant than Coenzyme Q, at least in yeast cells[189]. Both MitoQ and SkQ1 are commercially available to purchase and can easily support research endeavours. MitoQ but not SkQ1 has been evaluated in preclinical models of cancer cachexia as discussed in section 2.4.3.

Mitochondrial targeted antioxidants could also act through other mechanisms than just through mitochondrial biophysical properties. Indeed, SS tetrapeptides are aromatic-cationic peptides that bear alternating aromatic and basic amino acid residues with some compounds even containing a 2',6'-dimethyltyrosine (Dmt) residue [187]. These compounds bind directly to cardiolipin on the mitochondrial IM and are shown to improve oxidative phosphorylation, decrease ROS and prevent the dissociation of cytochrome *c* from cardiolipin, thus preventing cell death[190]. Experimentally, it is challenging to obtain SS tetrapeptides as they are not commercially available and are patented. However, One SS tetrapeptide, SS-31, has been tested in the C26 preclinical model of cancer cachexia and is discussed in section 2.4.3.

2.4 Mitochondria and Cancer Cachexia

There are several reports of mitochondrial stress in cancer cachectic skeletal muscle both in clinical and preclinical studies. As discussed earlier within the literature review, alterations in energy homeostasis are one of the several mechanisms that contribute to cancer cachexia muscle myopathy. The following section will review key clinical and preclinical studies evaluating mitochondrial function in cancer cachexia and discuss current studies that have pharmacologically targeted mitochondria in cancer cachexia pathology. While changes in mitochondrial morphology

have also been linked to cachexia, these alterations can also reflect mitochondrial function and thus this review will only focus on bioenergetic adaptations due to cancer.

2.4.1 Mitochondrial Oxidative Phosphorylation in Cancer Cachexia

As described above, mitochondrial OXPHOS is the multi-enzymatic process whereby mitochondria harvest energy in the form of ATP from macronutrients. In one preclinical study using the LLC model of cancer cachexia, decreases in mitochondrial respiration (OXPHOS) has been shown to occur prior to the onset of muscle atrophy using permeabilized muscle fibers[12]. This was established using the respiratory control ratio (RCR) – an index of ATP coupled mitochondrial oxygen consumption by using the ratio of state III respiration (ADP-stimulated) to State II (absence of ADP). A high RCR suggests mitochondrial capacity to oxidize substrate for the generation of ATP is highly efficient, while a low RCR can imply the capacity of mitochondria to generate ATP is inefficient[191]. Within the LLC model, decreases in the RCR were observed in the plantaris at timepoints during - and surprisingly, before- the onset of cachexia or muscle atrophy[12]. This is also observed in the C26 model, whereby RCR is decreased in the soleus of tumour bearing mice at the same time cachexia was established[10]. Similar to the LLC model, it would be interesting to observe if decreases in OXPHOS occurred before the onset of cachexia to understand if early decreases in ATP synthesis is a consistent myopathy within this disease. These findings are also consistent with cell culture experiments. Indeed, by coculturing C2C12 myotubes with LLC conditioned media for 2 and 24 hours, C2C12 myotubes exhibited decreased ATP-related oxygen consumption (oligomycin-supported respiration as a percent of basal respiration)[124]. Interestingly, C2C12 myoblasts cocultured with LCM seem to exhibit decreased maximal cytochrome oxidase activity, suggesting alterations could occur at Complex IV within the ETC[124]. However, there are

also some reports of unaltered mitochondrial OXPHOS in cancer cachexia. Indeed, in a rat model of cancer cachexia whereby rats were inoculated with peritoneal carcinosis (gastrointestinal cancer), mitochondrial oxygen consumption measured in isolated quadriceps mitochondria yielded no changes in the RCR of the tumour-bearing rats compared to pair-fed controls[192]. However, while the RCR was unchanged, State III mitochondrial respiration was still decreased compared to pair-fed controls, along with decreased maximal Cytochrome *c* oxidase protein content and activity[192]. Therefore, while there were no differences in the RCR, this model still exemplifies alterations in OXPHOS. To our knowledge, no study to date has evaluated mitochondrial ADP-sensitivity in cancer cachexia. While the RCR is a valuable index of mitochondrial efficiency, evaluation of ADP sensitivity would provide insight on OXPHOS across a range of metabolic demands for the cell. Indeed, most studies report maximal ATP synthesis by using maximal concentrations of ADP to challenge the cell. In reality, these physiological parameters do not exist *in-vivo*. While these evaluations are still useful, especially in the context of maximal enzymatic activity – a more physiologically-relevant index of mitochondrial OXPHOS could give better insight on mitochondrial function within this myopathy.

To our knowledge, only one study has evaluated mitochondrial OXPHOS in a clinical setting within cancer cachexia. Indeed, *Dolly et al*. recently used pectoralis major muscle from pancreatic or colorectal cancer patients to determine the association between mitochondrial energy efficiency and muscle atrophy[193]. Interestingly, this study identified decreases in the RCR between non cachectic cancer patients and severely cachectic cancer patients[193]. Moreover, there were no differences in coupled mitochondrial respiration (state III), however, there were increases in uncoupled mitochondrial respiration (State IV) in the mild and severe cancer cachectic groups versus non cachectic cancer control group[193]. Therefore, while there is no change in ATP-

producing oxygen consumption in cancer patients, there are increases in non-ATP producing oxygen consumption[193]. This is consistent with reports in preclinical studies whereby cancer cachectic muscle exhibits coupling inefficiency.

2.4.2 Mitochondrial Reactive Oxygen Species in Cancer Cachexia

A natural byproduct of OXPHOS is ROS emission through premature electron slip from the ETC. Oxidative stress in cancer cachexia has been well researched in preclinical models over the last number of years. In the LLC preclinical cancer cachexia model, H_2O_2 emissions is increased in the plantaris muscle as early as 1 week after LLC inoculation – well before the onset of cachexia (4 weeks post-inoculation in this preclinical model)[12]. These H_2O_2 emissions remained increased throughout cancer progression and actually decreased at the onset of cachexia, such that H_2O_2 emissions were the same as control mice by 4 weeks of tumour bearing [12]. Interestingly, within the C26 model, mitochondrial H_2O_2 emissions are actually decreased in the quadriceps of tumour bearing mice compared to control mice at the same time cachexia occurs[11]. Decreases in H_2O_2 emissions during cachexia could be reflective of less mitochondrial content at this time point[12]. Future work should identify if increases in H_2O_2 also occur early in cancer development within the C26 model as it does in the LLC to understand if increased ROS is an early signal in cancer cachexia myopathy.

Direct measures of H_2O_2 as an index of premature electron slip are valuable to identify the direct mitochondrial sources of ROS within a cell, however this measure can be rapidly removed by antioxidants. Thus, while these measures are physiologically relevant to recapitulate the conditions *in-vivo*, other markers or oxidative stress exist that can provide insight on the redox state of the cell albeit with minimal accuracy on the source of ROS. For example, proteins with exposed cysteines are a major target for radicals and two-electron oxidants in biological systems that can

be oxidized. Protein carbonylation, 3-nitrotyoisine and 2-hydroxy-4-noneal (4HNE) formation are commonly measured markers of protein oxidation by either ROS or even reactive nitrogen species (RNS)[194]. In the AH-130 Yoshida hepatoma cancer model, during the onset of cachexia at 7 days of tumour bearing, protein carbonylation, 3-nitrotyoisine and 4HNE are increased within the gastrocnemius muscle[195]. Interestingly, some data even suggests that oxidation of fatty acids directly induces muscle atrophy in cancer cachexia[196]. Indeed, using a unique cancer model whereby a highly cachectic renal cancer cell line from a human patient (RXF3930), *Fukawa et al.* identified RXF cachectic mice exhibit increased ROS assessed using MitoSOX-based flow cytometry[196]. Interestingly, when a fatty acid oxidation inhibitor is administered to RXF cachectic mice (etomoxir), mitochondrial ROS is decreased[196]. At the same time, myofiber size is increased compared to non-cachectic controls, suggesting that decreasing ROS through inhibition of fatty acid oxidation can lead to positive outcomes in this murine model of cachexia.

To our knowledge, this same study is the only study to suggest oxidative stress could be increased in cancer patients. Using muscle biopsies of gastrointestinal cancer patients, this study demonstrates a positive correlation between 8-oxoguanine formation (index of DNA lesion as a result of ROS modifications[197]) and cachexia[196]. While this is limited data in the context of oxidative stress in human cancer cachexia, this does suggest the possibility that oxidative stress is also increased in human cancer cachexia as it occurs in preclinical models.

2.4.3 Mitochondrial Therapeutics in Cancer Cachexia

To our knowledge, three studies to date have evaluated the effectiveness of mitochondrial therapeutics on preclinical cancer cachexia models. Interestingly, all studies were conducted using the C26 model.

Elamipretide, popularly known as SS-31, is a mitochondrial targeted drug that inhibits cardiolipin oxidation. Cardiolipin are phospholipids of the mitochondria comprising about 20% of the inner mitochondrial membrane[198]. Two studies have evaluated the effectiveness of this drug on C26 tumour bearing mice. Daily subcutaneous administration of 3mg/kg body weight SS-31 to C26 tumour bearing mice preserved diaphragm force production and fiber cross sectional area[139]. Moreover, SS-31 also improved respiratory function by improving tidal volume, breathing frequency and ventilation[139]. SS-31 lowered succinate-supported ROS production in both the heart and diaphragm using permeabilized fiber bundles and Amplex red-based spectrofluorometry[139]. In a separate investigation, whereby C26 mice received daily intraperitoneal injection of 2mg/kg body weight SS-31, body wasting, and glycolytic fiber area were partially preserved[141]. Moreover, succinate dehydrogenase total activity was also protected in SS-31 injected C26 mice, however these was not related to final ATP concentrations nor was there any change in oxygen consumption of gastrocnemius isolated mitochondria from C26 mice receiving chemotherapy (oxaliplatin and 5-fluorouracil) and C26 mice receiving chemotherapy and SS-31[141]. Last, protein content of some markers of autophagy were lowered with SS-31 treatment to C26-chemotherapy mice suggesting the drug may counteract excessive autophagy[141].

MitoquinoneQ (MitoQ) has also been tested in the C26 model of cancer cachexia. MitoQ is a lipophilic cation (tetraphenylphophonium – TPP) joined to an antioxidant quinone by a 10-carbon alkyl chain which is believed to insert in the inner mitochondrial membrane[199]. MitoQ administration of 25mg/kg in the drinking water of C26 mice improved body weight loss without affecting tumour size[140]. Moreover, MitoQ partially preserved tibialis anterior and gastrocnemius muscle mass while also partially preserving whole body grip strength[140]. Interestingly, there was also less mRNA content of E3 ligases Atrogin-1 and MURF-1 in C26 MitoQ treated mice

compared to C26 TPP treated controls consistent with preserved muscle mass[140]. While the current data on mitochondrial therapeutics in cancer cachexia is limited, future studies should assess its effectiveness in more preclinical models to establish its efficacy to be tested in humans.

3 RESEARCH PURPOSES & OBJECTIVES

Cancer can impair skeletal muscle mass and function. While previous literature has identified that cancer can induce skeletal muscle weakness, atrophy and alterations to mitochondrial function, it currently remains unknown what the time-dependent and muscle-specific myopathy of cancer is in both the C26-ectopic and epithelial ovarian cancer (EOC) – orthotopic model. Moreover, the direct relationships between mitochondrial stress and myopathy remain poorly understood.

3.1 Overview of thesis

The overall purpose of this thesis is to characterize cancer cachexia myopathy in two preclinical models as well as target mitochondria pharmacologically within this disease to 1) establish direct links between mitochondria and myopathy in cancer and 2) evaluate the efficacy of mitochondrial therapy in cancer cachexia.

3.2 Objectives and Hypothesis for Chapter 4, Chapter 5 and Chapter 6.

The purpose of this dissertation is 2-fold: to 1) better identify the time-dependent and muscle-specific metabolic and whole muscle responses that occur within cancer cachexia preclinical models and 2) target mitochondria pharmacologically thereafter to identify direct mitochondrial relationships to cancer myopathy and explore the efficacy of mitochondrial therapeutics as a cancer cachexia treatment. We intended to do this through 3 specific objectives:

1) Characterize time-dependent and muscle specific responses in muscle force, mass and mitochondrial alterations within a commonly used subcutaneous ectopic colon cancer model (C26) of cachexia (Chapter 4).
2) Using a similar research design as Objective 1, characterize time-dependent and muscle specific responses in muscle force, mass and mitochondrial alterations but within an

understudied type of cachexia – ovarian cancer – using a novel orthotopic, metastatic preclinical model (Chapter 5).

3) Given Complex I was identified as a source of ROS for Objective 1 and 2, use the mitochondrial-targeted therapeutic SkQ1 to evaluate the efficacy of targeting mitochondria pharmacologically in a clinically relevant orthotopic, metastatic model of ovarian cancer cachexia (Chapter 6).

Objective 1 allowed us to identify skeletal muscle myopathy throughout cancer progression using a rapid, ectopic and commonly used model within the cachexia literature. Objective 2 allowed us to identify if the same skeletal muscle myopathy exists in a clinically relevant, metastatic, and understudied type of cancer cachexia. Characterizing myopathy in two models strengthened our confidence in identified changes induced by cancer, especially considering some myopathy was paralleled between both models. Objectives 1 and 2 were aimed to characterize the muscle-specific and time-dependent myopathy of cancer and therefore insufficient evidence existed to form a hypothesis.

Finally, given from the data generated in Objective 1 and Objective 2, Complex I was identified as a source of ROS, therefore, we used the orthoptic, metastatic model of ovarian cancer cachexia to pharmacologically target mitochondria and evaluate its efficacy as a cancer cachexia therapeutic. While there are several mitochondrial antioxidants that could be used for the purpose of this investigation, SkQ1 was used given it is commercially available over the counter in some European countries and deemed safe in a small clinical trial for dry eye disease[200] and therefore has a history of use in humans. We therefore hypothesized the following for Chapter 6:

1) SkQ1 administration will reduce complex I oxidative stress in cancer skeletal muscle.
2) Lowering oxidative stress with SkQ1 will improve skeletal muscle health by attenuating skeletal muscle mass and force.
3) Modulating skeletal muscle oxidative stress with SkQ1 will improving skeletal muscle health and thus delay the onset of cachexia in tumour bearing mice.

4 Muscle weakness precedes atrophy during cancer cachexia and is linked to muscle-specific mitochondrial stress

This chapter is an original published article. It is presented in its published form.

Muscle weakness precedes atrophy during cancer cachexia and is linked to muscle-specific mitochondrial stress. LJ Delfinis, CA Bellissimo, S Gandhi, SN DiBenedetto, MC Garibotti, AK Thuhan, S Tsitkanou, ME Rosa-Caldwel, FA. Rahman, AJ Cheng, MP Wiggs, U Schlattner, J Quadrilatero, NP Greene, and CGR Perry. The Journal of Clinical Investigation Insight. DOI:10.1172/jci.insight.155147.

Author Contributions: The majority of experiments or this project were carried about by Luca Delfinis. L.J.D grew C26 cancer cells, injected and monitored all mice required for this project. L.J.D performed all functional testing and separated fibers for bioenergetic assessments. Due to the nature of these experiments, two people were required in order to efficiently complete all force and bioenergetic assays on fresh viable tissue. As such, L.J.D completed surgery while C.A.B completed force assessments while S.G assisted with collection and running bioenegetics. L.J.D, C.A.B, M.R.C., N.P.G. and C.G.R.P. contributed to the rationale and study design. L.J.D., C.A.B., S.G. and C.G.R.P. conducted all experiments and/or analyzed all data. C.G.R.P. and L.J.D. wrote the manuscript. All authors contributed to the interpretation of the data and manuscript preparation. All authors have approved the final version of the manuscript and agree to be accountable for all aspects of the work. All persons designated as authors qualify for authorship, and all those who qualify for authorship are listed.

MSc Vs PhD Data Collection:

Some of this work was collected in part throughout L.J.D's MSc. Below is a detailed table of the data that was collected exclusively within the MSc, partially throughout the MSc and exclusively throughout the PhD. No data collected exclusively within the MSc have been included in this dissertation.

	Data collected **exclusively** in **MSc**	Data collected **partially** during **MSc**	Data collected **exclusively** in **PhD**
Figure 4-1		A-F, J (7 of 10)	G-I (3 of 10)
Figure 4-2			ALL
Figure 4-3			ALL
Figure 4-4		ALL	
Figure 4-5			ALL
Figure 4-6			ALL
Figure 4-7		G, H, K (3 of 12)	A- F, I, J, L (9 of 12)
Figure 4-8		G, H, K (3 of 12)	A- F, I, J, L (9 of 12)
Figure 4-9		E, F, M, N (4 of 16)	A- D, G, H, I- L, O, P (12 of 16)
Figure 4-10			ALL
Figure 4-11			ALL
Figure 4-12			ALL
SFigure 4-1		B, D, F, H, J, L (6 of 12)	A, C, E, G, I, K (6 of 12)
SFigure 4-2		B, D, F, H, J, L (6 of 12)	A, C, E, G, I, K (6 of 12)
SFigure 4-3			ALL
SFigure 4-4		E-H, M-P (8 of 16)	A-D, I-L (8 of 16)

STable 4-1: Division of work completed in LJD MSc vs PhD.

Muscle weakness precedes atrophy during cancer cachexia and is linked to muscle-specific mitochondrial stress

Authors: Luca J. Delfinis[1*], Catherine A. Bellissimo[1], Shivam Gandhi[1], Sara N. DiBenedetto[1], Madison C. Garibotti[1], Arshdeep K. Thuhan[1], Stavroula Tsitkanou[2], Megan E. Rosa-Caldwell[2], Fasih A. Rahman[3], Arthur J. Cheng[1], Michael P. Wiggs[4], Uwe Schlattner[5], Joe Quadrilatero[3], Nicholas P. Greene[2], and Christopher G.R. Perry[1†].

Affiliations:

[1]Muscle Health Research Centre, School of Kinesiology, York University, 4700 Keele Street, Toronto, ON, Canada.

[2]Cachexia Research Laboratory, Department of Health, Human Performance and Recreation, University of Arkansas, Fayetteville, USA.

[3]Faculty of Applied Health Sciences, Department of Kinesiology, University of Waterloo, Waterloo, Ontario, Canada.

[4]Mooney Lab for Exercise, Nutrition, and Biochemistry, Department of Health, Human Performance and Recreation, Baylor University, Waco, TX, USA

[5]University Grenoble Alpes and Inserm U1055, Laboratory of Fundamental and Applied Bioenergetics, Grenoble, France, and Institut Universitaire de France, Paris, France.

Email Addresses:

delfinis@yorku.ca; cabellis@yorku.ca; shivamg@yorku.ca; sdiben@my.yorku.ca; mgarib@yorku.ca; thuhan@yorku.ca; st060@uark.edu; merosaca@bidmc.harvard.edu;

fasih.rahman@uwaterloo.ca; ajcheng@yorku.ca; uwe.schlattner@univ-grenoble-alpes.fr; jquadril@uwaterloo.ca; npgreene@uark.edu; cperry@yorku.ca

Key Words: Cancer cachexia, mitochondria, skeletal muscle

†Address for Correspondence:

Christopher Perry, PhD

School of Kinesiology and Health Science

Muscle Health Research Centre

344 Norman Bethune College

York University

4700 Keele Street

Toronto, Ontario M3J 1P3

(P) 416 736 2100 ext. 33232

cperry@yorku.ca

Conflict of Interest: The authors have declared that no conflict of interest exists.

Abstract

Muscle weakness and wasting are defining features of cancer-induced cachexia. Mitochondrial stress occurs before atrophy in certain muscles, but the possibility of heterogeneous responses between muscles and across time remains unclear. Using mice inoculated with Colon-26 (C26) cancer, we demonstrate that specific force production was reduced in quadriceps and diaphragm at 2 weeks in the absence of atrophy. At this time, pyruvate-supported mitochondrial respiration was lower in quadriceps while mitochondrial H_2O_2 emission was elevated in diaphragm. By 4 weeks, atrophy occurred in both muscles, but specific force production increased to control levels in quadriceps such that reductions in absolute force were due entirely to atrophy. Specific force production remained reduced in diaphragm. Mitochondrial respiration increased and H_2O_2 emission was unchanged in both muscles vs control while mitochondrial creatine sensitivity was reduced in quadriceps. These findings indicate muscle weakness precedes atrophy and is linked to heterogeneous mitochondrial alterations that could involve adaptive responses to metabolic stress. Eventual muscle-specific restorations in specific force and bioenergetics highlight how the effects of cancer on one muscle do not predict the response in another muscle. Exploring heterogeneous responses of muscle to cancer may reveal new mechanisms underlying distinct sensitivities, or resistance, to cancer cachexia.

Introduction

Cancer-induced cachexia is a multifactorial syndrome characterized, in part, by a loss of skeletal muscle mass that cannot be fully reversed by conventional nutritional support[3]. This condition leads to progressive reductions in functional independence and quality of life[201] . Such declines in muscle mass also reduce tolerance to anticancer therapies and overall survivability[6,27], and is associated with increased hospitalization time[202]. 20-80% of cancer patients are thought to develop cachexia depending on the type and stage of cancer[4]. However, the time-dependent relationship between muscle atrophy and weakness remains unclear, as does the degree to which this relationship may vary between muscle types. Exploring the natural divergence of muscle responses to cancer may be an opportunistic approach to identify distinct mechanisms underlying muscle weakness and wasting during cancer cachexia.

Contemporary theories posit that muscle wasting during cachexia is induced by circulating factors generated during cancer which trigger protein degradation and loss of myofibrillar proteins through various mechanisms[6–8]. However, recent literature suggests skeletal muscle mitochondria are also subject to damage during cancer cachexia [9–11] and may be direct contributors to either muscle weakness or atrophy. Current literature suggests oxidative phosphorylation is impaired in the soleus, gastrocnemius and plantaris muscle of tumour-bearing mice, while reactive oxygen species (ROS) - in the form of mitochondrial H_2O_2 emission (mH_2O_2) - can be increased or decreased depending on the muscle and duration of cancer[10–12]. This suggests cellular mechanisms contributing to muscle loss during cancer cachexia may be more complicated than previously believed. Moreover, in the Lewis lung carcinoma (LLC) xenograft mouse model, certain indices of skeletal muscle mitochondrial dysfunction preceded the onset of muscle atrophy, suggesting

mitochondria may be a potential therapeutic target[12]. This theory was supported by subsequent studies reporting positive effects of the mitochondria-targeting compound SS-31 in preventing certain indices of cachexia in some but not all muscles of the C26 xenograft mouse model[139,141]. However, given the multifactorial contributions to cachexia during cancer, it seems likely the relationship between mitochondria and myopathy may differ between muscle type and throughout cancer progression.

Indeed, skeletal muscle mitochondria are known to be highly adaptable to metabolic stressors and can super-compensate during an energy crisis[203,204]. In this light, the available literature does not provide sufficient information to predict the extent to which cancer will affect individual muscles, particularly in relation to their underlying mitochondrial responses to the systemic stress of this disease. Understanding the time-dependent nature of unique mitochondrial signatures during cancer-induced cachexia might better inform the development of mitochondrial therapies that have so far yielded disparate results across various muscle types in the C26 cancer mouse model[139,141].

In this study, we compared the time-dependent relationship of muscle dysfunction and mitochondrial bioenergetic responses to cancer between locomotor (quadriceps) and respiratory muscles (diaphragm). In so doing, we employed a careful consideration of mitochondrial substrate titration protocols modeling key parameters governing mitochondrial bioenergetics *in vivo*. Similar assay design considerations have been essential for identifying precise mitochondrial bioenergetic contributions to cellular function in our previous research[205–208]. Using the C26 tumour-bearing mouse model, we reveal muscle weakness precedes atrophy in quadriceps and diaphragm. Energetic insufficiencies were more pronounced in quadriceps whereas mitochondrial

redox stress was more evident in diaphragm, yet both muscles showed a delayed correction, if not super-compensation, as cancer progressed. In quadriceps, increased mitochondrial respiratory control was related to a surprising increase in specific force production at 4 weeks that likely mitigated the magnitude of reduction in absolute force due to atrophy. These findings demonstrate the effects of cancer on one muscle do not necessarily predict the response in another muscle type. Moreover, the heterogeneous muscle-specific and time-dependent mitochondrial relationships to cancer may provide an opportunity for informing a more targeted approach to developing mitochondrial therapies to improve muscle health in this debilitating disorder.

Results

C26 tumour-bearing mice show progressive reductions in body weight, muscle mass, fat mass and grip strength

All results were in male mice. Body weights were reduced 4 weeks after subcutaneous implantations of C26 cells **(Figure 4-1A)**, while tumour-free body weights progressively decreased beginning at 3 weeks to a net loss of 27% by 4 weeks **(Figure 4-1B, C)** at a time of substantial tumour growth (**Figure 4-1D)**. Tumours grew to ~0.2g at 2 weeks and ~2.2g at 4 weeks **(Figure 4-1E)**. C26 spleen mass (marker of inflammatory stress) was not different from PBS at 2 weeks but was significantly greater at 4 weeks **(Figure 4-1F)**. Adipose tissue from the inguinal fat pad was not different at 2 weeks, but significantly lower at 4 weeks (-65%; **Figure 4-1G)**. A similar pattern was observed with grip strength **(Figure 4-1H)**. The mass of specific muscles was similar between C26 and PBS at 2 weeks **(Figure 4-1I).** At 4 weeks soleus (SOL) mass was similar between C26 and PBS while lower muscle masses were observed in C26 for extensor digitorum longus (EDL; -23%), plantaris (PLA; -20%), tibialis anterior (TA; -26%), gastrocnemius (GA; -21%) and quadriceps (QUAD; -29%) vs PBS **(Figure 4-1J)**.

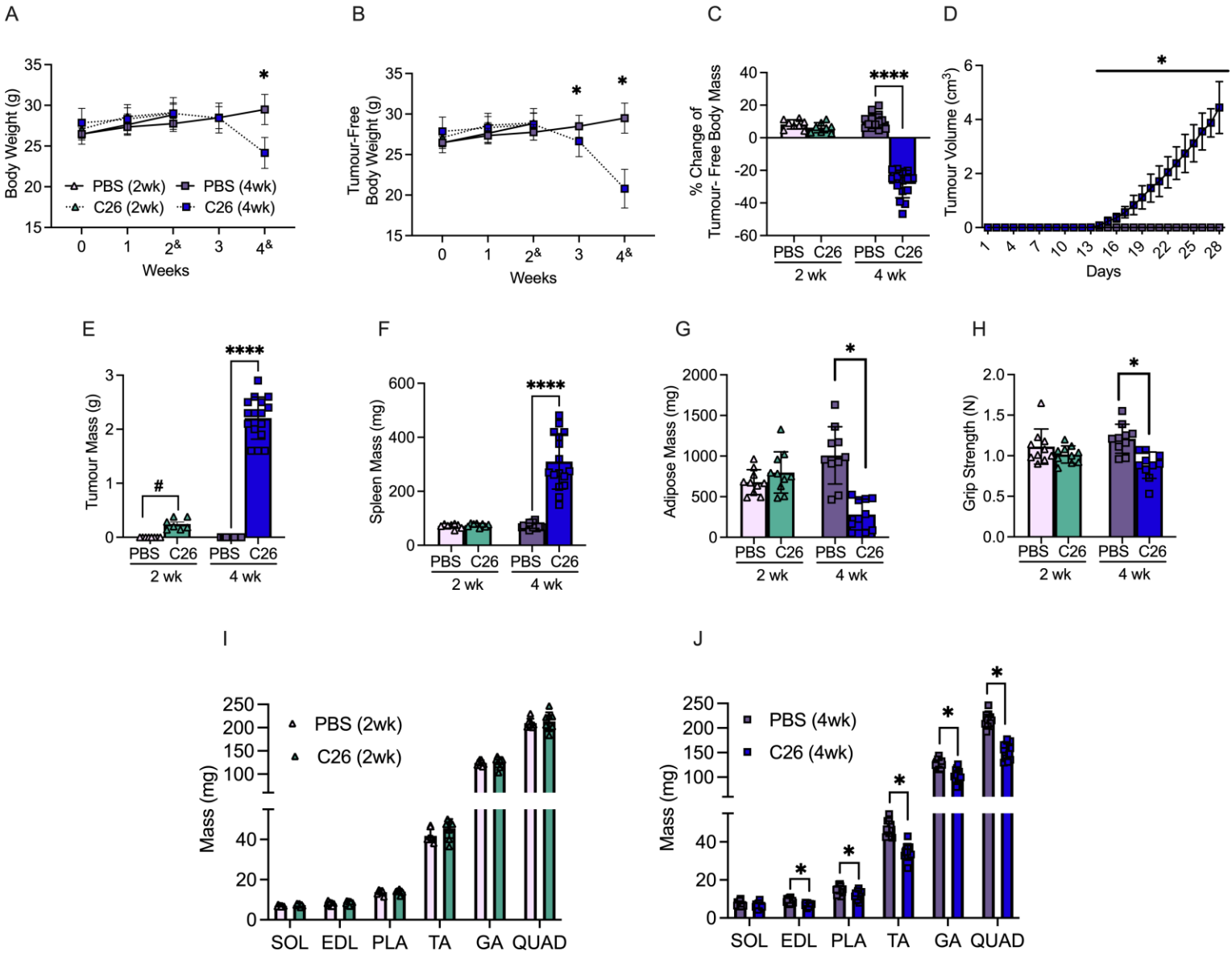

Figure 4-1 The effects of C26 colon cancer cells implantation on body size, tumour size, muscle mass and force. Analysis of CD2F1 mice with subcutaneous C26 implantations or with PBS were performed. Body weights (***A***, *n*=8-16) and tumour-free body weights (***B***, *n*=8-16) were analyzed every week ($2^{\&}$ mice were measured at a 14-17 day window and $4^{\&}$ mice were measured on a 26-29 day window). Percent change in tumour free body weights were analyzed from day 0 to end point (***C***, *n*=8-16). *In vivo* tumour volume measurements were made using calipers (***D***, *n*=16). Tumour mass (***E***, *n*=7-16) and spleen mass (***F***, *n*=8-16) measurements were also completed. Subcutaneous fat from the inguinal fat depot was weighed (**G**, n=10). Grip strength was assessed in all groups (**H**, n=10). Evaluation of hindlimb muscle wet weights were made in the 2-week cohort (***I***, *n*=8) and 4-week cohort (***J***, *n*=16). Results represent mean ± SD; Two tailed T-tests were used to determine the difference between PBS(2wk) vs. C26(2wk) and PBS (4wk) vs. C26(4wk). One-way ANOVA was used to determine the difference between PBS(4wk) vs. C26(4wk) tumour growth. # $P<0.05$ PBS(2wk) vs C26(2wk); * $P<0.05$ PBS(4wk) vs C26(4wk); **** $P<0.0001$ PBS(4wk) vs C26(4wk).

Muscle atrophy occurs in both the quadriceps and diaphragm after 4 weeks of tumour bearing.

Muscle atrophy is a hallmark of cancer cachexia. In both quadriceps and diaphragm, fibre CSA was similar between C26 and PBS groups for specific MHC isoforms **(Figure 4-2A-D)** and when pooling all MHC isoforms (data not shown) at 2 weeks. However, at 4 weeks, quadriceps muscle exhibited lower CSA in pooled fibres (-40%, $p<0.05$, data not shown) with specific reductions in MHC IIX (-32%) and MHC IIB (-49%) but not the MHC IIA isoform **(Figure 4-2E, F)** vs PBS. MHC I-positive fibres were not detected in the quadriceps (Figure 2B, F). At 4 weeks, diaphragm muscle also showed lower CSA in pooled fibres (-31%, $p<0.05$, data not shown) which mirrored changes in MHC I (-28%), MHC IIA (-21%), MHC IIB (-30%) and MHC IIX (-35%) vs PBS at 4 weeks **(Figure 4-2G, H)**.

We validated that these reductions in fibre CSA were a result of muscle atrophy by measuring key proteasomal markers of muscle wasting. In the quadriceps, muscle RING-finger protein-1 (MURF1) mRNA content was significantly increased at 4 weeks of tumour bearing compared to PBS controls **(Figure 4-3A)**. This was also the case for atrogin **(Figure 4-3B)**, ubiquitin C (UBC; **Figure 4-3C**) and growth arrest and DNA damage-inducible 45α (Gadd45a; **Figure 4-3D**). The diaphragm demonstrated similar results, such that MURF1, atrogin and Gadd45a were all significantly increased at 4 weeks of tumour-bearing, however this did not occur in UBC **(Figure 4-3E-H)**.

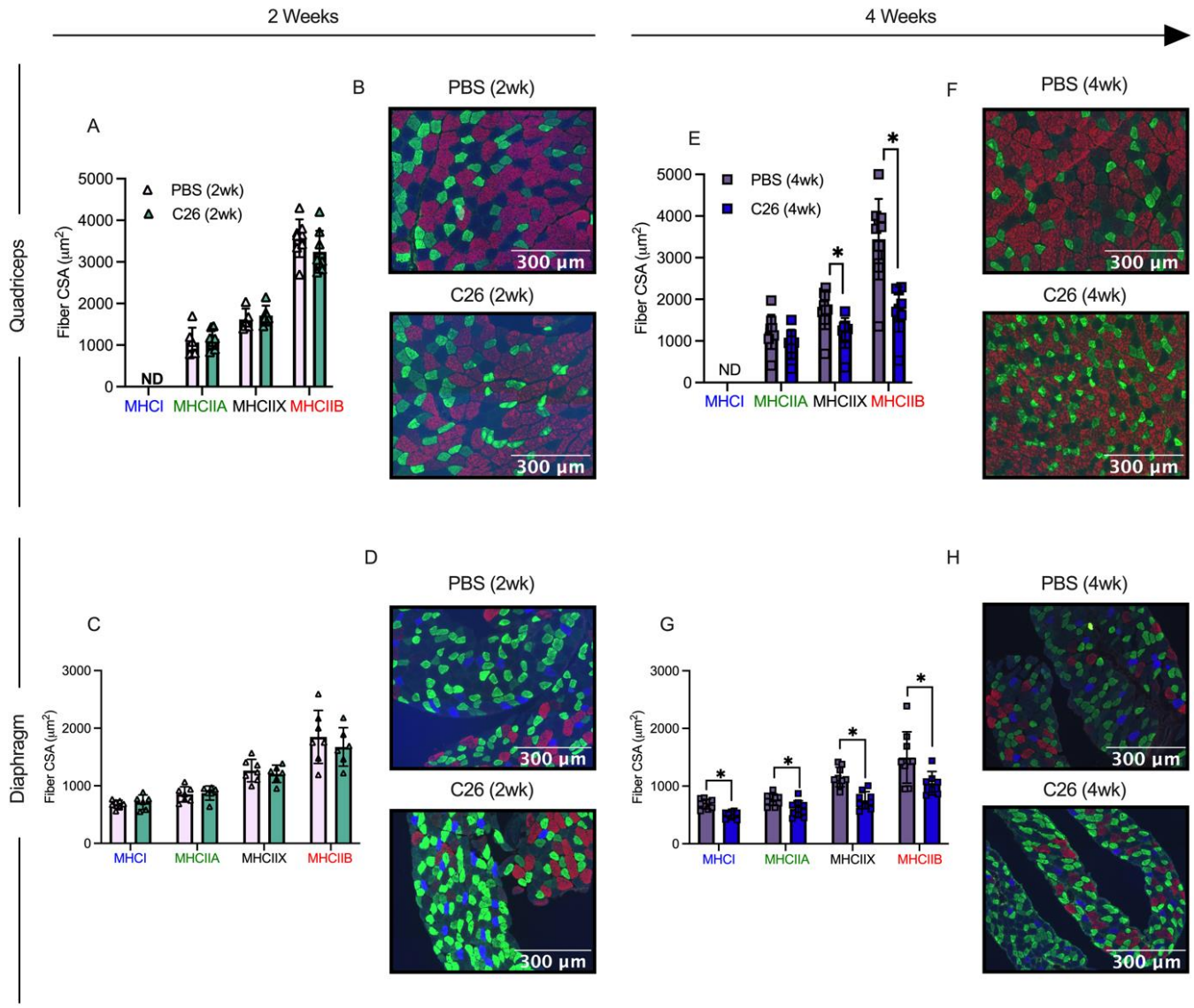

Figure 4-2 Evaluation of quadriceps and diaphragm fibre-type atrophy in skeletal muscle from C26 tumour-bearing mice. Analysis of fibre histology on MHC isoforms of PBS and C26 mice was performed. Cross-sectional area of MHC stains was evaluated in the quadriceps (*A*, *n*=8; *B*, representative image, magnification x 20) and diaphragm at 2 weeks of tumour bearing (*C*, *n*=6; *D*, representative image, magnification x 20). The same was completed for the quadriceps (*E*, *n*=9; *F*, representative image, magnification x 20) and diaphragm at 4 weeks of tumour bearing (*G*, *n*=9; *H*, representative image, magnification x 20). Results represent mean ± SD; Two tailed T-tests were used to determine the difference between PBS(2wk) vs. C26(2wk) and PBS (4wk) vs. C26(4wk). ***** *P*<0.05 PBS (4wk) vs C26(4wk).

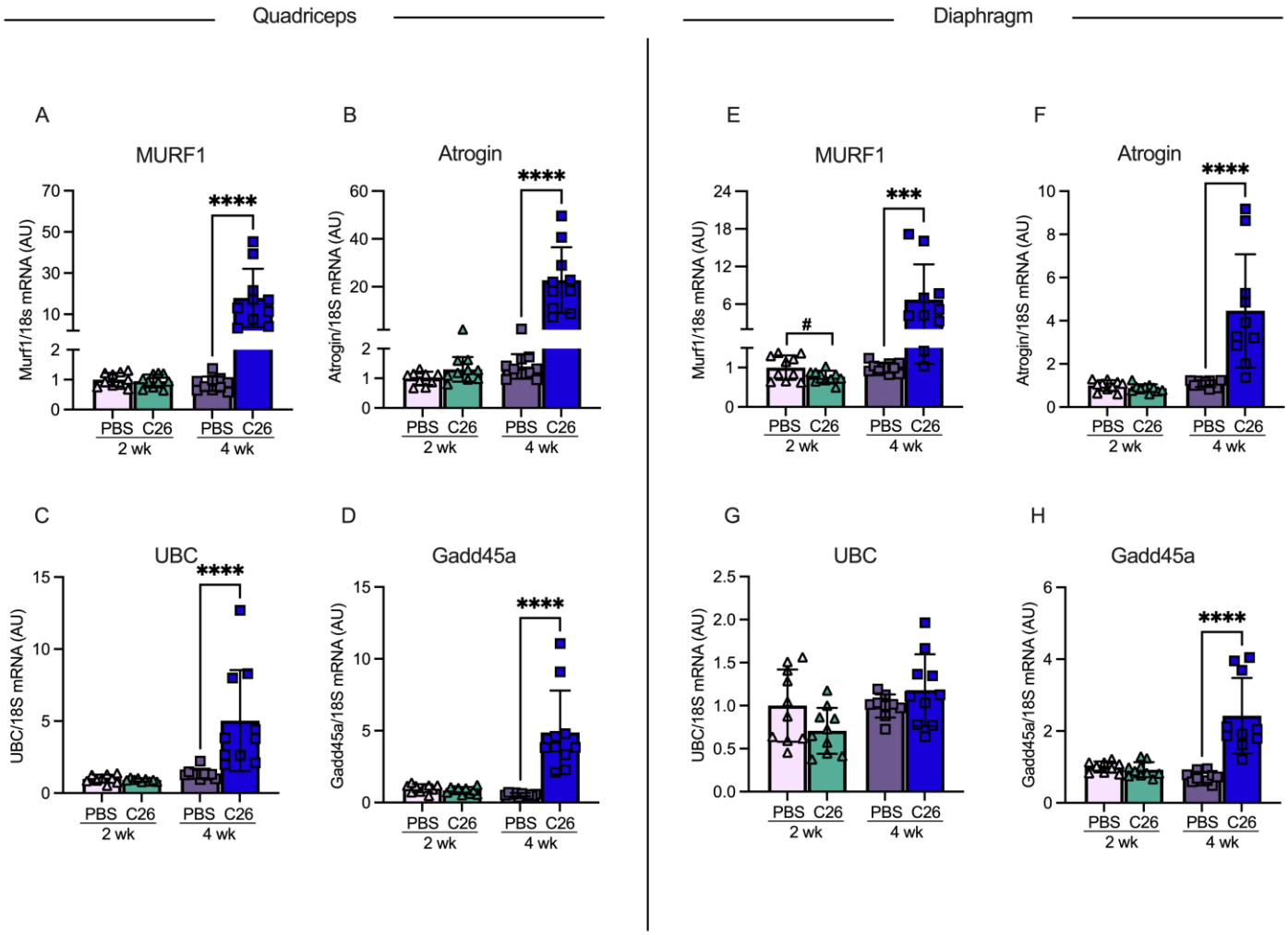

Figure 4-3 The effects of C26 colon cancer on the activation of atrophy markers in quadriceps and diaphragm muscle. mRNA content of atrophy markers muscle RING-finger protein-1 (MURF1) (A, *n*=10), Atrogin (B, n=10), Ubiquitin C (UBC) (C, *n*=10) and growth arrest and DNA damage-inducible 45*α* (Gdd45a) (D, *n*=10) were measured using qt-PCR in the quadriceps of all groups. This was also completed in the diaphragm (E-H; *n*=10). Results represent mean ± SD; Two tailed T-tests were used to determine the difference between PBS(2wk) vs. C26(2wk) and PBS (4wk) vs. C26(4wk). # *P*<0.05 PBS(2wk) vs C26(2wk); * *P*<0.05 PBS(4wk) vs C26(4wk); *** *P*<0.001 PBS(4wk) vs C26(4wk); **** *P*<0.0001 PBS(4wk) vs C26(4wk).

Force production is reduced prior to atrophy in quadriceps and diaphragm but returns to normal in quadriceps

At 2 weeks and 4 weeks, C26 absolute muscle force was lower in quadriceps relative to PBS as a group main effect **(Figure 4-4A)**. Interestingly, when absolute quadriceps force was normalized to muscle wet weight, specific force production remained decreased at 2 weeks of tumour bearing compared to PBS as a group main effect. However, at 4 weeks of tumour bearing, specific force was higher compared to 2 weeks and not different compared to PBS controls as a group main effect **(Figure 4-4B)**. In addition, there was an interaction whereby C26 at 2 weeks produced less force at 80Hz, 100Hz and 120Hz compared to both PBS groups and the C26 at 4 weeks (not shown).

We are unable to report absolute force in the diaphragm as dissected muscle strips of diaphragm were used to complete the in-*vitro* force assay, not the whole diaphragm. At 2 weeks and 4 weeks of tumour-bearing C26 specific muscle force was lower in the diaphragm relative to PBS controls as a group main effect **(Figure 4-4C)**.

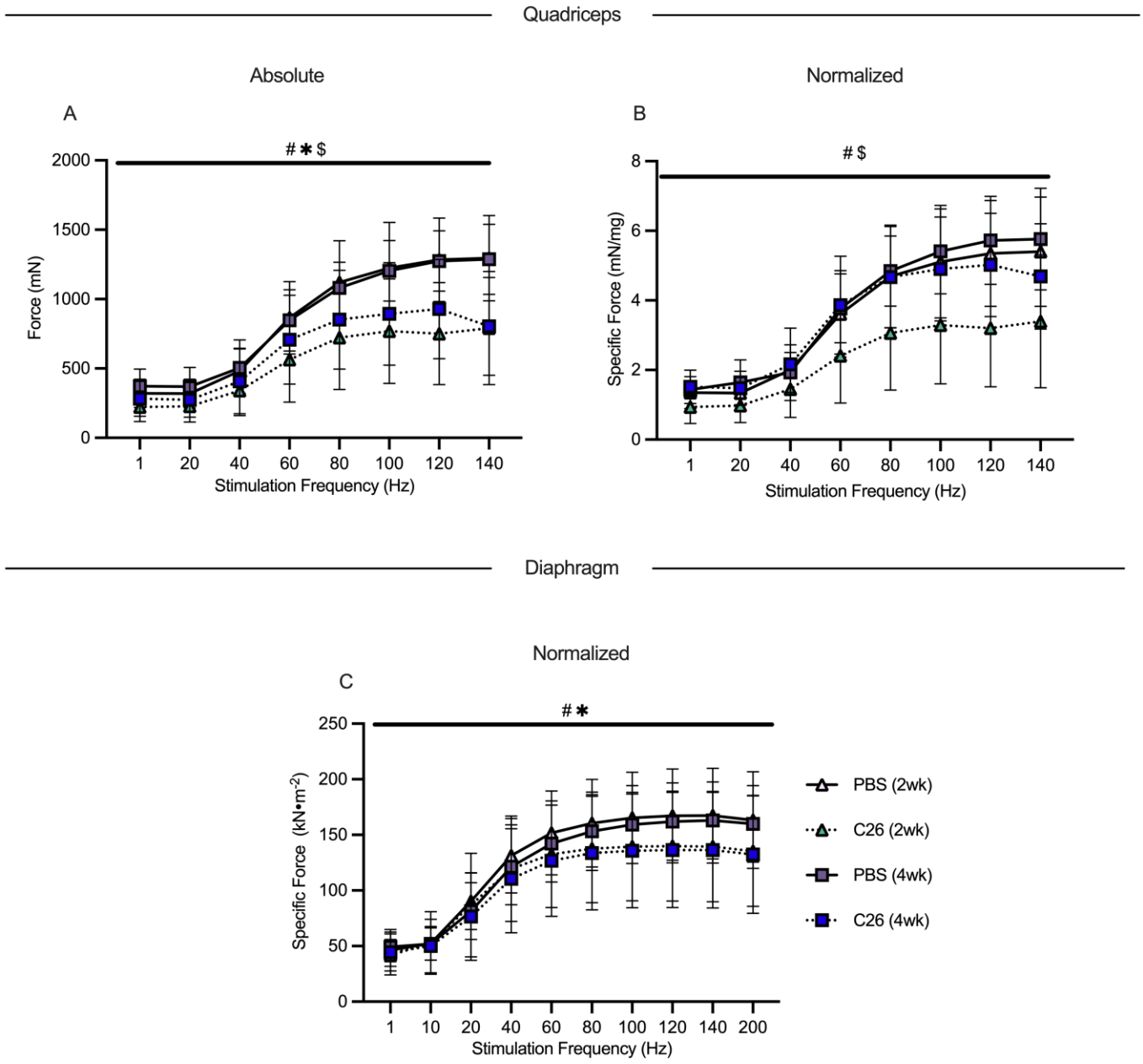

Figure 4-4 The effects of C26 colon cancer on quadriceps and diaphragm force production. *In situ* quadriceps force production was assessed using the force frequency relationship (*A* absolute force, B normalized force to total quadriceps weight; *n*=6-14) and *in vitro* diaphragm force production was also measured using the force frequency relationship (*C* normalized force; absolute force is not included as the method was performed on muscle strips; *n*=6-12). Results represent mean ± SD; A two-way ANOVA was used to determine the difference between PBS(2wk) vs. C26(2wk) vs. PBS (4wk) vs. C26(4wk). # $P<0.05$ PBS(2wk) vs C26(2wk); * $P<0.05$ PBS(4wk) vs C26(4wk); $ $P<0.05$ C26 (2wk) vs C26 (4wk).

Mitochondrial electron transport chain protein contents are reduced in quadriceps but do not change in diaphragm by 4 weeks of tumour development

At 2 weeks, electron transport chain (ETC) subunit contents in both muscles were unchanged in C26 relative to PBS controls **(Figure 4-5A, B)**. At 4 weeks, C26 showed lower contents in subunits of complex I (-31%), complex II (-18%), complex IV (-37%), complex V (-11%) and total ETC subunit content (-22%; **Figure 4-5C)** relative to PBS that were significant. ETC subunit contents did not change in diaphragm at 4 weeks relative to PBS **(Figure 4-5D)**.

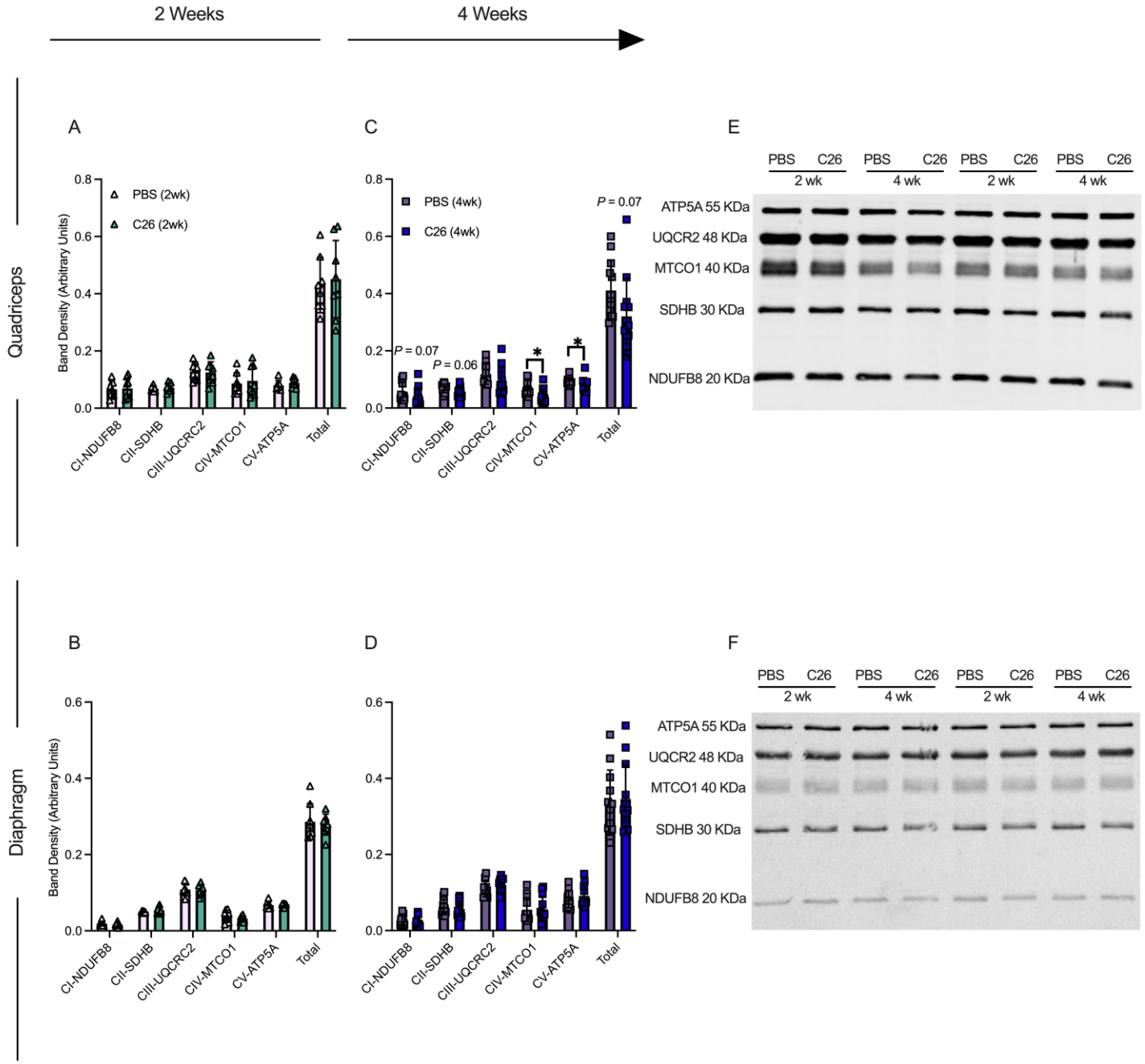

Figure 4-5 Muscle-specific changes in markers of electron transport chain complexes in C26 tumour-bearing skeletal muscle. Protein content of electron transport chain subunits were quantified in the quadriceps (***A***, *n*=8) and diaphragm at 2 weeks (***B***, *n*=8) and 4 weeks ***C***, ***D*** *n*=12). *E*, representative image for quadriceps and ***F***, representative image for diaphragm. Results represent mean ± SD; Two tailed T-tests were used to determine the difference between PBS(2wk) vs. C26(2wk) and PBS (4wk) vs. C26(4wk). * *P*<0.05 PBS (4wk) vs C26 (4wk).

Mitochondrial respiratory control by ADP is greater in both muscles by 4 weeks of tumour development despite early reductions in the quadriceps

We determined if the central role of ADP in stimulating respiration was impaired in both quadriceps and diaphragm at 2 and 4 weeks after subcutaneous implantations of C26 cancer cells. We stimulated complex I with NADH generated by pyruvate (5mM) and malate (2mM) across a range of ADP concentrations to challenge mitochondria with a spectrum of metabolic demands. The ADP titrations were repeated with (+Creatine) and without (-Creatine) 20mM creatine to model the two main theoretical mechanisms of energy transfer from mitochondria to cytosolic compartments that utilize or bypass mitochondrial creatine kinase (mtCK) respectively **(Figure 4-6)**. Briefly, the +Creatine system stimulates mitochondria to export phosphocreatine (PCr) whereas the -Creatine condition drives ATP export.

Low Metabolic Demand (Low ADP)

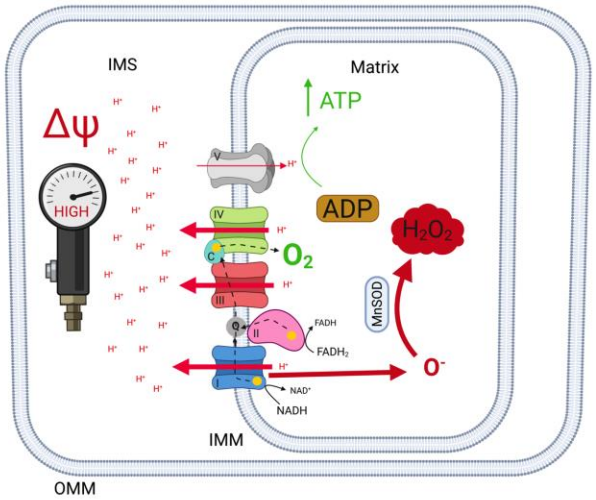

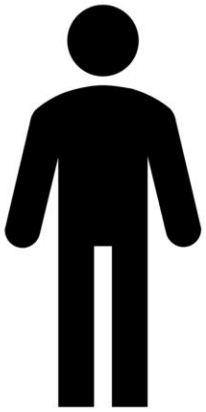

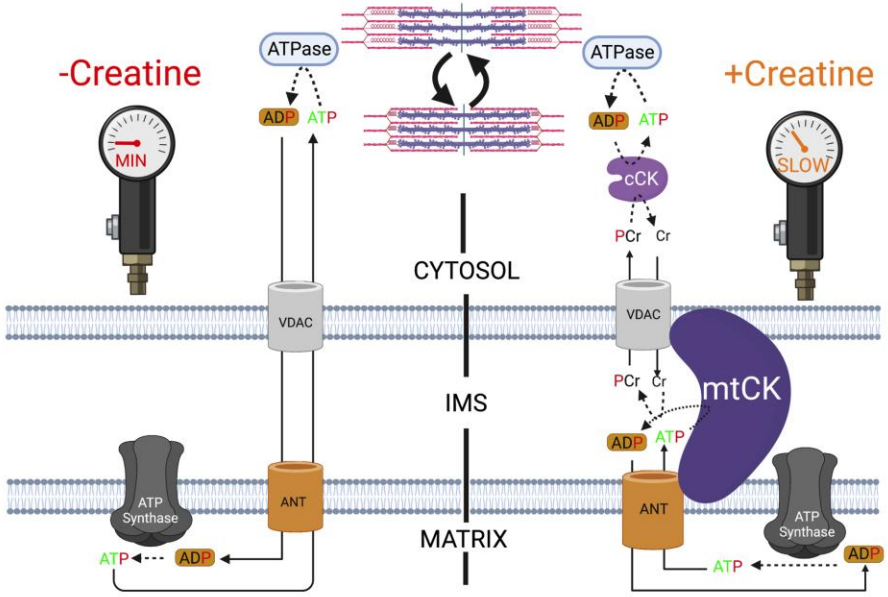

High Metabolic Demand (High ADP)

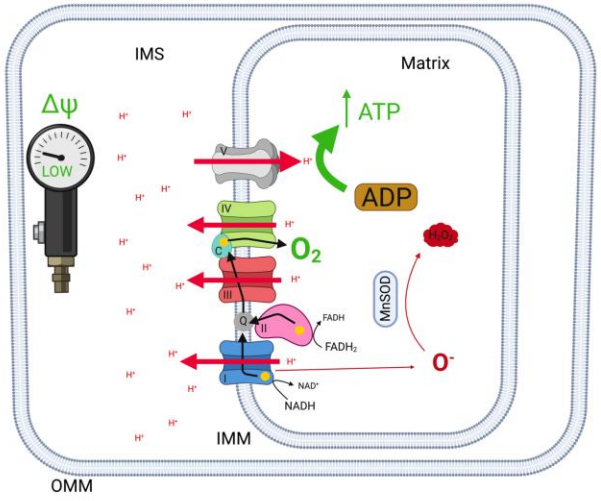

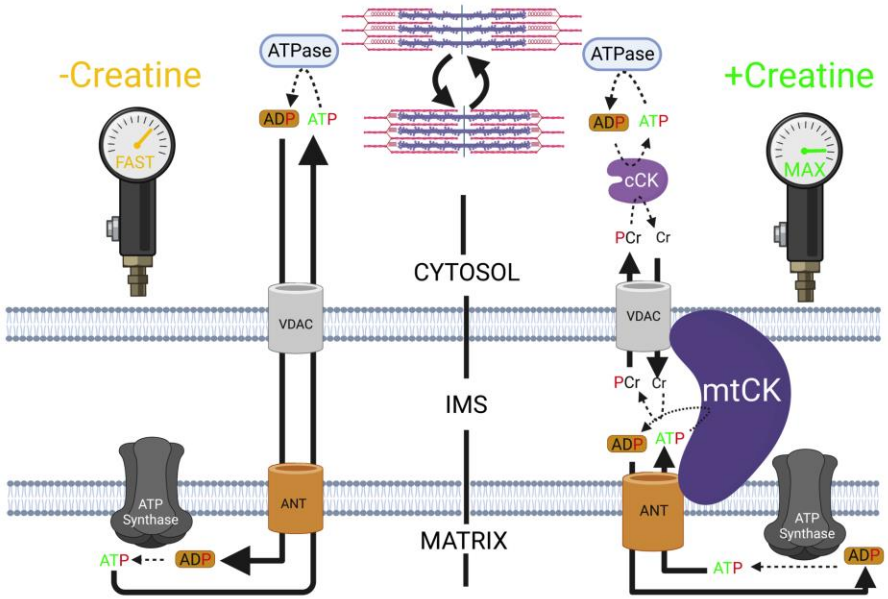

Figure 4-6 Schematic representation of energy homeostasis in low metabolic (left) vs. high metabolic (right) demand states. When ADP is low, less ATP is produced. A concomitant accumulation of $[H^+]$ in the inner membrane space (IMS) increases membrane potential ($\Delta\Psi$), attenuates H+ pumping, induces premature electron slip and generates superoxide ($O^{\bullet-}$) which is dismutated to H_2O_2 by manganese superoxide dismutase (MnSOD; top left). Only Complex I-derived superoxide is displayed. When ADP is high, more ATP is produced as $[H^+]$ diffuse from the IMS to the mitochondrial matrix through ATP synthase. The decrease in $\Delta\Psi$ lowers premature electron slip, generating less $O^{\bullet-}$ and H_2O_2 (top right). ADP generated by ATPases throughout the cell enter the matrix through the voltage dependent anion channel (VDAC) on the outer mitochondrial membrane (OMM) and the adenine nucleotide translocase (ANT) on the inner mitochondrial membrane (IMM; bottom left). Creatine accelerates matrix ADP/ATP cycling and ATP synthesis by reducing the diffusion distance of the slower diffusing ADP and ATP while shuttling phosphate to the cytoplasm through rapidly diffusing phosphocreatine which is used by cytosolic creatine kinase (cCK) to recycle local ATP to support the activity of various ATPases. Rapidly diffusing creatine returns to the IMS to be re-phosphorylated by mitochondrial creatine kinase (mtCK). Non-ATPase sites of ATP hydrolysis are not displayed but also contribute to net metabolic demand (kinases, and other ATP-dependent processes). The net effect of metabolic demand (global ATP hydrolysis) on matrix ADP/ATP cycling is displayed under the context of creatine independent (-Creatine) and creatine dependent (+Creatine) conditions. Figure adapted from *Aliev et al.*, 2011, *Guzun et al.*, 2012, *Wallimann et al.*, 2011 and *Nicholls* 2013[80,183–185]. Created with BioRender.com

In both the -Creatine and +Creatine conditions, pyruvate/malate-supported ADP-stimulated respiration normalized per mass of fibre bundles (not corrected for ETC subunit content) was lower 2 weeks after C26 implantations in the quadriceps compared to PBS with a main effect across all ADP concentrations with or without creatine **(Figure 4-7A, B)**. The general reduction in respiration for C26 normalized per mass of fibre bundle was also seen when data were normalized to ETC subunit content **(Figure 4-7C, D)**. This suggests respiratory control was reduced within mitochondria due to an inherent property of the ETC not related to ETC abundance. We also evaluated if creatine sensitivity was altered in the C26 tumour-bearing muscle by calculating the +Creatine/-Creatine respiratory ratio. This creatine sensitivity index is a measure of the ability of creatine to stimulate respiration by accelerating matrix ADP/ATP cycling and represents coupling of the creatine kinase system to ATP generation **(Figure 4-6)**, particularly at sub-maximal ADP concentrations[209,210] which we have reported previously[205,206]. In quadriceps, creatine sensitivities at 100μM and 500μM ADP were unchanged at 2 weeks in C26 vs PBS at this time point **(Figure 4-7E, F)**. Collectively, these findings indicate respiration was reduced to similar extents in both -Creatine and +Creatine conditions of energy exchange between mitochondria and cytoplasmic compartments.

These early decrements in quadriceps respiration in C26 at 2 weeks were reversed by 4 weeks. This apparent compensation was seen in both -Creatine and +Creatine conditions. Specifically, respiration was similar to PBS control mice at 4 weeks when normalized per mass of fibre bundle **(Figure 4-7G, H)** and higher than controls when normalized to ETC subunit protein content **(Figure 4-7I, J)** despite reductions in ETC content as described above **(Figure 4-5C)**. These findings suggest mitochondria in quadriceps are highly plastic and can super-compensate by

upregulating their responsiveness to ADP to levels exceeding PBS controls. Additionally, at 4 weeks, quadriceps mitochondrial creatine sensitivity was impaired in C26 relative to PBS when considering respiration normalized to ETC subunit content given the ratio did not exceed a value of 1.0 which indicates that creatine could not stimulate respiration above the level elicited by ADP alone **(Figure 4-7L)**. Thus, while C26 cancer strongly increased ADP-stimulated respiration by 4 weeks **(Figure 4-7I)**, it compromised the coupling of creatine kinase energy transfer, suggesting that this system did not contribute to restored force at this time point **(Figure 4-4B).**

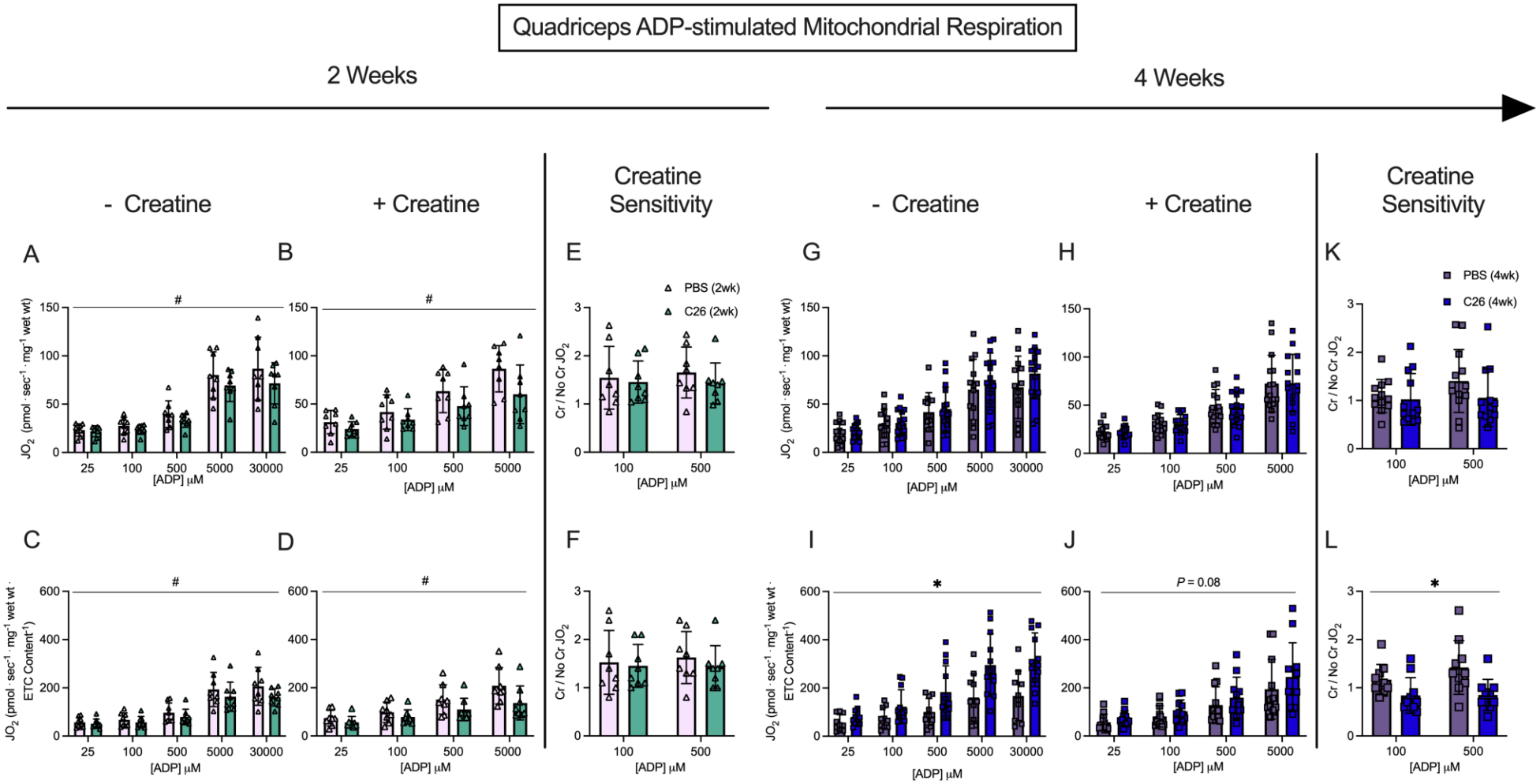

Figure 4-7 Complex I-supported mitochondrial respiration in quadriceps muscle of C26 tumour-bearing mice. ADP-stimulated (State III) respiration, supported by complex I supported (NADH) substrates pyruvate (5mM) and malate (2mM), was assessed in the absence (-Creatine) and presence (+Creatine) of 20mM creatine at a range of [ADP] until maximal respiration was achieved to model a spectrum of metabolic demands. Respiration was assessed in the quadriceps normalized to bundle size at 2 weeks (*A*, *B*) and normalized to ETC subunit content (*C*, *D)* to permit comparisons of intrinsic mitochondrial respiratory responses in each group. Creatine sensitivity was assessed by calculating the +creatine/-creatine ratio (*E*, *F*) given creatine normally increases ADP-stimulated respiration. The same measurements were completed at 4 weeks (*G-L*). Results represent mean ± SD; n=8-16; A two-way ANOVA was used to determine the difference between PBS(2wk) vs. C26(2wk) and PBS (4wk) vs. C26(4wk). # P<0.05, PBS(2wk) vs C26(2wk); * P<0.05, PBS(4wk) vs C26(4wk).

In the diaphragm, respiration was similar between C26 and PBS at 2 weeks **(Figure 4-8A-F)** but was greater in C26 compared to PBS at 4 weeks in both the -Creatine and +Creatine conditions **(Figure 4-8G-J)**. This upregulation by 4 weeks occurred despite no changes in ETC subunit content as noted above **(Figure 4-5D)** which suggests mitochondria increase their responsiveness to ADP through mechanisms that may be independent of mitochondrial content. No changes in creatine sensitivity were observed in C26 vs PBS at 4 weeks **(Figure 4-8K, L)** suggesting that coupling of creatine kinase to ATP generation was maintained, in contrast to impaired creatine sensitivity seen in the quadriceps as noted above. Lastly, there was a significant interaction whereby respiration was greater in C26 vs PBS at 5000μM and 7000μM ADP when normalized per mass of fibre bundles **(Figure 4-8G, H)** and at all ADP concentrations except 25μM and 100μM when normalized to total ETC subunit content **(Figure 4-8I, J)**.

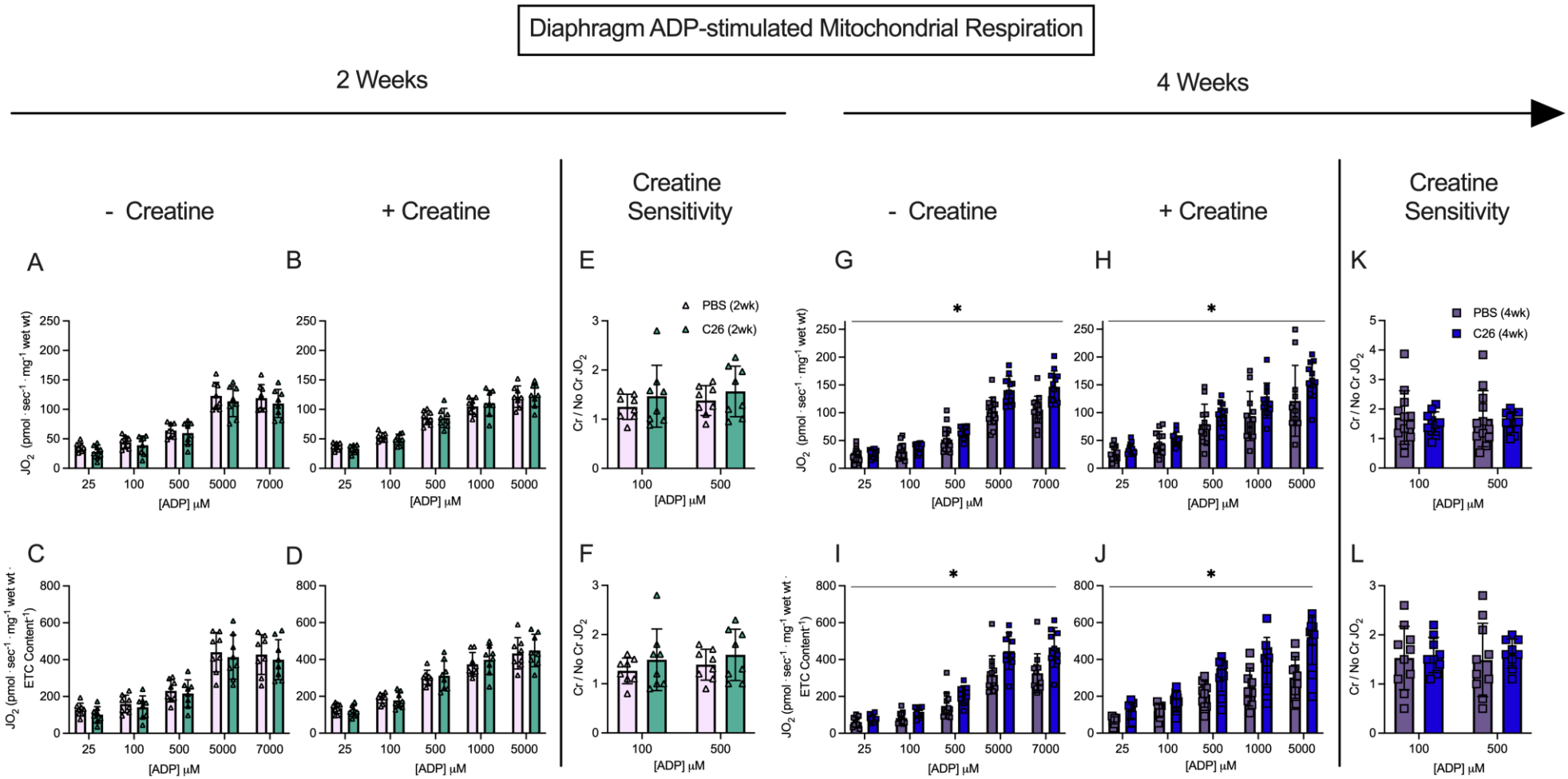

Figure 4-8 Complex I-supported mitochondrial respiration in diaphragm muscle of C26 tumour-bearing mice. ADP-stimulated (State III) respiration, supported by complex I supported (NADH) substrates pyruvate (5mM) and malate (2mM), was assessed in the absence (-Creatine) and presence (+Creatine) of 20mM creatine at a range of [ADP] until maximal respiration was achieved to model a spectrum of metabolic demands. Respiration was assessed in the diaphragm normalized to bundle size at 2 weeks (*A, B*) and normalized to ETC subunit content (*C, D)* to permit comparisons of intrinsic mitochondrial respiratory responses in each group. Creatine sensitivity was assessed by calculating the +creatine/-creatine ratio (*E, F*) given creatine normally increases ADP-stimulated respiration. The same measurements were completed at 4 weeks (*G-L*). Results represent mean ± SD; n=8-16; A two-way ANOVA was used to determine the difference between PBS(2wk) vs. C26(2wk) and PBS (4wk) vs. C26(4wk). * *P*<0.05, PBS(4wk) vs C26(4wk)

These alterations were specific to pyruvate/malate-supported ADP-stimulated respiration as there were no changes in respiration in response to glutamate (further NADH-generation) and succinate ($FADH_2$) generation when comparing C26 to PBS at either time point **(Figure S4-1, S4-2)**. By 2 weeks of C26, diaphragm showed a decrease in State II respiration (no ADP, supported by pyruvate/malate; Figure S1, S2) which is generally used as a marker of respiration driven by proton leak into the matrix from the inner membrane space through various sites that are not coupled to ATP synthesis[80]. However, State II respiration was greater than control by 4 weeks in both muscles suggesting greater uncoupling at occurs as cancer progresses **(Figure 4-S2)**. Lastly, changes in respiration noted above did not result in changes to the phosphorylation of AMPK in C26 relative to PBS at either 2- or 4-week timepoints **(Figure 4-S3)**; albeit increases in AMPK and the p-AMPK/AMPK ratio were trending in the C26 (4wk) group in the quadriceps.

H_2O_2 emission is increased in diaphragm early during tumour development and restored to normal by 4 weeks but is unaffected in quadriceps

We stimulated complex I with pyruvate (10mM) and malate (2mM) to generate NADH in the absence of ADP to elicit mH_2O_2 emission and determined ADP's ability to attenuate this emission as occurs naturally during oxidative phosphorylation (see schematic representation, **Figure 4-6)**. At 2 weeks following C26 implantations, quadriceps mH_2O_2 emission was similar to PBS controls under maximal emission conditions (no suppression by ADP, State II; **Figure 4-9A, C)** and during suppression by ADP **(Figure 4-9B, D)**. By 4 weeks of C26 growth, quadriceps mH_2O_2 was lower than PBS in both maximal and ADP-suppressive states **(Figure 4-9E, F).** However, when mH_2O_2 was normalized to total ETC subunit content, no differences were observed between C26 and PBS **(Figure 4-9G, H)**. This finding suggests eventual decreases in quadriceps mH_2O_2 by 4 weeks were

related to decreased ETC subunit content as shown in Figur*e* 4-5. Due to limited tissue availability, pyruvate-supported mH_2O_2 was assessed only in the +Creatine condition.

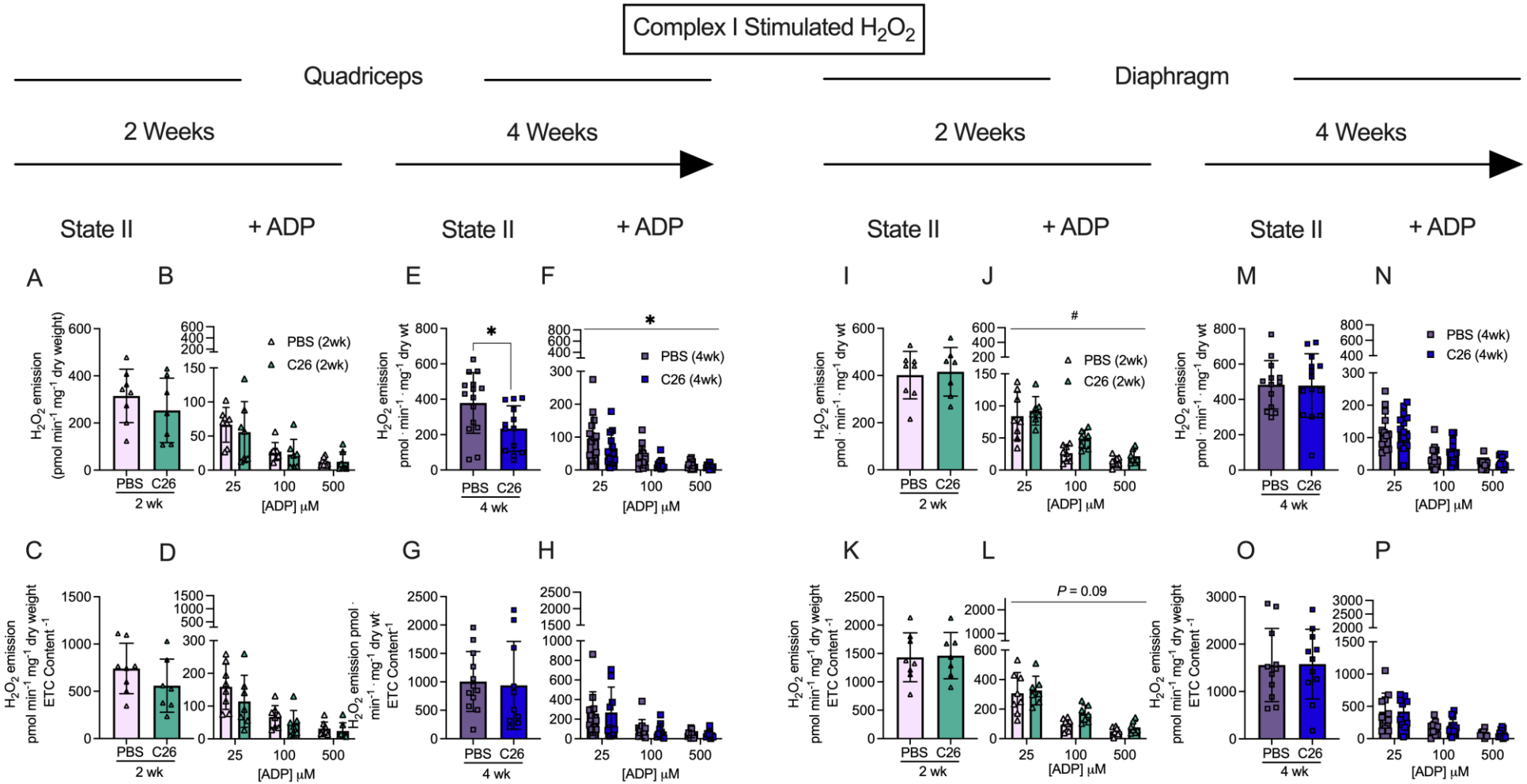

Figure 4-9 Complex I stimulated mH_2O_2 emission in quadriceps and diaphragm muscle of C26 tumour bearing mice. At 2 and 4 weeks, quadriceps mH_2O_2 emission supported by pyruvate (10mM) and malate (2mM) (NADH) was assessed under maximal State II (no ADP) conditions in the presence of 20mM creatine (*A, E*) and under a range of [ADP] to model metabolic demand (*B, F*). These measures were also normalized to total ETC subunit content (*C, D, G, H*) to permit comparisons of intrinsic mitochondrial respiratory responses in each group. These measures were repeated in the diaphragm (*I-P*). Results represent mean ± SD; n=8-16; Two tailed T-tests were used to determine the difference between PBS(2wk) vs. C26(2wk) and PBS (4wk) vs. C26(4wk) for state II H_2O_2 emission. A two-way ANOVA was used to determine the difference between PBS(2wk) vs. C26(2wk) and PBS (4wk) vs. C26(4wk). # P<0.05, PBS(2wk) vs C26(2wk); * P<0.05, PBS(4wk) vs C26(4wk).

In contrast to the lower mH_2O_2 in quadriceps, diaphragm mH_2O_2 was greater in C26 mice at 2 weeks relative to PBS in the presence of ADP despite no change in maximal mH_2O_2 **(Figure 4-9I, J)**. This finding reveals C26 induces early elevations in diaphragm mH_2O_2 that are likely due to a specific impairment in the ability of ADP to attenuate H_2O_2 emission. Moreover, when mH_2O_2 emission was normalized to total ETC subunit content at 2 weeks, maximal mH_2O_2 emission remained unchanged **(Figure 4-9K)**, while the higher emissions in the presence of ADP did not reach significance **(Figure 4-9L)** but mirrored patterns observed when normalized to wet mass of tissue as noted above. At 4 weeks, there were no differences in diaphragm mH_2O_2 under maximal or submaximal (presence of ADP) conditions using either normalization approach **(Figure 4-9M-P)** suggesting diaphragm mitochondria are plastic and can eventually restore mH_2O_2 to normal levels.

Succinate-supported mH_2O_2 emission generally did not change in either muscle in C26 vs PBS at either time point **(Figure S4-4)**. This finding suggests reverse electron flux to Complex I from Complex II[80] was not altered by C26 cancer, and the responses mentioned above using pyruvate/malate reveal a specific alteration in mH_2O_2 emission supported by forward electron flux through Complex I.

Inhibition of mitochondrial ATP synthase directly impairs force production in diaphragm

These observations suggest mitochondrial stress contributes to early weakness at 2 weeks in both muscles, and that restoration of force in quadriceps by 4 weeks is related to a natural compensatory increase in mitochondria respiratory control. In order to establish a direct link between mitochondria and force production, we designed an in-*vitro* experiment whereby we used

oligomycin to inhibit ATP synthase in diaphragm strips from of healthy CD2F1 mice. Within each strip, force-frequency relationships were assessed in standard assay media (CTRL) **(Figure 4-10A)**. Strips were then incubated with 0.2% ethanol (Vehicle) while relaxing in the apparatus for 40 minutes. A 2nd force-frequency assessment was then performed which demonstrated no effect of the vehicle (Figure 4-10A). We then repeated this experimental design on separate muscle strips but in the presence of 10μM oligomycin during the 40-minute incubation after a control stimulation. There was a main effect whereby oligomycin lowered force production **(Figure 4-10B).** Likewise, a main effect of lower force was exhibited within the oligomycin condition when the change in force production relative to control strips was analyzed. **(Figure 4-10C)**.

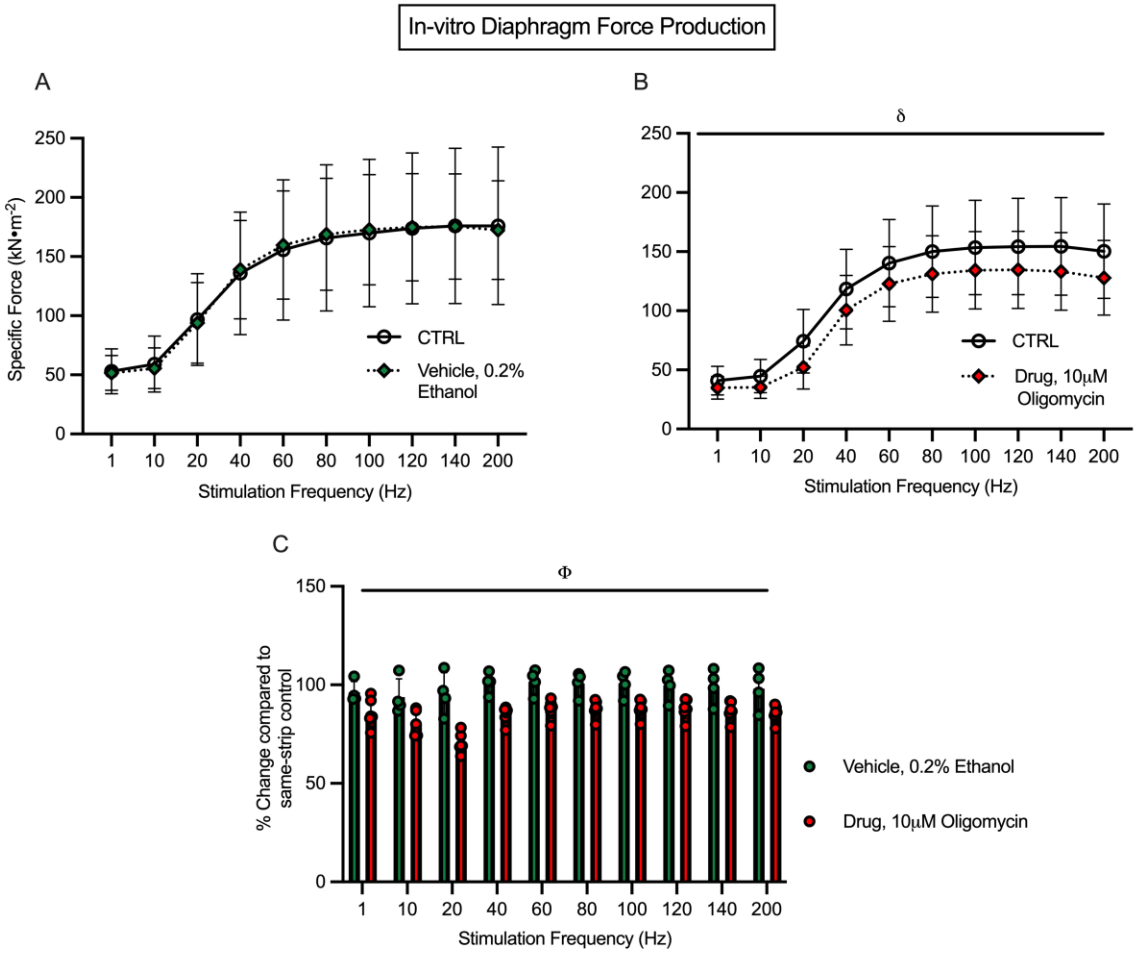

Figure 4-10 Inhibition of mitochondrial oxidative phosphorylation acutely lowers *in vitro* diaphragm force production. Diaphragm strips underwent an *in vitro* force-frequency protocol (CTRL) and were then incubated with 0.2% ethanol (Vehicle) while relaxing for 40 minutes followed by a 2nd assessment (A, *n*=4). A similar approach was used with 10μM oligomycin in separate strips. (B, *n*=6). The relative change in force production in both vehicle and oligomycin conditions compared to their respective CTRL was also analyzed (C, *n*=4-6). Results represent mean ± SD; A two-way ANOVA was used to determine the difference between CTRL vs. Vehicle, CTRL vs. Drug and Vehicle vs. Drug. n=4-6; δ *P*<0.05, CTRL vs Drug; Φ *P*<0.05, Vehicle vs Drug.

Reduced, oxidized and total glutathione are decreased in quadriceps after 4 weeks of tumour-bearing despite an increase in the reduced-oxidized glutathione ratio

Noting the mH_2O_2 patterns were also time- and muscle-dependent, we then determined whether there was a corresponding impact on cellular redox state by assessing the equilibrium of the

glutathione redox buffer. At 2 weeks, there were no differences in reduced glutathione (GSH), oxidized glutathione (GSSG), GSH:GSSG ratio and total glutathione in the either muscle **(Figure 4-11A-D, I-L**). At 4 weeks, quadriceps demonstrated a lower content of reduced, oxidized and total glutathione but interestingly there was an increase in the GSH:GSSG ratio (**Figure 4-11**E-H). No changes in any measure were observed in diaphragm at 4 weeks. **(Figure 4-11M-P).** A summary of the time-dependent and muscle-specific adaptations to C26 cancer is provided in **Figure 4-12**.

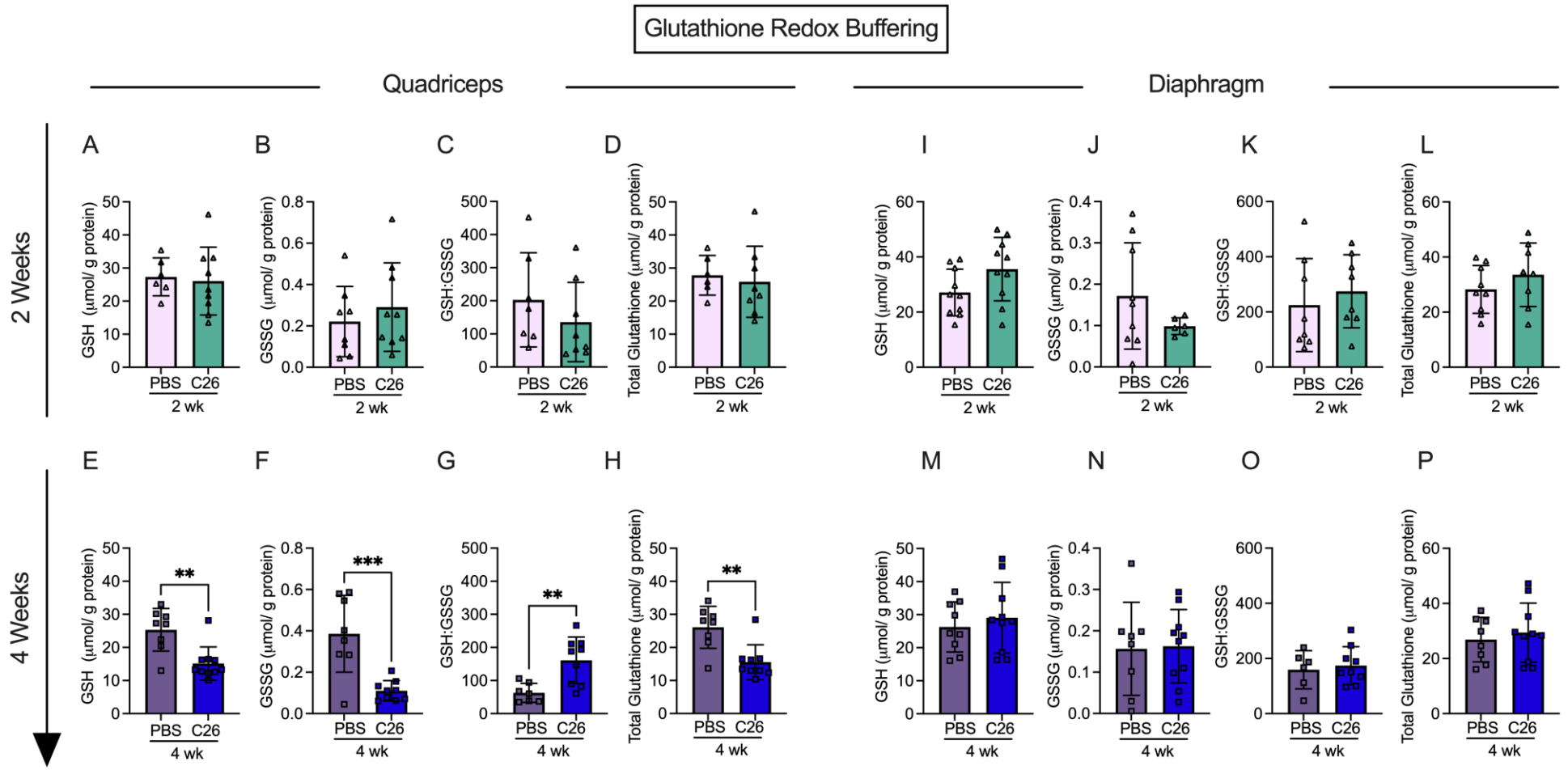

Figure 4-11 Glutathione redox buffering in quadriceps and diaphragm muscle of C26 tumour-bearing mice. Reduced glutathione was measured in the quadriceps of the 2 and 4 week cohort (A, E) along with oxidized glutathione (B, F). The ratio of reduced to oxidized glutathione was also analyzed (C, G) along with the total glutathione (D, H). This was repeated in the diaphragm (I-P). Results represent mean ± SD; n=8-10; Two tailed T-tests were used to determine the difference between PBS(2wk) vs. C26(2wk) and PBS (4wk) vs. C26(4wk). * P<0.05, PBS(4wk) vs C26(4wk); ** P<0.01 PBS(4wk) vs C26(4wk); *** P<0.001 PBS(4wk) vs C26(4wk).

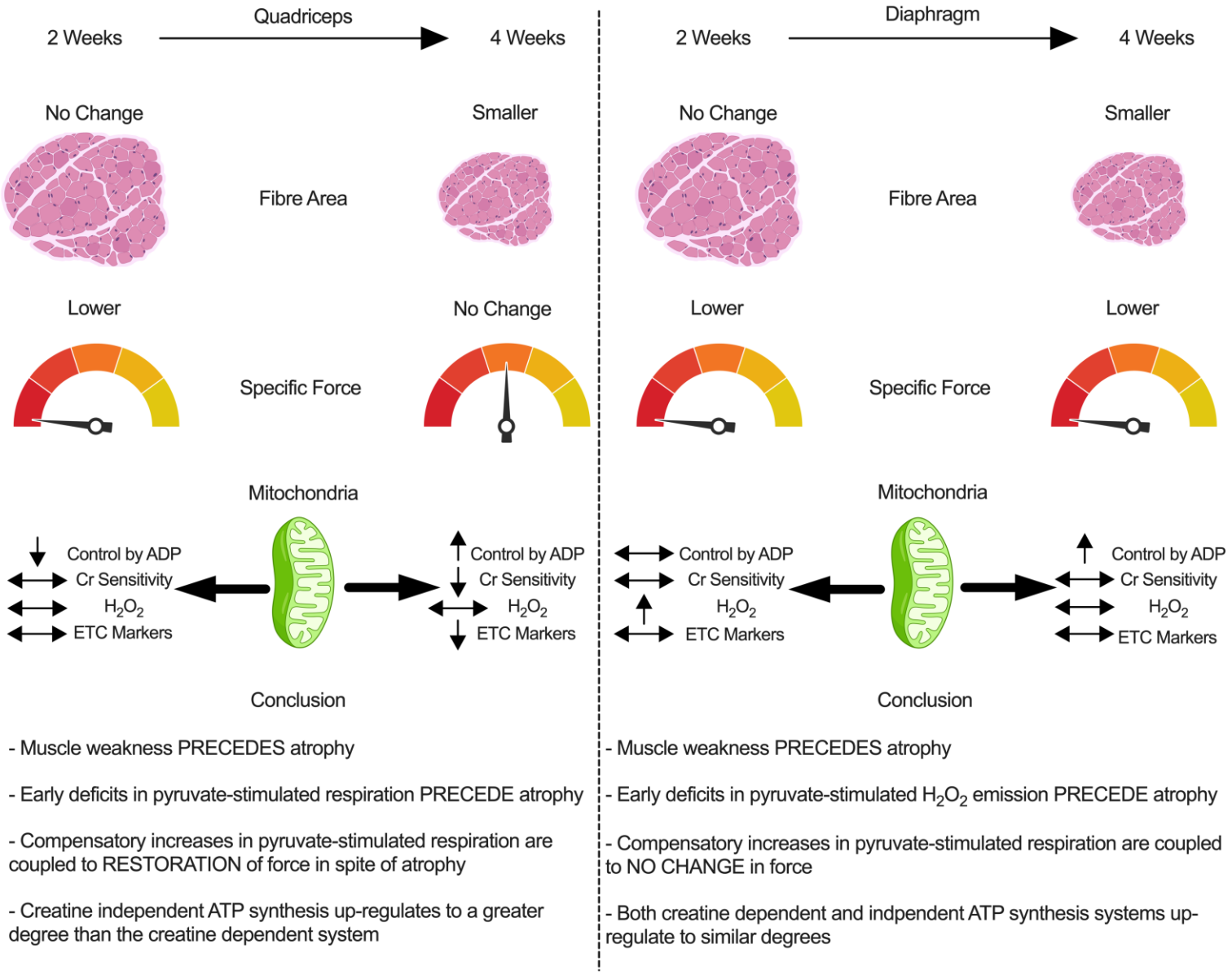

Figure 4-12 Summary of the time-dependent and muscle-specific adaptations to C26 xenografts in CD2F1 mice. At 2 weeks, early impairments in force generating capacity are associated with reductions in mitochondrial pyruvate/malate-supported ADP-stimulated respiration in quadriceps and elevated mH_2O_2 emission in diaphragm. These distinct mitochondrial responses precede atrophy in both muscles by 4 weeks. At this time, quadriceps and diaphragm responses to C26 become heterogeneous. The restoration of force generating capacity in quadriceps in spite of atrophy is not observed in the diaphragm even though both muscles demonstrate apparent compensatory increases in mitochondrial ADP-stimulated respiration. The mitochondrial responses to cancer are more diverse in quadriceps than diaphragm, with increases in respiration by 4 weeks occurring as a potential compensation for reductions in mitochondrial electron transport chain markers. Mitochondrial creatine metabolism is impaired in quadriceps by 4 weeks. ↓ represents decrease; ↑ represents increase; ↔ represents no change. Created with BioRender.com

Discussion

Certain indices of skeletal muscle mitochondrial stress have been associated with cancer cachexia in various mouse models [10,12,139,192,211], but the time- and muscle-dependent relationship remains unclear. Moreover, the early relationships between force production and atrophy have not been understood. Here, we demonstrate how quadriceps and diaphragm have both common and distinct time-dependent responses to cancer in the C26 colon carcinoma mouse model of cancer cachexia. First, a reduction in specific muscle force was observed prior to atrophy in both muscles, yet an eventual increase in specific force production to control levels by 4 weeks occurred only in quadriceps. This restoration of specific force indicates an apparent intrinsic compensation given absolute force was lower at this later timepoint due to atrophy. Second, atrophy in most fibre types was preceded by altered mitochondrial bioenergetics but the individual relationship differed between muscles with decreases in respiration occurring in quadriceps in contrast to elevated mH_2O_2 emission in diaphragm. Third, both muscles upregulated mitochondrial respiration supported specifically by pyruvate and malate substrates at 4 weeks which may reflect a hormetic adaptation to maintain energy homeostasis during cachexia. Likewise, the diaphragm restored Complex I-supported mitochondrial H_2O_2 emission to normal lower levels by 4 weeks which demonstrates the transient nature of this potential redox pressure.

Collectively, these findings suggest muscle weakness can occur before atrophy during C26 cancer, and this progression is related to dynamic time-dependent changes in mitochondrial bioenergetics that are unique to each muscle.

Mitochondrial bioenergetic alterations and skeletal muscle force reductions precede skeletal muscle atrophy

Work from *Brown* et al. suggested mitochondrial degradation and dysfunction precedes muscle atrophy in the LLC xenograft mouse model of cancer cachexia[12]. In this study, atrophy markers occurred after earlier indices of mitochondrial degeneration in comparator muscles (flexor digitorum brevis and plantaris) including mitochondrial degradation, respiratory control ratios and H_2O_2 emission. The findings of the present study support this proposal with a comparison of atrophy, mitochondrial respiration and mH_2O_2 emission within the same muscle types, namely quadriceps and diaphragm. These findings also extend the proposal by showing muscle-specific mitochondrial alterations occur concurrent to muscle weakness and before atrophy. Specifically, early decreases in respiratory kinetics in quadriceps were not seen in diaphragm suggesting more oxidative muscle might avoid such respiratory decrements. Conversely, early increases in mH_2O_2 emission seen in diaphragm did not occur in quadriceps. These relationships suggest targeted therapies to counter mitochondrial alterations during cancer cachexia could consider the specific bioenergetic function that is altered at precise timepoints in each muscle type.

This relationship between early mitochondrial stress prior to atrophy in both muscles becomes further complicated when considering force production. Muscle weakness occurred at 2 weeks in both muscles before atrophy which highlights a shared pattern in the progression of muscle dysfunction during cancer. While the purpose of this investigation was not to address other mechanisms regulating force production, reduced fibre sizes cannot be an explanation given atrophy did not occur until after weakness was first observed. In this regard, the reduction in absolute force in quadriceps at 2 weeks was therefore due to the lower specific force. However,

the distinct mitochondrial signatures in both muscles at 2 weeks could guide additional questions. For example, in the quadriceps, the early reductions in specific force were associated with early decreases in mitochondrial respiratory control by ADP. When specific force production was restored to control levels by 4 weeks, respiration actually increased above control levels when normalized to ETC subunit content. This dynamic relationship is intriguing and suggests early quadriceps weakness might be due to impairments in mitochondrial energy provision that is nonetheless plastic and capable of adapting – possibly as a hormetic response to the earlier respiratory deficiency – to correct this weakness through super-compensations in energy supply.

In contrast, the diaphragm weakness seen at 2 weeks might be linked to an early redox pressure given elevated mH_2O_2 was observed. This observation is consistent with prior observations of early and transient increases in H_2O_2 emission in diaphragm in the LLC mouse model of cancer cachexia[211]. However, these changes in mH_2O_2 did not alter glutathione in reduced or oxidized forms nor in the static measure of GSH:GSSG equilibrium. While these common measures of glutathione redox buffering are often used to interpret changes in the redox proteome[212], the measures do not necessarily capture the kinetic aspect by which GSH is recycled through glutathione reductases and glutathione peroxidases. As such, a lack of change in these variables does not rule out a signaling role for H_2O_2 in mediating the diaphragm's adaptive response as one possibility may be that the diaphragm was capable of sustaining greater glutathione recycling rates. These lysate-based measures also do not rule out changes in glutathione-mediated thiol oxidation in specific sub-compartments of the cell including mitochondrial or nuclear fractions[175,212,213]. Likewise, mitochondrial H_2O_2 can also oxidize peroxiredoxins through a thioredoxin-mediated recycling mechanism, the relevance of which to muscle adaptation during diseases is only now

being unravelled in more detail[214]. Consideration of such complexities in redox signaling, much of which is H_2O_2-dependent, demonstrates how no single assay can capture the impact of mH_2O_2 on redox signaling-mediated adaptive responses yet exemplifies the considerable research required to further explore the impact of the mH_2O_2 relationships to cancer cachexia reported in this and other studies[12]. Lastly, the degree to which mH_2O_2 influences mitochondrial respiratory control must also be considered more in-depth. For example, the diaphragm did not show reductions in respiration at 2 or 4 weeks yet demonstrated an unexpected increase in respiration at 4 weeks. The explanation for this increase is not apparent but might suggest an earlier energetic deficiency occurred outside of our selected time points. Alternatively, the use of pyruvate as a glucose-derived substrate to stimulate respiration does not rule out a possible change in substrate selection that may be occurring as part of grander adaptive processes. Future studies could compare both pyruvate and fatty acid substrates to determine if such responses are ubiquitous across all substrate oxidation pathways.

The mechanisms by which mitochondria contribute to weakness and atrophy continue to be an area of considerable research and cannot be resolved by a single investigation. However, we attempted to resolve whether mitochondrial stress can acutely suppress force production using an *in vitro* approach that is removed from potential systemic responses to cancer that might also contribute to weakness. As demonstrated in Figure 4-10, acute treatment of diaphragm muscle with the ATP synthase inhibitor oligomycin decreased specific force production. Oligomycin inhibits ATP synthesis but theoretically may also increase mitochondrial reactive oxygen species through increased membrane potential-related electron slip[80]. As this cannot be verified during contraction *in vitro* using our system, the findings nonetheless demonstrate that mitochondrial

stress can acutely depress specific force production. This observation matches previous findings of various mitochondrial inhibitors on single fibre contraction performed *in vitro*[215]. Likewise, in cultured myotubes, a mitochondrial-targeted antioxidant attenuated cisplatin (chemotherapy) induced atrophy by preventing increases in mitochondrial reactive oxygen species[216]. Similarly, a mitochondrial-targeted peptide administered to the same C26 cancer cachexia model used in the present study preserved diaphragm force production and fiber cross sectional area by preventing changes in indices of mitochondrial ATP synthesis and reactive oxygen species[139]. By comparing this prior literature to the time-dependent and muscle-specific responses to C26 cancer in the present study, the dynamic relationship between weakness, atrophy and mitochondrial stress-specific responses could now be explored with such mitochondrial enhancing compounds using a design that captures time-dependent responses across muscle types.

Perspectives on the potential for mitochondrial hormesis in quadriceps and diaphragm

The findings of lower respiration and increased mH_2O_2 emission at 2 weeks is consistent with prior reports at various time points and muscle in the LLC, C26 and peritoneal carcinosis mouse models [10,12,139,192,211]. To our knowledge, the eventual increase in pyruvate-supported respiration seen in both quadriceps and diaphragm in the present study is novel, while, the attenuation of mH_2O_2 emission seen in the diaphragm is consistent with past reports in the plantaris[12] and diaphragm[211] in the LLC mouse model of cachexia. As noted above, mitochondrial respiratory control by ADP increased above control in both muscles despite a stress being observed earlier only in quadriceps. We questioned whether this early reduction in respiration represented an energy crisis triggering compensatory signaling through the energy sensor AMPK – a pathway that triggers compensatory mitochondrial biogenesis or upregulation of substrate-specific oxidation[217]. We did not observe an

effect of cancer on AMPK phosphorylation at either time point **(Figure S4-3)**, although there was a trend in the quadriceps at 4 weeks of tumour bearing whereby AMPK content was increased. Nonetheless, these results do not rule out the potential for AMPK activation at other time points or a more sustained phosphorylation of downstream AMPK- targets. There are also multiple feedback control systems linking metabolic stress to respiratory control that are independent of AMPK which might be considered in future investigations[218].

The design of substrate titration protocols lends insight into the specific mechanisms by which respiration and mH_2O_2 become altered during cancer. For example, as pyruvate/malate were used as the substrates to generate NADH to stimulate complex I-supported respiration, future investigations might consider the potential for cancer to upregulate complex I or pyruvate dehydrogenase activity, albeit maximal activity given saturating pyruvate concentrations were used. Also, the consistent increase in respiration across a wide spectrum of ADP concentrations by 4 weeks in both muscles suggests mitochondrial responsiveness to a wide range of metabolic demands may have been enhanced such that key regulators of matrix ADP/ATP cycling could be considered for future directions (Figure 4-6). ADP was also more effective at attenuating mH_2O_2 [211] in quadriceps by 4 weeks (Figure 4-9) which supports this possibility. Collectively, these findings suggest cancer disrupts mitochondrial bioenergetics by specifically desensitizing mitochondria to ADP in both muscles.

Mitochondrial creatine metabolism appeared to be less capable of adapting in quadriceps by 4 weeks **(Figure 4-7L)** suggesting mitochondrial creatine kinase-dependent phosphate shuttling is more affected in this muscle than diaphragm which showed no such deficiency. In fact, the

creatine-independent (-Creatine) system showed homogeneous plasticity by upregulating in both muscles by 4 weeks while the creatine-dependent system upregulated only in the diaphragm. These findings suggest mitochondrial creatine metabolism may be disrupted in quadriceps muscle during cancer which may impact energy homeostasis given the importance of this system in certain muscles[209].

In general, the diaphragm appeared to be superior to quadriceps with respect to maintaining mitochondrial ETC content markers and respiratory control by ADP at 2 weeks with evidence of super-compensation in respiratory function at 4 weeks. Furthermore, reductions in ETC protein contents were observed in quadriceps at 4 weeks after C26 implantation whereas no changes were observed in diaphragm. This resilience of diaphragm appears to be a unique finding given prior reports have also shown lower mitochondrial protein markers from various pathways and muscle types in LLC and *APC*$^{(Min/+)}$ mouse models of cancer cachexia[9,12]. While the mechanisms for this muscle heterogeneity remain unclear, one possibility relates to muscle contractile activity. The diaphragm constantly contracts *in vivo* whereas quadriceps is used during locomotion. As mitochondrial content and substrate oxidation are regulated by contractile activity [218], future directions might consider whether the diaphragm holds a special mitochondrial 'resistance' to cancer with respect to energy homeostasis which might support the growing notion of chronic contractile activity in improving muscle health during cancer[219].

In conclusion, this investigation reports muscle weakness precedes atrophy in quadriceps and diaphragm in the C26 colon carcinoma mouse model of cancer cachexia. This progression was associated with heterogenous muscle-specific and time-dependent mitochondrial responses in both

muscles. Specifically, an early energetic stress (reduced respiratory control by ADP) was more apparent in quadriceps in contrast to a mitochondrial redox pressure in diaphragm. These early mitochondrial stressors were seemingly corrected as cancer progressed despite the development of atrophy in both muscles and a unique increase in specific force production in quadriceps. This apparent intrinsic compensation in quadriceps may have partially mitigated the contribution of atrophy to the reduced absolute force seen at 4 weeks. Moreover, C26 cancer caused a unique impairment in the coupling of the mitochondrial creatine kinase system to ATP generation in quadriceps whereas this system was not affected in diaphragm. This dynamic plasticity across time demonstrates how the effects of cancer on one muscle may not predict the response in another muscle type. The findings also highlight how understanding heterogeneity may identify mechanisms that determine whether a given muscle might be sensitive, or resistant, to cancer cachexia.

Methods

Animal Care

48 eight-week-old male CD2F1 mice were purchased from Envigo (Indianapolis, USA). Upon arrival, mice were housed and given a minimum of 72 h to acclimatize before cancer implantations. All mice were provided access to standard chow and water ad libitum. While food intake was not measured, reductions in food intake reported in this model of cachexia did not contribute to reduced muscle weights, fibre cross sectional area or muscle force given pair-fed mice retained normal muscle parameters compared to C26 mice[136,220]. Mice were monitored daily for general well-being, tumour ulcerations and tumour size. If mice demonstrated signs of extreme distress, mice would be sacrificed as soon as possible, however, this was never required.

C26 Cell Culture and Tumour Implantation

C26 cancer cells (Purchased from NCI – Frederick, MD USA) were plated at passage 2-3 in T-75 flasks in DMEM supplemented with 10% foetal bovine serum plus 1% penicillin and streptomycin. Once confluent, cells were trypsinized, counted and diluted in PBS. C26 cells (5×10^5) suspended in 100 μL sterile PBS were implanted subcutaneously to both flanks of mice at 8 weeks of age[10]. For control, mice received identical subcutaneous injections of 100 μL sterile PBS and aged for 2 weeks (PBS (2wk); n= 8) and 4 weeks (PBS (4wk); n= 16). Tumours developed for 14-17 days (C26 (2wk); n= 8) and 26-29 days (C26 (4wk); n= 16). Tumours were measured daily, recording the length and width of tumours with digital calipers using the following formula to obtain tumour volume (volume of a sphere): (4/3*π*(length/2)*(width/2)2) in accordance with York University Animal Care Committee guidelines. The same investigator was responsible for measuring tumour sizes throughout the length of the study as preliminary work demonstrated that tumour size

measurements can vary between individuals (data not shown; CV – 7.2% between 3 individuals, CV – 1.3 within designated individual).

Surgery Procedure

Quadriceps, soleus, plantaris, gastrocnemius, tibialis anterior, extensor digitorum longus and spleen were quickly collected under isoflurane anesthesia prior to euthanasia. Tissues were weighed and snap-frozen in liquid nitrogen and stored at -80°C. Quadriceps and diaphragm muscles were placed in BIOPS containing (in mM) 50 MES Hydrate, 7.23 K_2EGTA, 2.77 CaK_2EGTA, 20 imidazole, 0.5 dithiothreitol, 20 taurine, 5.77 ATP, 15 PCr, and 6.56 $MgCl_2 \cdot 6\ H_2O$ (pH 7.1) to be prepared for mitochondrial bioenergetic assays. Quadriceps from one leg and diaphragm strips were harvested for mitochondrial bioenergetic assays while the quadriceps from the contracted leg and a separate diaphragm strip were used for force measurements. The diaphragm strip used for force measurements was cut within 30 seconds of the entire diaphragm being placed in BIOPS prior to transferring the strip to Ringer's solution as noted below.

***In Situ* Quadriceps Force and *In Vitro* Diaphragm Force**

In situ force production for quadriceps muscle was partially adapted from previous literature[221]. Mice were anesthetized with isoflurane and shaved of all hair on their hindlimb. An incision was made above the patella to expose the femoral tendon which was then tightly secured with suture. Once the knot was in place, the tendon was carefully severed, and the suture was attached to an Aurora Scientific 305C muscle lever arm with a hook (Aurora, Ontario, Canada). The knee was secured with a vertical knee clamp immobilizing the knee joint with a 27G needle. Contraction of the quadriceps was controlled through percutaneous stimulation of the femoral nerve anterior to

the hip joint. Optimal resting length (L_o) was determined using single twitches (pulse width = 0.2ms) at varying muscle lengths. Once L_o was established, force as a function of stimulation frequency was measured during 8 isometric contractions at varying stimulation frequencies (1, 20, 40, 60, 80, 100, 120, 140 Hz). The quadriceps muscle was then weighed and used for normalization of force production ('specific force').

In vitro force production for diaphragm muscle was partially adapted from previous literature[222]. Briefly, the diaphragm strip used for force production was placed in a petri dish of ~25^{o}C Ringer's solution containing (in mM): 121 NaCl, 5 KCl, 1.8 $CaCl_2$, 0.5 $MgCl_2$ 0,4 $NaHPO_4$. 24 $NaHCO_3$, 5.5 glucose and 0.1 EDTA; pH 7.3 oxygenated with 95% O_2 and 5% CO_2. Diaphragm strips were cut from the central region of the lateral costal hemidiaphragm. Silk suture was tied to the central tendon as well the ribs, and the preparation was transferred to an oxygenated bath filled with Ringer solution, maintained at 25^{o}C. The suture secured to the central tendon was then attached to a lever arm while the suture loop secured to the ribs was attached to a force transducer. The diaphragm strip was situated between flanking platinum electrodes driven by a biphasic stimulator (Model 305C; Aurora Scientific, Inc., Aurora, ON, Canada). Optimal L_o was determined using twitches (pulse width = 0.2ms) at varying muscle lengths. Once L_o was established, force as a function of stimulation frequency was measured during 10 isometric contractions at varying stimulation frequencies (1, 10, 20, 40, 60, 80, 100, 120, 140, 200 Hz). Force production was normalized ('specific force') to the calculated cross-sectional area (CSA) of the muscle strip (m/l*d) where m is the muscle mass, l is the length, and d is mammalian skeletal muscle density (1.06mg.mm^3). Absolute force for whole muscle was reported for quadriceps but not diaphragm given the latter was assessed with muscle strips.

Mitochondrial Bioenergetic Assessments

Preparation of Permeabilized Muscle Fibres. The assessment of mitochondrial bioenergetics was performed as described previously in our publications [205–207]. Briefly, the quadriceps and diaphragm from the mouse was removed and placed in BIOPS. Muscle was trimmed of connective tissue and fat and divided into small muscle bundles (~1.2 – 3.7 mg wet weight for quadricep and 0.6 – 2.1 mg for diaphragm). Each bundle was gently separated along the longitudinal axis to form bundles that were treated with 40 μg/mL saponin in BIOPS on a rotor for 30 min at 4°C. Following permeabilization, the permeabilized muscle fibre bundles (PmFB) for respiration assessments were blotted and weighed in ~ 1.5mL of tared pre-chilled BIOPS (muscle relaxing media) to ensure PmFB remained relaxed and hydrated rather than exposed to open air. Wet weights were used given small pieces of muscle can detach during respirometry assessments, albeit greatly reduced by blebbistatin (described below). Mean ± SEM wet weights (mg) were 2.4 ± 0.07 for quadriceps and 1.3 ± 0.04 for diaphragm. The remaining PmFB for mH_2O_2 were not weighed at this step as this data was normalized to fully recovered dry weights taken after the experiments. All PmFB were then washed in MiRO5 on a rotator for 15 minutes at 4°C to remove the cytoplasm. MiRO5 contained (in mM) 0.5 EGTA, 10 KH_2PO_4, 3 $MgCl_2 \bullet 6H_2O$, 60 K-lactobionate, 20 Hepes, 20 Taurine, 110 sucrose, and 1 mg/ml fatty acid free BSA (pH 7.1).

Mitochondrial Respiration. High-resolution O_2 consumption measurements were conducted in 2 mL of respiration medium (MiRO5) using the Oroboros Oxygraph-2k (Oroboros Instruments, Corp., Innsbruck, Austria) with stirring at 750 rpm at 37°C. MiRO5 contained 20 mM Cr to saturate mitochondrial creatine kinase (mtCK) and promote phosphate shuttling through mtCK or was kept void of Cr to prevent the activation of mtCK[223] as described in Figure 5. For ADP-

stimulated respiratory kinetics, our previously published procedures to stimulate complexes I and II-supported respiration were employed[205–207]. 5 mM pyruvate and 2 mM malate were added as complex I-specific substrates (via generation of NADH to saturate electron entry into complex I) followed by a titration of sub-maximal ADP (25, 100 and 500 μM) and maximal ADP (up to 5000 μM in the presence of Cr or 30000 μM in the absence of Cr). 25 μM and 100 μM are close to low and high points of previous estimates of free ADP concentrations in human skeletal muscle in resting and high intensity exercise states and therefore allow the determination of mitochondrial responsiveness to a physiological spectrum of low to high energy demands[224–228]. Saturating [ADP] were different depending on the muscle and presence or absence of creatine in the experimental media. Mitochondrial respiration was normalized to mass of fibre bundles as well as total content of ETC subunits detected with the antibody cocktail listed below. This normalization was performed on a separate piece of the same muscle from the same mouse to evaluate whether changes in respiration per mass were due to alterations in mitochondrial content or intrinsic mitochondrial respiratory responses. While normalizing bioenergetic fluxes to ETC content markers within the same bundle would theoretically reduce variability, the occasional separation of 1-2 fibres in chambers after an experiment may cause under-estimations of total bundle ETC marker contents.

Kmapp for creatine to ADP was not established as we have observed that many permeabilized fibres from past studies do not fit Michaelis-Menten kinetics with these assay conditions (low to modest R^2). Creatine accelerates matrix ADP/ATP cycling at submaximal [ADP] and lowers the Kmapp for ADP in some muscles[209,218]. Therefore, in order to evaluate mitochondrial creatine sensitivity, 100 and 500 μM ADP were used to calculate a creatine sensitivity index. Following

the ADP titration, cytochrome *c* was added to test for mitochondrial membrane integrity. Finally, succinate (20 mM) was then added to saturate electron entry into Complex II.

All experiments were conducted in the presence of 5 μM blebbistatin (BLEB) in the assay media to prevent spontaneous contraction of PmFB, which has been shown to occur in response to ADP at 37°C that alters respiration rates [223,229]. Polarographic oxygen measurements were acquired in 2 second intervals with the rate of respiration derived from 40 data points and expressed as pmol/s/mg wet weight. PmFB were weighed in ~1.5 mL of tared BIOPS to relax muscle as noted above.

Mitochondrial H_2O_2 Emission (mH_2O_2). mH_2O_2 was determined spectrofluorometrically (QuantaMaster 40, HORIBA Scientific, Edison, NJ, USA) in a quartz cuvette with continuous stirring at 37°C, in 1 mL of Buffer Z supplemented with 10 μM Amplex Ultra Red, 0.5 U/ml horseradish peroxidase, 1mM EGTA, 40 U/ml Cu/Zn-SOD1, 5 μM BLEB and 20mM Cr. Buffer Z contained (in mM) 105 K-MES, 30 KCl, 10 KH_2PO_4, 5 $MgCl_2 \bullet 6H_2O$, 1 EGTA, and 5mg/mL BSA (pH 7.4). State II mH_2O_2 (maximal emission in the absence of ADP) was induced using the Complex I-supporting substrates (NADH) pyruvate (10mM) and malate (2mM) to assess maximal (State II, no ADP) mH_2O_2 as described previously[206]. Following the induction of State II mH_2O_2, a titration of ADP was employed to progressively attenuate mH_2O_2 as occurs when membrane potential declines during oxidative phosphorylation (Figure 5). After the experiments, the fibres were rinsed in double deionized H_2O, lyophilized in a freeze-dryer (Labconco, Kansas City, MO, USA) for > 4h and weighed on a microbalance (Sartorius Cubis Microbalance, Gottingen

Germany). The rate of mH_2O_2 emission was calculated from the slope (F/min) using a standard curve established with the same reaction conditions and normalized to fibre bundle dry weight.

Western Blotting

A frozen piece of quadriceps and diaphragm from each animal was homogenized in a plastic microcentrifuge tube with a tapered Teflon pestle in ice-cold buffer containing (mm) 20 Tris/HCl, 150 NaCl, 1 EDTA, 1 EGTA, 2.5 $Na_4O_7P_2$, 1 Na_3VO_4, 1% Triton X-100 and PhosSTOP inhibitor tablet (Millipore Sigma, Burlington, MA, USA) (pH 7.0) as published previously[230]. Protein concentrations were determined using a bicinchoninic acid (BCA) assay (Life Technologies, Carlsbad, CA, USA). 15-30 μg of denatured and reduced protein was subjected to 10-12% gradient SDS-PAGE followed by transfer to low-fluorescence polyvinylidene difluoride membrane. Membranes were blocked with Odyssey Blocking Buffer (LI-COR, Lincoln NE, USA) and immunoblotted overnight (4°C) with antibodies specific to each protein. A commercially available monoclonal antibody was used to detect electron transport chain proteins (rodent OXPHOS Cocktail, ab110413; Abcam, Cambridge, UK, 1:250 dilution), including V-ATP5A (55kDa), III-UQCRC2 (48kDa), IV-MTCO1 (40kDa), II-SDHB (30 kDa), and I-NDUFB8 (20 kDa). Commercially available polyclonal antibodies were used to detect AMP-activated protein kinaseα (AMPKα) (rabbit, CST, 2532; 62kDa; 1:1000) and Phospho-AMPKα Thr172 (P-AMPK) (rabbit CST, 2535, 62kDa; 1:500) as used previously[230].

After overnight incubation in primary antibodies, membranes were washed 3x5 minutes in TBST and incubated for 1 hour at room temperature with the corresponding infrared fluorescent secondary antibody (LI-COR IRDye 680nm or 800nm) at a dilution previously optimized (1:20

000). Immunoreactive proteins were detected by infrared imaging (LI-COR CLx; LI-COR) and quantified by densitometry using ImageJ. All images were normalized to Amido Black total protein stain (A8181, Sigma) using the entire lane corresponding to each sample.

Immunofluorescence Analysis

Quadriceps (cut longitudinally to include half the vastus intermedius & full vastus lateralis) and diaphragm muscle samples embedded in O.C.T medium (Fisher Scientific) were cut into 10-μm-thick sections with a cryostat (HM525 NX, Thermo Fisher Scientific, Mississauga, ON, Canada) maintained at -20°C. Muscle fibre type was determined as previously described[231], with minor modifications. All primary antibodies were purchased from the Developmental Studies Hybridoma Bank (University of Iowa), and secondary antibodies were purchased from Invitrogen (Burlington, ON, Canada). Briefly, slides were blocked with 5% goat serum (Sigma Aldrich) in PBS for 1 hour at room temperature. Next, slides were incubated with primary antibodies against myosin heavy chain (MHC) I (BA-F8; 1:25), MHC IIA (SC-71; 1:1000) and MHC IIB (BF-F3; 1:50) for 2 hours at room temperature. Afterwards, slides were washed 3x in PBS for 5 minutes and then incubated with secondary antibodies (MHCI; Alexa Fluor 350 IgG2b; 1:1000), (MHCIIa; Alexa Fluor 488 IgG1; 1:1000), (MHC Iib; Alexa Fluor 568 IgM; 1:1000) for 1 hour at room temperature. Slides were then washed 3x in PBS for 5 minutes and mounted with ProLong antifade reagent (Life Technologies, Burlington, ON, Canada). Images were acquired the next day using EVOS FL Auto 2 Imaging System (Invitrogen, Thermo Fisher Scientific, Mississauga, ON, Canada). Individual images were taken across the entire cross section and then assembled into a composite image. 20-30 muscle fibres per fibre type were selected randomly throughout the cross section and traced

with ImageJ software to assess CSA after calibrations with a corresponding scale bar. Muscle fibres that appeared black were recorded as MHC IIX[231].

Real-time RT-PCR analyses of mRNA

Measurement of mRNA was completed as previously described[232]. Briefly, frozen tissues were homogenized with TriZol agent (Life Technologies, Cat# 15596026) and RNA isolated with a commercial kit. RNA concentrations were quantified with a Biotek Take3 micro-volume microplate with a BioTek PowerWave XS microplate reader (BioTek Instruments Inc., Winooski, VT). RNA was only used if the sample was of sufficient quality (260/280 ratio >2). Isolated RNA was then reverse transcribed into cDNA using commercial reagents (Superscript Vilo, Cat#11755500; Life Technologies). cDNA was then serially diluted to 1:100 and used for quantitative real time PCR analysis. cDNA was combined with appropriate probes, master mix and amplified in a reaction of 40 cycles of denaturation, annealing, and extension at 95, 60, and 72°C. Data were quantified with the ΔΔCt method. Data were normalized to control groups. 18s was used as an internal housekeeping gene (clone #Mm03928990_g1) and did not differ between groups. Probes of interest included: Atrogin/FBXO32 (Clone #Mm00499523_m1), Murf1/Trim63 (Clone #Mm01185221_m1), Gadd45a (Clone # Mm00432802_m1), and Ubc (Clone #Mm02525934_g1).

Glutathione Analysis

Glutathione was measured as previously published [206,208]. Briefly, reduced (GSH) and oxidized (GSSG) glutathione were measured using the Shimadzu Nexera X2 UHPLC system (Mandel Scientific Company Inc. Guelph, Canada). Quadriceps and diaphragm were homogenized in

50mM Tris buffer with 10mM boric acid, 2mM L-serine, 20 μM acivicin, and 5 mM *N*-ethylamide, and acidified using TCA (for GSH) and PCA (for GSSG). Samples were separated with a Zorbax C18 column (Agilent Technologies, Mississauga, ON, Canada). GSH was assessed by UV-HPLC (265 nm wavelength) monitoring of NEM-GSH using a 0.25% glacial acetic acid mobile phase with 6% acetonitrile at 1.05ml/min flow rate detected at 265nm. GSSG was assessed by fluorescent-HPLC (excited at 350nm and detected at 420nm emission) using HPLC/UHPLC fluorescence detector (Mandel scientific). GSSG samples were diluted in 0.5M NaOH and run using 25mM Na_2HPO_4 in HPLC-grade water with 15% methanol mobile phase at a 0.5mL/min flow rate by tracking O-pthalymide (OPA) tagged GSH.

Statistics

Results are expressed as mean ± SD. The level of significance was established at $P < 0.05$ for all statistics. The D'Agostino – Pearson omnibus normality test was first performed to determine whether data resembled a Gaussian distribution, and all data was subject to the ROUT test to identify and exclude outliers. Western blot results for proteins in the electron transport chain subunit complexes I, IV and V in quadriceps failed normality as did proteins in complexes I, II, IV and V for diaphragm. In addition, quadriceps and diaphragm delta glutamate respiration failed normality and were analyzed using a non-parametric Mann-Whitney t-test. Quadriceps and diaphragm mRNA content markers at 4 weeks all failed normality (MURF1, atrogin, UBC, Gadd45a) and were assessed by a non-parametric Mann-Whitney t-test. All other data passed normality. A two-tailed unpaired t-test was used to compare C26 to PBS within each time point with respect to muscle mass, fibre cross-sectional area, remaining western blots, qt-PCR, and glutathione measures. A two-way ANOVA with factors of timepoint (2 vs 4 week) and treatment

(C26 vs PBS) was used for mitochondrial respiration, mH_2O_2 and all force-frequency experiments followed by Benjamini, Krieger and Yekutieli's post-hoc analysis.[233] when a significant interaction was observed. All statistical analyses were performed with GraphPad Prism Software 8.4.2 (La Jolla, CA, USA).

Study Approval

All experiments and procedures were approved by the Animal Care Committee at York University (AUP Approval Number 2019-10) in accordance with the Canadian Council on Animal Care.

Author Contributions

L.J.D., C.A.B, M.R.C., N.P.G. and C.G.R.P. contributed to the rationale and study design. L.J.D., C.A.B., S.G. and C.G.R.P. conducted all experiments and/or analyzed all data. C.G.R.P. and L.J.D. wrote the manuscript. All authors contributed to the interpretation of the data and manuscript preparation. All authors have approved the final version of the manuscript and agree to be accountable for all aspects of the work. All persons designated as authors qualify for authorship, and all those who qualify for authorship are listed.

Acknowledgments

Funding was provided to C.G.R.P. by the National Science and Engineering Research Council (no. 436138-2013 and no.2019-06687) and an Ontario Early Researcher Award (C.G.R.P., no. 2017-0351) with infrastructure supported by the Canada Foundation for Innovation, the Ontario Research Fund and the James. H. Cummings Foundation. L.J.D. was supported by a NSERC CGS-D scholarship. C.A.B. was supported by a NSERC PGS-D scholarship. S.G. was supported by an

Ontario Graduate Scholarship. N.P.G. was funded by U.S. National Institutes of Health under Award Number R01AR075794 from the National Institute of Arthritis and Musculoskeletal and Skin Disease

Supplementary Data – Included in published manuscript

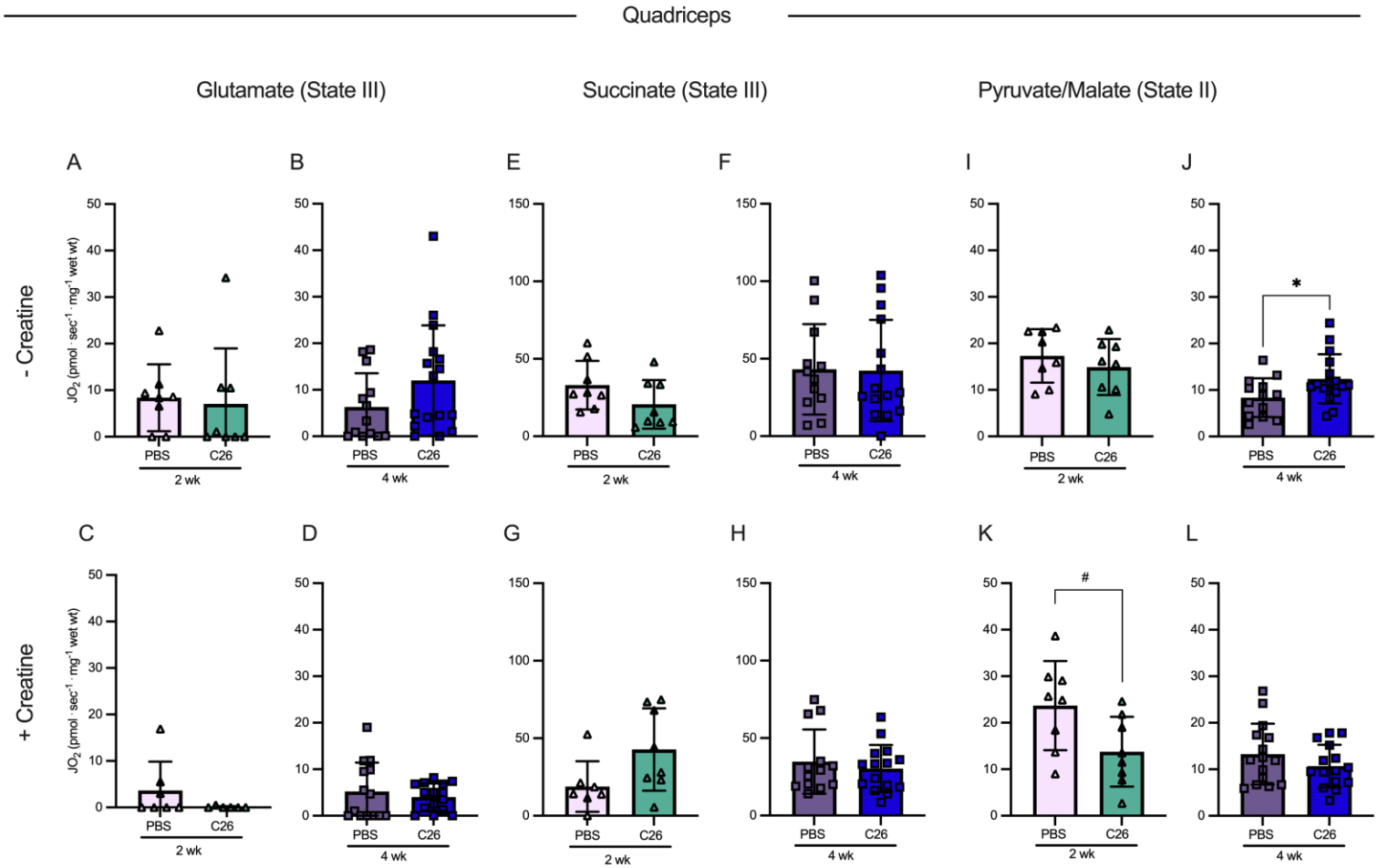

Figure S4-1 Multiple substrate evaluation of oxygen consumption in quadriceps permeabilized muscle fibre bundles. Oxygen consumption was evaluated in the absence of creatine at 2 weeks and 4 weeks post C26 implantation or PBS injections in permeabilized muscle fibres when stimulated with glutamate (*A*, *B*), succinate (*E*, *F*) and pyruvate/malate (*I*, *J*). This was repeated in the presence of 20mM Creatine (*C*, *D*, *G*, *H*, *K*, *L*). Results represent mean ± SD; n=8-16; Two tailed T-tests were used to determine the difference between PBS(2wk) vs. C26(2wk) and PBS (4wk) vs. C26(4wk). # $P<0.05$ PBS (2wk) vs C26 (2wk); * $P<0.05$ PBS (4wk) vs C26 (4wk)

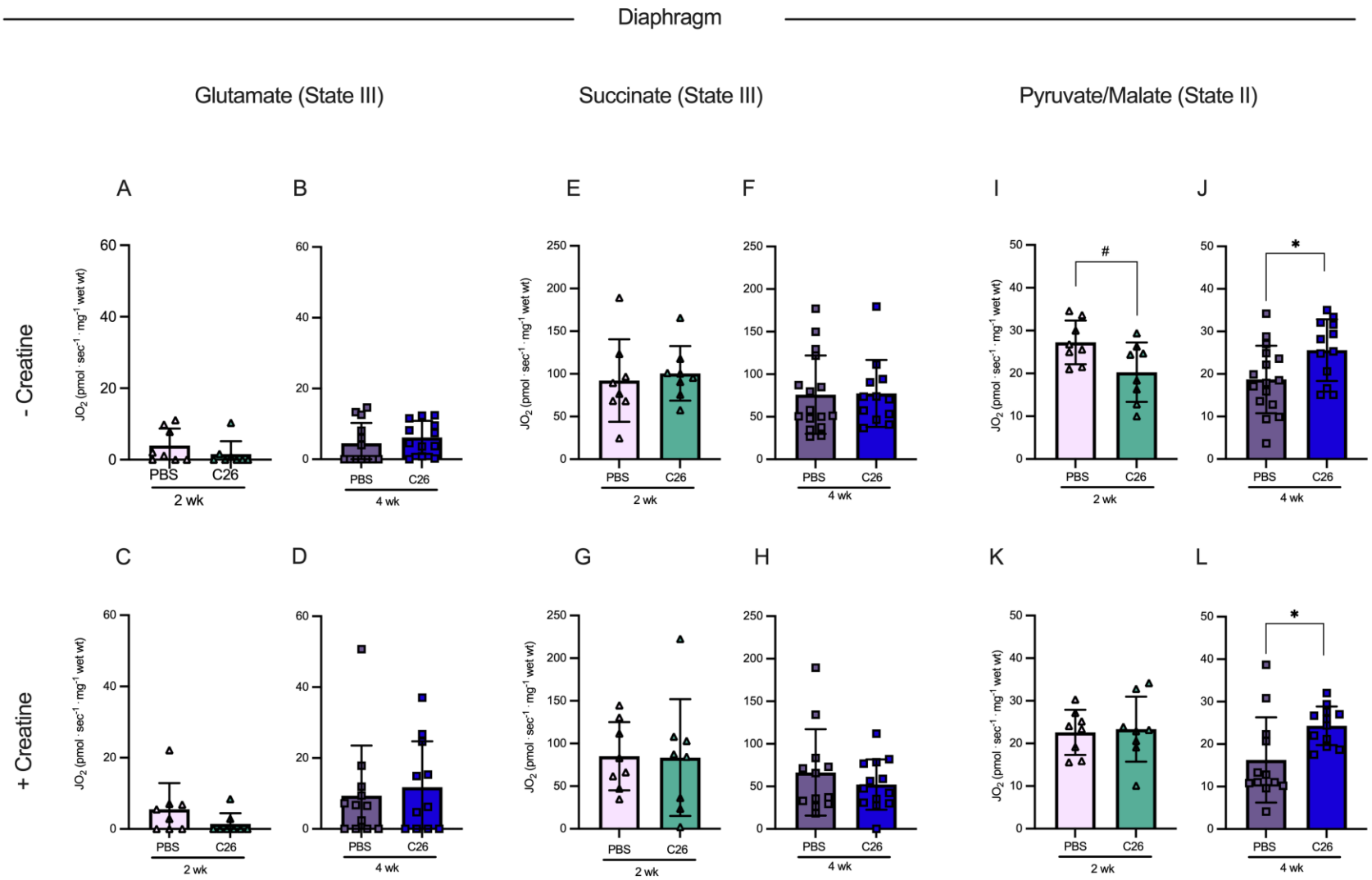

Figure S4-2 Multiple substrate evaluation of oxygen consumption in diaphragm permeabilized muscle fibre bundles. Oxygen consumption was evaluated in the absence of creatine at 2 weeks and 4 weeks post C26 implantation or PBS injections in permeabilized muscle fibres when stimulated with glutamate (*A*, *B*), succinate (*E*, *F*) and pyruvate/malate (*I*, *J*). This was repeated in the presence of 20mM Creatine (*C*, *D*, *G*, *H*, *K*, *L*). Results represent mean ± SD; n=8-16; Two tailed T-tests were used to determine the difference between PBS(2wk) vs. C26(2wk) and PBS (4wk) vs. C26(4wk). # $P<0.05$ PBS (2wk) vs C26 (2wk); * $P<0.05$ PBS (4wk) vs C26 (4wk).

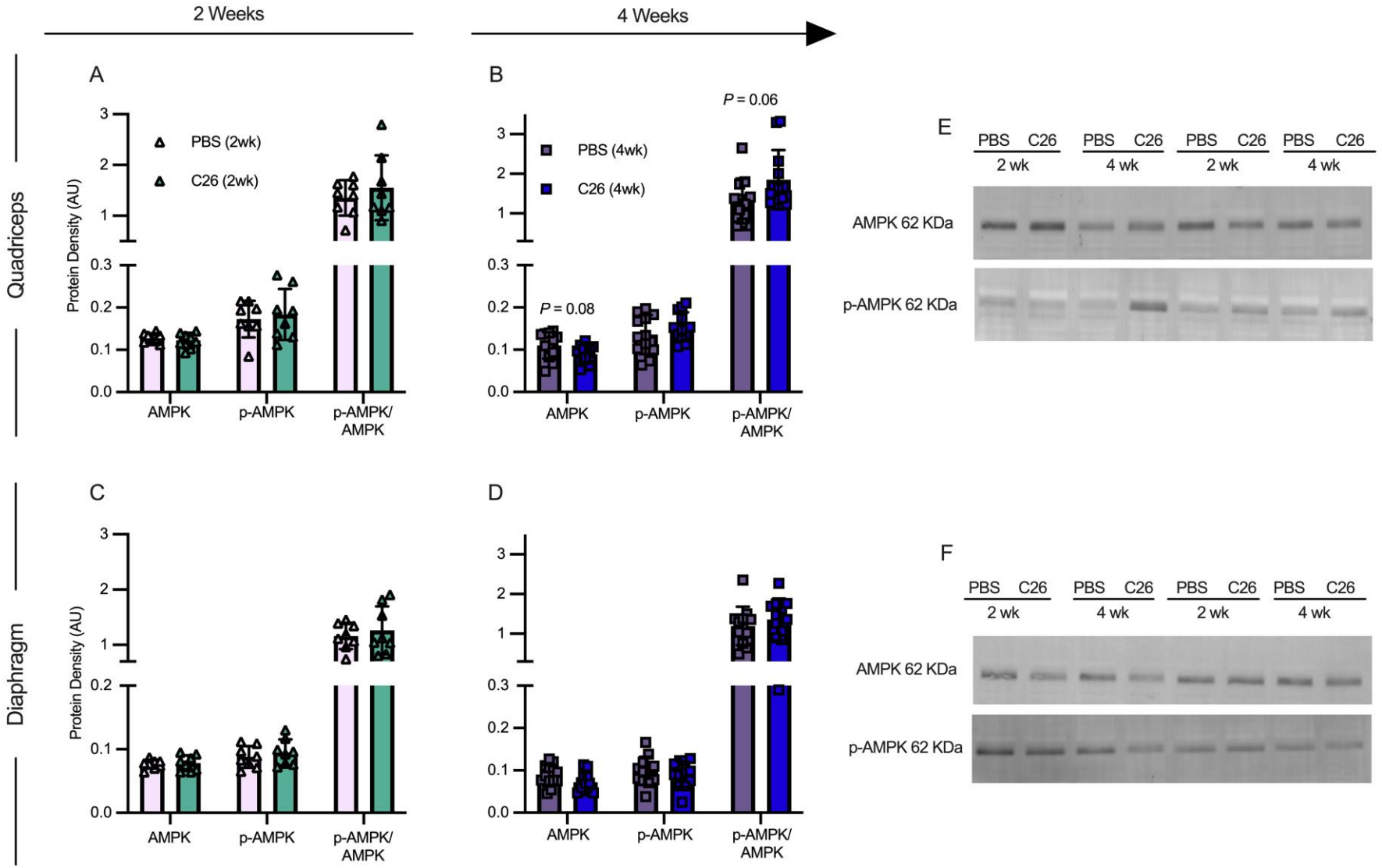

Figure S4-3 Muscle-specific changes in markers of growth in C26 tumour-bearing skeletal muscle.
Protein content of AMPKα and P-AMPKα were quantified at in the quadriceps at 2 weeks (*A*, *n*=8) and 4 weeks (*B*, *n*=12). Markers were also quantified at in the diaphragm at 2 weeks (*C*, *n*=8) and 4 weeks (*D*, *n*=12). *E*, representative image for quadriceps and *F*, representative image for diaphragm. Results represent mean ± SD. Two tailed T-tests were used to determine the difference between PBS(2wk) vs. C26(2wk) and PBS (4wk) vs. C26(4wk).

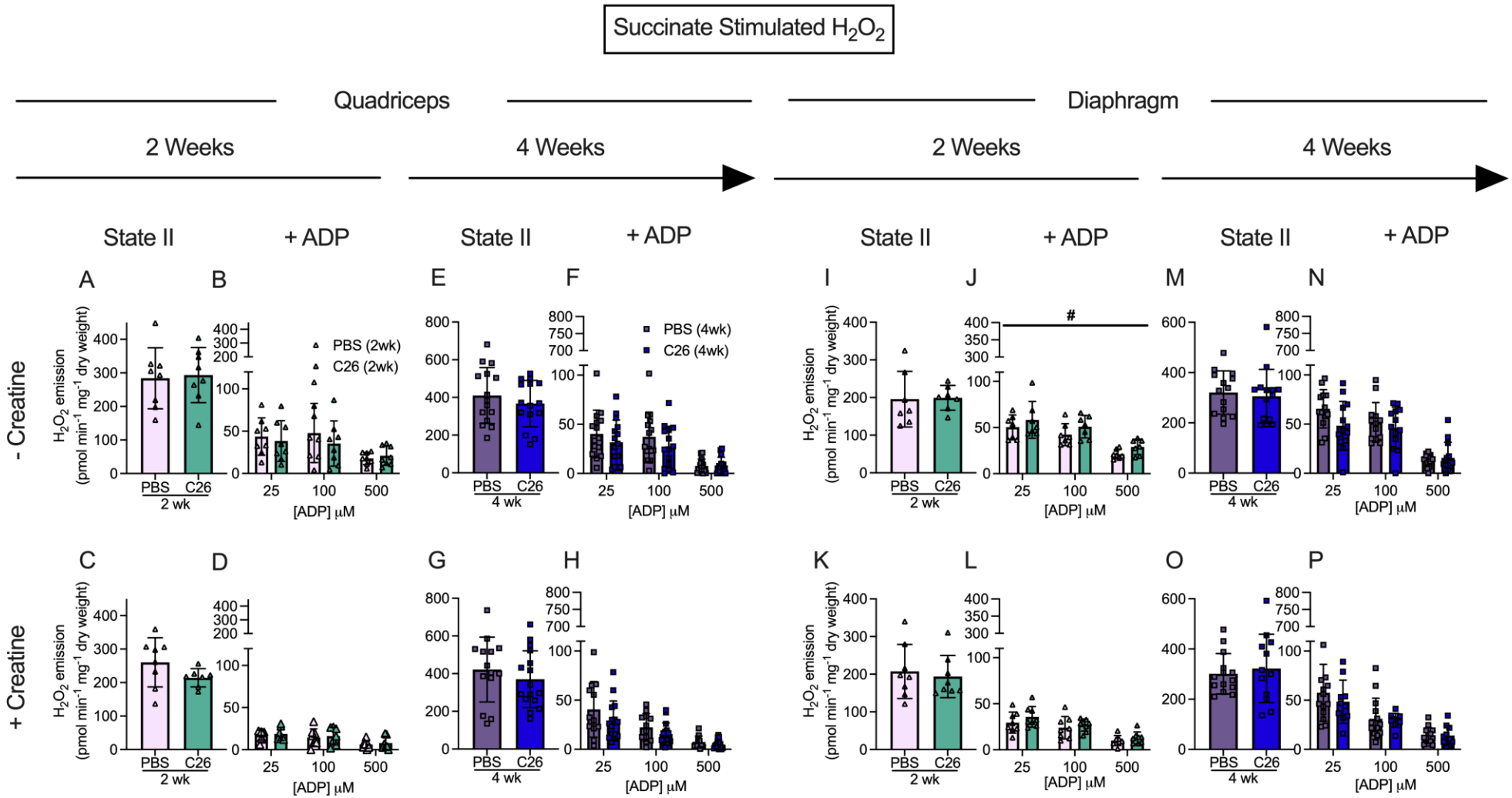

Figure S4-4 Succinate stimulated mH_2O_2 emission in quadriceps and diaphragm muscle of C26 tumour bearing mice. At 2 and 4 weeks, quadriceps mH_2O_2 emission supported by succinate (10mM) ($FADH_2$) was assessed under maximal State II (no ADP) conditions in the absence of creatine (*A*, *E*) and in the presence of 20mM Creatine (*C*, *G*). State III (range of [ADP] to model metabolic demand) was also assessed in the absence of creatine (*B*, *F*) and in the presence of 20mM creatine (*D* and *H*). These measures were repeated in the diaphragm (I-P). Results represent mean ± SD; n=7-16; Two tailed T-tests were used to determine the difference between PBS(2wk) vs. C26(2wk) and PBS (4wk) vs. C26(4wk) for state II H_2O_2 emission. A two-way ANOVA was used to determine the difference between PBS(2wk) vs. C26(2wk) and PBS (4wk) vs. C26(4wk). # P<0.05, PBS (2wk) vs C26 (2wk); * P<0.05, PBS (4wk) vs C26 (4wk).

5 Muscle weakness and mitochondrial stress occur before severe metastasis in a novel mouse model of ovarian cancer cachexia

This chapter is an original published article. It is presented in its published form.

Muscle weakness and mitochondrial stress occur before severe metastasis in a novel mouse model of ovarian cancer cachexia. LJ Delfinis, LM Oglivie, S Khajehzadehshoushtar, S Gandhi, MC Garibotti, AK Thuhan, K Matuszewska, M Pereira, RG Jones III, AJ Cheng, TJ Hawke, NP Greene, KA Murach, JA Simpson, J Petrik, and CGR Perry. Molecular Metabolism. In Press.

Author Contributions: The majority of experiments or this project were carried about by Luca Delfinis. J.P, K.M, M.P and L.M.O grew EOC cancer cells, injected and monitored all mice until transport from University of Guelph to York University. L.J.D performed all functional testing and separated fibers for bioenergetic assessments. Due to the nature of these experiments, two people were required in order to efficiently complete all force and bioenergetic assays on fresh viable tissue. As such, L.J.D completed force assessments while S.G /S.K/M.G assisted with collection and running bioenergetics. L.J.D, L.M.O, J.P, J.A.S. and C.G.R.P. contributed to the rationale and study design. L.J.D., L.M.O., S.K and C.G.R.P. conducted all experiments and/or analyzed all data. R.G.J and K.M helped complete and analyze RNA Sequencing. C.G.R.P. and L.J.D. wrote the manuscript. All authors contributed to the interpretation of the data and manuscript preparation. All authors have approved the final version of the manuscript and agree to be accountable for all aspects of the work. All persons designated as authors qualify for authorship, and all those who qualify for authorship are listed.

Muscle weakness and mitochondrial stress occur before severe metastasis in a novel mouse model of ovarian cancer cachexia

Luca J. Delfinis[1], Leslie M. Ogilvie[2], Shahrzad Khajehzadehshoushtar[1], Shivam Gandhi[1], Madison C. Garibotti[1], Arshdeep K. Thuhan[1], Kathy Matuszewska[3], Madison Pereira[3], Ronald G. Jones III[4], Arthur J. Cheng[1], Thomas J. Hawke[5], Nicholas P. Greene[4], Kevin A. Murach[4], Jeremy A. Simpson[2], Jim Petrik[3] and Christopher G.R. Perry[1]†.

Affiliations

[1]School of Kinesiology & Health Science, Muscle Health Research Centre, York University, Toronto, ON, Canada

[2]Department of Human Health and Nutritional Sciences, University of Guelph, Guelph, ON, Canada

[3]Department of Biomedical Sciences, University of Guelph, Guelph, ON, Canada

[4]Exercise Science Research Center, Department of Health, Human Performance, and Recreation, University of Arkansas, Fayetteville, AR, USA

[5]Department of Pathology and Molecular Medicine, McMaster University, Hamilton, ON, Canada

Email Addresses:

delfinis@yorku.ca; ogilviel@uoguelph.ca; shar99@yorku.ca; shivamg@yorku.ca; mgarib@yorku.ca; thuhan@yorku.ca; kmatusze@uoguelph.ca; mperei02@uguelph.ca; ronaldj@uark.edu; ajcheng@yorku.ca; hawke@mcmaster.ca; npgreene@uark.edu; kmurach@uark.edu; jeremys@uoguelph.ca; jpetrik@uoguelph.ca; cperry@yorku.ca

Key Words: Ovarian cancer cachexia, mitochondria, skeletal muscle, metastasis.

†Address for Correspondence:

Christopher Perry, PhD

School of Kinesiology and Health Science

Muscle Health Research Centre

344 Norman Bethune College

York University

4700 Keele Street

Toronto, Ontario M3J 1P3

(P) 416 736 2100 ext. 33232

cperry@yorku.ca

Highlights:

- This study reports the first orthotopic model of metastatic ovarian cancer cachexia that can be induced in adult immunocompetent mice
- Diaphragm and limb muscle weakness precedes severe metastasis and atrophy during ovarian cancer
- Skeletal muscle mitochondrial oxidative and redox stress signatures occur during pre-severe-metastatic stages of ovarian cancer
- Specific muscle force as well as mitochondrial pyruvate oxidation and creatine metabolism demonstrate compensation in later stages
- Ovarian cancer has heterogeneous effects on distinct muscle types across time

Abstract

Objectives: A high proportion of women with advanced epithelial ovarian cancer (EOC) experience weakness and cachexia. This relationship is associated with increased morbidity and mortality. EOC is the most lethal gynecological cancer, yet no preclinical cachexia model has demonstrated the combined hallmark features of metastasis, ascites development, muscle loss and weakness in adult immunocompetent mice.

Methods: Here, we evaluated a new model of ovarian cancer-induced cachexia with the advantages of inducing cancer in adult immunocompetent C57BL/6J mice through orthotopic injections of EOC cells in the ovarian bursa. We characterized the development of metastasis, ascites, muscle atrophy, muscle weakness, markers of inflammation, and mitochondrial stress in the tibialis anterior (TA) and diaphragm ~45, ~75 and ~90 days after EOC injection.

Results: Primary ovarian tumour sizes were progressively larger at each time point while severe metastasis, ascites development, and reductions in body, fat and muscle weights occurred by 90 Days. There were no changes in certain inflammatory (TNFα), atrogene (MURF1 and Atrogin) or GDF15 markers within both muscles whereas IL-6 was increased at 45 and 90 Day groups in the diaphragm. TA weakness in 45 Day preceded atrophy and metastasis that were observed later (75 and 90 Day, respectively). The diaphragm demonstrated both weakness and atrophy in 45 Day. In both muscles, this pre-severe-metastatic muscle weakness corresponded with considerable reprogramming of gene pathways related to mitochondrial bioenergetics as well as reduced functional measures of mitochondrial pyruvate oxidation and creatine-dependent ADP/ATP cycling as well as increased reactive oxygen species emission (hydrogen peroxide). Remarkably, muscle force per unit mass at 90 days was partially restored in the TA despite the presence of atrophy and severe metastasis. In contrast, the diaphragm demonstrated progressive weakness. At this advanced stage, mitochondrial pyruvate oxidation in both muscles exceeded control mice suggesting an apparent metabolic super-compensation corresponding with restored indices of creatine-dependent adenylate cycling.

Conclusion: This mouse model demonstrates the concurrent development of cachexia and metastasis that occurs in women with EOC. The model provides physiologically relevant advantages of inducing tumour development within the ovarian bursa in immunocompetent adult

mice. Moreover, the model reveals that muscle weakness in both TA and diaphragm precedes severe metastasis while weakness also precedes atrophy in the TA. An underlying mitochondrial bioenergetic stress corresponded with this early weakness. Collectively, these discoveries can direct new research towards the development of therapies that target pre-atrophy and pre-severe-metastatic weakness during EOC in addition to therapies targeting cachexia.

1.Introduction

Cancer-induced cachexia is a multifactorial syndrome characterized by muscle loss and weakness[3]. Severe cachexia is linked to reductions in quality of life, tolerance to anticancer therapies and overall survivability [6,27,201]. The prevalence of cachexia varies widely (20-80%) across different types and severity of cancer [4,31]. Raising the possibility that cachexia may have both ubiquitous and distinct mechanisms related to the host organ. With growing awareness that cancer itself can induce cachexia even in the absence of cytotoxic cancer therapies, it is imperative to develop pre-clinical models for each type of cancer cachexia that captures critical phenotypic hallmarks of this disease in humans.

Dozens of clinical investigations examining prospective therapeutics to treat cancer cachexia have been conducted to date, but none have resulted in an approved treatment [5]. It has been suggested that such pitfalls could be mitigated by developing new pre-clinical models of cancer cachexia. Such models would consider the complex and multifactorial aspects of cancer cachexia including the interactions between cancer and the host organ, the immune system, metastasis, rate of cancer development, and the influence of age. Some pre-clinical models develop tumours spontaneously in adulthood but can require large animal colonies and expenses. Other models involve either a genetic mutation, whereby mice are born with cancer, or injections of cancer cells under the skin. While these approaches are generally used to research many types of cancer[128,234], it is unclear if the mechanisms underlying their cachectic phenotype are limited in their translational potential. Thus, researchers have questioned the utility of existing models in regard to pre-clinical therapy development and elucidating underlying mechanisms of cachexia [13–15]. Indeed, the lack of appropriate preclinical models has been a strong criticism for all forms of cancer cachexia – not just ovarian cancer - over the last number of years [13,42,133]. Models with cancer in the host organ that can be induced at any age in immunocompetent mice, that also demonstrate metastasis, has been suggested to be important for improving the predictive power of *in vivo* models of cancer cachexia[13–15].

With regards to epithelial ovarian cancer (EOC) cachexia – the most lethal gynecological cancer in women [147] - several models to date have shown robust primary outcomes of muscle atrophy, muscle weakness, and loss of adipose tissue. Some of the existing models used for ovarian cancer cachexia use injection techniques that are ectopic to the ovaries, in immunodeficient mice, and can

develop cachexia at rapid rates (as little as 8 days in some cases) [118,148,149]. Furthermore, none of these preclinical models have demonstrated the presence of metastasis [118,148,149]. The development of a new preclinical model would ideally capture metastasis given this defining event is associated with severe cachexia and reduced survival rates during advanced stages of ovarian cancer [235]. Indeed, when ovarian cancer is detected at early stages and before metastasis, the cure rate is estimated to be as high as 90% [236] in contrast to much lower survival rates once metastasis has occurred. As more than 70% of ovarian cancer cases are diagnosed at late stages, improving our understanding of how cachexia develops could lead to new insight into improved patient management and perhaps early detection of ovarian cancer itself [235].

Characterizing cachexia warrants careful consideration of how changes in muscle mass and force production occur over time as the tumour develops, and in relation to underlying mechanisms regulating both aspects of muscle quality. Recently, we reported that muscle weakness precedes atrophy in the C26 (Colon-26) colorectal mouse [237]. This pre-atrophy weakness also occurred without any changes in expression of classic atrophy-related gene programs suggesting muscle weakness during cancer could also be caused by unknown atrophy-independent mechanisms. In this study, a strong relationship was found between pre-atrophy weakness and mitochondrial pathway-specific reprogramming as an apparent early metabolic stress response to the initial appearance of tumours. Remarkably, once locomotor muscle atrophy occurred, mitochondria appeared to adapt by increasing pyruvate oxidation, which was related to an unexpected restoration of mass-specific force production [237]. Of interest, this relationship was heterogeneous across different types of muscles suggesting the effects of cancer on one muscle type do not necessarily predict the response in another muscle. This phenomenon demonstrates the value of comparing muscle force to muscle mass across time and between muscle types in relation to tumour size. In this regard, muscle weakness during the pre-atrophy and atrophy (cachexia) phases of ovarian cancer have not been investigated, nor in relation to metastasis or metabolic dysfunction. Understanding this could lead to more precise understanding of ovarian cancer cachexia pathology to aid better mechanism elucidation and therapy development.

The purpose of this study was to identify the time-dependent and muscle-specific development of weakness and atrophy in a novel model of ovarian cancer cachexia in relation to metabolic reprogramming. In this model, spontaneously transformed ovarian epithelial cells from the same mouse strain (syngeneic) were injected into the ovarian bursa (orthotopic) in immunocompetent

mice with the intention of retaining the normal immune response to this type of cancer. These results demonstrate a new *in vivo* model of ovarian cancer cachexia that captures metastasis characteristic of advanced stages of EOC seen in women [238,239] that also has considerable utility for identifying new relationships between the development of muscle weakness, atrophy, and metabolic reprogramming across time during ovarian cancer.

2. Materials and Methods

2.1 Animal Care and ID8 Inoculation

Two cohorts of 48 (n=12 per group; **SFigure 5-1A and 5-1B**) female C57BL/6 mice were ordered at 7-9 weeks of age from Charles River Laboratories. These mice were housed at the University of Guelph in accordance with the Canadian Council on Animal Care. Tumours were induced as described previously at the University of Guelph [240–243]. Briefly, ID8 cells (epithelial ovarian cancer cells; 1.0 x 10^6 in 5μL) were injected directly under the left ovarian bursa of C57BL/6J mice generating an orthotopic, syngeneic, immunocompetent cancer mouse model. ID8 cells were originally gifted by Drs. Paul Terranova and Kathy Roby from Kansas State University to Dr. Jim Petrik at the University of Guelph. ID8 cells are transformed murine ovarian surface epithelial cells that do not contain mutations, however, after orthotopic implantation and interaction with the ovarian microenvironment, ID8 cells that metastasize spontaneously develop a gain-of-function p53 mutation that is identical to the mutation seen in 95% of women with high-grade serous carcinoma [244]. Control mice were sham injected with equivalent volumes of sterile phosphate buffered saline (PBS). Two weeks after ID8 inoculation, mice were transported from University of Guelph to York University where they were housed for the remainder of the study in accordance with the Canadian Council on Animal Care. All mice were provided access to standard chow and water *ad libitum*.

Control (CTRL) and 75 Day mice were injected at 9-11weeks old with PBS and ID8 cells respectively and aged for 72–78 days post injection. 45 Day mice were injected at 16-17 weeks old and aged for 42-48 days post injection. 90 Day mice were injected at 9-10 weeks old and aged for 83-107 days post injection (**SFigure 5-1A and 5-1B)**. These ranges were chosen given force and mitochondrial assessments limit daily experimental throughput, and health metrics used to determine the date of euthanasia were variable in the more advanced stages of cancer. Specifically, at the 90 Day time point, mice were euthanized upon presentation of some of the following endpoint criteria: >10% body weight loss, >20mL of ascitic volume collected during paracentesis, > 5 ascites paracentesis taps completed, and/or subjective changes in behavioural patterns consistent with removal criteria as per animal care guidelines (self-isolation, ruffled fur/poor self-grooming and irregular gait). Ascitic taps were necessary to pro-long the survival of mice as it would occur in human ovarian cancer and to reach >10% body weight loss which is highly suggestive of a cancer cachexia phenotype. Staggering the age at which mice received cancer cells

permitted a consistent age at euthanasia for all mice (20-24 weeks old) to reduce aging effects on all measures.

2.2 Volitional Wheel Running & Forelimb Grip Strength

72 hours before euthanasia, a subset of mice were placed in individual cages with a 14 cm diameter running wheel and rotation counter (VDO m3 bike computer, Mountain Equipment Co-Op, Vancouver, Canada) as done previously [206]. Any mice that had ascites within the 90 Day group were tapped immediately prior to introduction in the cage with a running wheel to reduce the potential interference of ascites volume on running performance. 24 hours later, distance and time ran were recorded and mice were placed in separate caging with no running wheel. Muscle measurements were made 48 hours thereafter. On the day of euthanasia, mice were removed from cages and brought towards a metal grid until such time the mice grasped the grid with the forepaws. Upon grasping, animals were pulled away from the grid until the grasp was released. Peak tension was recorded, and this was repeated twice more with the maximum peak tension of 3 trials was used for analyses as done previously [206].

2.3 Tissue Collection Procedure

Mice were anesthetized with isoflurane and hearts were removed for euthanasia. All hindlimb muscles, inguinal subcutaneous fat and spleens were weighed and snap-frozen in liquid nitrogen and stored at -80^{o}C. Primary ovarian tumours were also collected by removing the ovary and tumour at the site of injection and carefully separating the tumour mass from the ovary mass and stored in liquid nitrogen. Hindlimb muscles were also embedded in optimal cutting temperature (OCT) medium and frozen (see section below). Tibialis anterior (TA) and diaphragm muscle were placed in BIOPS containing (in mM) 50 MES Hydrate, 7.23 K_2EGTA, 2.77 CaK_2EGTA, 20 imidazole, 0.5 dithiothreitol, 20 taurine, 5.77 ATP, 15 PCr, and 6.56 $MgCl_2 \cdot 6\ H_2O$ (pH 7.1) to be prepared for mitochondrial bioenergetic assays.

2.4 Sectioning, histochemical & immunofluorescent staining

Tibialis anterior and diaphragm muscle samples were embedded in OCT medium (Thermo Fisher Scientific) and frozen in 2-methylbutane. These muscles were then sectioned into 10μm sections with a cryostat (HM525 NX, Thermo Fisher Scientific) maintained at -20^{o}C on Fisherbrand Superfrost Plus slides (Thermo Fisher Scientific). Hematoxylin and eosin (H&E) staining was used to assess mononuclear cell infiltration. Images were taken using EVOS M7000 imager (Thermo Fisher Scientific) using 20x magnification and analyzed on ImageJ. Immunofluorescent analysis of myosin heavy chain (MHC) expression was completed as previously described [231]. Images were taken with EVOS M7000 equipped with standard red, green and blue filter cubes. Fibers that did not fluoresce were considered IIx fibers. A total of 25-50 fibers were then randomly selected and measured. Type IIb fibers in the diaphragm strips were in low abundance, therefore, 5-27 fibers were measured and used for analysis. Type I fibers were extremely low in abundance in the TA and thus were not analyzed [231]. These images were also analyzed for cross sectional area (CSA) on ImageJ in a blinded fashion. Immunofluorescent analysis of embryonic myosin heavy chain (eMHC) were adapted from previous literature [245]. Briefly, sections were fixed with 10% formalin, blocked with 10% goat serum, followed by mouse IgG block (BML 2202; Vector Laboratories Inc., Burlingame, CA), and incubated with anti-eMHC (15μg/mL; DHSB F1.652) overnight. Secondary Alexa Fluor 647 IgG (1:1000; Abcam, ab150107) was then used to fluoresce eMHC primary antibody. Sections were then re-blocked once again and incubated with wheat-germ agglutinin (WGA; 1:1000; Invitrogen W11261) pre-conjugated to Alexa Fluor 488. Last, samples were mounted with DAPI mounting medium (Abcam, ab104139). D2.*mdx* muscle tissue saved from previous studies in our lab was used to evaluate the efficacy of the antibodies (**SFigure 5-2**).

2.5 In Situ Tibialis Anterior Force and In Vitro Diaphragm Force

In situ TA force production was partially adapted from previous literature [246,247]. Mice were anesthetized with isoflurane and the distal tendon of the TA was exposed by incision at the ankle. The distal tendon was tied with suture thread as close to the muscle attachment as possible. Once the knot was secured the distal tendon was severed. Small cuts were made up the lateral side of the TA to expose the muscle for needle electrode placement. The knot was tied to an Aurora Scientific 305C (Aurora Scientific Inc., Aurora, ON, Canada) muscle lever arm with a hook. The foot of the mouse was secured with tape and the knee was immobilized with a needle and set screw

with the length of the limb parallel to the direction of force. The two needle electrodes were placed in the gap of fascia between the TA and tibia to stimulate the common peroneal nerve (10-50 mA). The mouse was heated with a heating pad or heat lamp throughout force collection. Optimal resting length (L_o) was determined using single twitches (pulse width=0.2ms) at 1 Hz stimulation frequency with 1 minute rest in between contractions to avoid fatigue. Once L_o was established, a ruler was used to determine length before the start of force-frequency collection (1, 10, 20, 30, 40, 50, 60, 80, 100, 120 and 200Hz with 1 minute rest in between contractions). Force production was normalized to the calculated CSA of the muscle strip (m/l*d) where m is the muscle mass, l is the length, and d is mammalian skeletal muscle density (1.06mg.mm^3).

In vitro force production for diaphragm muscle was done as completed previously [237,248,249]. Briefly, the diaphragm strip was carefully sutured in Ringer's solution (containing in mM: 121 NaCl, 5 KCl, 1.8 $CaCl_2$, 0.5 $MgCl_2$ 0.4 $NaHPO_4$, 24 $NaHCO_3$, 5.5 glucose and 0.1 EDTA; pH 7.3 oxygenated with 95% O_2 and 5% CO_2) such that the thread secured to the central tendon and ribs. The strip was then placed in an oxygenated bath filled with Ringer's and maintained at 25^{o}C. The suture secured to the central tendon was then attached to the lever arm and the loop secured to the ribs was attached to the force transducer. The strip was situated between flanking platinum electrodes driven by biphasic stimulator (model 305C; Aurora Scientific Inc.). L_o determined using single twitches (pulse width=0.2ms) at 1 Hz stimulation frequency with 1 minute rest in between contractions to avoid fatigue. Once L_o was determined, the strip acclimatized for 30 minutes in the oxygenated bath. L_o was re-assessed and measured with a ruler and the start of the force-frequency protocol was initiated (1, 10, 20, 40, 60, 80, 100, 120, 140 and 200Hz with 1 minute rest in between contractions). Force production was normalized to CSA of the muscle strip (m/l*d) where m is the muscle mass, l is the length, and d is mammalian skeletal muscle density (1.06mg.mm^3).

2.6 Western Blotting

A frozen piece of TA and diaphragm from each animal was homogenized in a plastic microcentrifuge tube with a tapered Teflon pestle in ice-cold buffer containing (in mM) 20 Tris/HCl, 150 NaCl, 1 EDTA, 1 EGTA, 2.5 $Na_4O_7P_2$, and 1 Na_3VO_4 and 1% Triton X-100 with PhosSTOP inhibitor tablet (Roche; 4906845001) and protease inhibitor cocktail (Sigma Aldrich; P8340) (pH7.0) as published previously [230,237]. Protein concentrations were determined using a

bicinchoninic acid assay (life Technologies, Thermo Fisher Scientific). 15-20 μg of denatured and reduced protein was subjected to 10%-12% gradient SDS-PAGE followed by transfer to low-fluorescence polyvinylidene difluoride membrane. Membranes were blocked with Odyssey Blocking Buffer (Li-COR) and immunoblotted overnight (4°C) with antibodies specific to each protein. A commercially available monoclonal antibody was used to detect electron transport chain proteins (rodent OXPHOS Cocktail, ab110413; Abcam, Cambridge, UK, 1:250 dilution), including V-ATP5A (55kDa), III-UQCRC2 (48kDa), IV-MTCO1 (40kDa), II-SDHB (30 kDa), and I-NDUFB8 (20 kDa). A commercially available monoclonal antibody was used to detect mitochondrial creatine kinase (mtCK C-1 43 kDa; Santa Cruz 376320, 1:500 dilution).

After overnight incubation in primary antibodies, membranes were washed 3 times for 5 minutes in TBS-Tween and incubated for 1 hour at room temperature with the corresponding infrared fluorescent secondary antibody (LI-COR IRDye 680RD 925-68020, 1:20 000).

2.7 Preparation of permeabilized muscle fibers

The assessment of mitochondrial bioenergetics was performed as described previously in our publications[206,229,237,250,251]. Briefly, the TA and diaphragm from the mouse was removed and placed in ice cold BIOPS. Muscle was separated gently along the longitudinal axis to from bundles that were treated with 40 μg/mL saponin in BIOPS on a rotor for 30 minutes at 4°C. Following permeabilization the permeabilized muscle fiber bundles (PmFBs) for respiration were blotted and weighed in 1.5mL of tared prechilled BIOPS for normalization of respiratory assessments. The remaining PmFBs for mitochondrial H_2O_2 (mH_2O_2) were not weighed at this step as these data were normalized to fully recovered dry weights taken after the experiments. All PmFBs were then washed in Buffer Z on a rotator for 15 minutes at 4°C to remove the cytoplasm. Buffer Z contained (in mM) 105 K-MES, 30 KCl, 10 KH_2PO_4, 5 $MgCl_2 \cdot 6\ H_2O$, 1 EGTA and 5mg/mL BSA (pH 7.1).

2.8 Mitochondrial respiration

High-resolution respirometry (O_2 consumption) were conducted in 2 mL of respiration medium (Buffer Z) using the Oroboros Oxygraph-2k (Oroboros Instruments, Corp., Innsbruck, Austria) with stirring at 750 rpm at 37°C. Buffer Z contained 20 mM Cr to saturate mtCK and promote

phosphate shuttling through mtCK or was kept void of Cr to prevent the activation of mtCK [223]. All experiments were conducted in the presence of 5 μM blebbistatin (BLEB) in the assay media to prevent spontaneous contraction of PmFB, which has been shown to occur in response to ADP at 37°C that alters respiration rates [223]. Complex I-supported respiration was stimulated using 5mM pyruvate and 2mM malate (NADH) followed by a titration of ADP concentrations from physiological ranges (25 μM, 100 μM; [225]) to high submaximal (500 μM) and saturating to stimulate maximal coupled respiration (5000 μM in the presence of creatine and 7000 μM in the absence of creatine). 10mM glutamate (further NADH generation) was added at the end of the ADP titration. Cytochrome *c* was then added to test mitochondrial outer membrane integrity. Experiments with low ADP-stimulated respiration (bundles that did not respond to ADP) with high cytochrome *c* responses (>15% increase in respiration) were removed from analysis (13 of 370 bundles). Last, 20mM Succinate ($FADH_2$) was added to stimulate complex-II supported respiration. These protocols were designed to understand the regulation of respiration coupled to oxidative phosphorylation of ADP to ATP (Adenosine triphosphate).

2.9 mH_2O_2

mH_2O_2 was determined spectrofluorometrically (QuantaMaster 40, HORIBA Scientific) in PmfB placed in a quartz cuvette with continuous stirring at 37ºC in 1 mL of Buffer Z supplemented with 10 μM Amplex Ultra Red, 0.5 U/ml horseradish peroxidase, 1mM EGTA, 40 U/ml Cu/Zn-SOD1, 5 μM BLEB and 20mM Cr to saturate mtCK. No comparisons were made to PmFB in the absence of creatine due to tissue limitations. State II mH_2O_2 (maximal emission in the absence of ADP) was induced using the Complex I-supporting substrates (NADH) pyruvate (10mM) and malate (2mM) mH_2O_2 to generate forward electron transfer (FET)-supported electron slip at Complex I [252] as described previously [206]. These PmFBs were incubated with 35 μM CDNB during the 30-minute permeabilization to deplete glutathione and allow for detectable rates of mH_2O_2. Following the induction of State II mH_2O_2, a titration of ADP was employed to progressively attenuate mH_2O_2 as it occurs when membrane potential declines during oxidative phosphorylation [80]. A separate PmFB was used to stimulate electron slip at Complex I through reverse electron transfer (RET) from complex II using succinate ($FADH_2$) [252]. followed by ADP titrations as used in the previous protocol. After the experiments, the fibres were lyophilized in a freeze-dryer (Labconco,

Kansas City, MO, USA) for > 4h and weighed on a microbalance (Sartorius Cubis Microbalance, Gottingen Germany). The rate of mH_2O_2 emission was calculated from the slope (F/min) using a standard curve established with the same reaction conditions and normalized to fibre bundle dry weight.

2.10 Serum GDF15

Blood was collected through cardiac puncture and allowed to clot at room temperature for 30 minutes. Blood was then spun at 1000g for 10 minutes and serum was collected. GDF15 (Growth differentiation factor 15) levels were analyzed in serum using the mouse GDF-15 DuoSet ELISA kit according to the manufacturer's instructions (R&D Systems DY6385).

2.11 RNA isolation and Rt-PCR

To perform reverse transcription- polymerase chain reaction (Rt-PCR), tissue was used from a separate cohort of mice. These mice were ID8-inoculated as done previously and housed at the University of Guelph. These mice had cancer for similar times (~45, ~75, ~90 days), and mice at the 45-day time point were 15-16 weeks old at the time of euthanasia. RNA isolation was performed twice for two separate analyses.

In the first analysis, RNA isolation was performed at the University of Guelph using a TRIzol (Invitrogen) and RNeasy (Qiagen) hybrid protocol. Briefly, snap frozen TA tissue was homogenized in 1mL of TRIzol reagent according to the manufacturer instructions. The RNA mixture was transferred to a RNeasy spin column (Qiagen) and processed according to the RNeasy kit instructions. RNA was quantified spectrophotometrically at 260nm using a NanoDrop (ND1000, ThermoFisher Scientific INC.) and used for RNA sequencing.

In the second analysis, RNA isolation was performed at York University on a separate cohort of tissue as previously described [249]. TA and diaphragm samples were lysed using TRIzol reagent (Invitrogen) and RNA was separated to an aqueous phase using chloroform. The aqueous layer containing RNA was then mixed with isopropanol and loaded to Aurum Total RNA Mini Kit columns (Bio-Rad, Mississauga, ON, Canada). Total RNA was then extracted according to the manufacturer's instructions. RNA was quantified spectrophotometrically using the NanoDrop

attachment for the Varioskan LUX Multimode Microplate reader (Thermo Scientific). Reverse transcription of RNA into cDNA was performed by M-MLV reverse transcriptase and oligo(dT) primers (Qiagen, Toronto, ON, Canada). cDNA was then amplified using aCFX384 Touch Real-Time PCR Detection Systems (Bio-Rad) with a SYBR Green master mix and specific primers **(STable 1)**. Gene expression was normalized to β-actin (Actb) and relative differences were determined using the ΔΔCt method. Values are presented as fold changes relative to the control group.

2.12 RNA Sequencing

RNA libraries were prepared using the NEBNext Ultra II Directional RNA Library Prep Kit for Illumina (NEB, E7760) according to manufacturer's polyA mRNA workflow at the Advanced Analysis Center at the University of Guelph (Guelph, Ontario, Canada). Libraries were normalized, denatured, diluted, and sequenced on an Illumina 2x100 bp NovaSeq S4 flowcell usingv1.5 chemistry according to manufacturer's instructions.

After demultiplexing, fastq files were uploaded into Partek and pre- and post-alignment quality control (QC) was performed in Partek (average phred quality score >35). Paired-end reads (100bp or 150bp) were aligned using STAR 2.7.8a [253] with mm39 – RefSeq Transcripts 98 (05/05/2021) in Partek. A minimum read cutoff of 20 was applied; all other settings were default. Data were normalized using counts per million (CPM), and Limma-voom [254] was used for differential gene expression analysis: sham vs 45d, sham vs 75d, and sham vs 90d. Raw p-values were adjusted for false discovery rate (FDR) using the FDR step-up procedure. Gene Ontology and Reactome pathway enrichment analysis was completed using Enrichr and ConsensusPathDB with a background list, using DEGs with $p < 0.05$. Significance threshold for volcano plots were set at P <0.01.

2.13 Statistics

Results are expressed as mean ± SD. The level of significance was established at $p < 0.05$ for all statistics. The D'Agostino-Pearson omnibus normality test was first performed to determine whether data resembled a Gaussian distribution, and all data were subject to the ROUT test

(Q=0.5%) to identify and exclude outliers which was a rare occurrence. When data fit normal distributions, standard one way and two-way ANOVAs were performed. When data did not fit a Gaussian distribution for analysis with one independent variable, the Kruskal-Wallis test was used. Moreover, when data did not fit a Gaussian distribution for analysis with two independent variables, data was first log transformed then analyzed using a standard two-way ANOVA (See **SFigure 5-8** for log transformed analysis of **Figure 5-6A, 5-6B, 5-6E, 5-7D, 5-7F, 5-7I and 5-7K**) but data was still presented in the Results as non-transformed data. Respective statistical tests are provided in figure legends. When significance was observed with an ANOVA, post-hoc analyses were performed with a two-stage set-up method of Benjamini, Krieger and Yekutieli for controlling false discovery rate (FDR) for multiple-group comparisons. With this method, all reported *p* values are FDR adjusted (traditionally termed "q"). All statistical analyses were performed in GraphPad Prism 10 (La Jolla, CA, USA).

3. Results

3.1 Orthotopic epithelial ovarian cancer induces metastasis, ascites, impaired functional capacity and body weight loss at advanced stages.

Immunocompetent C57BL6J mice received orthotopic injections of murine ID8 epithelial ovarian cancer cells **(Figure 5-1A)**. Tumours were allowed to develop for ~45 days, ~75 days and ~90days post tumour injection to evaluate muscle responses across tumour development. This study was completed in two cohorts of mice to obtain sufficient tissue to complete all experiments. Weekly body weights (BW) in both cohorts were tracked post tumour injection **(SFigure 5-1A and 5-1B).** BW, tumour weight, ascitic volume, muscle mass and spleen mass data were then merged as these data were collected in both cohorts.

Primary ovarian tumour mass grew progressively, reaching a maximum of ~400mg by ~90 days **(Figure 5-1B)**. Metastatic tumour spread to the diaphragm was noted at the 90 day timepoint **(Figure 5-1C)** observed with abundant mononuclear cell infiltration **(Figure 5-1D & 5-1E).** Another common secondary complication in ovarian cancer patients is the development of ascites fluid within the intraperitoneal space. Ascites developed as early as 77 days post ID8-inoculation (data not shown); and there was a significant increase in the amount of ascites paracentesis taps performed and total volume of ascites collected per mouse by 90 days post-inoculation **(Figure 5-1F-H)**. At this time, decreases in voluntary wheel running and grip strength were noted **(Figure 5-1I & 5-1J).** Change in weekly BW, tibia length and peak body mass demonstrate how all groups grew similarly post cancer injection, as there were no significant differences between groups (**Figure 5-1K-M)**. However, final primary tumour-free BW and % change of peak BW to final BW were significantly decreased in the 90 Day group indicative of cachexia **(Figure 5-1N & 5-1O)**. All BW measurements were made after ascitic taps in the 90 Day group. We acknowledge that primary-tumour free BW does not accurately represent the full tumour load as it was not feasible to measure all metastasized cells. However, assessing final BW without subtracting primary tumour yielded the same statistical results (data not shown).

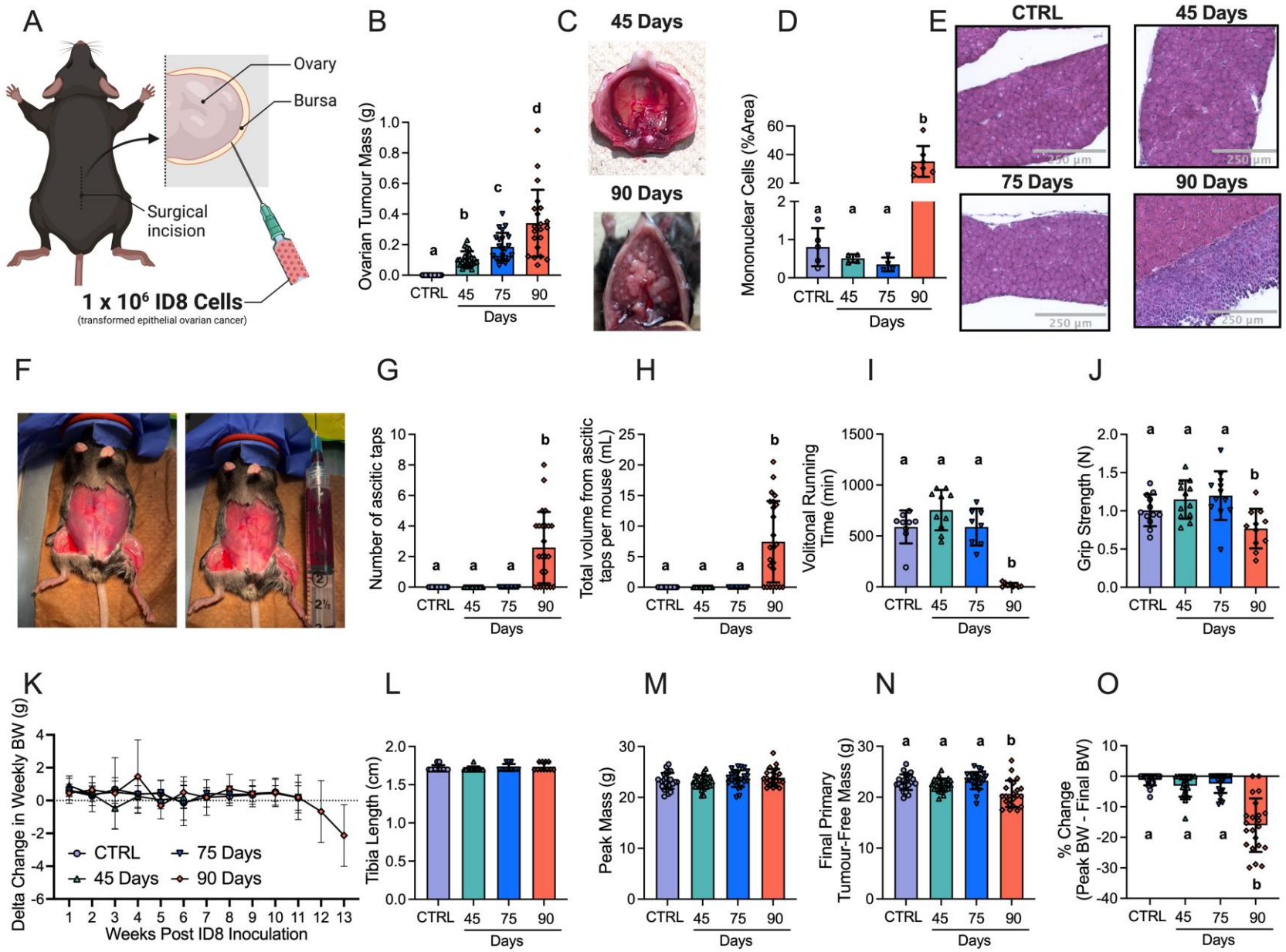

Figure 5-1. The effects of transformed epithelial ovarian cancer cells (ID8) implantation underneath the ovarian bursa of C57BL6 mice. 1 x 10^6 ID8 cells were injected underneath the ovarian bursa (A) and developed for 42-48, 72-78 and 83-107 days (45 Day, 75 Day and 90 Day time points respectively). Control mice were injected with identical volumes of PBS and aged for 72-78 days.

Primary ovarian tumour mass was measured at sacrifice (B, n = 21-24). Noticeable metastasis of ovarian cancer cells occurred by the 90-day time point and were photographed for qualitative assessment (C). Hematoxylin & eosin staining was used to assess mononuclear cell infiltration as an index of metastasis (D, n = 4-7, E Representative images; original magnification, x20). Mice developed ascites after ~75 days of ovarian cancer (F) and were tapped to prolong their survival (G & H, n = 24). Volitional wheel running (I, n = 8-11) and grip strength (J, n = 11-12) were used to assess voluntary motor function. Body weights were also measured every week and the delta weekly body weight (BW) was analyzed (K, n = 22-24). Tibia length (L, n = 11-12), peak body weight (M, n = 22-24), and final primary ovarian tumour-free body weight (N, n = 22-24) were also assessed. Percent change from peak body weight to final body weight was analyzed (O, n = 22-24). Results represent mean ± SD. Lettering denotes statistical significance when different from each other ($p < 0.05$). All data was analyzed using a one-way ANOVA and followed by a two-stage step-up method of Benjamini, Krieger and Yukutieli multiple comparisons test. Data that was not normally distributed was analyzed with a Kruskal-Wallis test followed by the same post-hoc analysis. C57BL/6J female mice ~75 days post PBS injection as controls (CTRL); C57BL/6J female mice ~45 days post ovarian cancer injection (45 Days); C57BL/6J female mice ~75 days post ovarian cancer injection (75 Days); C57BL/6J female mice ~90 days post ovarian cancer injection (90 Days).

3.2 Muscle loss and fat loss occur at advanced stages of ovarian cancer with no increases in GDF15, inflammatory markers or atrogenes.

In addition to BW loss, muscle mass and fat mass loss are hallmarks of cancer cachexia. Muscle mass was lower in the 90 Day group in the extensor digitorum longus (EDL; -11%), plantaris (PLT; -18%), tibialis anterior (TA; -19%), gastrocnemius (GA; -13%), and quadriceps (Quad; -13%) muscles compared to control (CTRL) whereas Soleus (SOL) mass did not change **(Figure 5-2A).** Adipose tissue from the inguinal fat pad was lower in the 45 Day and 90 Day groups post ovarian cancer inoculation **(Figure 5-2B).** Serum GDF15 – a recently identified cachexia regulator [116] – did not change **(Figure 5-2C).** Spleen mass was greater in the 75 and 90 Day groups suggesting an increased inflammatory response **(Figure 5-2D)**. We then measured cytokines and atrophy markers known to be elevated in certain clinical and preclinical models of cancer cachexia[42,116]. In the TA, Interleukin 6 (IL-6) mRNA was not different between groups while tumour necrosis factor alpha (TNF-α) was lower at 45 days compared to control **(Figure 5-2E).** In addition, atrogin and muscle RING-finger protein-1 (MURF-1) mRNA followed similar patterns whereby mRNA levels were lower at early time points with no differences compared to control in the 90 Day group **(Figure 5-2F)**. In the diaphragm, IL-6 mRNA was higher in the 45 and 90 Day groups, while TNF-α was lower at the 45 and 75 Day groups **(Figure 5-2G).** Atrogin mRNA was lower than control in the 90 Day group while MURF-1 was not different between groups **(Figure 5-2H)**. It is important to note that these cytokines could be elevated in the serum of these mice throughout cancer development, but we were unable to make this assessment due to limited serum following GDF15 analysis. Future studies should measure the protein content of the cytokines in both serum and muscle.

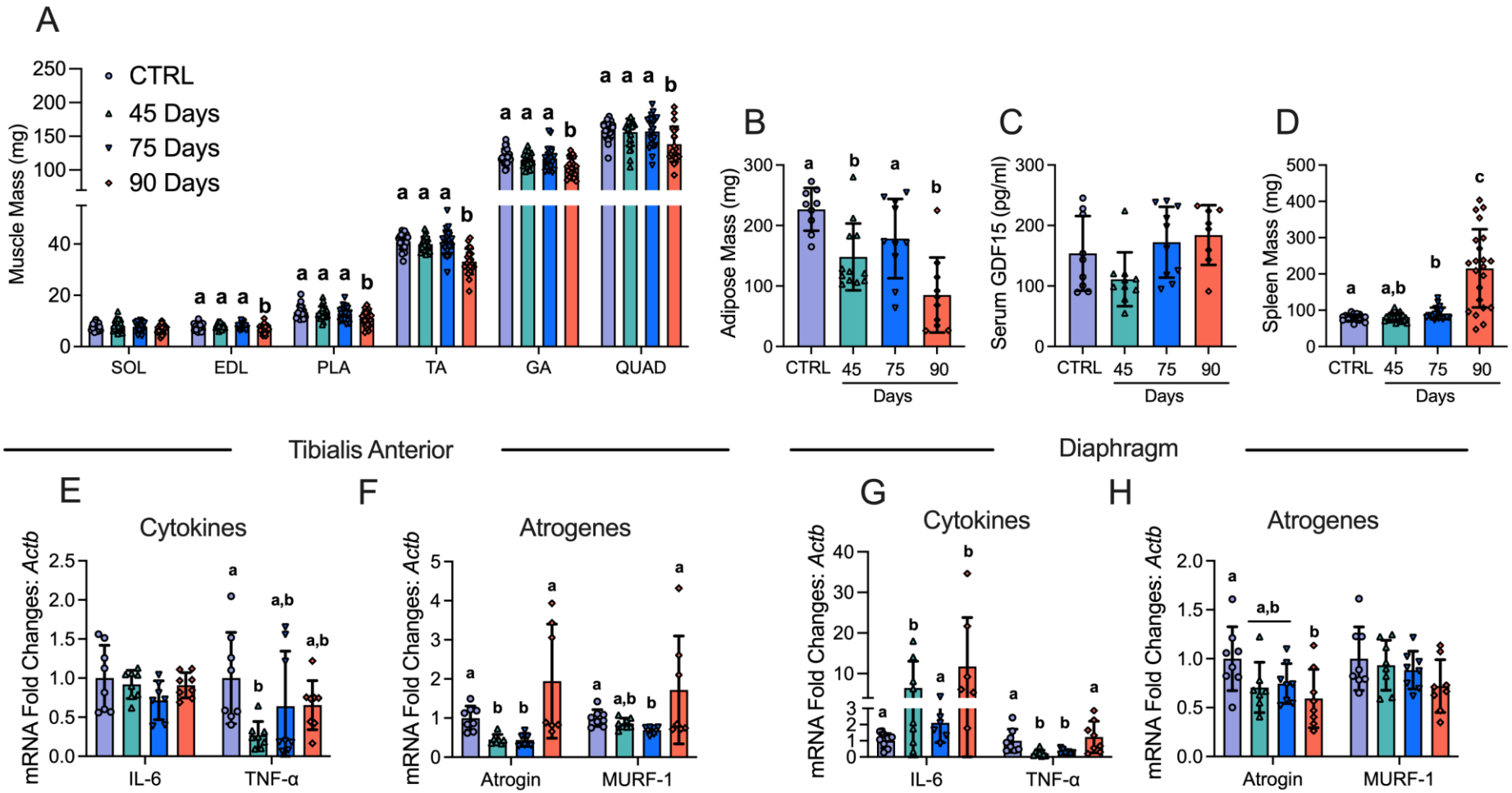

Figure 5-2. The effects of ID8 implantation on muscle mass, fat mass, spleen mass, GDF15 and gene expression of inflammation and atrogenes. Analysis of muscle mass at all time points in hindlimb muscles was completed (A, n = 22-24; soleus (SOL), extensor digitorum longus (EDL), plantaris (PLA), tibialis anterior (TA), gastrocnemius (GA) and quadriceps (QUAD)). Subcutaneous adipose mass in the inguinal fat depot (B, n = 9-12), serum GDF15 (C, n=8-11) and spleen mass (D, n = 21-22) were also analyzed. mRNA content of inflammatory and atrophy markers interleukin-6 (IL-6), tumour necrosis factor – alpha (TNF-α), atrogin and muscle RING-finger protein-1 (MURF-1) were measured using quantitative PCR in the TA and diaphragm of all groups (E-H, n = 6-8). Results represent mean ± SD. Lettering denotes statistical significance when different from each other ($p < 0.05$). C57BL/6J female mice ~75 days post PBS injection as controls (CTRL); C57BL/6J female mice ~45 days post ovarian cancer injection (45 Days); C57BL/6J female mice ~75 days post ovarian cancer injection (75 Days); C57BL/6J female mice ~90 days post ovarian cancer injection (90 Days). All data was analyzed using a one-way ANOVA or Kruskal-Wallis test when data did not fit normality. All ANOVAs were followed by a two-stage step-up method of Benjamini, Krieger and Yukutieli multiple comparisons test.

3.3 Muscle atrophy in the absence of muscle regeneration occurs earlier in the diaphragm compared to TA throughout ovarian cancer development.

Muscle atrophy is also a hallmark of cancer cachexia. TA and diaphragm muscles were sectioned and tagged for MHC isoforms I, IIA and IIB; black fibers were assumed IIx. In the TA, fiber CSA was not different in the 45 Day group in any isoform or when isoforms were pooled **(Figure 5-3A-C)**. In the 75 Day group, TA exhibited lower CSA in pooled fibers (-11%) with specific reductions in MHCIIx isoforms **(Figure 5-3A-C).** In the 90 Day group, TA exhibited an exacerbated reduction in pooled fiber CSA (-23%) with specific reductions in all isoforms compared to control **(Figure 5-3A-C).** This is further exemplified when pooled fibers are presented in a histogram as a higher frequency of smaller fibers exist in the TA in the 90 Day group compared to control **(Figure 5-3D)**. We also demonstrate muscle atrophy was occurring in the absence of apparent regeneration by measuring eMHC to evaluate if new fibers were developing. In the TA no eMHC fibers were identified in any groups **(Figure 5-3E and 5-3F)**. We also performed a fiber type distribution analysis in the red TA between the CTRL and 90 Day group to evaluate if a fiber type shift occurred throughout cancer development. No differences were found between groups (**SFigure 5-3**).

In the diaphragm, muscle atrophy was evident earlier than in the TA. In the 45 Day group, diaphragm fibers exhibited lower CSA stained with MHCIIa and MHCIIb isoforms as well as lower CSA in pooled fibers (-12%) **(Figure 5-3G-I)**. In the 75 Day group, fiber CSA remained lower in pooled fibers (-13%) specifically in MHCIIa and MHCIIb isoforms compared to control and were similar to the 45 Day group **(Figure 5-3G-I).** In the 90 Day group, diaphragm CSA exhibited extensive reductions when isoforms were assessed separately or pooled (-24%) **(Figure 5-3G-I).** This is further demonstrated when pooled fibers are displayed in a histogram as a higher frequency of smaller fibers were present at 90 days **(Figure 5-3J).** This atrophy in the diaphragm also occurred in the absence of apparent regeneration as no eMHC fibers were identified **(Figure 5-3K and 5-3L).** As muscle strips were used for diaphragm histology, a fiber type distribution analysis could not be performed as done on the TA.

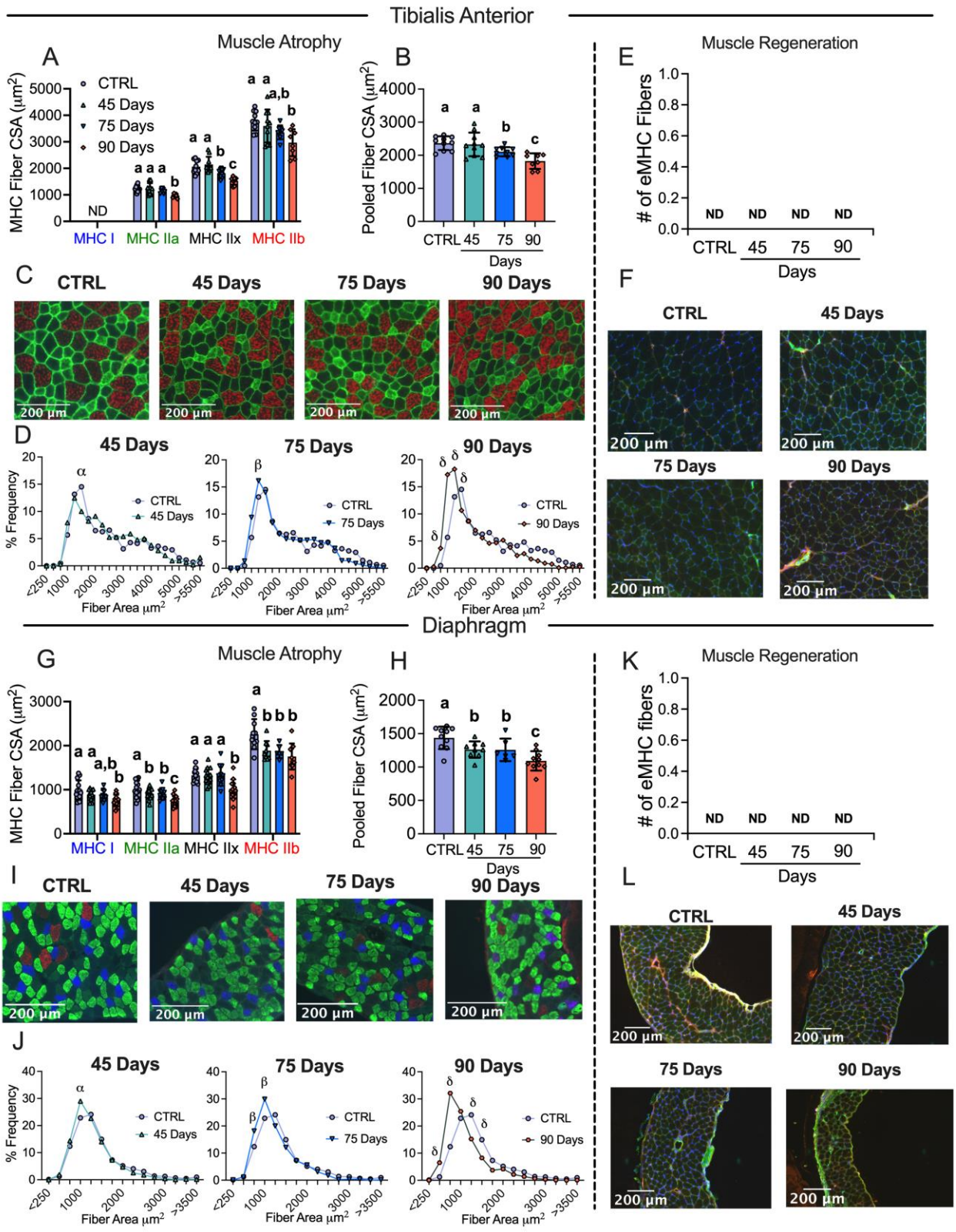

Figure 5-3. Evaluation of tibialis anterior and diaphragm fiber type atrophy and fiber regeneration in epithelial ovarian cancer injected mice. Analysis of fiber histology on myosin

heavy chain (MHC) isoforms and eMHC was performed in control and EOC mice. Cross-sectional area (CSA) of MHC isoforms were evaluated in the tibialis anterior (A-C, n = 7-10). All fiber types were also pooled, binned and averaged based off fiber area and plotted by frequency distribution at each time point compared to control (D, n =7-10). Embryonic MHC (eMHC) was tagged in separate sections to evaluate the presence of new fibers (E & F, n = 7-10). This was repeated within the diaphragm (G-L, n 10 = 14). Results represent mean ± SD. Lettering denotes statistical significance when different from each other ($p < 0.05$). α $p < 0.05$ Control versus 45 Days; β $p < 0.05$ Control versus 75 Days; δ $p < 0.05$ Control versus 90 Days. A one-way ANOVA was used for figures A, B, G and H . Data that was not normally distributed was analyzed with a Kruskal-Wallis test. A two-way ANOVA was used for figures D and J (interactions shown only). All ANOVAs were followed by a two-stage step-up method of Benjamini, Krieger and Yukutieli multiple comparisons test. C57BL/6J female mice ~75 days post PBS injection as controls (CTRL); C57BL/6J female mice ~45 days post ovarian cancer injection (45 Days); C57BL/6J female mice ~75 days post ovarian cancer injection (75 Days); C57BL/6J female mice ~90 days post ovarian cancer injection (90 Days).

3.4 Early muscle weakness is further reduced in the diaphragm throughout ovarian cancer progression but gradually recovers in the TA.

Muscle weakness is another hallmark of cancer cachexia. In the 45 Day group, TA specific force production was lower compared to control **(Figure 5-4A & 5-4B)**. In contrast, force production increased progressively by 75 days and 90 days, while still remaining lower compared to control (main effect) **(Figure 5-4A & 5-4B)**. The rate of contraction (Df/dt) at 1Hz stimulation frequency was lower at 45 Day group compared to control but not different at 100Hz **(Figure 4C)**. In addition, the half relaxation time (HRT) was significantly longer in the 90 Day group at both stimulation frequencies **(Figure 5-4D)**. This suggests that at 45 days the TA exhibits a slower rate of contraction at lower stimulation frequencies, and at 90 days the TA exhibits slower relaxation. We also measured mRNA content of ryanodine receptors (RyR1) and sarcoendoplasmic reticulum calcium ATPase (SERCA) as these proteins are integral for the regulation of calcium release and reuptake that regulates contraction. RyR1 mRNA content was not different across the time points, however, SERCA1 mRNA content was higher in the 90 Day group compared to control **(Figure 5-4E)**.

Diaphragm force production was also significantly lower compared to control in the 45 Day group as a main effect (interaction at 40Hz onward; not shown), with no changes in contractile properties but decreases in RyR1 and SERCA2 mRNA contents **(Figure 5-4F-J).** Interestingly, in the 75 Day group, diaphragm specific force transiently increased compared to the 45 Day group while still

remaining lower than control as a main effect (interaction at 40Hz onward; not shown), with no changes in the rate of contraction, time to relaxation or mRNA content of RyR1 or SERCA2 **(Figure 5-4F-J)**. In the 90 Day group, force production was further lowered compared to all time points as a main effect (interaction at 40Hz onward; not shown) with longer half relaxation time at 100Hz stimulation frequency **(Figure 5-4F-I)**. This decrease in force production and increase in half relaxation time was coupled to decreases in RyR1 and SERCA2 mRNA content **(Figure 5-4J)**. These data demonstrate that each muscle demonstrates unique contractile adaptations to ovarian cancer over time.

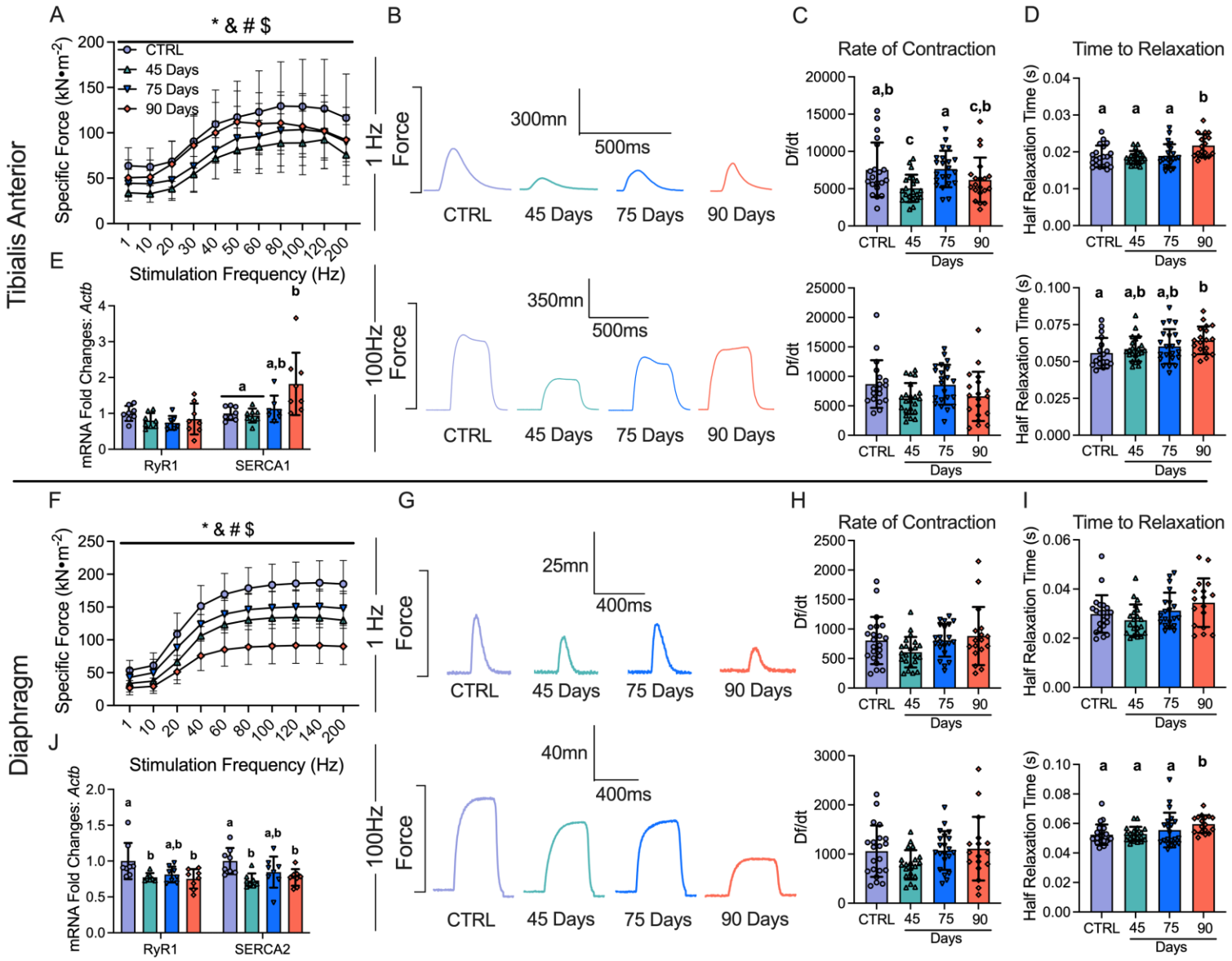

Figure 5-4. The effects of epithelial ovarian cancer (EOC) on tibialis anterior and diaphragm force production, contractile properties and calcium handling gene expression. In situ tibialis anterior force production was assessed using the force-frequency relationship (A, n = 9-10; B, Representative twitches at 1 Hz and 100Hz). Rate of twitch contractions along with the half relaxation time were also assessed at 1Hz and 100Hz (C & D, n = 18-22). mRNA expression of ryanodine receptors (RyR1) and sarcoplasmic/endoplasmic reticulum ATPase (SERCA; SERCA1 used for tibialis anterior (fast twitch) and SERCA2 for diaphragm (slow twitch) was also measured (E, n = 8). This was repeated for the diaphragm (F-J, n = 8-22) Results represent mean ± SD. * $p < 0.05$ Control versus all time points; & $p < 0.05$ 45 Days versus all time points; # $p < 0.05$ 75 Days versus all time points; $ $p < 0.05$ 90 Days versus all time points. Lettering denotes statistical significance at an alpha set at $p < 0.05$. A two-way ANOVA was used for figures A and J (main effects shown only) and all other data was analyzed using a one-way ANOVA or Kruskal-Wallis test when data did not fit normality. All ANOVAs were followed by a two-stage step-up method of Benjamini, Krieger and Yukutieli multiple comparisons test. C57BL/6J female mice ~75 days post PBS injection as controls (CTRL); C57BL/6J female mice ~45 days post ovarian cancer injection (45 Days); C57BL/6J female mice ~75 days post ovarian cancer injection (75 Days); C57BL/6J female mice ~90 days post ovarian cancer injection (90 Days).

3.5 Mitochondrial genes are downregulated in the TA during early and advanced stages of epithelial ovarian cancer.

Given there were no changes in markers of atrophy-related mechanisms that have been found in other cachexia models (GDF15, TNF-α, Atrogin and MURF-1[42,116], we examined the potential role for mitochondrial stress responses that have been identified in other models[12,237]. In the TA, RNA-seq revealed 691, 795 and 3402 differentially expressed genes (DEGs) in the 45, 75, and 90 Day groups compared to control, respectively. Some of these DEGs are shared among time points **(Figure 5-5A)**. We then used a volcano plot to demonstrate DEGs that were upregulated or downregulated compared to control **(Figure 5-5B-D).** Gene ontology (GO) enrichment analyses was then performed on DEGs to investigate up and down regulated biological processes altered across time points compared to control **(Figure 5-5E-G)**. Several pathways were significantly enriched, with the majority of downregulated pathways being mitochondrial-related. The two most significantly different upregulated and downregulated pathways from the enrichment analysis were represented in a chord plot to exemplify the specific genes changing across ovarian cancer progression **(Figure 5-5H-J)**. These results largely demonstrate how more mitochondrial genes are down regulated as ovarian cancer progresses with increases in certain muscle contraction related genes in the 90 Day group **(Figure 5-5H-J)**.

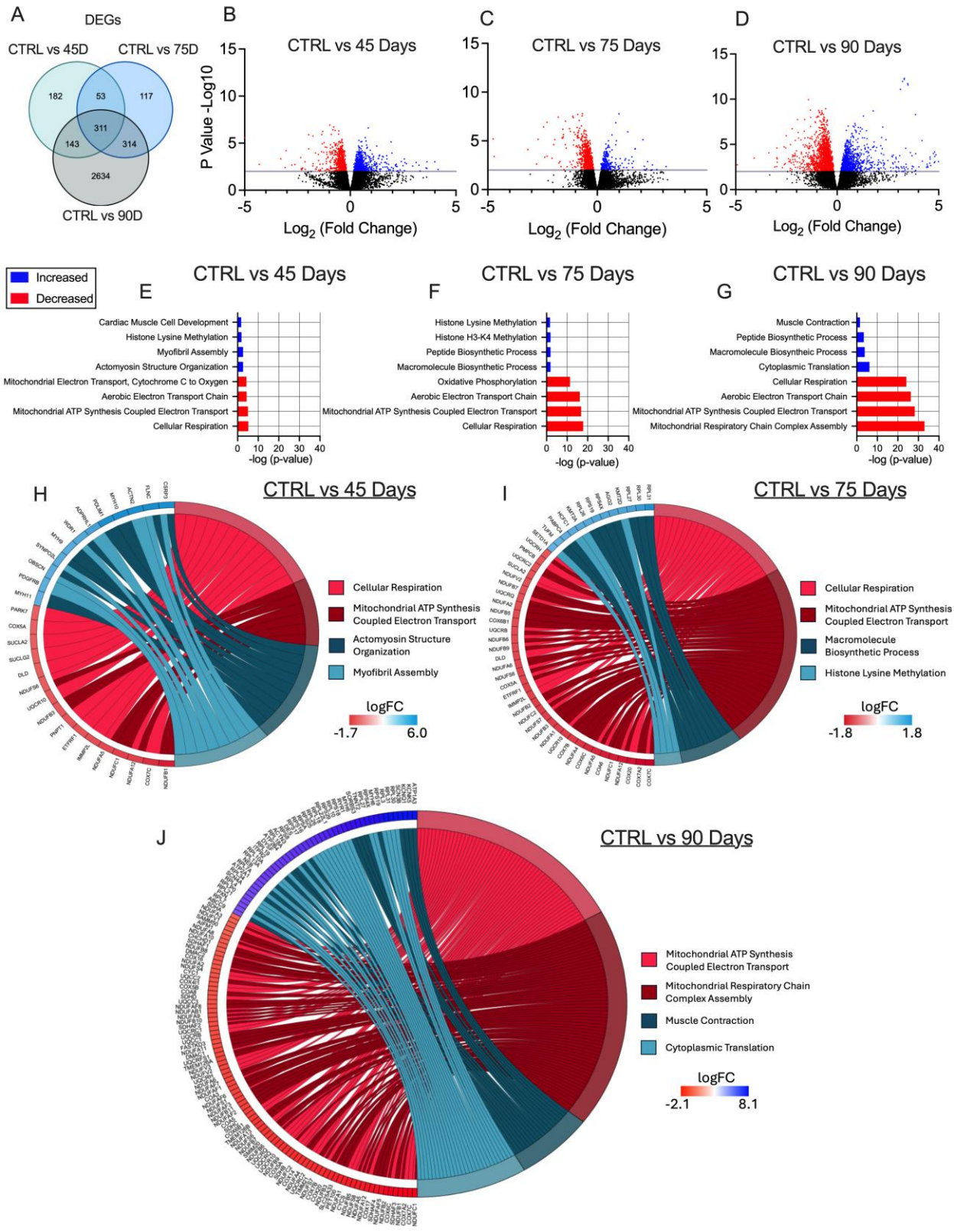

Figure 5-5. RNA sequencing analysis of tibialis anterior muscle in epithelial ovarian cancer (EOC) injected mice. Number of differentially expressed genes (DEGs) in each comparison were

exemplified in a Venn diagram (A). Volcano plot showing -log10 p-value and log2 fold changes of DEGs for each comparison were also completed (B-D). Top 3 upregulated and top 3 downregulated biological processes enriched in DEGs at each time point were also analyzed and graphed (E-G) Top two upregulated and down regulated biological processes were also used to generate a chord plot with the corresponding DEGs and respective log fold changes at each time point (H-J). n = 6. C57BL/6J female mice ~75 days post PBS injection as controls (CTRL); C57BL/6J female mice ~45 days post ovarian cancer injection (45 Days); C57BL/6J female mice ~75 days post ovarian cancer injection (75 Days); C57BL/6J female mice ~90 days post ovarian cancer injection (90 Days).

3.6 Decreases in carbohydrate supported mitochondrial respiration occur in early stages of ovarian cancer progression but is restored by late-stage disease.

Using permeabilized muscle fibres, mitochondrial respiration was assessed by stimulating complex I with NADH generated by pyruvate (5mM; carbohydrate substrate) and malate (2mM) across a range of ADP concentrations to challenge mitochondria over a spectrum of metabolic demands. The ADP titrations were repeated without (-Creatine; **Figure 5-6A & 5-6D**) and with creatine (+Creatine; **Figure 5-6B & 5-6E**) in the assay media to model the two main theoretical mechanisms of high energy phosphate shuttling from the mitochondria to the cytosol [80,183–185]. Briefly, in the absence of creatine, ATP is exported across the double membranes while in the presence of creatine, matrix-derived ATP crosses the inner membrane and is used by mitochondrial creatine kinase in the intermembrane space to phosphorylate creatine. The phosphocreatine product is then exported across the outer membrane which is then used by cytosolic creatine kinases to re-phosphorylate ADP local to ATP consuming proteins. Previous studies have shown that ADP/ATP flux is much slower than creatine/phosphocreatine due to the diffusion limitations of ATP/ADP vs phosphocreatine/creatine [210]. Prior modeling experiments have posited that up to 80% of the phosphate exchange between mitochondria and cytoplasm (in muscle) is likely comprised of the creatine-dependent system. 25μM, 100μM and 500μM ADP were selected to reflect creatine sensitivity as this is within the predicted range that is sensitive to the effects of mitochondrial creatine kinase (mtCK) [206,209,210,255]. Maximal ADP-stimulated respiration was unchanged in both muscles, in each condition, at all-time points **(SFigure 5-5A-D)** indicating that cancer alters the regulation of mitochondrial pyruvate oxidation stimulated by submaximal ADP concentrations**.**

Within the 45 and 75 Day groups, TA and diaphragm exhibit a decrease in mitochondrial respiration in the -Creatine condition with an apparent supercompensation by 90 days **(Figure 5-6A & 5-6D)**. In the +Creatine condition, early decreases in mitochondrial respiration in both muscles returned to normal by the 90-day time point **(Figure 5-6B & 5-6E)**. A summary of all respiration changes across time and between conditions as a main effect versus control is provided for both muscles **(Figure 5-6C & 5-6F).** All changes in mitochondrial respiratory control were not influenced by changes in mitochondrial electron transport chain (ETC) content as there were no changes in ETC subunit content estimated via western blot **(SFigure 5-4A & 5-4B).**

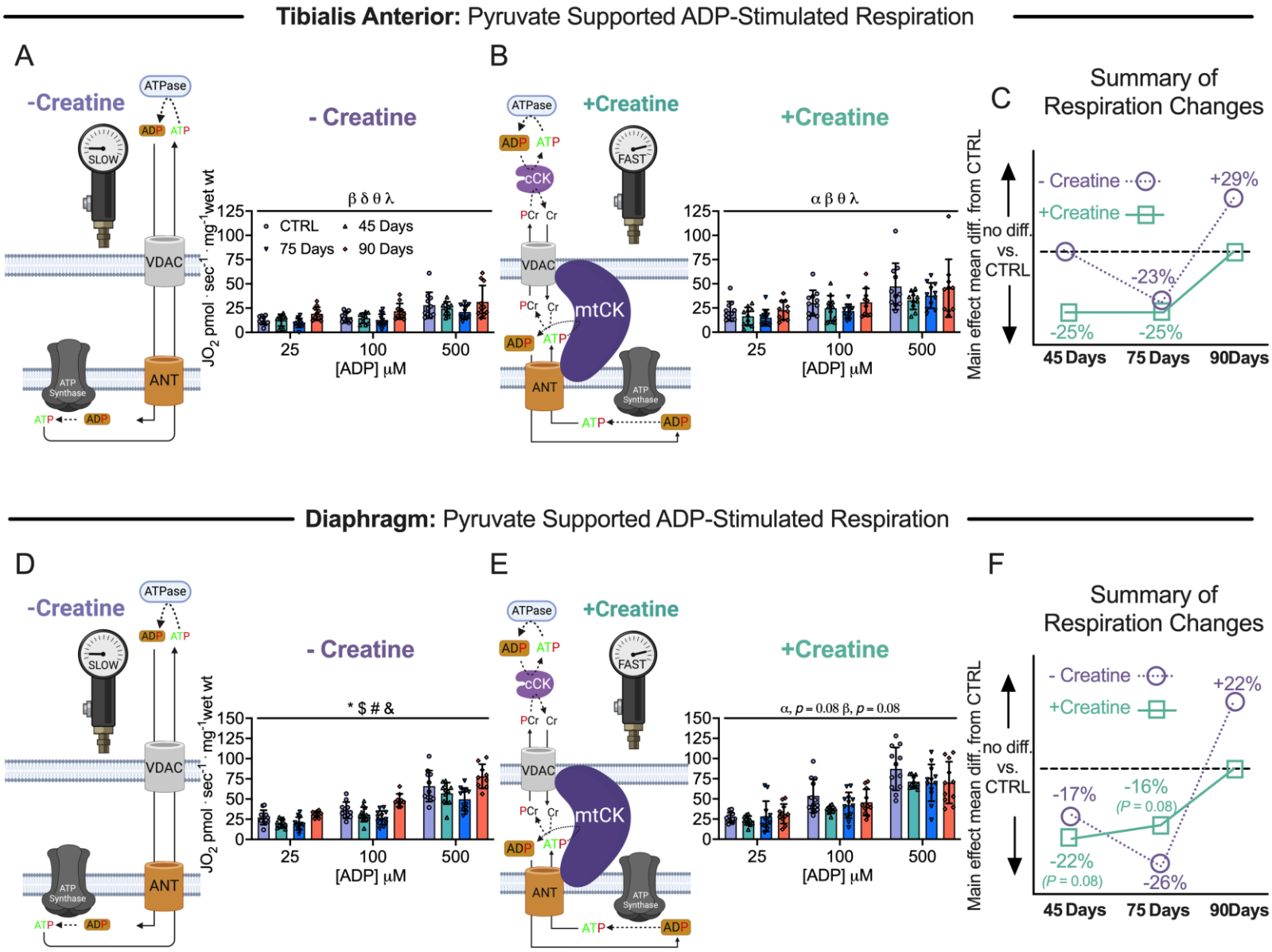

Figure 5-6. Pyruvate & malate supported mitochondrial respiration in tibialis anterior and diaphragm muscle of epithelial ovarian cancer (EOC) injected mice. ADP-stimulated (State III) respiration supported by pyruvate (5mM) and malate (2mM) generating NADH was assessed in the absence (-creatine) and presence (+creatine) of creatine within tibialis anterior and diaphragm PmFBs of EOC injected mice. Mitochondrial respiration in the absence of creatine was assessed at submaximal concentrations (25μM,

100μM and 500μM) in tibialis anterior of EOC injected (A). Mitochondrial respiration in the presence of creatine was also assessed at submaximal concentrations (25μM, 100μM and 500μM) in tibialis anterior of EOC injected (B). A schematic representative summary of changes in -Creatine/+Creatine pathways is depicted (C). This was repeated for the diaphragm (D-F) Results represent mean ± SD. n = 9-12. α $p < 0.05$ Control versus 45 Day; β $p < 0.05$ Control versus 75 Day; δ $p < 0.05$ Control versus 90 Day; θ $p < 0.05$ 45 Day versus 90 Day; λ $p < 0.05$ 75 Day vs 90 Day; * $p < 0.05$ Control versus all time points; & $p < 0.05$ 45 Days versus all time points; # $p < 0.05$ 75 Days versus all time points; $ $p < 0.05$ 90 Days versus all time points. All ANOVAs were followed by a two-stage step-up method of Benjamini, Krieger and Yukutieli multiple comparisons test. Voltage dependent anion channel (VDAC); adenine nucleotide translocator (ANT); mitochondrial creatine kinase (mtCK); adenosine diphosphate (ADP); adenosine triphosphate (ATP); phosphocreatine (PCr); creatine (Cr); creatine-independent phosphate shuttling (-Creatine); creatine-dependent phosphate shuttling (+Creatine). All data was analyzed suing a two-way ANOVA (main effects shown only). C57BL/6J female mice ~75 days post PBS injection as controls (CTRL); C57BL/6J female mice ~45 days post ovarian cancer injection (45 Days); C57BL/6J female mice ~75 days post ovarian cancer injection (75 Days); C57BL/6J female mice ~90 days post ovarian cancer injection (90 Days).

Another approach for evaluating changes in the relative control exerted by mitochondrial creatine kinase on ADP-stimulated respiration, or 'mitochondrial creatine sensitivity', is to calculate the ratio of respiration at submaximal ADP concentrations in both +Creatine/-Creatine conditions [205,206,210,237,248]. In the TA, creatine sensitivities were unchanged across time points indicating alterations in respiration were similar between both high energy phosphate shuttling systems **(SFigure 5-5E)**. While both -Creatine and +Creatine respiration changed across time points, the relative changes were disproportionate within the diaphragm, particularly in the 90 Day group compared to control. More specifically, the -Creatine system exhibited a greater increase in respiration compared wo the +Creatine system, thus, mitochondrial sensitivity to creatine was decreased compared to control in the 90 Day group, but this does not necessarily reflect compromised energy transfer from mitochondria to cytoplasm given both systems nonetheless improved. **(SFigure 5-5F)**, indicating the creatine-dependent phosphate shuttling system is selectively impaired compared to the creatine-independent system. This effect was not explained by mtCK protein contents given they were unchanged at all time points **(SFigure 5-5G & 5-5H).**

We also measured fat oxidation in each muscle in order to determine if these changes in respiration were unique to pyruvate stimulation of respiration through Complex I (NADH). In the TA, there were no changes in palmitoyl CoA- supported respiration (**SFigure 5-6B & 5-6D**) suggesting that the decreases in pyruvate oxidation were not due to a dysfunction that impacted all substrates. Likewise, there were no changes in Complex II-supported respiration (succinate; $FADH_2$) and glutamate- supported respiration (further NADH generation; Complex I) in both +Creatine/-Creatine conditions **(SFigure 5-7A-D)**. This suggests that the decrease in pyruvate oxidation were also not due to Complex I impairments per se nor ETC components downstream of both Complex I and II (see discussion). Interestingly, there was an increase in state II pyruvate/malate respiration in the 90 Day group in the absence of creatine suggesting increased proton leak, but no changes were observed in the presence of creatine **(SFigure 5-7E & 5-7F)** nor in response to palmitoyl CoA (**SFigure 5-6A**).

The diaphragm also exhibited no changes in palmitoyl CoA (**SFigure 5-6C & 5-6D**) respiration. However, Complex II-supported respiration (succinate; $FADH_2$) in the -Creatine condition was higher in the 90 day group along with glutamate-supported respiration (further NADH generation; Complex I) in both creatine conditions (**SFigure 5-7G-J**). There were no changes in state II pyruvate/malate-supported respiration **(SFigure 5-7K & 5-7L).**

3.7 Increased mitochondrial H_2O_2 emissions occur in complex I forward and reverse electron transfer in this EOC model.

We stimulated complex I-supported mH_2O_2 with forward electron transfer (pyruvate and malate (2mM) to generate NADH) **(Figure 5-7A)** and reverse electron transfer (succinate to generate $FADH_2$) **(Figure 5-7B** [256–259]). These substrate-specific maximal mH_2O_2 kinetics were followed by titration of ADP to determine the ability of ADP to attenuate mH_2O_2 during oxidative phosphorylation (OXPHOS). In the TA, pyruvate/malate and succinate supported maximal mH_2O_2 was not different at any time point compared to control **(Figure 5-7C & 5-7E)**. However, pyruvate/malate supported mH_2O_2 during OXPHOS were increased in the 75 Day group which returned to control levels by the 90 Day group, while succinate supported mH_2O_2 was increased at the 75 and 90 Day groups **(Figure 5-7D & 5-7F).** There were no changes in diaphragm pyruvate/malate and succinate supported maximal mH_2O_2 at any time point **(Figure 5-7H & 5-7J).** The diaphragm exhibited no changes in pyruvate & malate-supported H_2O_2 during OXPHOS but exhibited higher succinate-supported mH_2O_2 during OXPHOS in the 75 Day group that returns to baseline by the 90 Day group **(Figure 5-7I & 5-7K)**. A summary of mH_2O_2 changes across time and between conditions as a main effect versus control is provided for the TA **(Figure 5-7G)** and diaphragm **(Figure 5-7L)**.

A comprehensive summary of all changes between the TA and diaphragm captured within this study design is provided **(Figure 5-8).**

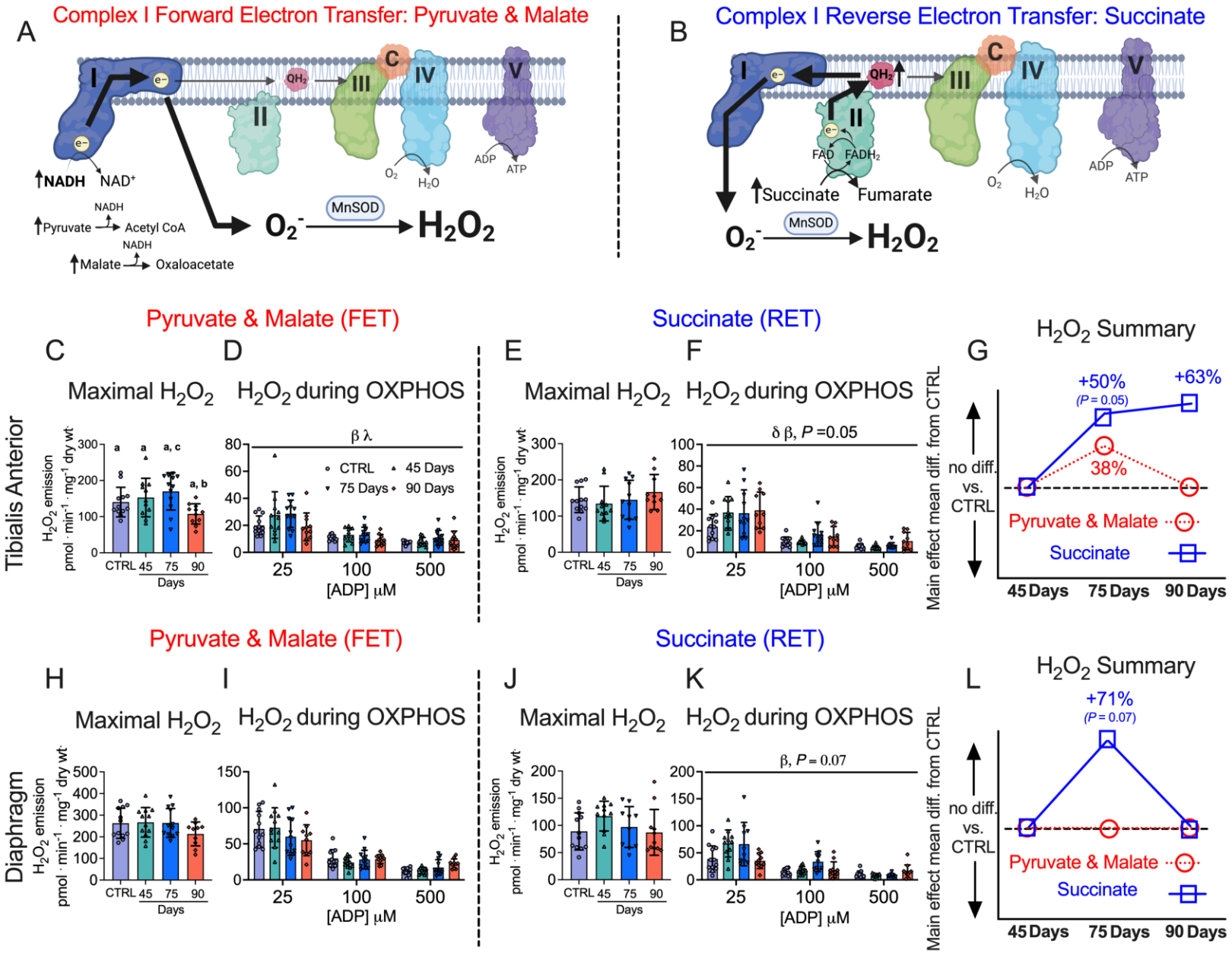

Figure 5-7. Complex I forward and reverse electron transfer emissions in tibialis anterior and diaphragm muscle of epithelial ovarian cancer (EOC) injected mice. Complex I forward electron transfer (FET) and complex I reverse electron transfer (RET) is schematically depicted (A & B). In FET mitochondrial H_2O_2 emission was supported by pyruvate (10mM) and malate (2mM) to generate

maximal rates and with ADP to assess H_2O_2 emission during OXPHOS. This experiment was repeated to assess RET H_2O_2 emission by using succinate (10mM) as opposed to pyruvate and malate. FET and RET H_2O_2 emissions were assessed in the TA of EOC injected mice and a summary of changes compared to control is depicted (C-G). This was repeated in the diaphragm (H-L). Results represent mean ± SD. Lettering denotes statistical significance when different from each other ($p < 0.05$). β $p < 0.05$ Control versus 75 Day; λ $p < 0.05$ 75 Day vs 90 Day; δ $p < 0.05$ Control versus 90 Day. A one-way ANOVA or Kruskal-Wallis test was used when data did not fit normality in figure C, E, H and J. A two-way ANOVA was used in figured D, F, I and K. All ANOVAs were followed by a two-stage step-up method of Benjamini, Krieger and Yukutieli multiple comparisons test. Oxidative phosphorylation (OXPHOS); manganese superoxide dismutase (MnSOD); electron (e-); superoxide (O_2^-). C57BL/6J female mice ~75 days post PBS injection as controls (CTRL); C57BL/6J female mice ~45 days post ovarian cancer injection (45 Days); C57BL/6J female mice ~75 days post ovarian cancer injection (75 Days); C57BL/6J female mice ~90 days post ovarian cancer injection (90 Days).

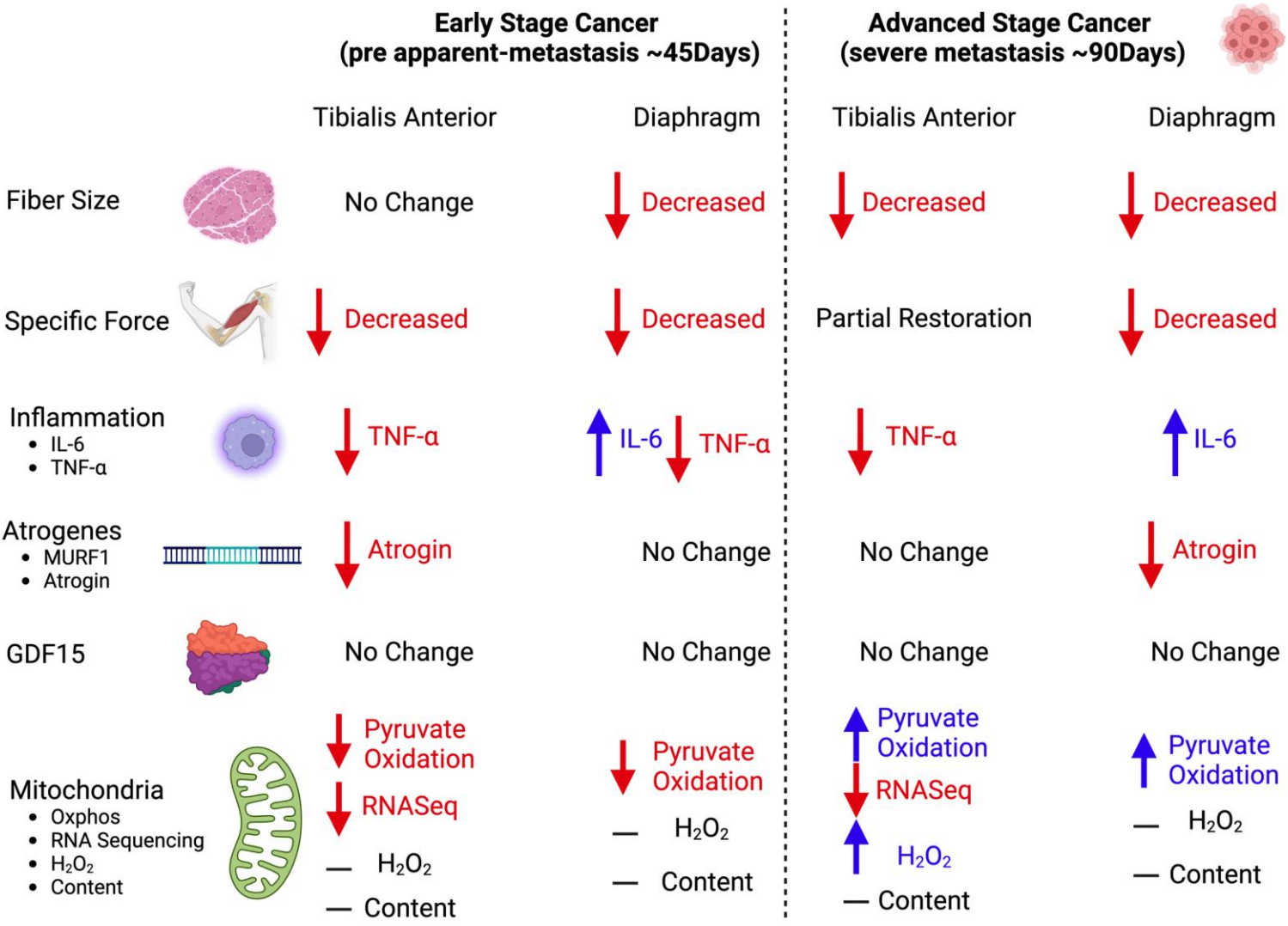

Figure 5-8. Summary of changes in a metastatic epithelial ovarian cancer cachexia model. When mice were injected with epithelial ovarian cancer, at a pre-metastasis time point (45 days post-injection) early muscle weakness was associated with decreases in pyruvate oxidation in both the tibialis anterior and diaphragm muscles. At this time, the tibialis anterior muscle did not exhibit muscle atrophy while the diaphragm did. With the exception of IL-6 in the diaphragm, there were no increases in TNF-α and atrophy markers of cancer cachexia at this time. During severe metastasis (90 days post-injection) both muscles exhibited muscle atrophy and muscle weakness, however the tibialis anterior recovered specific force production. Moreover, both muscles exhibited compensatory increases in submaximal pyruvate oxidation. Last, with the exception of IL-6 there were still no increases in TNF-α and atrophy markers of cancer cachexia.

4. Discussion

Epithelial ovarian cancer is the most lethal gynecological cancer in women. Advanced stages of this disease cause severe muscle weakness, yet the mechanisms remain unknown due in part to the inherent challenges of studying clinical population as well as a limited selection of pre-clinical models. Moreover, it has been suggested that the paucity of metastatic, orthotopic models for cancer cachexia has contributed to failures in clinical trials of therapies designed to preserve muscle mass and/or function that were otherwise based on evidence from other types of preclinical models [13]. Modelling cachexia in a metastatic context is believed to greatly improve the predictive power of preclinical models for identifying mechanisms and therapy development [13]. Here, we developed a new immunocompetent mouse model of metastatic cancer cachexia reflective of late-stage ovarian cancer while retaining the clinically relevant aspects of tumour growth in the nascent organ that can be induced during adulthood. Importantly the findings of this study demonstrate that early muscle weakness precedes clinical signs of ovarian cancer including metastasis and ascites formation as well as atrophy. The eventual development of atrophy seemingly triggers an adaptive response whereby specific force is restored in a sustained manner within limb muscle but only transiently in diaphragm. These pathological and adaptive responses in muscle quality during ovarian cancer coincided with dynamic alterations in pyruvate oxidation and mRNA contents related to numerous mitochondrial pathways but without increases in the cachexia-regulating atrogene programs, TNF-α or GDF15 that have been attributed in this process for other cancers [42,116].

Collectively, the time-dependent responses in force production and fibre size in this new model of ovarian cancer-induced cachexia serve as a foundation for exploring numerous potential mechanisms underlying the development of atrophy-independent and -dependent weakness in relation to metastasis. The findings also highlight how mitochondrial stress is a defining feature of muscle weakness during ovarian cancer[12,237].

4.1 A novel atrophy-independent weakness in locomotor muscle during ovarian cancer

At the earliest time point assessed (45 Day group), both TA and diaphragm demonstrate lower specific force production. As this measurement is normalized to the size of muscle, any occurrence of atrophy cannot explain this observation. In fact, while modest atrophy was observed in the

diaphragm, fibre size was unchanged in the TA at this timepoint. Therefore, the TA demonstrated a pre-atrophy weakness similar to our previous findings in the C26 colorectal cancer model that weakness precedes atrophy in the quadriceps and the diaphragm [237]. Hence, pre-atrophy weakness has now been reported in two distinct models suggesting it is a common phenomenon during cancer. This finding is important because it raises questions regarding the atrophy-independent mechanisms of muscle weakness during cancer – a topic that is considerably understudied in contrast to the literature on atrophy-dependent muscle weakness during cachexia. While it is possible that weakness precedes atrophy in the diaphragm of the current EOC model, future studies would need to examine an earlier time course design.

4.2 Reduced mitochondrial pyruvate oxidation is associated with early muscle weakness during ovarian cancer

In the TA, RNAseq identified nuclear genes encoding mitochondrial proteins as the most dominant gene expression stress response early during cancer (45 Day group) when tumours were just appearing, and well before severe metastasis or atrophy developed. High resolution respirometry revealed that this stress response corresponds with reduced pyruvate oxidation – an index of carbohydrate oxidation – but with no corresponding changes in the capacity for long chain fatty acid oxidation. This finding of a substrate-specific change in respiration was similar in diaphragm at this early time point. There were also no changes in the oxidation of the amino acid-derived substrate glutamate or succinate (generation of $FADH_2$ at complex II). As both pyruvate and glutamate generate NADH through their respective dehydrogenases (pyruvate dehydrogenase (PDH) and glutamate dehydrogenase (GDH)), the findings suggest that the ability of Complex I to oxidize NADH may not have been altered in the TA. This suggests that the unique reduction in pyruvate oxidation at 45-days may be due to changes in PDH itself. While there were no changes in PDH or PDH phosphatases mRNA expression identified with RNAseq at this time point (data not shown), future studies could determine if isolated PDH activity is inhibited similar to indications from previous reports in C26 mice[260].

Considering that measurements of oxygen consumption reflect reduction of O_2 at Complex IV downstream of both Complex I and II, the lack of decreases in both glutamate and succinate oxidation in both TA and diaphragm indicates that the integrated function of the electron transport

chain was not altered, at least as could be detected within the physiologically relevant context of ADP-stimulated (coupled) respiration. This finding is interesting given that protein contents of specific subunits of ETC complexes were not changed across time points. In the 75 Day and 90 Day groups, the protein contents of ETC protein subunits measured by western blot were not changed, but mRNA content of these subunits were decreased (data not shown; C1 - NDUFB8, CII – SDHB, CIII – UQCRC2, CV – ATP5A). While speculative, these findings suggest a number of possibilities including increased ETC protein stability or that reductions in mRNA reflect increased translation rather than decreased gene expression [261].

Given that ovarian cancer does not reduce oxidation of the other substrates explored at this early timepoint, it is also difficult to define the unique reductions in pyruvate oxidation as a 'mitochondrial dysfunction' *per se*. This is a critical outcome of the present investigation and highlights the importance of comparing substrates to each other and to defined primary outcomes of myopathy tracked over time, and across muscle types. This approach determines whether mitochondrial stress responses affect a central governance of oxidative phosphorylation or an adaptive reprogramming - a concept and perspective we have proposed previously for the study of myopathies [262].

4.3 Recovery of specific force during the development of atrophy is more sustained in limb muscle versus diaphragm

As atrophy developed by the 75 Day group in both muscles, specific force partially recovered despite the appearance of atrophy in the TA with even greater atrophy in the diaphragm. As specific force is a measure that is independent of muscle mass, this finding raises questions regarding the mechanism of intrinsic improvements within the atrophied muscle itself. This remarkable adaptive response in both muscles diverged in the 90 Day group. Particularly, specific force recovered even further in the TA, whereas diaphragm force plummeted to very low levels. Interestingly, severe metastasis occurred on the diaphragm in the 90 Day group, suggesting that metastases to the diaphragm may contribute directly to the progressive loss of force production at advanced stages of ovarian cancer cachexia.

Unlike the 45 Day group, changes in force production were not consistently related to changes in pyruvate oxidation given this function remained low as force recovered at 75 days, with increases

in pyruvate oxidation at 90 days being positively or inversely related to muscle force production in the TA and diaphragm, respectively. Nonetheless, decrements in pyruvate oxidation were more strongly related to pre-atrophy weakness early during cancer. This finding warrants further examination with targeted approaches that determine whether altered glucose metabolism contributes to weakness uniquely at early stages of ovarian cancer.

As the mechanisms underlying the progressive vs transient increase in force production in both muscles require further investigation, RNAseq analyses in the TA demonstrated mRNA contents related to chromatin regulation and biosynthetic processes that can be explored for the generation of numerous hypotheses in future investigations. Likewise, increased mRNA contents corresponding to genes related to myofibril assembly and actomyosin structure organization during the pre-atrophy period at 45 days in the TA suggests potential turnover of sarcomeric structures may have occurred. Future studies could consider whether pre-atrophy weakness was due to declining quality of contractile machinery. Last, Reactome enrichment analysis identified 19 "muscle contraction" genes upregulated at the 90-day time point in the TA. Some of these genes are related to calcium handling (ATP2b4, ITPR2, RyR1, and ATP2a1), suggesting increases in force production could be related to calcium regulation. While RNAseq was not performed in the diaphragm, Rt-PCR analysis did identify decreases in RyR and SERCA mRNA content concurrent with a decrease in force-frequency production. Functional calcium handling measures could be performed in the future to explore potential relationships between mitochondrial ATP supply supported by carbohydrate oxidation and the energetic cost of contraction[263].

4.4 Mitochondrial-cytoplasmic phosphate shuttling: two systems, two different responses during ovarian cancer

This study was also designed to consider how mitochondria shuttle phosphate to the cytoplasm in the form of both PCr (Phosphocreatine) and ATP in order to gain deeper insight into the precise mechanisms by which skeletal muscle mitochondria demonstrate metabolic reprogramming (as explained in *Results* and in [210]). These modeling approaches identify early reductions in pyruvate oxidation in both TA and diaphragm that were observed more consistently in the dominant creatine-dependent pathway (PCr export) yet both phosphate shuttling systems (ATP and PCr export) improved over time. The late stage increases in both systems, with an apparent

supercompensation in the creatine-independent (ATP) shuttling system, indicate a mitochondrial 'hormesis' consistent with a perspective that mitochondria attempt to enhance the supply of ATP to a failing muscle fibre as the stress of cancer intensifies.

Collectively, this experimental design led to findings that can guide pre-clinical therapy development to treat cancer-induced muscle weakness. For example, the relationships would support further investigation into therapies that preserve pyruvate oxidation or creatine-dependent metabolism early in cancer could be explored to determine if the pre-atrophy weakness can be prevented.

4.5 mH_2O_2 emission: a delayed relationship with weakness?

mH_2O_2 emission was not elevated at the early 45 Day timepoint corresponding to muscle weakness in both muscles. Therefore, there was a stronger relationship between early weakness and reduced pyruvate oxidation and creatine-dependent respiration in both muscles than to oxidative stress. Rather, mH_2O_2 emission was increased by the 75 Day group in both muscles. By the 90 Day group, mH_2O_2 emission returned to control levels in both muscles although this depended on the pathway assessed. While mH_2O_2 emission derived from the reverse electron transfer pathway was more consistently elevated in both muscles, the unique time-dependent patterns of both systems further highlight the complexities of mitochondrial reprogramming that would not be captured by traditional single pathway analyses. Collectively, there is a clear increase in mH_2O_2 in mid to late stages of cancer corresponding to atrophy. Therefore, the findings serve as a basis for examining the potential roles of mitochondrial-derived redox signals in regulating muscle fibre size distinct from mechanisms governing earlier muscle weakness that was more strongly related to changes in oxidative phosphorylation in this model. The findings also suggest that mitochondrial-targeted antioxidants could be tested to determine if these mH_2O_2 responses are partially contributing to atrophy during ovarian cancer. Indeed, a previous study in C26 cancer mice demonstrated the mitochondrial cardiolipin-targeting small peptide SS-31 prevented atrophy at later stages of development in relation to lower mH_2O_2 emission [139].

4.6 Mechanisms regulating cachexia in an orthotopic, metastatic, epithelial ovarian cancer model appear to differ from other pre-clinical models

Contemporary theories propose muscle wasting during cancer cachexia is induced by circulating factors generated by the host or tumour which trigger protein degradation and loss of myofibrillar proteins [6–8]. Several genes and cytokines are thought to regulate this skeletal muscle degradation but atrogin, Murf-1, TNF-a, IL-6, and GDF15 are perhaps most commonly identified and measured [42,116]. However, the current investigation using an immunocompetent, orthotopic, metastatic model of ovarian cancer does not demonstrate robust activation of these pathways. Indeed, with the exception of IL-6 in the diaphragm, the factors regulating muscle atrophy seem to be different within the current model. The time-specific increases in IL-6 in the diaphragm could be explored given this cytokine is integral for the development of muscle loss in the *Apc*$^{min/+}$ mouse (genetic spontaneous colorectal cancer model) [9,264].

The absence of atrogene responses is similar to a patient-derived xenograft (PDX) model whereby, pancreatic ductal adenocarcinoma (PDAC) tumours from cancer patients are orthotopically injected into immunodeficient NSG mice[132]. Within this model, the TA demonstrates up-regulation in canonical atrophy-associated pathways (ubiquitin-mediated protein degradation), while the diaphragm demonstrates an up-regulation in genes related to the inflammatory response [132]. This could suggest that orthotopic models demonstrate distinct cachexia profiles between muscles that are unique to ectopic models.

Reductions in food intake and physical activity are thought to contribute partially to cachexia [74,75]. The degree to which these patterns contribute to pre-atrophy weakness or atrophy itself in the current study requires further investigation. However, previous work in C26 mice has shown that reductions in food intake did not contribute to reduced muscle weights, fiber CSA, or muscle force given pair-fed mice retained normal muscle parameters compared to tumour bearing mice [136].

4.7 Perspectives, Limitations and Conclusions

The discovery that muscle weakness and mitochondrial stress precedes severe metastasis and ascites accumulation in ovarian cancer raises the question of whether pre-atrophy weakness could be an early diagnostic marker of cancer, given that ovarian malignancy is largely undetectable at

premetastatic stages. Indeed, most women are diagnosed with ovarian cancer at stage III – a time where metastasis/ascites have already started, and survival rates are low [238,239,265]. Thus, early cancer detection is suggested to be one of the best strategies for cancer prevention [266]. Exploring this possibility would be complex given muscle weakness and altered mitochondrial functions could occur in other health conditions such as ageing and muscle disuse [267,268]. These findings also position mitochondrial reprogramming as a potential therapeutic target in pre-atrophy weakness and cachexia during metastatic ovarian cancer.

While we measured monocular cell infiltration to the diaphragm, we could not repeat these measures in all organs within the intraperitoneal space (e.g. stomach, colon, liver, spleen, etc.) to confirm the lack of metastasis at the earlier time points with high confidence. In this regard, we cannot definitively state that muscle weakness precedes metastasis *per se*, but rather severe metastasis as evidenced by the visual confirmation in the diaphragm and lack of obvious tumours by sight throughout the abdominal cavity (data not shown). Future studies could use dye-based imaging methods to track and characterize metastatic disease as done previously [269] to identify if mitochondrial stress and muscle weakness precede the earliest onset of metastasis.

Of interest, chemoresistance during ovarian cancer is commonly associated with disease recurrence after platinum-based treatments [270] at which point cachexia can become more evident. Although not investigated in the current study, it is worth highlighting that this EOC model is responsive to platinum-based chemotherapies [271]. Thus, future studies could consider using this model to investigate the interactions of chemotherapy and ovarian tumour-related stressors on cachexia.

In conclusion, this is the first mouse model of epithelial ovarian cancer-induced muscle weakness that offers the advantages of orthotopic injections of EOC cells into the ovarian bursa that can be performed in immunocompetent mice during adulthood. The model also demonstrates the critical clinical feature of metastasis in the abdominal cavity similar to what occurs in women with late-stage ovarian cancer. The identification of an early muscle weakness that precedes both atrophy and severe metastasis provide a new direction for research in understanding the atrophy-independent mechanisms of muscle weakness during ovarian cancer. We identified substrate-specific alterations in mitochondrial oxidative phosphorylation and increases in mitochondrial reactive oxygen species that coincide with early pre-metastatic weakness. The model also

demonstrates late-stage apparent compensatory relationships between mitochondrial metabolism and specific force restoration in limb muscle suggesting a remarkable adaptive mechanism that appears to be muscle-specific. The time-dependent and muscle-specific relationships described in this new model will support continued efforts in defining atrophy-independent and -dependent mechanisms of weakness during ovarian cancer in relation to metastasis and for guiding the design of pre-clinical therapy development investigations.

Authors' Contributions

Luca J. Delfinis: conceptualization, methodology, validation, formal analysis, investigation, writing -original draft, writing – review & editing, visualization, project administration; **Leslie M. Ogilvie:** conceptualization, methodology, investigation, writing – review & editing; **Shahrzad Khajehzadehshoushtar**: conceptualization, methodology, investigation, writing – review & editing; **Shivam Gandhi:** investigation and writing – review & editing; **Madison C. Garibotti:** investigation and writing – review & editing; **Arshdeep K. Thuhan**: investigation and writing – review & editing; **Kathy Matuszewska:** methodology; **Madison Periera**: methodology; **Ronald G. Jones III:** formal analysis, data curation and writing – review & editing; **Arthur J. Cheng**: validation and writing – review & editing; **Thomas J. Hawke**: validation and writing – review & editing; **Nicholas P. Greene**: validation and writing – review & editing; **Kevin A. Murach**: formal analysis, validation and writing – review & editing; **Jeremy A. Simpson:** conceptualization and writing – review & editing; **Jim Petrik:** conceptualization, methodology and writing – review & editing; **Christopher G.R. Perry:** conceptualization, methodology, validation, writing -original draft, writing – review & editing, visualization, project administration, supervision, funding acquisition.

Acknowledgment

Funding was provided to CGRP by the National Science and Engineering Research Council (NSERC, 436138-2013 and 2019-06687) and an Ontario Early Research Award (2017-0351) with infrastructure supported by the Canada Foundation for Innovation, the Ontario Research Fund, and the James H. Cummings Foundation. LJD and LMO were supported by NSERC CGS-D

scholarship. SK was supported by NSERC CGS-M scholarship. SG and AKT were supported by Ontario Graduate Scholarship (OGS). KAM was supported by National Institute of Health (NIH) R01 AG080047. JP was supported by Canadian Institute of Health Research (CIHR) 450209. NPG was supported by the National Institute of Arthritis and Musculoskeletal and Skin Disease of the National Institutes of Health Award R01AR075794-01A1/AR/NIAMS.

Conflict of Interest

None declared.

Supplementary Data – Included in the published manuscript

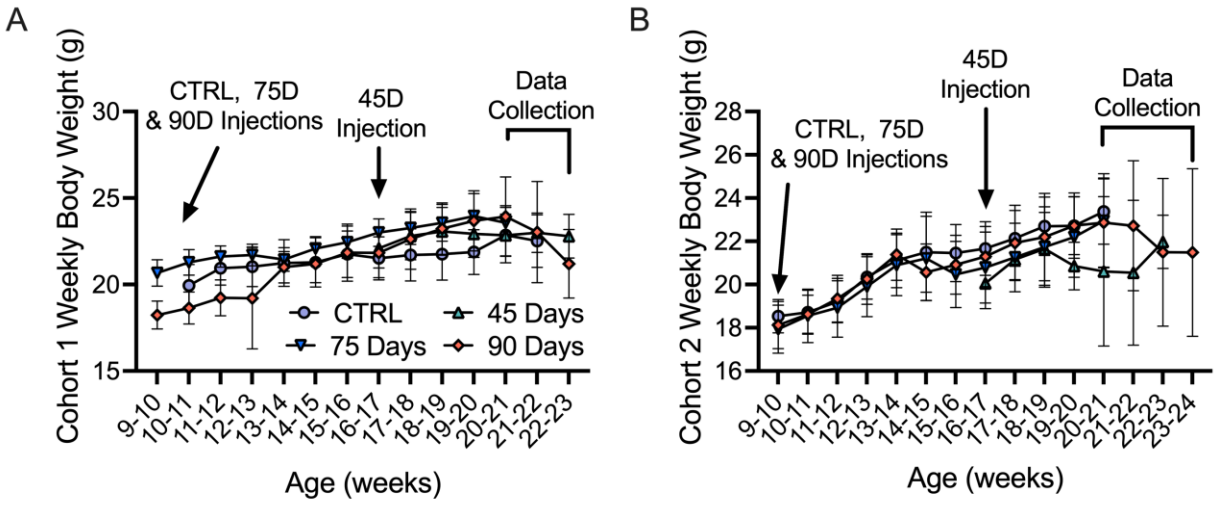

SFigure 5-1. Weekly body weights and age of EOC injections throughout study. This study used two mice per "n" from separate cohorts to obtain enough tissue to complete all experiments. Weekly body weights were measured in mice from cohort 1 (A, n =12) and cohort 2 (B, n =12). Results represent mean ± SD. All data was analyzed using a one-way ANOVA and followed by a two-stage step-up method of Benjamini, Krieger and Yukutieli multiple comparisons test. C57BL/6J female mice ~75 days post PBS injection as controls (CTRL); C57BL/6J female mice ~45 days post ovarian cancer injection (45 Days); C57BL/6J female mice ~75 days post ovarian cancer injection (75 Days); C57BL/6J female mice ~90 days post ovarian cancer injection (90 Days).

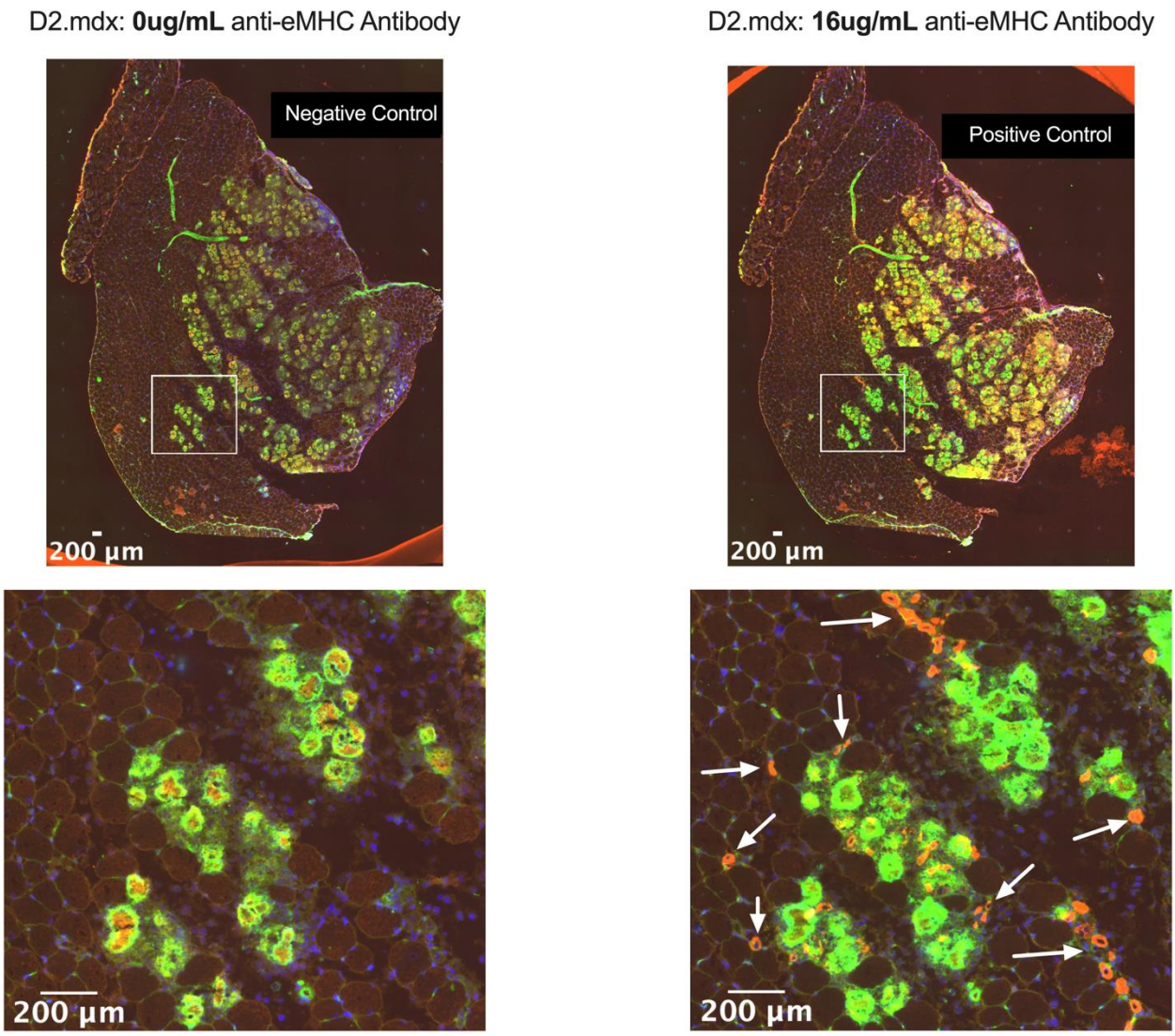

SFigure 5-2. Positive and negative control experiments of eMHC protocol. Tibialis anterior muscle from D2.mdx mice were used as a positive control to validate the eMHC histology technique. Technical replicates of the same tissue were incubated with no eMHC antibody (left) and with 16μg/mL of eMHC primary antibody (right).

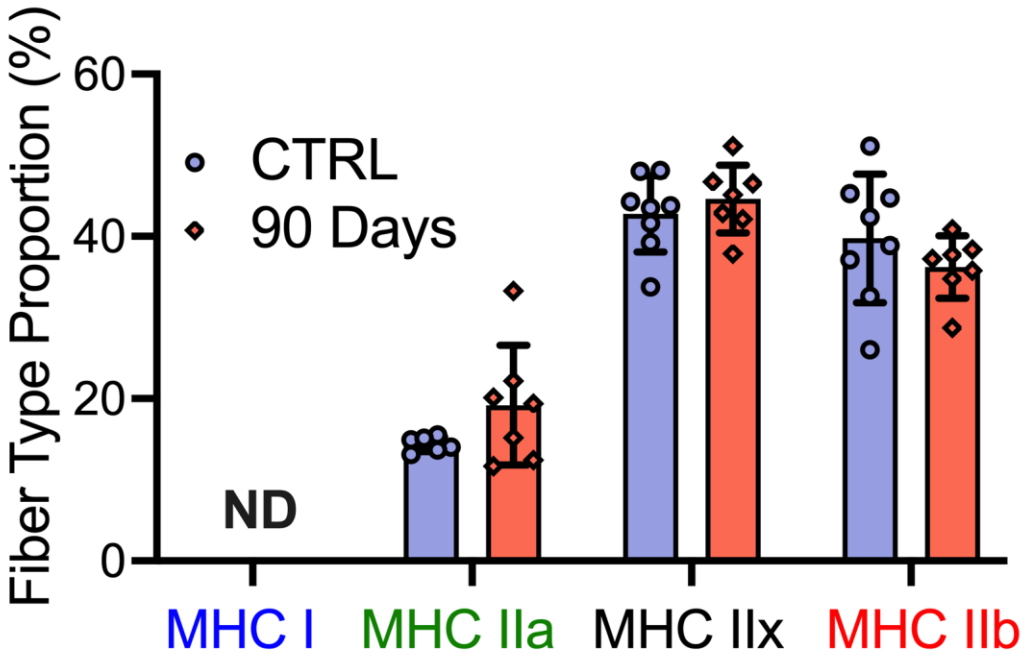

SFigure 5-3. Fiber type analysis of red tibialis anterior. Fiber type distribution of type IIa, type IIx and type IIb. n=7-8. Results represent mean ± SD. All data was analyzed using an unpaired T-Test. C57BL/6J female mice ~75 days post PBS injection as controls (CTRL); C57BL/6J female mice ~90 days post ovarian cancer injection (90 Days).

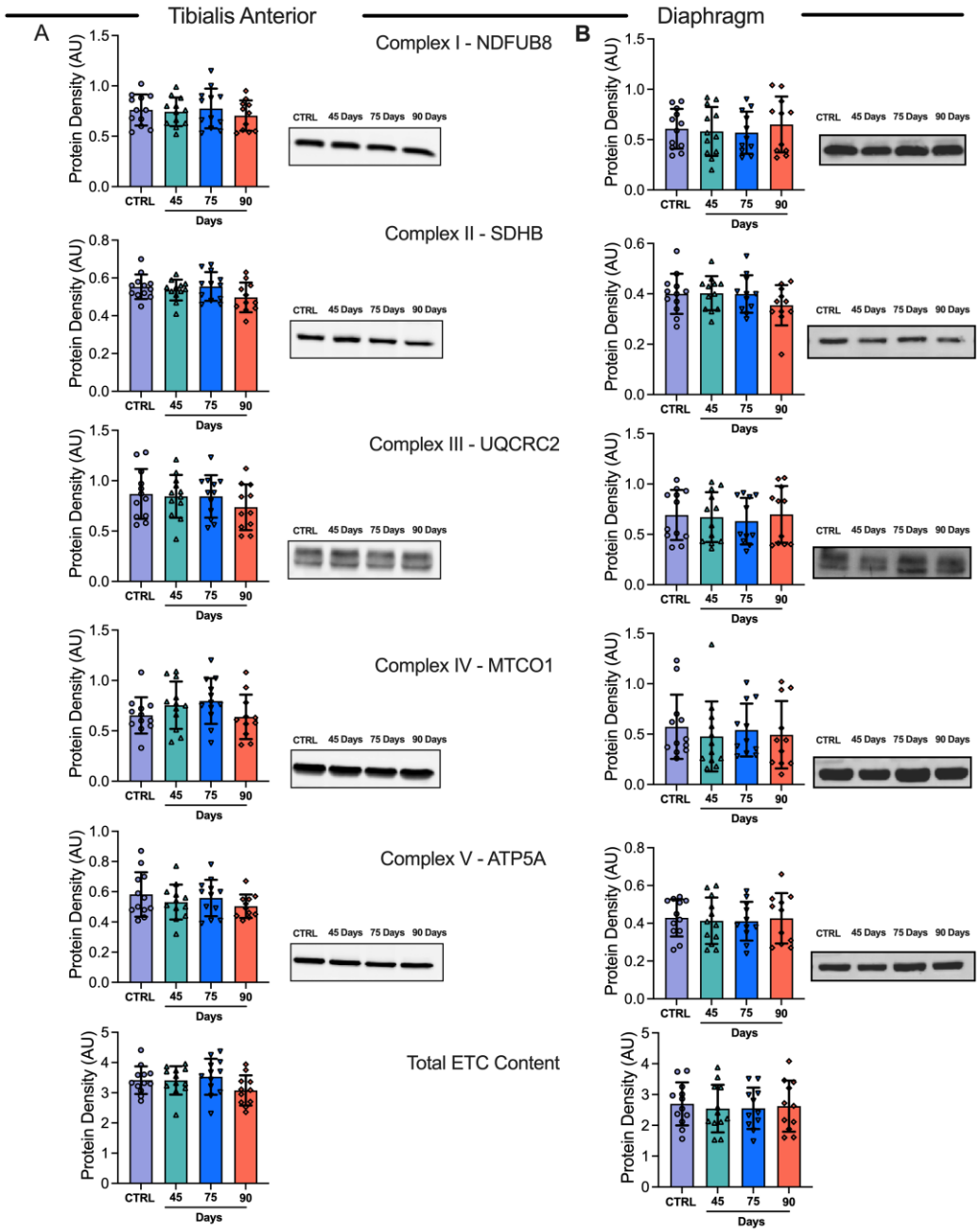

SFigure 5-4. Muscle-specific evaluation of electron transport chain (ETC) complex subunit markers in EOC injected tibialis anterior and diaphragm skeletal muscle. Protein content of ETC subunits was quantified in the tibialis anterior (A, n = 12) and diaphragm (B, n = 12) Results represent mean ± SD. All data was analyzed using a one-way ANOVA or Kruskal-Wallis test when data did not fit normality. All ANOVAs were followed by a two-stage step-up method of Benjamini, Krieger and Yukutieli multiple comparisons test. C57BL/6J female mice ~75 days post PBS injection as controls (CTRL); C57BL/6J female mice ~45 days post ovarian cancer injection (45 Days); C57BL/6J female mice ~75 days post ovarian cancer injection (75 Days); C57BL/6J female mice ~90 days post ovarian cancer injection (90 Days).

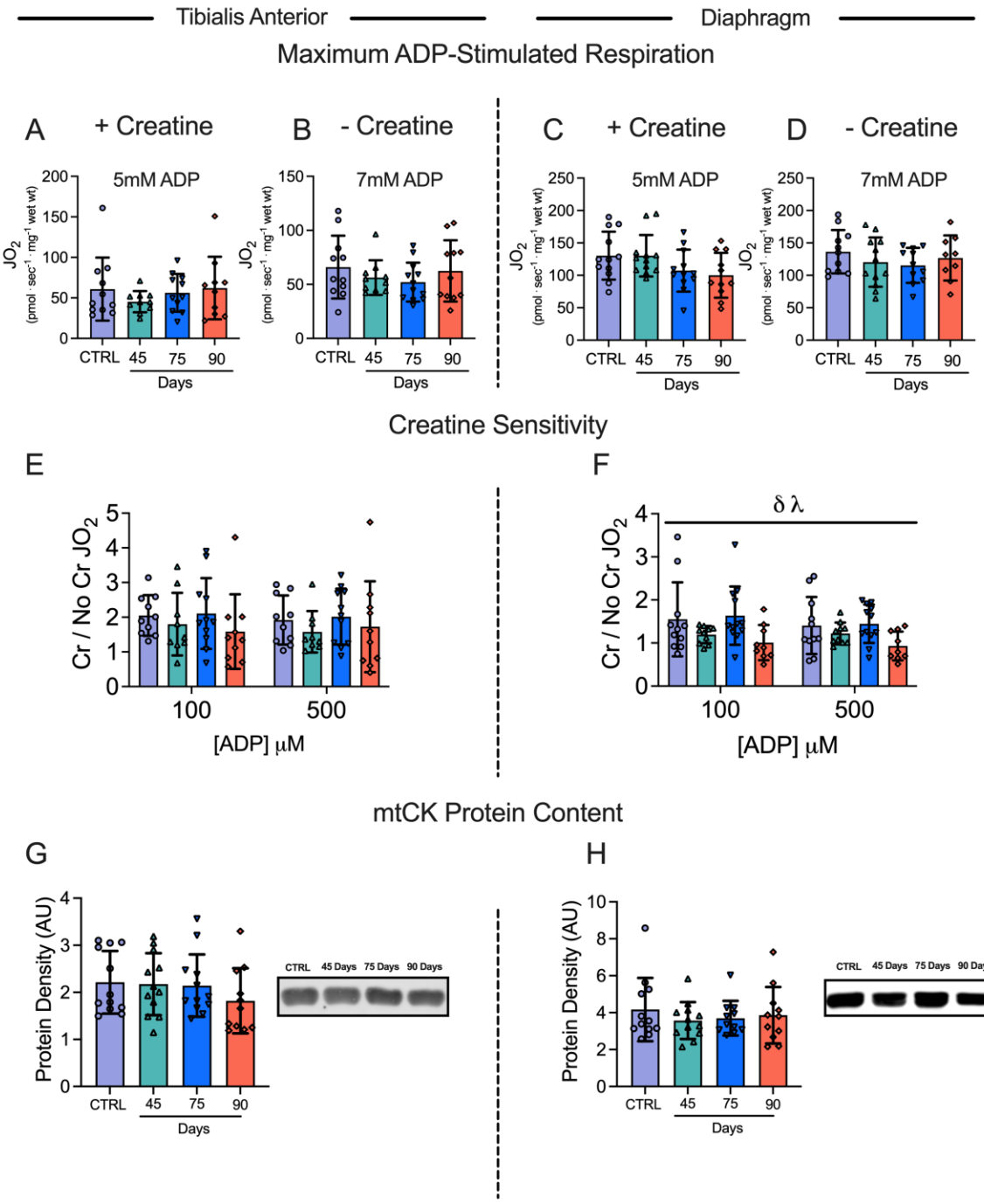

SFigure 5-5. Maximum ADP-stimulated respiration, creatine sensitivity ratios and mitochondrial creatine kinase (mtCK) protein content in tibialis anterior and diaphragm muscle of EOC injected mice. Maximum ADP-stimulated mitochondrial respiration was evaluated in the tibialis anterior and diaphragm both in the presence and absence of creatine (A-D, n = 9-12). A ratio of +Creatine/-Creatine respiration in the tibialis anterior and diaphragm muscle was generated at 100μM and 500μM (apparent Km of mtCK) as an index of creatine sensitivity (E & F, n = 9-12). mtCK protein content was also quantified in both muscles (n = 12). Results represent mean ± SD. λ $p < 0.05$ 75 Day vs 90 Day; δ $p < 0.05$ Control versus 90 Day. Figures A-D, G and H were analyzed using a one-way ANOVA or Kruskal-Wallis test when data

did not fit normality. Figures E and H were analyzed using a two-way ANOVA (main effect shown only). All ANOVAs were followed by a two-stage step-up method of Benjamini, Krieger and Yukutieli multiple comparisons test. C57BL/6J female mice ~75 days post PBS injection as controls (CTRL); C57BL/6J female mice ~45 days post ovarian cancer injection (45 Days); C57BL/6J female mice ~75 days post ovarian cancer injection (75 Days); C57BL/6J female mice ~90 days post ovarian cancer injection (90 Days).

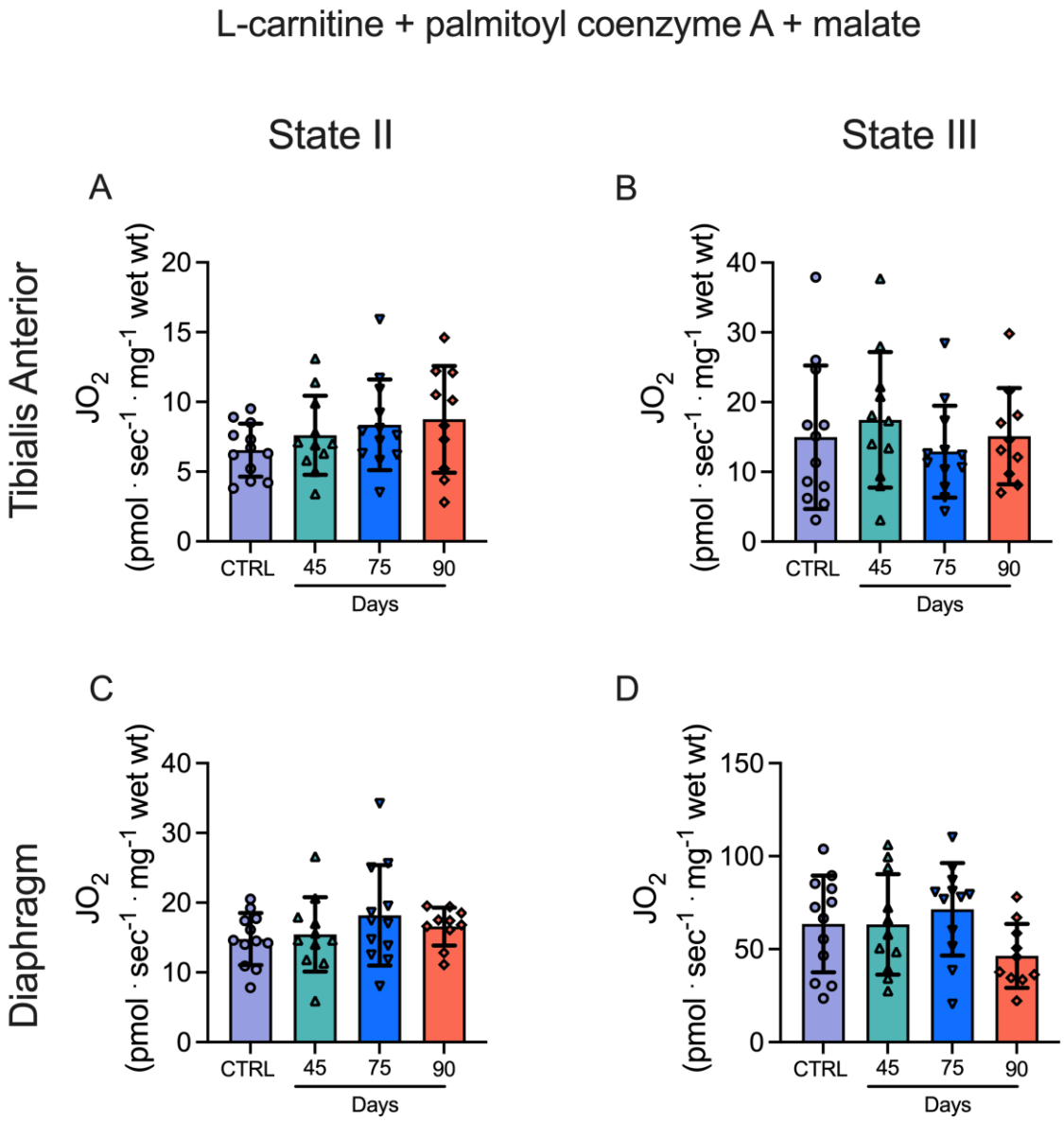

SFigure 5-6. Fatty acid-supported mitochondrial respiration in tibialis anterior and diaphragm of EOC injected mice. State II (L-carnitine + palmitoyl coenzyme A + malate; absence of ADP) mitochondrial respiration was evaluated in the tibialis anterior and diaphragm muscle in the presence of 20mM creatine (A & C, n = 10-12). State III (5mM ADP) mitochondrial respiration was also evaluated in TA and diaphragm muscle (B & D, n =10-12) Results represent mean ± SD. All data was analyzed using a one-way ANOVA or Kruskal-Wallis test when data did not fit normality. All ANOVAS were followed by a two-stage step-up method of Benjamini, Krieger and Yukutieli multiple comparisons test. C57BL/6J female mice ~75 days post PBS injection as controls (CTRL); C57BL/6J female mice ~45 days post ovarian cancer injection (45 Days); C57BL/6J female mice ~75 days post ovarian cancer injection (75 Days); C57BL/6J female mice ~90 days post ovarian cancer injection (90 Days).

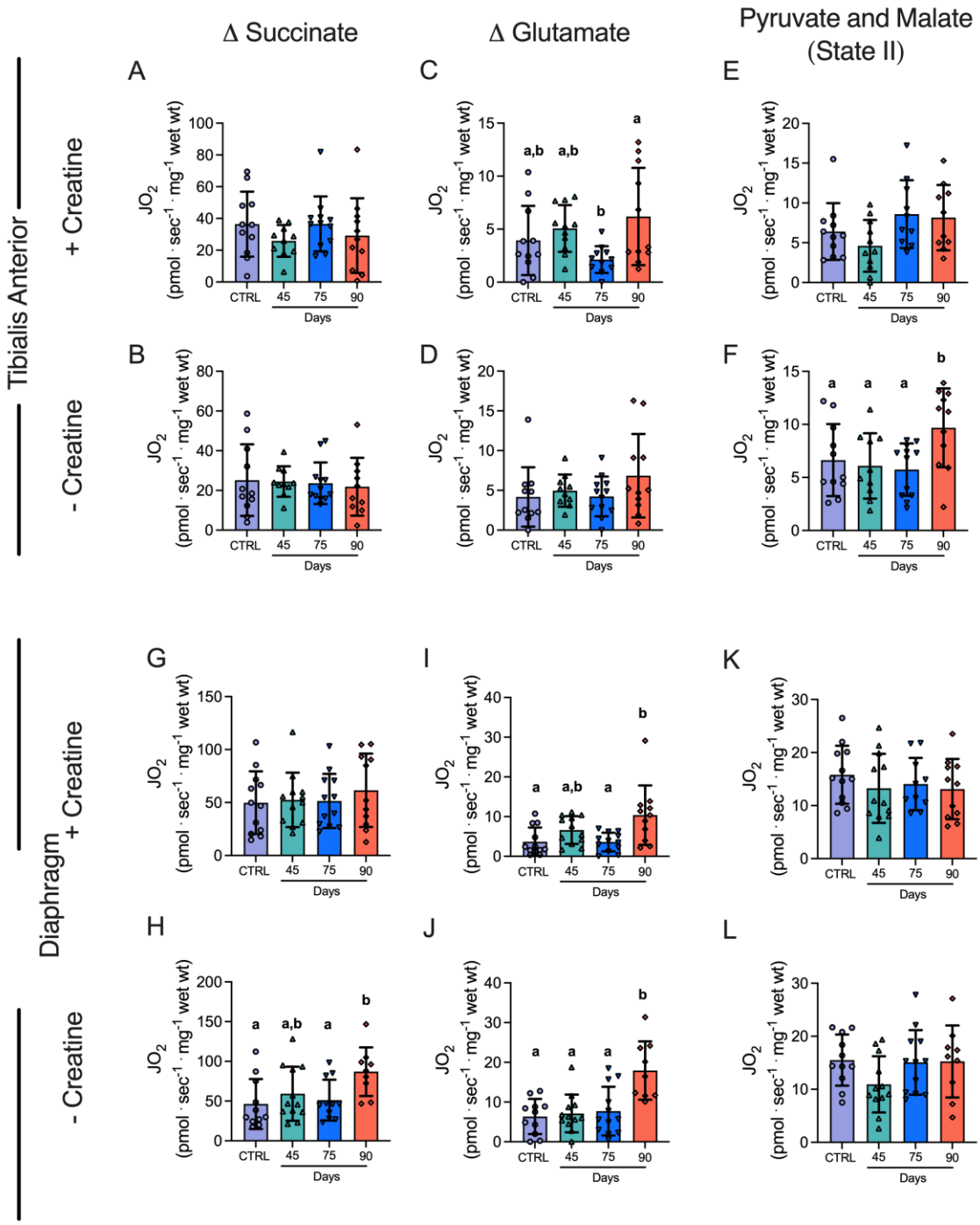

SFigure 5-7. Multiple substrate evaluation of oxygen consumption in tibialis anterior and diaphragm of EOC injected mice. Oxygen consumption was evaluated in tibialis anterior bundles using succinate both in the presence and absence of creatine (A & B). Glutamate-supported respiration was also evaluated in the presence and absence of creatine (C & D). State. II (absence of ADP) was also evaluated in the presence and absence of creatine (E & F). This was repeated in the diaphragm (G-L). Results represent mean ± SD. n = 9-12. Lettering denotes statical significance when different from each other ($p < 0.05$). All data was analyzed using a one-way ANOVA or Kruskal-Wallis test when data did not fit normality. All ANOVAs were followed by

a two-stage step-up method of Benjamini, Krieger and Yukutieli multiple comparisons test. C57BL/6J female mice ~75 days post PBS injection as controls (CTRL); C57BL/6J female mice ~45 days post ovarian cancer injection (45 Days); C57BL/6J female mice ~75 days post ovarian cancer injection (75 Days); C57BL/6J female mice ~90 days post ovarian cancer injection (90 Days).

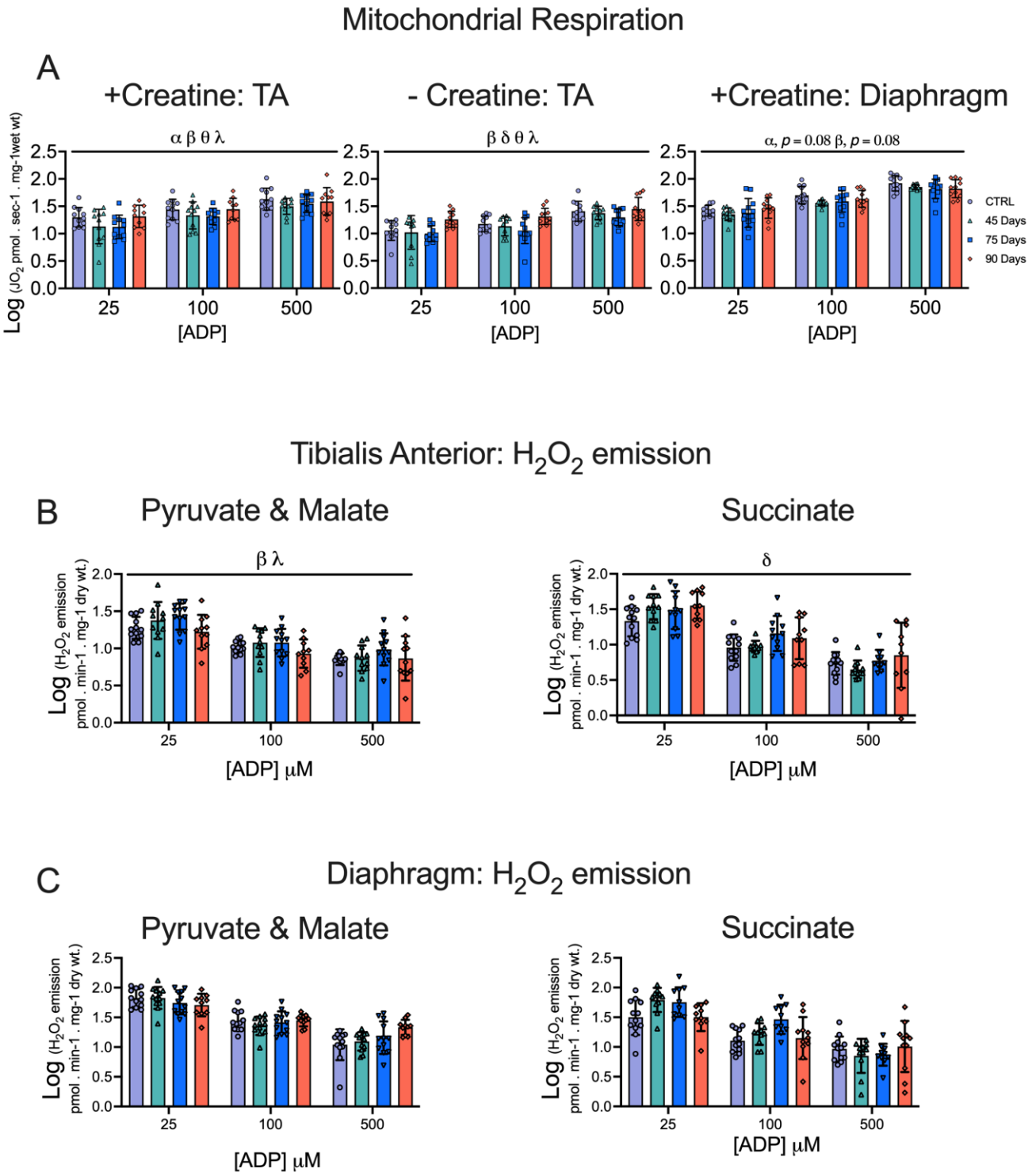

SFigure 5-8. Log transformed data for analysis in tibialis anterior and diaphragm that did not fit a normal distribution. Data that did not fit normality were log transformed and then analyzed using standard 2-way ANOVAs. Results represent mean ± SD. n = 9-12. α $p < 0.05$ Control versus 45 Day; β $p < 0.05$ Control versus 75 Day; δ $p < 0.05$ Control versus 90 Day; θ $p < 0.05$ 45 Day versus 90 Day; λ $p < 0.05$ 75 Day vs 90 Day. All Data were analyzed using a two-way ANOVA. All ANOVAs were followed by a two-stage step-up method of Benjamini, Krieger and Yukutieli multiple comparisons test. C57BL/6J female mice ~75 days post PBS injection as controls (CTRL); C57BL/6J female mice ~45 days post ovarian cancer injection (45 Days); C57BL/6J female mice ~75 days post ovarian cancer injection (75 Days); C57BL/6J female mice ~90 days post ovarian cancer injection (90 Days).

Oligo name	Oligo sequence (5' to 3')
m-actb Fwd	CATTGCTGACAGGATGCAGAAGG
m-actb Rev	TGCTGGAAGGTGGACAGTGAGG
m-TNFa Fw	AGAATGAGGCTGGATAAGAT
m-TNFa Rev	GAGGCAACAAGGTAGAGA
m-IL6 Fw	ACAGAAGGAGTGGCTAAG
m-IL6 Rev	AGAGAACAACATAAGTCAGATAC
m-Murf1 Fw	ACCTGCTGGTGGAAAACATC
m-Murf1 Rev	AGGAGCAAGTAGGCACCTCA
m-Atrogin1 Fw	AGCGCTTCTTGGATGAGAAA
m-Atrogin1 Rev	ACGTCGTAGTTCAGGCTGCT
m-RyR1 Fw	TGCTCAAGGAACAGCTGAAG
m-RyR1 Rev	GGGCTCGAACTGACAGAGAC
m-Serca 1 (Atp2a1) -Fw	ACACAGACCCTGTCCCTGAC
m-Serca 1 (Atp2a1) -Rev	TGCAGTGGAGTCTTGTCCTG
m-Serca 2 (Atp2a2) -Fw	TACTGACCCTGTCCCTGACC
m-Serca 2 (Atp2a2) -Rev	CACCACCACTCCCATAGC

STable 5-1. List of primers used for qtPCR

6 Muscle weakness before and during ovarian cancer-induced cachexia is partially prevented by the mitochondrial-targeted drug SkQ1 in mice.

This chapter is currently in preparation for submission to an academic journal.

Author Contributions: The majority of experiments or this project were carried about by Luca Delfinis. J.P, B.G, S.L, and C.A grew EOC cancer cells, injected and monitored all mice until transport from University of Guelph to York University. L.J.D performed all functional testing and separated fibers for bioenergetic assessments. Due to the nature of these experiments, two people were required in order to efficiently complete all force and bioenergetic assays on fresh viable tissue. As such, L.J.D completed force assessments while S.K assisted with collection and running bioenergetics. L.D.F completed in-vitro force testing on FDB. N.J.A completed single fiber experiments on FDB. M.C.G, S.G, A.N.B and B.A.M helped on surgery collection days with daily logistical tasks. L.J.D, S.K, J.P and C.G.R.P. contributed to the rationale and study design. L.J.D., S.K and C.G.R.P. conducted all experiments and/or analyzed all data. C.G.R.P. and L.J.D. wrote the manuscript. All persons designated as authors qualify for authorship, and all those who qualify for authorship are listed.

Muscle weakness before and during ovarian cancer-induced cachexia is partially prevented by the mitochondrial-targeted drug SkQ1 in mice.

Luca J. Delfinis[1], Shahrzad Khajehzadehshoushtar[1], Luke D. Flewwelling[1], Nathaniel J. Andrews[1], Madison C. Garibotti[1], Shivam Gandhi[1], Aditya N. Brahmbhatt[1], Brooke A. Morris[1], Bianca Garlisi[2], Sylvia Lauks[2], Caroline Aitken[2], Arthur J. Cheng[1], Jim Petrik[2] and Christopher G.R. Perry[1]†.

Affiliations
[1]School of Kinesiology & Health Science, Muscle Health Research Centre, York University, Toronto, ON, Canada
[2]Department of Biomedical Sciences, University of Guelph, Guelph, ON, Canada

Email Addresses:

Key Words: Ovarian cancer cachexia, mitochondria, skeletal muscle

†Address for Correspondence:
Christopher Perry, PhD
School of Kinesiology and Health Science
Muscle Health Research Centre
344 Norman Bethune College
York University
4700 Keele Street
Toronto, Ontario M3J 1P3
(P) 416 736 2100 ext. 33232
cperry@yorku.ca

Conflict of Interest: The authors have declared that no conflict of interest exists.

Abstract

Introduction: Muscle weakness and wasting are defining features of ovarian cancer-induced cachexia, a disease that currently has no treatment. Recent literature suggests that atrophy-independent mechanisms of muscle weakness exist within cancer myopathy. In addition, an orthotopic, metastatic model of epithelial ovarian cancer (EOC) cachexia demonstrates Complex I-stimulated mitochondrial H_2O_2 (mH_2O_2) is a source of oxidative stress at a time when muscle weakness occurs. Therefore, we used the mitochondrial-targeted therapeutic SkQ1 to identify the direct relationship between mitochondria and cancer myopathy and explore it's efficacy as a cancer cachexia therapeutic.

Methods: C57BL/6J female mice were injected with $1x10^6$ epithelial ovarian cancer (EOC) cells underneath the ovarian bursa, generating a metastatic model of ovarian cancer. Mice received the mitochondrial-enhancing drug SkQ1 in their drinking-water or standard drinking-water while cancer developed for ~40 (Early-Stage: 40Veh and 40SkQ - no apparent metastasis) and ~80 (Late-Stage: 80Veh and 80SkQ - robust metastasis) days. Control mice were age matched, injected with saline and provided standard drinking-water (CTRL).

Results: SkQ1 had heterogenous effects on Complex I-stimulated mH_2O_2. In the tibialis anterior (TA), mH_2O_2 was increased in Late-Stage mice decreased in 80SkQ vs 80Veh, suggesting the drug lowered oxidative stress. Interestingly, in the diaphragm, mH_2O_2 was increased at Late-Stage mice vs CTRL, however, 80SkQ mH_2O_2 was further increased vs 80Veh. TA weakness and atrophy occurred in Early-Stage vs CTRL mice. SkQ1 partially preserved force production at Early-Stage in TA and diaphragm, and at Late-Stage in diaphragm, but did not prevent atrophy in either muscle. High-force muscle weakness linked to lower calcium release in Flexor Digitorum Brevis in 80Veh

vs CTRL was completely prevented by SkQ1 at Late-Stage. SkQ1 did not affect primary tumour size.

Conclusion: These findings suggest that SkQ1 treatment can improve force production independent of atrophy in mice injected with EOC. Moreover, these improvements are associated with lower mH_2O_2 and improved calcium handling albeit, these relationships are heterogenous across muscles. Thus, this study establishes a direct contribution of mitochondria to muscle weakness throughout cancer-induced myopathy, supporting the further exploration of mitochondria in cancer cachexia for disease mechanism elucidation and therapy development.

Introduction

Cancer-induced cachexia is a multifactorial syndrome characterized by muscle loss and functional impairment[3]. This condition leads to reductions in quality of life, tolerance to anticancer therapies and overall survivability[6,201,272]. Although dozens of clinical investigations have been completed for cancer cachexia therapy development, none have produced sufficiently positive results to yield a therapeutic intervention[5]. Experts suggest this could be due to a mismatch between clinical reality and current animal models, resulting in poor translation of preclinical studies[13]. Indeed, most animal models have been considered insufficient due to the lack of metastasis or ectopic tumour growth (tumour growth that does not occur in host organ), among other reasons. It is for this reason orthotopic, and metastatic models are believed to improve the predictive power of preclinical models in terms of both mechanism and therapy elucidation for cancer cachexia[13].

While most research has focused on the mechanisms of muscle atrophy in cancer cachexia, our group was the first to report muscle weakness precedes atrophy[237]. We showed this in both limb and respiratory muscles within the C26 model[237] and an orthotopic, metastatic epithelial ovarian cancer (EOC) model[273] suggesting pre-atrophy weakness could be a ubiquitous phenomenon across muscles and cancer types. Moreover, while past literature has shown mitochondrial dysregulation occurs before the onset of atrophy in cancer cachexia[12], we showed mitochondrial stress occurs concurrently with pre-atrophy weakness in two cancer cachexia models [237,273]. More specifically, we showed early weakness corresponded to attenuated pyruvate oxidation and elevated reactive oxygen species (ROS) depending on the muscle type as well as attenuated gene programs related to oxidative phosphorylation[273]. The mitochondrial-targeted compounds MitoQ and SS-31 were shown to attenuate atrophy to some effect and, in the case of SS-31, preserve muscle force generating capacity in relation to certain indices of mitochondrial function in the C26

model. However, the degree to which mitochondrial stress responses contribute to pre-atrophy weakness vs atrophy itself remains unresolved. Likewise, it remains unknown if mitochondrial mechanisms govern early-atrophy-independent and late-atrophy-dependent weakness during cancer progression. Last, the efficacy of mitochondrial-targeted therapies in an orthoptic model of cancer cachexia has yet to be explored.

The primary purpose of this investigation was to determine the degree to which pharmacological enhancement of mitochondria could prevent the recently identified pre-atrophy weakness that occurs during cancer. The secondary purpose of this investigation was to determine the degree to which atrophy, and weakness during atrophy, could be prevented with mitochondrial-targeted therapy. Using the lipophilic (tissue penetrating) cationic (mitochondrial-targeting) quinone-based antioxidant SkQ1, we report that muscle force generating capacity is partially preserved prior to the onset of cachexia as well as during cachexia without any effect on muscle fiber cross sectional area. These findings highlight that quinone-based mitochondrial targeting therapies can partially preserve muscle force and identifies mitochondrial dysfunctions as a causal factor for weakness that occurs independent of a loss of muscle during ovarian cancer.

Methods

Animal Care and ID8 Inoculation

108 female C57BL/6J mice were ordered at 7-9 weeks of age from Charles River Laboratories. These mice were housed at the University of Guelph in accordance with the Canadian Council on Animal Care. Tumours were induced as described previously at the University of Guelph [240–243,273]. Briefly, ID8 cells (epithelial ovarian cancer cells; 1.0 x 10^6 in 5μL) were injected under the left ovarian bursa of C57BL/6J mice generating an orthotopic model of ovarian cancer. Control mice were sham injected with equivalent volumes of sterile phosphate buffered saline (PBS). Two weeks after ID8 inoculation, mice were transported from University of Guelph to York University where they were housed for the remainder of the study in accordance with the Canadian Council on Animal Care. All mice were provided access to standard chow and water *ad libitum*.

Cancer Timepoints and Drug Incubations

Control mice (CTRL; n =24) were injected at 10 weeks old with PBS and aged to ~23 weeks (13-15 weeks/91-105 days post PBS injection). Early-Stage SkQ1 treated (40SkQ; n=12) and vehicle treated (40Veh; n=12) mice were injected at 16-17 weeks and aged to ~22-23 weeks (5-6 weeks/35 days-46 days post ID8 injection). Late-Stage SkQ1 treated (80SkQ; n=30) and vehicle treated (80Veh; n=30) mice were injected at 10 weeks and aged to ~18-22 weeks (8-12 weeks/58-82 days post ID8 inoculation). These ranges in ages were chosen given force, myoplasmic calcium and mitochondrial assessments are all live assays that require fresh tissue and thus limit daily experimental throughput. The range was largest in the Late-Stage group because mice were euthanized at the end of their survivability upon presentation combinations of the following criteria: 10% body weight loss, >20mL of ascitic volume collected during paracentesis, > 5 ascites

paracentesis taps completed in total, and/or subjective changes in behavioural patterns consistent with removal criteria as per animal care guidelines (self-isolation, ruffled fur/poor self-grooming and irregular gait) and as done previously [273]. Presentation of these criteria was variable as expected in a metastatic model of ovarian cancer cachexia. Staggering the age at which mice received cancer injections permitted a similar age at euthanasia for all mice to reduce aging effects on all measures.

50mg/ml of SkQ1 was purchased from Cayman Chemical (Item No 19891) in a solution of 1:1 ethanol: water. SkQ1 was administered to mice in the drinking water and 40SkQ and 80SkQ both received 250nmol/kg body weight/day as done previously [274]. Mice were estimated to weigh 25g on average and drink 5 mL/day. Therefore, a 1.25nmol/mL concentration of SkQ1 was provided to all 40SkQ and 80SkQ mice from the day they received cancer injections. The estimated percentage of ethanol in the 1.25nmol/mL drinking water was 0.0008% as it was taken from the 50mg/mL 1:1 ethanol: water stock. Considering this was a very small percentage, 40Veh and 80Veh mice were treated with standard drinking water.

Voluntary Wheel Running

48 hours before euthanasia, a subset of mice were placed in individual cages with a 14 cm diameter running wheel and rotation counter (VDO m3 bike computer, Mountain Equipment Co-Op, Vancouver, Canada) as done previously [206,273]. 24 hours later, distance and time ran were recorded and mice were placed in sperate caging with no running wheel. Muscle measurements were made 24 hours thereafter. We were unable to predict mouse survivability 48 hours in advance at the Late-Stage timepoint, therefore there was no voluntary wheel running data at this time. However,

previous work in this model has shown that mice do not typically run volitionally at this time point [273].

Tissue Collection Procedure

Mice were anesthetized with isoflurane and hearts were removed for euthanasia. All hindlimb muscles, inguinal subcutaneous fat and spleens were weighed and snap-frozen in liquid nitrogen and stored at -80^{o}C. Primary ovarian tumours were also collected by removing the ovary and tumour at the site of injection and carefully separating the tumour mass from the ovary mass and stored in liquid nitrogen. Hindlimb muscles were also embedded in optimal cutting temperature (OCT) medium and frozen (see section below). Tibialis anterior (TA) and diaphragm muscle were placed in BIOPS containing (in mM) 50 MES Hydrate, 7.23 K_2EGTA, 2.77 CaK_2EGTA, 20 imidazole, 0.5 dithiothreitol, 20 taurine, 5.77 ATP, 15 PCr, and 6.56 $MgCl_2 \cdot 6\ H_2O$ (pH 7.1) to be prepared for mitochondrial bioenergetic assays. The flexor digitorum brevis muscle was isolated and used for both *in-vitro* force production and enzymatic dissociation for myoplasmic calcium assessments (see sections below).

In Situ Tibialis Anterior Force, *In Vitro* Diaphragm Force an *In Vitro* FDB Force

In Situ TA force production was partially adapted from previous literature [246,247] and completed as done previously [273]. Briefly, mice were anesthetized with isoflurane and the distal tendon of the TA was exposed by incision at the ankle. The distal tendon was tied with suture thread as close to the muscle attachment as possible. Once the knot was secured the distal tendon was severed. Small cuts were made up the lateral side of the TA to expose the muscle for needle electrode placement. The knot was tied to an Aurora Scientific 305C (Aurora Scientific Inc., Aurora, ON, Canada) muscle lever arm with a hook. The foot of the mouse was secured with tape and the knee was

immobilized with a needle and set screw with the length of the limb parallel to the direction of force. The two needle electrodes were placed in the gap of fascia between the TA and tibia to stimulate the common peroneal nerve (10-50 mA). The mouse was heated with a heating pad or heat lamp throughout force collection. Optimal resting length (L_o) was determined using single twitches (pulse width=0.2ms) at 1 Hz stimulation frequency with 1 minute rest in between contractions to avoid fatigue. Once L_o was established, a ruler was used to determine length before the start of force-frequency collection (1, 10, 20, 30, 40, 50, 60, 80, 100, 120 and 200Hz with 1 minute rest in between contractions). Force production was normalized to the calculated CSA of the muscle strip (m/l*d) where m is the muscle mass, l is the length, and d is mammalian skeletal muscle density (1.06mg.mm^3).

In Vitro diaphragm force production was completed as done previously [237,248,249,273]. Briefly, the diaphragm strip was carefully sutured in Ringer's solution (containing in mM: 121 NaCl, 5 KCl, 1.8 $CaCl_2$, 0.5 $MgCl_2$ 0.4 $NaHPO_4$, 24 $NaHCO_3$, 5.5 glucose and 0.1 EDTA; pH 7.3 oxygenated with 95% O_2 and 5% CO_2) such that the thread secured to the central tendon and ribs. The strip was then placed in an oxygenated bath filled with Ringer's and maintained at 25^{o}C. The suture secured to the central tendon was then attached to the lever arm and the loop secured to the ribs was attached to the force transducer. The strip was situated between flanking platinum electrodes driven by biphasic stimulator (model 305C; Aurora Scientific Inc.). L_o determined using single twitches (pulse width=0.2ms) at 1 Hz stimulation frequency with 1 minute rest in between contractions to avoid fatigue. Once L_o was determined, the strip acclimatized for 30 minutes in the oxygenated bath. L_o was re-assessed and measured with a ruler and the start of the force-frequency protocol was initiated (1, 10, 20, 40, 60, 80, 100, 120, 140 and 200Hz with 1 minute rest in between

contractions). Force production was normalized to CSA of the muscle strip (m/l*d) where m is the muscle mass, l is the length, and d is mammalian skeletal muscle density (1.06mg.mm^3).

In Vitro FDB force production was completed by attaching FDB tendons to 3D-printed clips and suture thread. The FDBs were then moved to a bath containing Tyrode solution oxygenated with 95% O_2, 5% CO_2 and pH ~7.4 (model 6350*358, Aurora Scientific, Inc). One suture connected to the proximal end of FDB was attached to a lever arm, while the suture attached to the distal end of the FDB was attached to a force transducer. The FDB was placed between platinum electrodes connected to a stimulator (Aurora Scientific Integrated Muscle Test Controller). L_o was determined using twitches (pulse width = 0.2ms) at varying muscle lengths. Once L_o was determined, the strip acclimatized for 30 minutes in the oxygenated bath. Finally, force as a function of stimulation frequency was measured during 10 isometric contractions at varying stimulation frequencies (10, 20, 30, 40, 50, 60, 80, 100, 120, 200 Hz). Fatigue was tested during 120 repeated contractions every second (60Hz, 0.2ms pulse width, 0.3ms duration). Force production was normalized to the calculated CSA of the muscle strip (m/l*d) where m is the muscle mass, l is the length, and d is mammalian skeletal muscle density (1.06mg.mm^3).

Preparation of Permeabilized Muscle Fibers

The assessment of mitochondrial bioenergetics was performed as described previously in our publications [206,229,237,250,251,273]. Briefly, the TA and diaphragm from the mouse was removed and placed in ice cold BIOPS. Muscle was separated gently along the longitudinal axis to form bundles that were treated with 40 μg/mL saponin in BIOPS on a rotor for 30 minutes at 4^{o}C. Following permeabilization the permeabilized muscle fiber bundles (PmFBs) for respiration were blotted and weighed in 1.5mL of tared prechilled BIOPS for normalization of respiratory assessments. The

remaining PmFBs for mitochondrial H_2O_2 (mH_2O_2) were not weighed at this step as these data were normalized to fully recovered dry weights taken after the experiments. All PmFBs were then washed in Buffer Z on a rotator for 15 minutes at 4°C to remove the cytoplasm. Buffer Z contained (in mM) 105 K-MES, 30 KCl, 10 KH_2PO_4, 5 $MgCl_2 \cdot 6\ H_2O$, 1 EGTA and 5mg/mL BSA (pH 7.1).

Mitochondrial Respiration

High-resolution respirometry (O_2 consumption) were conducted in 2 mL of respiration medium (Buffer Z) using the Oroboros Oxygraph-2k (Oroboros Instruments, Corp., Innsbruck, Austria) with stirring at 750 rpm at 37°C. Buffer Z contained 20 mM Cr to saturate mtCK and promote phosphate shuttling through mtCK or was kept void of Cr to prevent the activation of mtCK mH_2O_2 [223]. All experiments were conducted in the presence of 5 μM blebbistatin (BLEB) in the assay media to prevent spontaneous contraction of PmFB, which has been shown to occur in response to ADP at 37°C that alters respiration rates [223]. Complex I-supported respiration was stimulated using 5mM pyruvate and 2mM malate (NADH) followed by a titration of ADP concentrations from physiological ranges (25 μM, 100 μM; [225]) to high submaximal (500 μM) and saturating to stimulate maximal coupled respiration (5000 μM in the presence of creatine and 7000 μM in the absence of creatine). 10mM glutamate (further NADH generation) was added at the end of the ADP titration. Cytochrome *c* was then added to test mitochondrial outer membrane integrity. Experiments with low ADP-stimulated respiration (bundles that did not respond to ADP) with high cytochrome *c* responses (>15% increase in respiration) were removed from analysis. Last, 20mM Succinate ($FADH_2$) was added to stimulate complex-II supported respiration. These protocols were designed to understand the regulation of respiration coupled to oxidative phosphorylation of ADP to ATP.

Mitochondrial H_2O_2 (mH_2O_2)

mH_2O_2 was determined spectrofluorometrically (QuantaMaster 40, HORIBA Scientific) in PmfB placed in a quartz cuvette with continuous stirring at 37°C in 1 mL of Buffer Z supplemented with 10 μM Amplex Ultra Red, 0.5 U/ml horseradish peroxidase, 1mM EGTA, 40 U/ml Cu/Zn-SOD1, 5 μM BLEB and 20mM Cr to saturate mtCK. No comparisons were made to PmFB in the absence of creatine due to tissue limitations. State II mH_2O_2 (maximal emission in the absence of ADP) was induced using the Complex I-supporting substrates (NADH) pyruvate (10mM) and malate (2mM) to generate forward electron transfer (FET)-supported electron slip at Complex I [252] as described previously [206]. These PmFBs were incubated with 35 μM CDNB during the 30-minute permeabilization to deplete glutathione and allow for detectable rates of mH_2O_2. Following the induction of State II mH_2O_2, a titration of ADP was employed to progressively attenuate mH_2O_2 as it occurs when membrane potential declines during oxidative phosphorylation [80]. After the experiments, the fibres were lyophilized in a freeze-dryer (Labconco, Kansas City, MO, USA) for > 4h and weighed on a microbalance (Sartorius Cubis Microbalance, Gottingen Germany). The rate of mH_2O_2 emission was calculated from the slope (F/min) using a standard curve established with the same reaction conditions and normalized to fibre bundle dry weight.

Myoplasmic Calcium

Enzymatic Dissociation of Intact Muscle Fibers

Enzymatic dissociation was partially adapted from previous work[275]. FDB muscles were dissected at room temperature in experimental Tyrode solution consisting of 121 mM NaCl, 5.0 mM KCl,

1.8 mM $CaCl_2$, 0.5 mM $MgCl_2$, 0.4 mM NaH_2PO_4, 24 mM $NaHCO_3$, 0.1 mM EDTA, and 5.5 mM glucose. Glass-bottomed Petri dishes with a diameter of 35 mm were placed on a sterilized incubator tray, coated with laminin (cat. no. CB-40232, Thermo Fisher Scientific, Waltham, MA, USA) and left at room temperature for ~2 hours.

Isolated FDBs were transferred to a multiwell plate containing 3 mL of: Dulbecco's modified Eagle's medium (DMEM)/nutrient mixture F-12, pH 7.4 (cat. no. 12800017, Thermo Fisher Scientific, Waltham, MA, USA); 20% heat-inactivated newborn calf serum (cat. no. 16010159, Gibco, New Zealand); antibiotic antimycotic solution (6 µL/mL; cat. no. P4333 Sigma-Aldrich, St Louis, MO, USA); 0.6% collagenase Type I (cat. no. SCR103, EMD Millipore Corp., Burlington, MA, USA), and 0.01% sodium bicarbonate. The multiwell plate was then incubated at 37°C in a water-saturated incubator for 2-3 hours. Afterwards, FDB muscles were transferred into 1 mL of fresh DMEM/F-12 with 20% newborn calf serum and antibiotic antimycotic solution and carefully mechanically dissociated via pipetting the solution ~30 times. The glass-bottomed Petri dishes coated with laminin for 2 hours were then washed with PBS and loaded with 165 µL of DMEM-F-12 solution containing the muscle fibres. The dish was left for ~45 minutes at room temperature to allow muscle fibres to adhere to the laminin coated glass. Afterwards, 3 mL of DMEM/F-12 with 20% newborn calf serum and antibiotic antimycotic solution were added. The petri dishes were then placed into the incubator and stored at 37 °C overnight and used the following day.

Dye Loading

In order to assess myoplasmic free [Ca^{2+}] ($[Ca^{2+}]_i$), Indo-1AM (Cat. No. I1223, Invitrogen, Eugene, OR, USA) dye was excited at 346 ± 5 nm and the two emission wavelengths were recorded by two photomultipliers at 405±5 nm and 495±5 nm (Horiba Ratiomaster, London, ON,

Canada) as done previously [276,277]. The petri dishes containing the dissociated FDB muscle fibres were then loaded with [3.5 uM] of indo-1 AM and placed in a water saturated incubator (37 °C) for 30 minutes.

After the loading phase, the petri dish was then moved to a dark room and placed into a custom-made chamber and mounted on an inverted microscope (Nikon Eclipse Ts2R-FL, Tokyo, Japan) where the remainder of the experiment was conducted at room temperature. To allow for Indo-1 AM ester hydrolysis, the dishes were then washed for 30 minutes with a combination of experimental Tyrode solution, 0.5% newborn calf serum and bubbled with a mixture of 95% O_2– 5% CO_2 (~7.4 pH). After washing the dishes containing muscle fibres, a background fluorescence reading was acquired by focusing on an empty section of the dish. To electrically stimulate the FDB muscles, a custom chamber was used to house the 35 mm glass plated dishes containing FDB muscle, which used two platinum electrodes (1 cm apart). The custom chamber was then connected to an electrical stimulator (Model 701C, Aurora Scientific, Aurora, ON, Canada) controlled via Aurora Scientific 600A software (Aurora Scientific, Aurora, ON, Canada) and Felix32 software (Horiba, London, ON, Canada) was used to acquire $[Ca^{2+}]_i$ readings (resting and tetanic values).

$[Ca^{2+}]_i$-frequency assessment and fatigue protocol

$[Ca^{2+}]_i$-frequency assessment was partially adapted from previous literature [278]. The $[Ca^{2+}]_i$-frequency relationship was assessed by stimulating the fibres with 300 ms tetani (0.2ms pulse duration) at progressively increasing stimulation frequencies of 1-200Hz (1, 10, 20, 30, 40, 50, 60, 80, 100, 120, 200Hz) with 1-minute intervals of rest between each tetanus. Repeated contractions

were induced by stimulating the fibres with 60Hz, 300ms tetani (0.2ms pulse width) every two second for a total of 120 tetani.

Sectioning & Immunofluorescence

Tibialis anterior and diaphragm muscle samples were embedded in OCT medium (Thermo Fisher Scientific) and frozen in 2-methylbutane. These muscles were then sectioned into 10μm sections with a cryostat (HM525 NX, Thermo Fisher Scientific) maintained at -20^{o}C on Fisherbrand Superfrost Plus slides (Thermo Fisher Scientific). Immunofluorescent analysis of myosin heavy chain (MHC) expression was completed as previously described [231]. Images were taken using a fluorescence slide scanner at wavelengths 350nm (blue), 488nm (green) and 555nm (red) (Zeiss AxioScan) at 20x magnification. Sections were analyzed using the ImageJ extension on QuPath-0.4.0 software while blinded to the groups. Fibers that did not fluoresce were considered IIx fibers. A total of 25-50 fibers were then randomly selected and measured. Type I fibers were extremely low in abundance in the TA and thus were not analyzed [231].

RNA Isolation and Rt-PCR

RNA isolation was performed as previously described [249,273]. TA and diaphragm samples were lysed using TRIzol reagent (Invitrogen) and RNA was separated to an aqueous phase using chloroform. The aqueous layer containing RNA was then mixed with isopropanol and loaded to Aurum Total RNA Mini Kit columns (Bio-Rad, Mississauga, ON, Canada). Total RNA was then extracted according to the manufacturer's instructions. RNA was quantified spectrophotometrically using the NanoDrop attachment for the Varioskan LUX Multimode Microplate reader (Thermo Scientific). Reverse transcription of RNA into cDNA was performed by M-MLV reverse transcriptase and oligo(dT) primers (Qiagen, Toronto, ON, Canada). cDNA

was then amplified using aCFX384 Touch Real-Time PCR Detection Systems (Bio-Rad) with a SYBR Green master mix and specific primers **(STable 1)**. Gene expression was normalized to β-actin (Actb) and relative differences were determined using the ΔΔCt method. Values are presented as fold changes relative to the control group.

Western Blotting

A frozen piece of TA and diaphragm from each animal was homogenized in a plastic microcentrifuge tube with a polytron homogenizer in ice-cold buffer containing (in mM) 20 Tris/HCl, 150 NaCl, 1 EDTA, 1 EGTA, 2.5 $Na_4O_7P_2$, and 1 Na_3VO_4 and 1% Triton X-100 with PhosSTOP inhibitor tablet (Roche; 4906845001) and protease inhibitor cocktail (Sigma Aldrich; P8340) (pH7.0) as published previously [230,237,273]. Protein concentrations were determined using a bicinchoninic acid assay (life Technologies, Thermo Fisher Scientific). 15-40 μg of denatured and reduced protein was subjected to 10%-12% gradient SDS-PAGE followed by transfer to low-fluorescence polyvinylidene difluoride membrane. Membranes were blocked with Odyssey Blocking Buffer (Li-COR) and immunoblotted overnight (4°C) with antibodies specific to each protein. A commercially available monoclonal antibody was used to detect electron transport chain proteins (rodent OXPHOS Cocktail, ab110413; Abcam, Cambridge, UK, 1:500 dilution), including V-ATP5A (55kDa), III-UQCRC2 (48kDa), IV-MTCO1 (40kDa), II-SDHB (30 kDa), and I-NDUFB8 (20 kDa). A commercially available monoclonal antibody was used to detect PDH (Abcam Anti-PDHA1 ab110330, 1:500 dilution), polyclonal antibody for P-PDH (P-PDHα1 (Ser293) CST #31866, 1:250 dilution), monoclonal antibody for PDK4 (Abcam Anti-PDK4 ab214938, 1:500 dilution) and monoclonal antibody for 4HNE (Abcam HNEJ-2 ab48506, 1:500 dilution).

After overnight incubation in primary antibodies, membranes were washed 3 times for 5 minutes in TBS-Tween and incubated for 1 hour at room temperature with the corresponding infrared fluorescent secondary antibody (LI-COR IRDye 680LT 925-68021 Goat anti-Rabbit, 1:20 000; 680RD 925-68070 Goat anti-Mouse, 1:20, 000). Images were then normalized to a whole membrane Amido Black total protein stain (A8181, Sigma).

Statistics

Results are expressed as mean ± SD. The level of significance was established at $p < 0.05$ for all statistics. The D'Agostino-Pearson omnibus normality test was first performed to determine whether data resembled a Gaussian distribution, and all data were subject to the ROUT test (Q=0.5%) to identify and exclude outliers which was a rare occurrence. When data fit normal distributions, standard one way and two-way ANOVAs were performed. When data did not fit a Gaussian distribution for analysis with one independent variable, the Kruskal-Wallis test was used. Moreover, when data did not fit a Gaussian distribution for analysis with two independent variables, data was first log transformed then analyzed using a standard two-way ANOVA (See **SFigure 7** for log transformed analysis of **Figure 4F, 5F, 6J and 6K**) but data was still presented in the Results as non-transformed data. Respective statistical tests are provided in figure legends. When significance was observed with an ANOVA, post-hoc analyses were performed with a two-stage set-up method of Benjamini, Krieger and Yekutieli for controlling false discovery rate (FDR) for multiple-group comparisons. With this method, all reported *p* values are FDR adjusted (traditionally termed "q"). All statistical analyses were performed in GraphPad Prism 10 (La Jolla, CA, USA).

The purpose of this study was to evaluate the effect of SkQ1 at both the Early-Stage and Late-Stage time points. Consequently, we have chosen to separate our statistical analysis by completing separate tests on Early- and Late-Stage timepoints but compared to a shared control group to reduce the number of mice used in this study in accordance with the Animal Care Committee. We did not analyze the impact of cancer over time (40Veh vs 80Veh comparisons) as this analysis has already been completed by our group in the past [273].

Results

SkQ1 administration in drinking water does not modulate mouse survival, body weight, fat weight, tumour weight, muscle wet weight or 4HNE protein adducts.

C57BL6J mice were injected at 10 and 16 weeks of age with 1 million EOC cells and treated with SkQ1 or Veh to develop Early-Stage (40Veh and 40 SkQ) and Late-Stage (80Veh and 80 SkQ) cancer timepoints **(Figure 6-1A)**. The Late-Stage timepoint was characterized by amount of time post-EOC inoculation (58-82 days), severe metastasis and extensive ascites **(Figure 6-1B and SFigure 6-1A)**, while the Early-Stage timepoint was characterized by time post-EOC inoculation (35-46 days) and no apparent metastasis or ascites **(SFigure 6-1A).** There were no statistical differences in Kaplan-Meier estimates of survival between 80SkQ and 80Veh treated mice **(Figure 6-1C)** and no statistical difference in the days alive post-EOC inoculation, suggesting SkQ1 did not improve survival **(Figure 6-1D)**. There were no differences in peak body weight between the CTRL group and Early-Stage mice as well as CTRL and Late-Stage mice **(Figure 6-1E).** Moreover, there were no differences in final body weight of CTRL vs Early-Stage mice, but there was a significant decrease in final body weight in Late-Stage mice compared to CTRL suggestive of cachexia development in Late-Stage mice **(Figure 6-1F).** There was a significant decrease in percent body weight change from peak body weight in both Early-Stage (-8% in 40Veh and -5% in 40SkQ) and Late-Stage mice (-33% in 80Veh and 80SkQ) compared to CTRL **(Figure 6-1G)**. Mice at the Early-Stage time point exhibited no changes in subcutaneous adipose mass in the inguinal fat pad compared to CTRL, but there were significant reductions in Late-Stage mice compared to CTRL **(Figure 6-1H).** There were also no statistical differences in estimated average daily food consumption in Early-Stage mice vs CTRL but interestingly, there was a trend in decreased food consumption between CTRL and Late-Stage mice **(*P* = 0.07; SFigure 6-1B)**, albeit

food consumption calculations were estimated as mice were group housed and food weights were taken once a week. Similarly, there were no changes in estimated daily water consumption in CTRL vs Early- or Late-Stage mice **(SFigure 6-1C).** There was a significant increase in primary ovarian tumour mass at both the Early-Stage and Late-Stage timepoints compared to CTRL **(Figure 6-1I),** but interestingly no differences in spleen mass (marker of inflammation) at the Early- and Late-Stage timepoints compared to CTRL **(SFigure 6-1D).** There were no reductions in hindlimb muscle wet weights in Early-Stage mcice compared to CTRL, but significant reductions in soleus (SOL), extensor digitorum longus (EDL), plantaris (PLT), tibialis anterior (TA), gastrocnemius (GA) and quadriceps (QUAD) skeletal muscle in Late-Stage mice compared to CTRL **(Figure 6-1J)**. We also evaluated volitional wheel running distance after 24 hours of exposure to a running wheel as an assessment of muscle disuse within the model and found no differences in CTRL vs Early-Stage mice **(SFigure 6-1E)**. We were unable to assess volitional wheel running in Late-Stage mice due to the inability to predict mouse survival 48 hours ahead of collection in an advanced cancer time point. We also measured 4HNE as a global marker of oxidative stress to identify a potential mechanism of decreased oxidative stress with SkQ1 treatment. Within the TA muscle, we found no changes in the protein content of 4HNE adducts in Early-Stage mice but perplexing found a decrease in Late-Stage mice vs CTRL **(Figure 6-1K)**. There were no differences in the protein content of 4HNE adducts in Early- and Late-Stage mice vs CTRL within the diaphragm **(Figure 6-1L).**

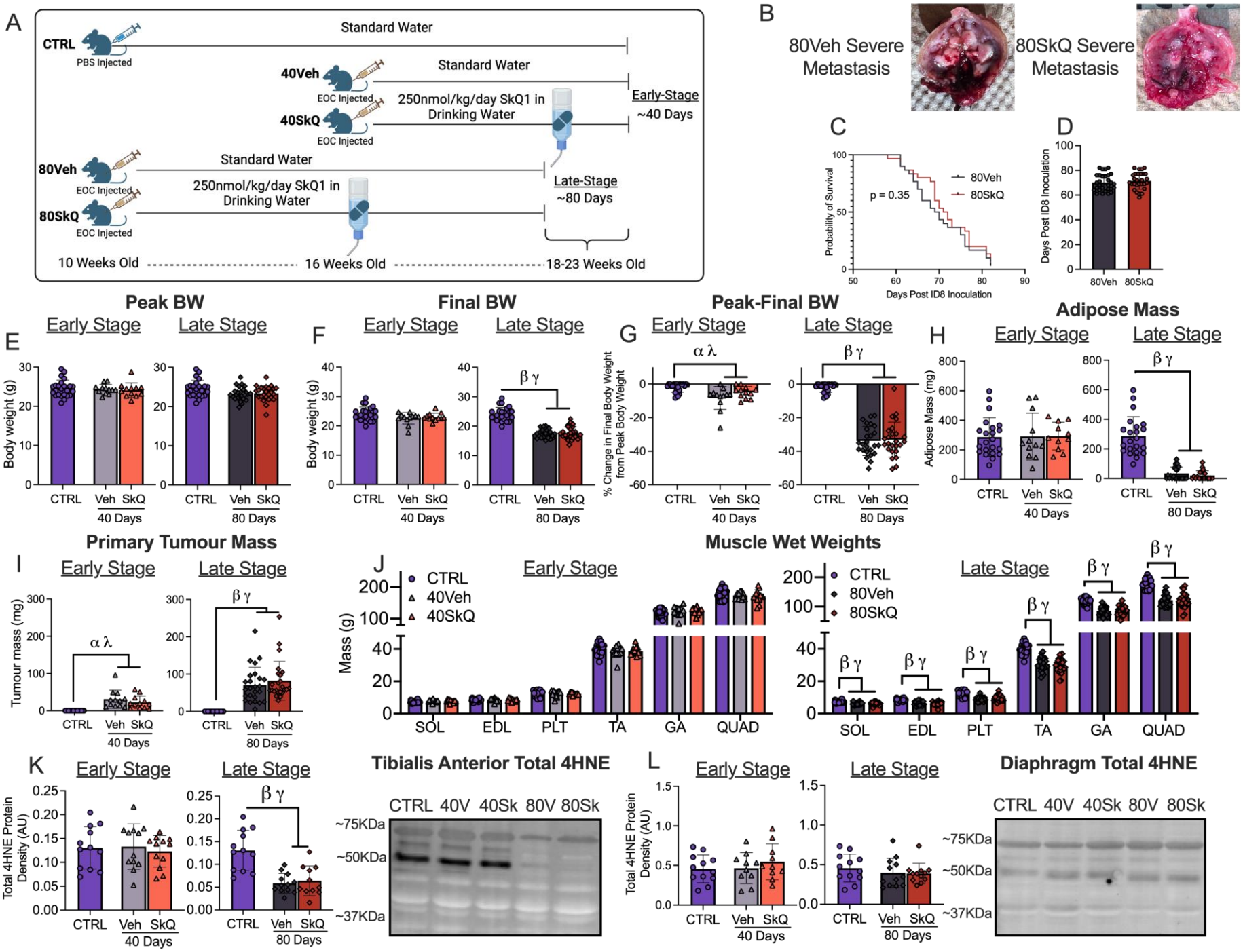
A
CTRL
PBS Injected
Standard Water
40Veh
EOC Injected
Standard Water
40SkQ
EOC Injected
250nmol/kg/day SkQ1 in Drinking Water
Early-Stage
~40 Days
80Veh
EOC Injected
Standard Water
80SkQ
EOC Injected
250nmol/kg/day SkQ1 in Drinking Water
Late-Stage
~80 Days
10 Weeks Old
16 Weeks Old
18-23 Weeks Old
B
80Veh Severe Metastasis
80SkQ Severe Metastasis
C
Probability of Survival
p = 0.35
80Veh
80SkQ
Days Post ID8 Inoculation
D
Days Post ID8 Inoculation
80Veh
80SkQ
Peak BW
Early Stage
Late Stage
E
Body weight (g)
CTRL
Veh
SkQ
40 Days
80 Days
Final BW
F
Body weight (g)
β γ
Peak-Final BW
G
% Change in Final Body Weight from Peak Body Weight
α λ
β γ
Adipose Mass
H
Adipose Mass (mg)
β γ
Primary Tumour Mass
I
Tumour mass (mg)
α λ
β γ
Muscle Wet Weights
J
CTRL
40Veh
40SkQ
80Veh
80SkQ
Mass (g)
SOL
EDL
PLT
TA
GA
QUAD
β γ
K
Total 4HNE Protein Density (AU)
Tibialis Anterior Total 4HNE
CTRL 40V 40Sk 80V 80Sk
~75KDa
~50KDa
~37KDa
L
Total 4HNE Protein Density (AU)
Diaphragm Total 4HNE
CTRL 40V 40Sk 80V 80Sk
~75KDa
~50KDa
~37KDa

Figure 6-1. SkQ1 treatment in drinking water does not change survivability, body weight loss, adipose mass, tumour mass, muscle wet weight or 4HNE formation at Early- or Late-stage tumour development in a metastatic ovarian cancer cachexia mouse model. 1 x 10^6 ID8 cells were injected underneath the ovarian bursa and developed for 35-46 or 58-82 days (Early-Stage and Late-Stage respectively). Mice at each time point were treated with standard drinking water (40Veh and 80Veh) or 250nmol/kg/day SkQ1 (40SkQ and 80SkQ). Control mice were injected with identical volumes of PBS and developed for 91-105 days (CTRL) **(A).** Metastasis is imaged in Late-Stage mice **(B)**. Kaplein-meier probability of survivability and days alive post cancer injection analysis (**C**, **D** n=30). Peak body weight (**E**, n=12-27, Final body weight (**F**, n=12-27) and percent change from peak to final body weight (**G**, n=12-27) was assessed. Subcutaneous adipose mass from the inguinal fat pad (**H**, n=11-23), primary ovarian tumours (**I**, n=12-25) and muscle wet weights (**J**, n=12-25) were also analyzed. Western blot assessment of 4HNE was assessed in the TA (**K**, n=11-12) and diaphragm (**L**, n=10-12). Figure C was analyzed with a Simple Survival Analysis (Kaplan-Meier) and Figure D with an unpaired T-Test. All other data was analyzed using a one-way ANOVA and followed by a two-stage step-up method of Benjamini, Krieger and Yukutieli multiple comparisons test. Data that was not normally distributed was analyzed with a Kruskal-Wallis test followed by the same post-hoc analysis. Control (CTRL), Early-Stage Vehicle (40Veh), Early-Stage SkQ1 (40SkQ), Late-Stage Vehicle (80Veh), Late-Stage SkQ1 (80SkQ), 4 hydroxynonenal (4HNE), Body weight (BW). Results represent mean ± SD. α P<0.05 CTRL Vs 40Veh; λ P<0.05 CTRL Vs 40SkQ; β P<0.05 CTRL Vs 80Veh; γ P<0.05 CTRL Vs 80SkQ.

SkQ1 administration in drinking water lowers mRNA expression of Atrogin, interleukin -6 (IL6) and tumour necrosis factor alpha (TNFα).

We also evaluated the mRNA expression of canonical markers of muscle atrophy and inflammation in the TA and diaphragm muscles at both cancer time points[42]. In the TA, there were no changes in mRNA expression of IL6 or TNFα at both timepoints **(Figure 6-2A & 6-2B)**. Interestingly, SkQ1 reduced cancer-induced increases in mRNA expression of Atrogin in Late-Stage cancer mice **(*P* = 0.05, Figure 6-2C)**, but did not reduce cancer-induced elevated levels of MURF1 **(Figure 6-2D).** In the diaphragm, SkQ1 reduced cancer-induced increases in IL6 mRNA expression in Early-Stage and Late-Stage mice **(*P* = 0.08, Figure 6-2E)**. Nor SkQ1 or EOC had an effect on Early-Stage mRNA expression of TNFα but SkQ1 reduced Late-Stage cancer induced increases in TNFα mRNA expression **(*P* = 0.07, Figure 6-2F)**. Atrogin mRNA expressions were unchanged at the Early-Stage time point but was interestingly decreased in 80Veh and 80 SkQ1 mice at the Late-Stage time point **(Figure 6-2G)**. Last, MURF1 mRNA expression was unchanged at the Early-Stage and Late-Stage time points **(Figure 6-2H)**.

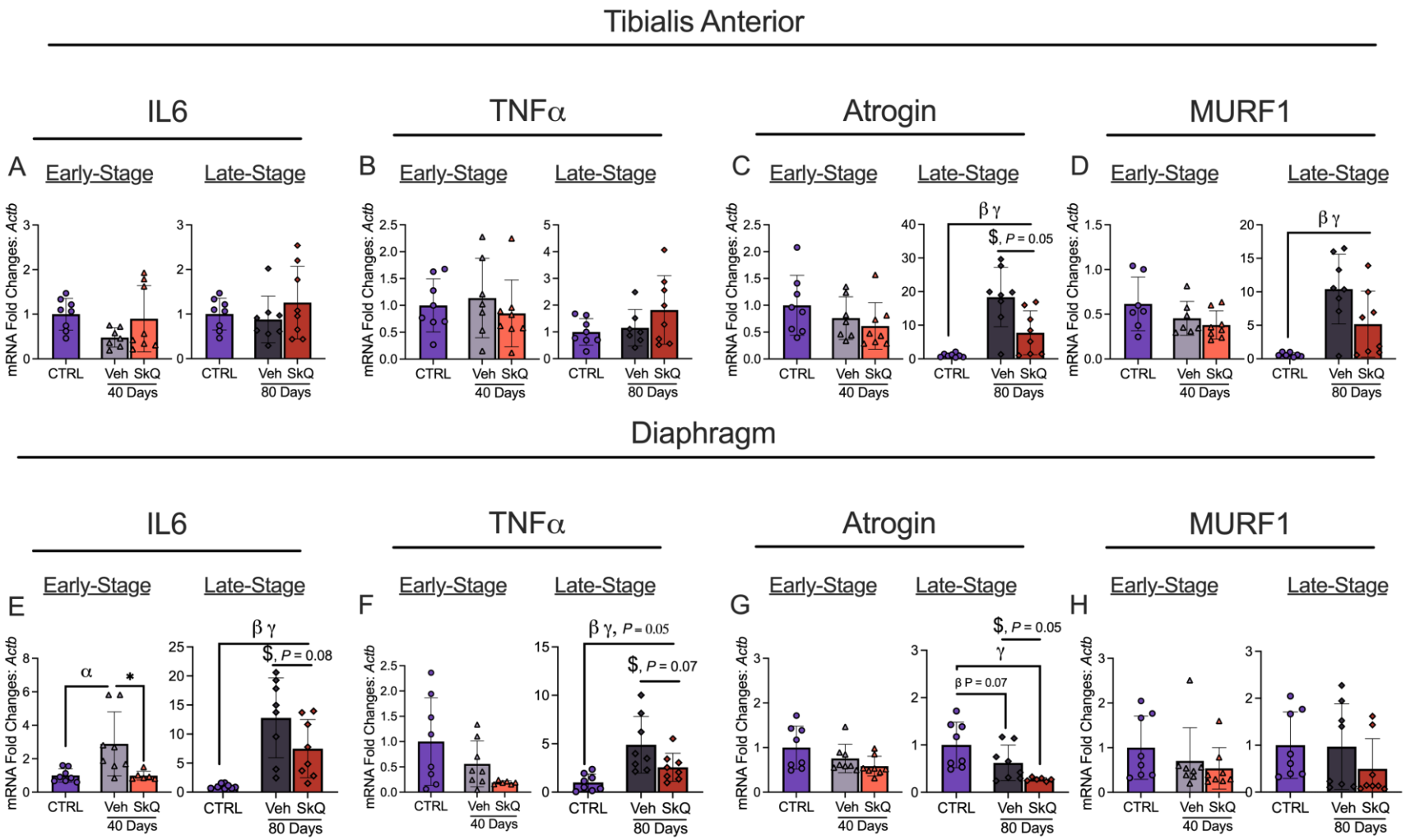

Figure 6-2. SkQ1 treatment in drinking water reduces Atrogin mRNA expression in tibialis anterior at Late-Stage tumour development and and IL-6 /TNFa mRNA expression in the diaphragm within a metastatic ovarian cancer cachexia mouse model. Analysis of mRNA expression fold changes in IL6, TNFα, Atrogin and MURF1 was completed in the TA in Early-Stage and Late-Stage mice (**A-D**, n=8). This was repeated in the diaphragm (**E-H**, n=8). All data was analyzed using a one-way ANOVA and followed by a two-stage step-up method of Benjamini, Krieger and Yukutieli multiple comparisons test. Data that was not normally distributed was analyzed with a Kruskal-Wallis test followed by the same post-hoc analysis. Control (CTRL), Early-Stage Vehicle (40Veh), Early-Stage SkQ1 (40SkQ), Late-Stage Vehicle (80Veh), Late-Stage SkQ1 (80SkQ), IL6 (Interleukin-6), TNF α (Tumour necrosis factor alpha), MURF1 (RING-finger protein-1), TA (tibialis anterior). Results represent mean ± SD. α P<0.05 CTRL Vs 40Veh; β P<0.05 CTRL Vs 80Veh; γ P<0.05 CTRL Vs 80SkQ, * P<0.05 40Veh Vs 40SkQ, $ P<0.05 80Veh Vs 80SkQ.

SkQ1 administration in drinking water attenuates Early-Stage cancer-induced muscle weakness in the TA but does not attenuate atrophy.

Muscle force production was decreased in 40Veh and 40SkQ mice compared to CTRL, however, 40SkQ mice exhibited increased force production relative to 40Veh mice **(Figure 6-3A & 6-3B)**. This suggests that SkQ1 treatment improved force production in the Early-Stage timepoint within the TA. There were no differences in rate of contraction and time to relaxation at 100Hz stimulation frequency in Early-Stage mice **(Figure 6-3C & 6-3D).** We were unable to collect force production at the Late-Stage time point as mice did not survive the *in-situ* force protocol due to their advanced illness from cancer. MHCIIa, MHCIIx and pooled fiber CSA were decreased in the 40Veh group compared to CTRL **(Figure 6-3E & 6-3F)**. This relationship was similar with SkQ1 treatment with the exception that 40SkQ mice did not exhibit a reduction in MHCIIa fibers CSA, suggesting that SkQ1 treatment attenuated Early-Stage MHCIIa fiber CSA. Nevertheless, this suggests that SkQ1 treatment improved force production without improving overall fiber CSA in the Early-Stage timepoint. Last, 80Veh and 80SkQ mice exhibited decreases in all MHC isoforms (MHCIIa, MHCIIx and MHCIIb) compared to CTRL, with no fiber CSA attenuation due to SkQ1 **(Figure 6-3G-I).**

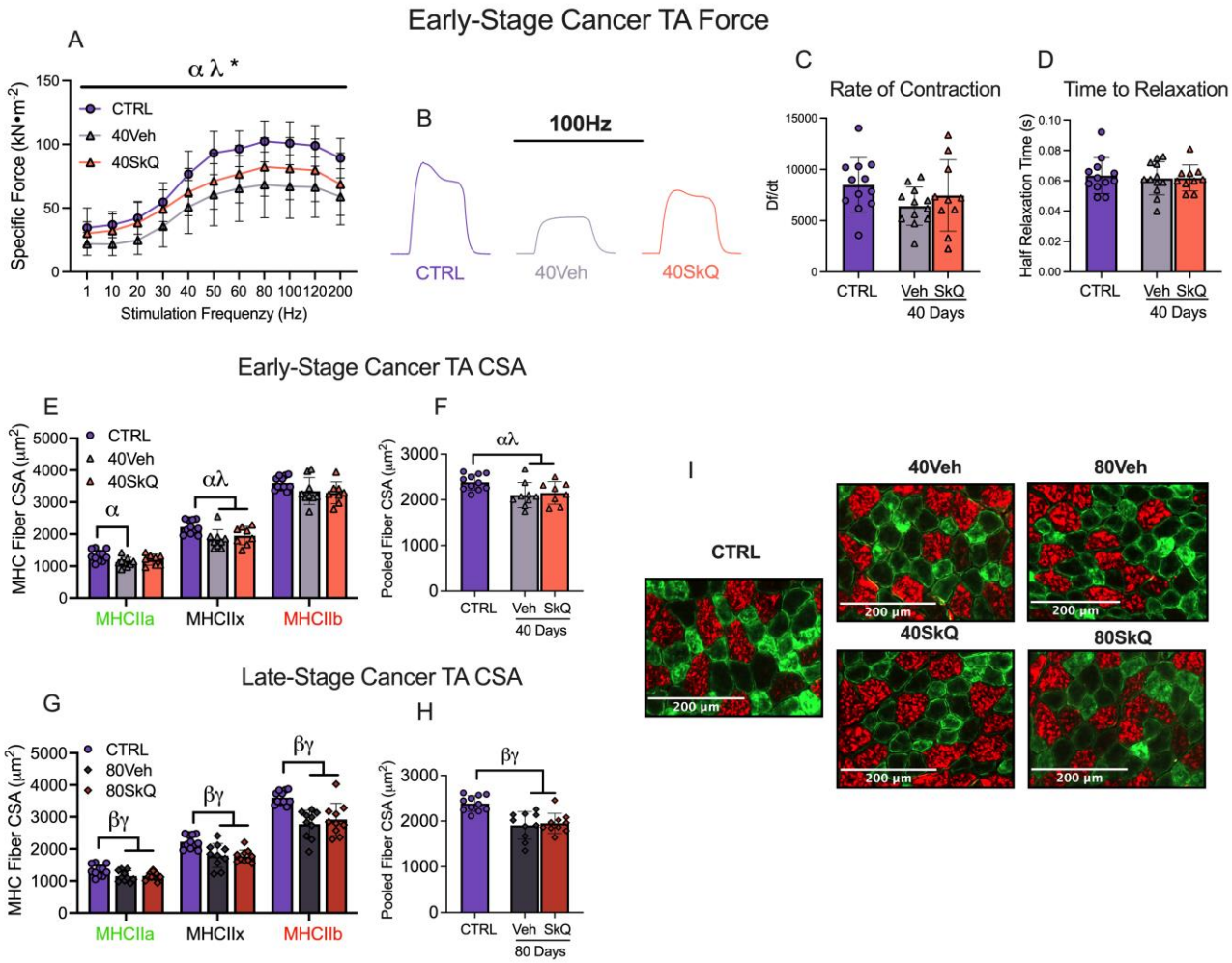

Figure 6-3. SkQ1 treatment in drinking water attenuates Early-Stage muscle weakness but does not change Early- or Late-Stage fiber cross-sectional area in tibialis anterior muscle in a metastatic ovarian cancer cachexia mouse model. In situ TA force production was assessed using the force-frequency relationship (**A** n=10-12; **B** representative twitches at 100Hz). Rate of twitch contraction along with the half relaxation time was also analyzed at 100Hz (**C, D** n=10-12). Analysis of fiber histology on MHC isoforms was performed in all groups. CSA of MHC isoforms were evaluated in the TA along with pooled fibers (**E-H**, n =8-11; **I** representative images at 20x magnification). A two-way ANOVA was used for figure A. All other data was analyzed using a one-way ANOVA and followed by a two-stage step-up method of Benjamini, Krieger and Yukutieli multiple comparisons test. Data that was not normally distributed was analyzed with a Kruskal-Wallis test followed by the same post-hoc analysis. Control (CTRL), Early-Stage Vehicle (40Veh), Early-Stage SkQ1 (40SkQ), Late-Stage Vehicle (80Veh), Late-Stage SkQ1 (80SkQ) CSA (cross-sectional area), MHC (myosin heavy chain), TA (tibialis anterior). Results represent mean ± SD. α P<0.05 CTRL Vs 40Veh; λ P<0.05 CTRL Vs 40SkQ; * P<0.05 40Veh Vs 40SkQ β P<0.05 CTRL Vs 80Veh; γ P<0.05 CTRL Vs 80SkQ.

SkQ1 administration in drinking water lowers Complex I-supported mH_2O_2 but also decreases Complex I-supported mitochondrial respiration.

Consider SkQ1 did not attenuate fiber CSA to improve force production, we evaluated mitochondrial respiration and mH_2O_2 within the TA to identify if mitochondrial bioenergetics is a mechanism by which SkQ1 improved force. Using permeabilized muscle fibers, we stimulated complex I-supported mH_2O_2 with forward electron transfer (pyruvate and malate) to generate NADH (Cadenas 1977) **(Figure 6-4A).** Substrate-specific maximal mH_2O_2 kinetics were followed by titration of ADP to determine the ability of ADP to attenuate mH_2O_2 during oxidative phosphorylation (State III). There were no differences in maximal mH_2O_2 emissions nor after the addition of ADP and after expressing the effect of ADP as a percentage of maximal mH_2O_2 emissions within the TA at the Early-Stage timepoint **(Figure 6-4B-D)**. At the Late-Stage timepoint, there was a significant decrease in maximal mH_2O_2 in 80Veh mice compared to CTRL but not in 80SkQ mice compared to CTRL **(Figure 6-4E).** Moreover, there was a significant increase in mH_2O_2 in 80Veh and 80SkQ mice compared to CTRL after titration of ADP suggestive of increased complex I-supported oxidative stress during oxidative phosphorylation at this timepoint **(Figure 6-4F)**. Interestingly, when ADP mH_2O_2 attenuation is expressed as a percentage of maximal mH_2O_2, 80SkQ mice exhibit decreases in mH_2O_2 compared to 80Veh mice **(Figure 6-4G)**. This suggests that 80SkQ mice exhibit decreased complex I-supported mH_2O_2 during oxidative phosphorylation and therefore decreased oxidative stress. Mitochondrial respiration was also assessed by stimulating complex I with NADH generated by pyruvate and malate across a range of ADP concentrations to challenge mitochondria over a spectrum of metabolic demands. The ADP titrations were repeated without (No Creatine) and with creatine (20mM Creatine) in the assay to model the two main theoretical mechanisms of high energy phosphate shuttling from the

mitochondria to the cytosol[80,184,185]. See *Delfinis et al. 2024* for mechanistic modeling and theoretical framework[273]. There were no differences in mitochondrial respiration in either creatine conditions within the Early-Stage time point **(Figure 6-4H & 6-4I).** This was consistent with pyruvate and malate in the absence of ADP (State II), glutamate (further NADH stimulation) and succinate (Complex II stimulation via $FADH_2$) supported mitochondrial respiration in the absence and presence of creatine **(SFigure 2A-2F)**. Within the Late-Stage timepoint, mitochondrial respiration was decreased in 80Veh mice compared to CTRL but perplexingly further decreased in 80SkQ mice **(Figure 6-4J and 6-4K).** Interestingly, this effect of SkQ1 seemed to be specific to pyruvate and malate supported mitochondrial respiration as other substrates did not show a further decrease of mitochondrial respiration with SkQ1 treatment **(SFigure 6-2A-F).** While perplexing, this may reflect a mitochondrial adaptation after prolonged exposure to SkQ1 (see discussion). Last, none of the changes in mitochondrial function were explained by mitochondrial protein content given there were no changes at all timepoints and conditions **(Figure 6-4L-N).**

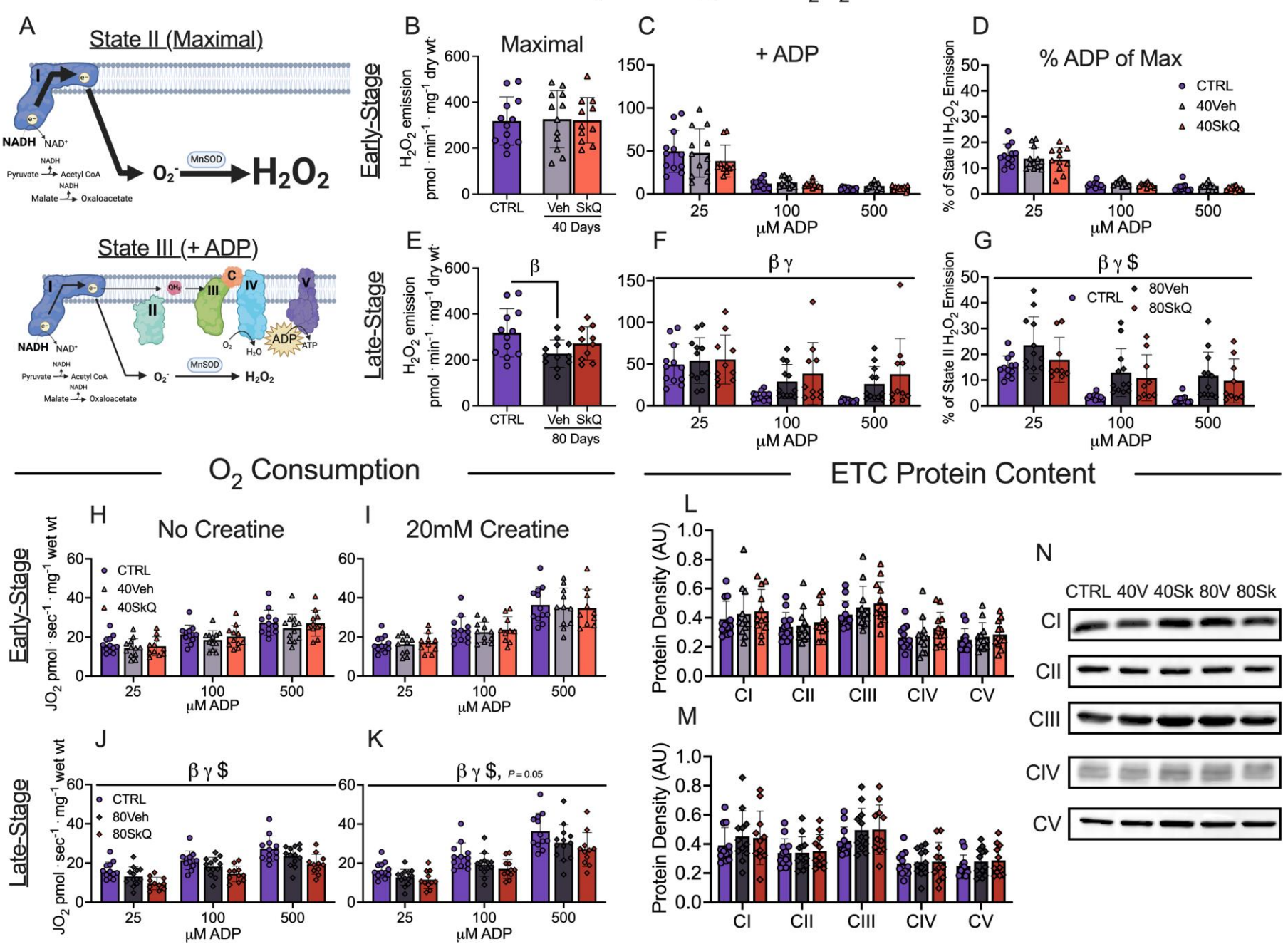
Tibialis Anterior: Complex I-Supported H2O2 Emission
A
State II (Maximal)
NADH
NAD+
Pyruvate
Acetyl CoA
Malate
Oxaloacetate
MnSOD
O2-
H2O2
State III (+ADP)
ADP
ATP
B
Maximal
Early-Stage
H2O2 emission
pmol · min-1 · mg-1 dry wt
CTRL
Veh
SkQ
40 Days
C
+ ADP
μM ADP
D
% ADP of Max
% of State II H2O2 Emission
CTRL
40Veh
40SkQ
E
β
Late-Stage
80 Days
F
β γ
G
β γ $
80Veh
80SkQ
O2 Consumption
H
No Creatine
I
20mM Creatine
JO2 pmol · sec-1 · mg-1 wet wt
J
β γ $
K
β γ $, P=0.05
ETC Protein Content
L
Protein Density (AU)
CI
CII
CIII
CIV
CV
M
N
CTRL 40V 40Sk 80V 80Sk

Figure 6-4. SkQ1 treatment in drinking water reduces Late-Stage Complex I stimulated H_2O_2 and, ADP-supported mitochondrial respiration in tibialis anterior muscle within a metastatic ovarian cancer cachexia mouse model. Complex I stimulated H_2O_2 is schematically depicted. (A). H_2O_2 emission was supported by pyruvate (10mM) and malate (2mM) to generate maximal rates and with ADP to assess H_2O_2 emission during OXPHOS. Maximal mitochondrial H_2O_2 along with the addition of ADP and an analysis of ADP's attenuating effects as a percentage of maximal H_2O_2 was assessed in Early-Stage mice permeabilized muscle fiber bundles (B-D). This was repeated in Late-Stage mice (E-G). ADP-stimulated respiration supported by pyruvate (5mM) and malate (2mM) generating NADH was also assessed in the absence (No Creatine) and presence (20mM Creatine) of creatine within permeabilized fiber bundles. Mitochondrial respiration was assessed at submaximal concentrations (25μM, 100μM and 500μM) (H-K). Protein contents of ETC subunits was also quantified within the TA (L-N). A two-way ANOVA was used for figures C, D, F, G, H-K. All data was analyzed using a one-way ANOVA and followed by a two-stage step-up method of Benjamini, Krieger and Yukutieli multiple comparisons test. Data that was not normally distributed was analyzed with a Kruskal-Wallis test followed by the same post-hoc analysis. Control (CTRL), Early-Stage Vehicle (40Veh), Early-Stage SkQ1 (40SkQ), Late-Stage Vehicle (80Veh), Late-Stage SkQ1 (80SkQ), electron transport chain (ETC). Results represent mean ± SD. n= 10-12. β P<0.05 CTRL Vs 80Veh; γ P<0.05; \$ P<0.05 80Veh Vs 80SkQ.

SkQ1 administration in drinking water attenuates Early- and Late-Stage cancer-induced muscle weakness but not atrophy in the diaphragm.

Muscle force production was decreased in 40Veh and 40SkQ mice compared to CTRL, however, 40SkQ mice exhibited increased force production relative to 40Veh mice **(Figure 6-5A & 6-5B)** similar to the TA. This also suggests that SkQ1 treatment improved force production in the Early-Stage timepoint within the diaphragm. There were no differences in rate of contraction and time to relaxation at 100Hz stimulation frequency between CTRL and 40Veh or 40SkQ **(Figure 6-5C & 6-5D).** This same relationship existed at the Late-Stage timepoint such that 80Veh mice exhibited decrease in muscle force production which was partially improved in 80SkQ mice with no changes in rate of contraction or time to relaxation at 100Hz stimulation frequency **(Figure 6-5E – 5H)**. There was no effect of SkQ1 on the development of fatigue at Early-Stage or Late-Stage cancer development within the diaphragm **(SFigure 6-3A and 6-3B)**. Similar to the TA, SkQ1 treatment did not change fiber CSA **(Figure 6-5I-M)**. Indeed, while muscle atrophy did not occur in Early-Stage mice but did occur in Late-Stage, SkQ1 treatment seemed to improve force production independent of fiber CSA.

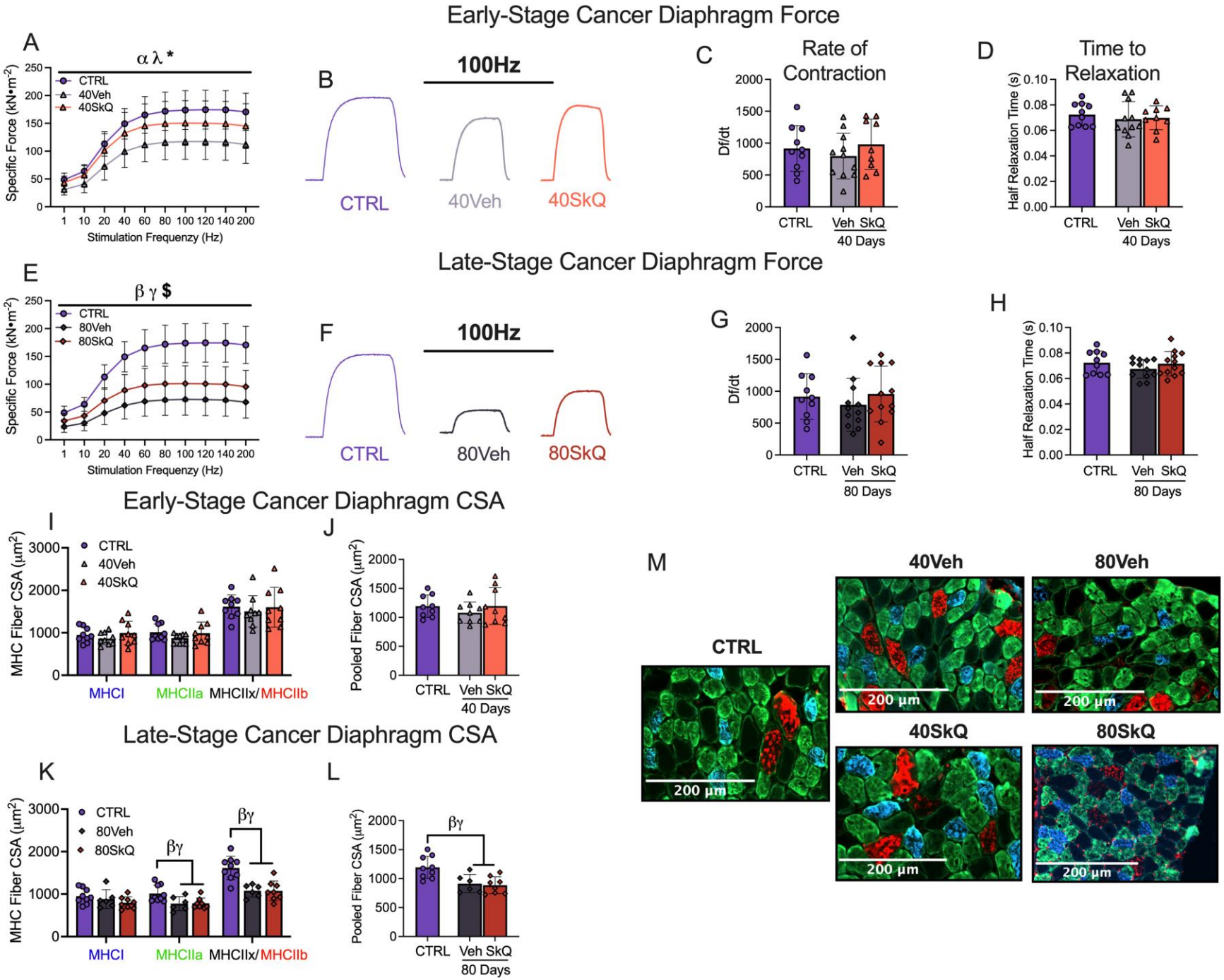
Early-Stage Cancer Diaphragm Force
A
α λ *
CTRL
40Veh
40SkQ
Specific Force (kN•m-2)
Stimulation Frequenzy (Hz)
B
100Hz
CTRL
40Veh
40SkQ
C
Rate of Contraction
Df/dt
CTRL
Veh SkQ
40 Days
D
Time to Relaxation
Half Relaxation Time (s)
CTRL
Veh SkQ
40 Days
Late-Stage Cancer Diaphragm Force
E
β γ $
CTRL
80Veh
80SkQ
Specific Force (kN•m-2)
Stimulation Frequenzy (Hz)
F
100Hz
CTRL
80Veh
80SkQ
G
Df/dt
CTRL
Veh SkQ
80 Days
H
Half Relaxation Time (s)
CTRL
Veh SkQ
80 Days
Early-Stage Cancer Diaphragm CSA
I
MHC Fiber CSA (μm2)
CTRL
40Veh
40SkQ
MHCI
MHCIIa
MHCIIx/MHCIIb
J
Pooled Fiber CSA (μm2)
CTRL
Veh SkQ
40 Days
Late-Stage Cancer Diaphragm CSA
K
MHC Fiber CSA (μm2)
CTRL
80Veh
80SkQ
βγ
βγ
MHCI
MHCIIa
MHCIIx/MHCIIb
L
Pooled Fiber CSA (μm2)
βγ
CTRL
Veh SkQ
80 Days
M
CTRL
40Veh
80Veh
40SkQ
80SkQ
200 μm

Figure 6-5. SkQ1 treatment in drinking water attenuates Early- and Late-stage muscle weakness but does not change Early- or Late-stage fiber cross-sectional area in diaphragm muscle in a metastatic ovarian cancer cachexia mouse model. In Vitro diaphragm force production was assessed using the force-frequency relationship (**A & E** n=9-12; **B & F** representative twitches at 100Hz). Rate of twitch contraction along with the half relaxation time was also analyzed at 100Hz (**C, D & G, H** n=10-12). Analysis of fiber histology on MHC isoforms was performed in all groups. CSA of MHC isoforms were evaluated in the diaphragm along with pooled fibers (**I-L**, n =6-9; **I** representative images at 20x magnification). A two-way ANOVA was used for figures A and E. All other data was analyzed using a one-way ANOVA and followed by a two-stage step-up method of Benjamini, Krieger and Yukutieli multiple comparisons test. Data that was not normally distributed was analyzed with a Kruskal-Wallis test followed by the same post-hoc analysis. Control (CTRL), Early-Stage Vehicle (40Veh), Early-Stage SkQ1 (40SkQ), Late-Stage Vehicle (80Veh), Late-Stage SkQ1 (80SkQ) CSA (cross-sectional area), MHC (myosin heavy chain). Results represent mean ± SD. α P<0.05 CTRL Vs 40Veh; λ P<0.05 CTRL Vs 40SkQ; * P<0.05 40Veh Vs 40SkQ β P<0.05 CTRL Vs 80Veh; γ P<0.05 CTRL Vs 80SkQ $ P<0.05 80Veh Vs 80SkQ.

SkQ1 administration in drinking water increases complex I-stimulated H_2O_2 production at Early- and Late-Stage cancer time points but attenuated cancer-induced reductions in Complex I protein content.

Similar to the TA, we evaluated mitochondrial bioenergetics to identify mechanisms of improved force production independent of atrophy. Complex I stimulated mH_2O_2 emission was completed in an identical paradigm as the TA **(Figure 6-6A)**. Interestingly, within the Early-Stage timepoint, maximal mH_2O_2 emissions and mH_2O_2 after the addition of ADP were unchanged in CTRL vs 40Veh and 40SkQ mice **(Figure 6-6B & 6-6C)**, however, mH_2O_2 emission were increased in 40SkQ mice when ADP mH_2O_2 attenuation was expressed as a percentage of maximal mH_2O_2 emissions **(Figure 6-6D).** This perplexingly suggests Complex I-supported mH_2O_2 emissions are increased with SkQ1 treatment at Early-Stages of cancer development. Moreover, within the Late-Stage timepoint, maximal mH_2O_2 emissions were unchanged but mH_2O_2 emissions during oxidative phosphorylation were increased in 80Veh mice and further increased in 80SkQ1 mice **(Figure 6-6E & 6-6F)**. This trend remained when ADP's attenuating effects were expressed as a percentage of maximal mH_2O_2 emissions **(Figure 6-6G).** There were no differences in mitochondrial respiration in either creatine conditions within the Early-Stage time point in the diaphragm **(Figure 6-6H & 6-6I).** This relationship was consistent across pyruvate & malate in the absence of ADP (State II), glutamate and succinate supported respiration **(SFigure 6-4A-F)**. Interestingly, pyruvate/malate supported, ADP-stimulated mitochondrial respiration was decreased at Late-Stages in 80Veh and 80SkQ mice compared to CTRL but marginally increased in 80SkQ mice compared to 80Veh mice within the 20mM Creatine condition **(Figure 6-6J & 6-6K)**. This marginal increase in mitochondrial respiration with SkQ1 was unique considering this trend did not exist with other substrates in either creatine conditions, albeit a slight improvement

in respiration was also observed with succinate in the presence of creatine **(SFigure 6-4A-F)**. Interestingly, these relationships could be explained at least in part by attenuated cancer-induced reductions Complex I mitochondrial protein content **(Figure 6-6L-M)**. Indeed, SkQ1 preserved Complex I protein content given 80Veh mice exhibited a decrease in protein content compared to CTRL mice but 80SkQ mice and CTRL mice Complex I protein content were not different. Interestingly, when complex I supported mH_2O_2 emissions were normalized to ETC Complex I protein content, the same relationships are seen in Early-Stage mice, but mH_2O_2 emissions remained increased in Late-Stage mice and now only a trend remains such that SkQ1 increased oxidative stress **(SFigure 6-5A & 6-5B)**. This suggests that increases in Complex I-supported mH_2O_2 could be explained at least in part by Complex I protein content.

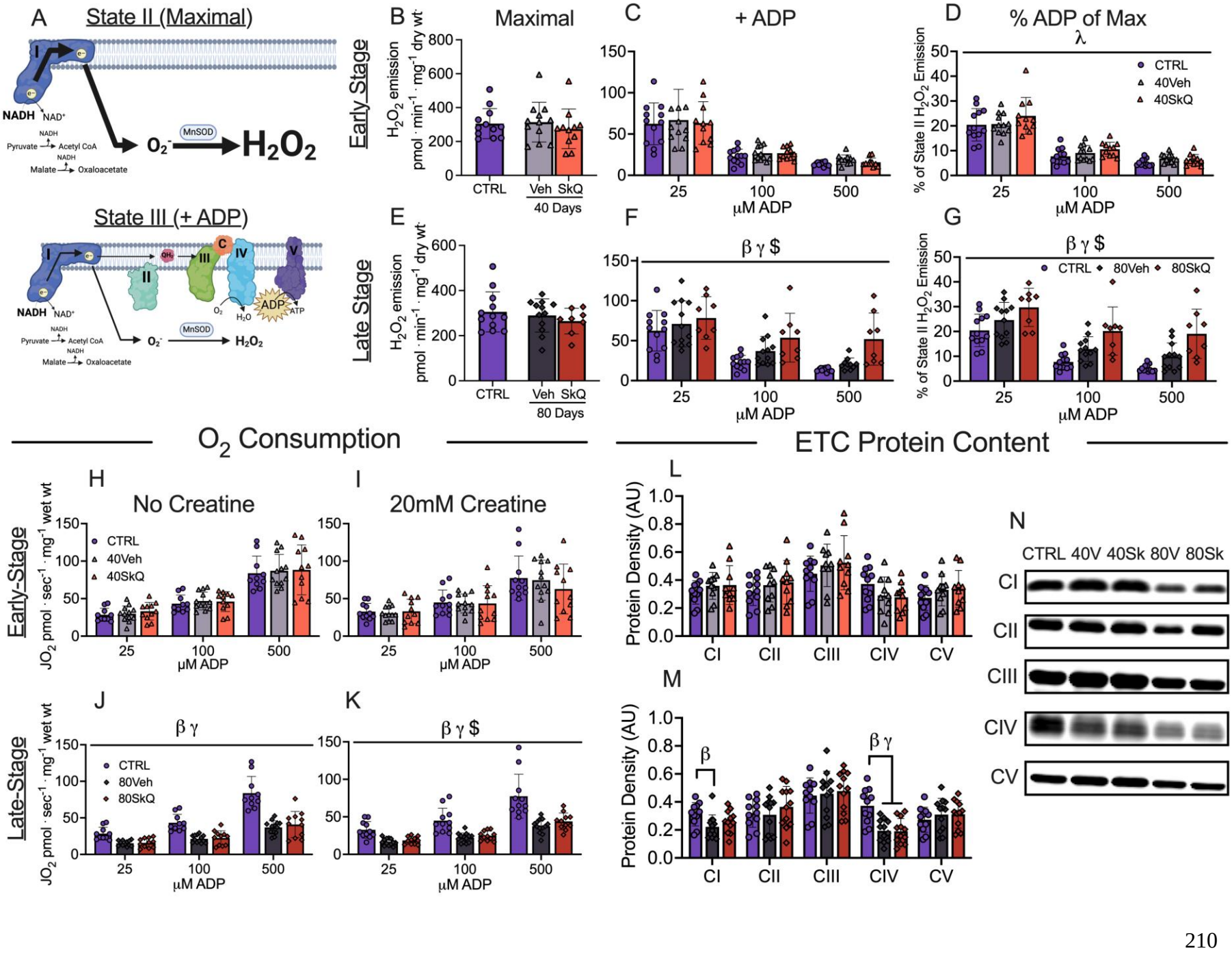
Diaphragm: Complex I-Supported H_2O_2 Emission
A
State II (Maximal)
NADH
NAD+
Pyruvate
Acetyl CoA
Malate
Oxaloacetate
MnSOD
O_2^-
H_2O_2
State III (+ ADP)
ADP
ATP
B
Maximal
C
+ ADP
D
% ADP of Max
Early Stage
H_2O_2 emission
pmol · min^{-1} · mg^{-1} dry wt
CTRL
Veh SkQ
40 Days
μM ADP
% of State II H_2O_2 Emission
CTRL
40Veh
40SkQ
E
F
G
Late Stage
80 Days
80Veh
80SkQ
O_2 Consumption
ETC Protein Content
H
No Creatine
I
20mM Creatine
Early-Stage
JO_2 pmol · sec^{-1} · mg^{-1} wet wt
J
K
Late-Stage
L
Protein Density (AU)
CI
CII
CIII
CIV
CV
M
N
CTRL 40V 40Sk 80V 80Sk

Figure 6-6. SkQ1 treatment in drinking water increases Late-Stage complex I stimulated H_2O_2 and, ADP-supported mitochondrial respiration in diaphragm muscle within a metastatic ovarian cancer cachexia mouse model. Complex I stimulated H_2O_2 is schematically depicted. (A). H_2O_2 emission was supported by pyruvate (10mM) and malate (2mM) to generate maximal rates and with ADP to assess H_2O_2 emission during OXPHOS. Maximal mitochondrial H_2O_2 along with the addition of ADP and an analysis of ADP's attenuating effects as a percentage of maximal H_2O_2 was assessed in Early-Stage mice permeabilized muscle fiber bundles (B-D). This was repeated in Late-Stage mice (E-G). ADP-stimulated respiration supported by pyruvate (5mM) and malate (2mM) generating NADH was also assessed in the absence (No Creatine) and presence (20mM Creatine) of creatine within permeabilized fiber bundles. Mitochondrial respiration was assessed at submaximal concentrations (25μM, 100μM and 500μM) (H-K). Protein contents of ETC subunits was also quantified within the diaphragm (L-N). A two-way ANOVA was used for figures C, D, F, G, H-K. All data was analyzed using a one-way ANOVA and followed by a two-stage step-up method of Benjamini, Krieger and Yukutieli multiple comparisons test. Data that was not normally distributed was analyzed with a Kruskal-Wallis test followed by the same post-hoc analysis. Control (CTRL), Early-Stage Vehicle (40Veh), Early-Stage SkQ1 (40SkQ), Late-Stage Vehicle (80Veh), Late-Stage SkQ1 (80SkQ), electron transport chain (ETC). Results represent mean ± SD. n= 10-12. β P<0.05 CTRL Vs 80Veh; γ P<0.05; \$ P<0.05 80Veh Vs 80SkQ.

SkQ1 administration in drinking water changes the phosphorylation status of pyruvate dehydrogenase (PDH) in the diaphragm.

Pyruvate entry into the mitochondria can be dictated by the phosphorylation status of PDH. Indeed, phosphorylation of PDH by pyruvate dehydrogenase kinase (PDK) -4 can inhibit PDH activity, disabling pyruvate entry into the mitochondria for further oxidation[182] **(Figure 6-7A)**. Protein content of PDH, phosphorylation of PDH at the serine 293 cite (P-PDH), ratio of P-PDH/PDH and PDK4 contents were unchanged within the TA in Early-Stage mice **(Figure 6-7B-E).** These results in the TA were the same in Late-Stage mice, with the exception of increased PDK-4 protein content in 80Veh and 80SkQ mice **(Figure 6-7F-I)**, which is consistent with the C26 model (pin bonetto 2019). Within the diaphragm in Early-Stage mice, PDH, P-PDH and P-PDH/PDH protein contents were unchanged compared to CTRL, however, PDK4 protein expression was increased in 40Veh and 40SkQ mice compared to CTRL **(Figure 6-7J-M).** Within the diaphragm in Late-Stage mice, there was decreased PDH protein content between 80Veh mice and CTRL **(*P* = 0.06, Figure 6-7N),** and no changes in P-PDH protein content between all groups **(Figure 6-7O)**. Interestingly, the ratio of P-PDH/PDH was increased in 80Veh mice vs both CTRL and 80SkQ mice suggesting there is pyruvate blockade into mitochondria in 80Veh mice that is somehow reversed with SkQ1 treatment **(*P* = 0.05, Figure 6-7P).** This could partially explain the increases in complex-I supported mH_2O_2 emissions within the diaphragm of 80SkQ mice. Indeed, an increased PDH phosphorylation status in 80Veh mice could theoretically decrease pyruvate entry into the cell at this time and therefore decrease mH_2O_2 emissions in permeabilized fibers. If 80Veh mice exhibit decreases in mH_2O_2 emissions due to PDH phosphorylation status but this is reversed in 80SkQ mice, then 80SkQ mice may exhibit increased mH_2O_2 emissions relative to 80Veh diaphragm

fibers. There were no differences in PDK4 content within the diaphragm in Late-Stage mice **(Figure 6-7Q)**. See **Figure 6-7R and 6-7S** for representative blots.

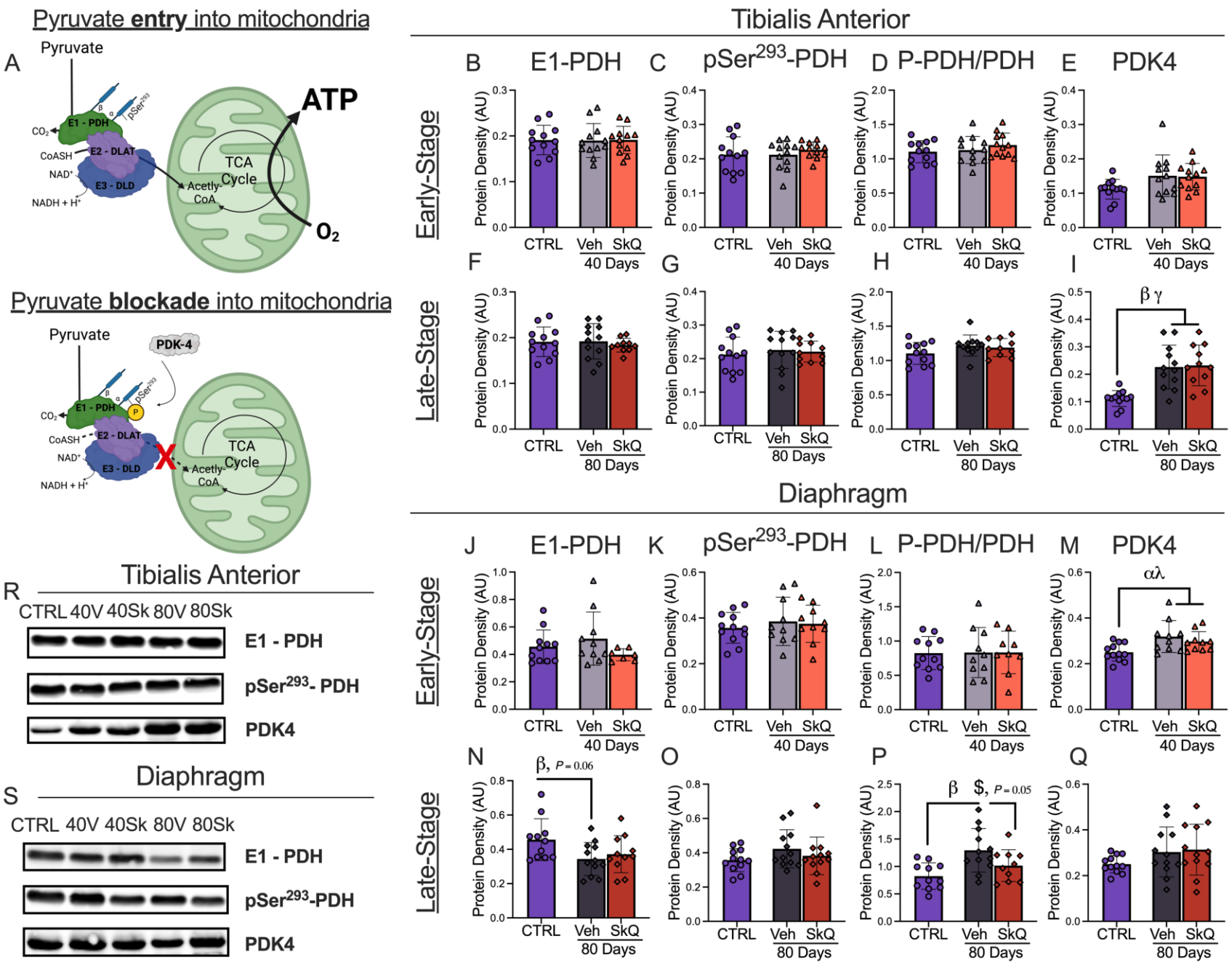
Pyruvate entry into mitochondria
A
Pyruvate
E1 - PDH
E2 - DLAT
E3 - DLD
CoASH
NAD+
NADH + H+
CO2
Acetyl-CoA
TCA Cycle
ATP
O2
Pyruvate blockade into mitochondria
PDK-4
Tibialis Anterior
R
CTRL 40V 40Sk 80V 80Sk
E1 - PDH
pSer293- PDH
PDK4
Diaphragm
S
CTRL 40V 40Sk 80V 80Sk
E1 - PDH
pSer293-PDH
PDK4
Tibialis Anterior
B E1-PDH
C pSer293-PDH
D P-PDH/PDH
E PDK4
Early-Stage
Late-Stage
Protein Density (AU)
CTRL
Veh
SkQ
40 Days
80 Days
F
G
H
I
β γ
Diaphragm
J E1-PDH
K pSer293-PDH
L P-PDH/PDH
M PDK4
αλ
N
O
P
Q
β, P = 0.06
β $, P = 0.05

Figure 6-7. SkQ1 treatment in drinking water modulates phosphorylation status of pyruvate dehydrogenase in the diaphragm within a metastatic ovarian cancer cachexia mouse model. Theoretical schematic representation of pyruvate entry into mitochondria is depicted **(A)**. Protein contents of E1-PDH, P-PDH (Ser293), P-PDH/PDH and PDK4 were quantified in TA of Early- and Late-Stage mice (**B-I**, n=10-12). This was repeated in the diaphragm (**J-Q**, n=10-12). Representative blots (**R** and **S**). All data was analyzed using a one-way ANOVA and followed by a two-stage step-up method of Benjamini, Krieger and Yukutieli multiple comparisons test. Data that was not normally distributed was analyzed with a Kruskal-Wallis test followed by the same post-hoc analysis. Control (CTRL), Early-Stage Vehicle (40Veh), Early-Stage SkQ1 (40SkQ), Late-Stage Vehicle (80Veh), Late-Stage SkQ1 (80SkQ), Pyruvate dehydrogenase (PDH), Pyruvate dehydrogenase kinase (PDK). Results represent mean ± SD. α P<0.05 CTRL Vs 40Veh; λ P<0.05 CTRL Vs 40SkQ; * P<0.05 40Veh Vs 40SkQ β P<0.05 CTRL Vs 80Veh; γ P<0.05 CTRL Vs 80SkQ $ P<0.05 80Veh Vs 80SkQ.

SkQ1 administration in the drinking water improves high-force cancer-induced muscle weakness and single fiber myoplasmic calcium concentrations in the FDB.

To further explore mechanisms of improved force production with SkQ1, we next evaluated *in-vitro* whole FDB muscle force production and single fiber myoplasmic calcium concentrations in Early-Stage and Late-Stage mice. Completing this calcium analysis in diaphragm and TA single muscle fibers would have been ideal, however, this experimental technique has been previously optimized within the FDB and thus was used for this investigation[276]. Interestingly, FDB muscle did not exhibit muscle weakness in Early-Stage mice across all frequencies, however, single fiber myoplasmic calcium concentrations was decreased in 40Veh and 40SkQ mice compared to CTRL **(Figure 6-8A & 6-8B)** suggesting disruptions to calcium handling occur in early cancer myopathy. While there was an increase trend in tetanic $[Ca^{2+}]_i$ in 40SkQ mice vs 40Veh across all frequencies **(*P* =0.08, Figure 6-8B)**, high-frequency stimulation analysis demonstrates no muscle weakness, decreases in tetanic $[Ca^{2+}]_i$ within 40Veh and 40SkQ mice compared to CTRL and no changes due to SkQ1 administration **(Figure 6-8C & 6-8D)**. No muscle weakness existed in the FDB across all frequencies in Late-Stage mice, however, decreases in cancer-induced tetanic $[Ca^{2+}]_i$ in 80Veh vs CTRL were partially improved with SkQ1 treatment such that 80SkQ mice exhibited increases in tetanic $[Ca^{2+}]_i$ compared to 80Veh **(Figure 6-8E & 6-8F)**. Interestingly, high-frequency analysis demonstrates decreased FDB force production in 80Veh vs CTRL mice but not 80SkQ mice, such that 80SkQ mice exhibited increases in force production compared to 80Veh **(*P* =0.05, Figure 6-8G)**. Moreover, high-frequency stimulation analysis also demonstrates SkQ1 improves cancer-induced decreases in single fiber myoplasmic calcium concentrations such that 80SkQ mice exhibited increased tetanic $[Ca^{2+}]_i$ compared to 80Veh. Therefore, this could suggest that improvements in muscle force production due to SkQ1 are coupled to improvements in calcium

handling. Results were similar in the context of fatigue within the FDB. Indeed, SkQ1 treatment actually improved cancer-induced fatigue at Early-Stage within 40SkQ mice compared to 40Veh mice but did not increase single fiber myoplasmic calcium concentrations throughout the fatigue protocol **(SFigure 6-6A & 6-6B).** Interestingly, SkQ1 treatment at Late-Stage also improved cancer-induced fatigue but this was also interestingly coupled to improvements in single fiber myoplasmic calcium concentrations throughout the fatigue protocol **(SFigure 6-6C & 6-6D).**

Flexor Digitorum Brevis: Early-Stage Cancer

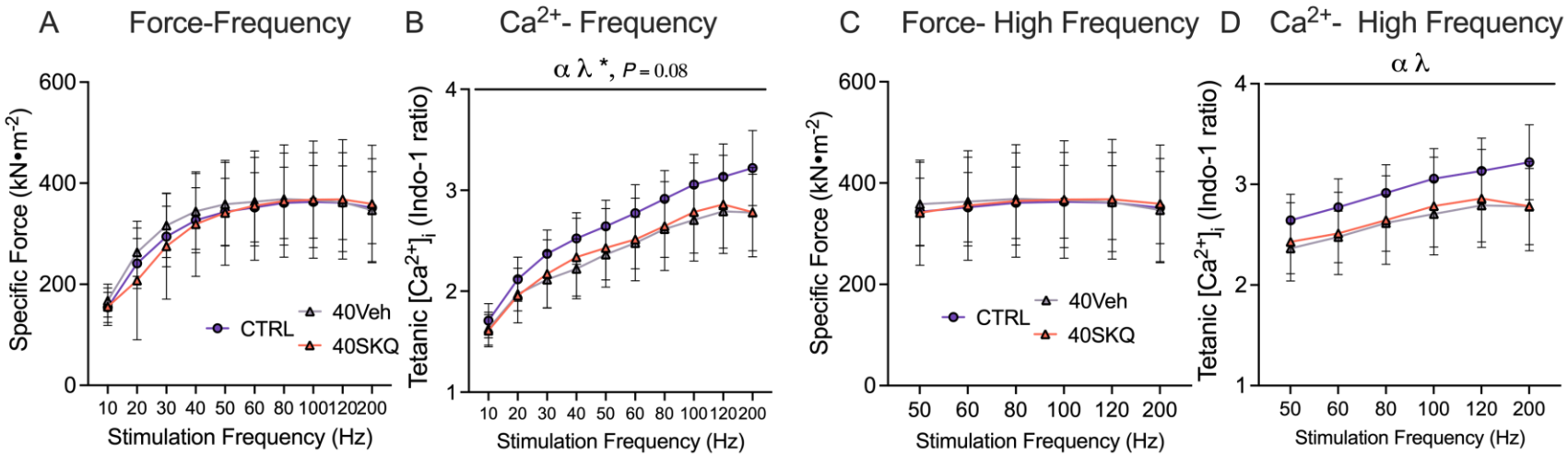

Flexor Digitorum Brevis: Late-Stage Cancer

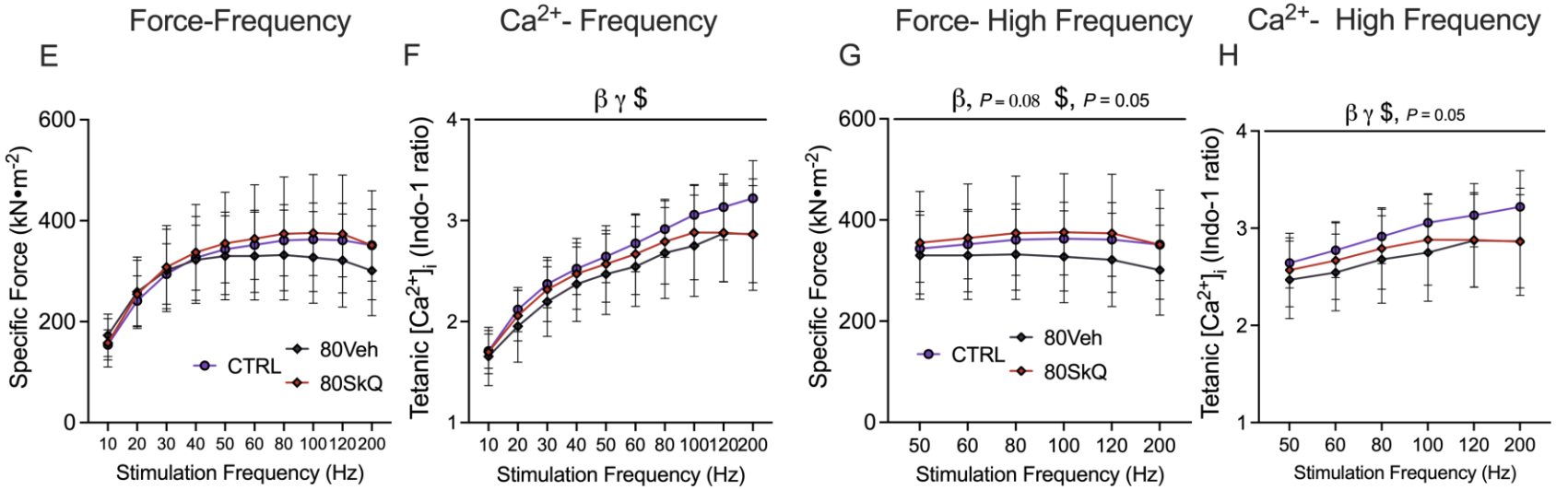

Figure 6-8. SkQ1 treatment in drinking water increases single fiber myoplasmic calcium concentrations and force production in the flexor digitorum brevis within a metastatic ovarian cancer cachexia mouse model. In Early-Stage mice, in-vitro FDB force production was assessed using the force-frequency relationship (A, n =6-10). Myoplasmic calcium as assessed using tetanic $[Ca^{2+}]_i$ across a range of frequencies (B, n=17-20), This analysis was repeated but only evaluating high-stimulation frequencies (C, D). All analysis was repeated in Late-Stage mice (E-H, n=8-17). A two-way ANOVA was used for all figures followed by a two-stage step-up method of Benjamini, Krieger and Yukutieli multiple comparisons test. $[Ca^{2+}]_i$ (intracellular calcium), Control (CTRL), Early-Stage Vehicle (40Veh), Early-Stage SkQ1 (40SkQ), Late-Stage Vehicle (80Veh), Late-Stage SkQ1 (80SkQ). Results represent mean ± SD. α P<0.05 CTRL Vs 40Veh; λ P<0.05 CTRL Vs 40SkQ; * P<0.05 40Veh Vs 40SkQ β P<0.05 CTRL Vs 80Veh; γ P<0.05 CTRL Vs 80SkQ $ P<0.05 80Veh Vs 80SkQ.

Discussion

We have recently shown that mitochondrial stress is associated with muscle weakness in the C26-ectopic and EOC-orthotopic cancer models[237,273]. Within these studies, we also identified atrophy-independent contributions to muscle weakness exist in cancer irrespective of the well-established atrophy-dependent mechanisms to muscle weakness[237,273]. While our past work identifies mitochondrial-associations to atrophy-independent muscle weakness in cancer myopathy, the purpose of the current investigation was to use the mitochondrial targeted-antioxidant SkQ1 to establish a direct link between mitochondria and weakness in cancer. To our knowledge, this is the first study to identify a causal relationship between mitochondria and cancer-induced muscle weakness independent of atrophy. In addition, dozens of clinical investigations have yielded insufficiently positive results to produce a licensed therapy for cancer cachexia[5] and experts believe that usage of orthotopic and metastatic models of cancer cachexia could aid in the pursuit of therapy development[13]. This study is also the first to explore the efficacy of mitochondrial-targeted therapy in an orthotopic model of cancer cachexia that demonstrates improved skeletal muscle function but not mass. Collectively, these results support the further exploration of mitochondrial therapies in preclinical models of cancer cachexia due to its beneficial impact on muscle weakness. Future studies could explore SkQ1 in conjunction with exercise as part of a multi-modal approach – as done in current clinical trials (MECAC Study[279]) – to further enhance skeletal muscle health outcomes within this disease.

SkQ1 administration improves force production potentially through modulated calcium handling

We found that SkQ1 administration increased force production within the TA, diaphragm and partially in the FDB. While the mitochondrial therapeutic SS-31 has been previously shown to

improve force production within the diaphragm of C26-ectopic tumour bearing mice, SS-31 also protected skeletal muscle fiber CSA[139]. It thus remains unclear if SS-31 improved force production or simply protected muscle mass, which, consequently improved force producing capabilities in C26 tumour bearing mice. In the current investigation, SkQ1 improves force production without protecting muscle CSA within the TA and diaphragm, thus establishing a direct relationship between mitochondria and muscle weakness in cancer myopathy. Interestingly, SkQ1 administration improved force production in the diaphragm of Early-Stage tumour bearing mice at a time when atrophy was not evident. This study thus establishes a direct link between mitochondrial oxidative stress and atrophy-independent skeletal muscle weakness in cancer myopathy.

While the exact mechanism by which SkQ1 improves force production remains unclear, we demonstrate that SkQ1 increases cancer-induced reductions in myoplasmic calcium concentrations at the single fiber level within the FDB. Interestingly, increases in single fiber myoplasmic calcium were coupled to SkQ1-induced improvements in force production, albeit only at high stimulation frequencies. This suggests that mitochondrial antioxidants can improve calcium handling in cancer myopathy. Literature on calcium release and mitochondrial antioxidants is limited, however, one studied identifies SS-31 administration *in-vitro* interestingly restores fatigue-induced decreases in sarcoplasmic reticulum calcium release but does not improve force recovery[280]. This study supports the current proposal that SkQ1 can increase myoplasmic calcium, albeit still through an unknown mechanism. Interestingly, calcium leak from ryanodine receptor 1(RyR1) channels are identified as a mechanism of muscle weakness within ageing[223]. Indeed, RyR1s are shown to be oxidized, cysteine-nitrosylated and depleted of callstabin1 – a channel stabilizing subunit – which is shown to directly induce muscle weakness[223]. Interestingly, aged MCat mice (mice with

overexpression of the human catalase gene to increase mitochondrial antioxidant activity) demonstrated less oxidation and improved calcium release properties of RyR1 which then directly improved muscle function[281]. While speculative, this a potential mechanism by which an antioxidant drug like SkQ1 could improve calcium release and thus muscle weakness in cancer. There is no evidence within the current study to suggest RyR1s are the source of muscle weakness in cancer myopathy, however, future literature could investigate the antioxidant effects of SkQ1 on RyR1 in cancer progression to identify a potential mechanism for improved calcium release and consequential muscle force production.

SkQ1 administration exhibits muscle-specific effects on mitochondrial bioenergetics

Our results demonstrate the effects of SkQ1 on mitochondrial bioenergetics to be heterogenous between the TA and diaphragm. While this is to be expected as we have previously published time-dependent and muscle-specific responses to cancer myopathy in both the C26 and EOC cachexia models[237,273], the divergent impact of SkQ1 on Complex I-mH_2O_2 emissions and respiration remains perplexing.

First, while we found SkQ1 lowered Complex I-mH_2O_2 emissions in the TA of Late-Stage mice, SkQ1 also seemed to decrease pyruvate/malate supported respiration. We first evaluated the protein content of mitochondrial electron transport chain (ETC) protein content to identify if changes in function were related to protein content and found no differences between vehicle and SkQ1 treated mice in the TA. We then evaluated the phosphorylation state of PDH to identify if SkQ1 administration induced a blockade of pyruvate entry into mitochondria due to increased PDH phosphorylation. This also yielded no differences between vehicle and SkQ1 treated mice in the TA. Thus, it is currently unclear within the current study why SkQ1 could have decreased

mitochondrial respiration, however, we speculate that this could be a mitochondrial adaptation related to mitochondrial membrane potential. Indeed, there is some data to suggest that cationic plastoquinone derivatives (SkQs) contain uncoupling properties[189,282]. If SkQ1 induces mild uncoupling during prolonged administration *in-vivo*, then this could theoretically induce a mitochondrial adaptation that lowers ATP producing capabilities due to decreased membrane potential. While it would still remain trivial as to why this would only occur within the TA and not the diaphragm, future work could measure mitochondrial membrane potential to better explore this relationship.

Second, we found SkQ1 raised Complex I-mH_2O_2 emissions in Early-Stage and Late-Stage tumour bearing mice. Similar to the TA, we measured mitochondrial ETC protein content and PDH phosphorylation status to evaluate if protein content or pyruvate blockade into mitochondria governs these perplexing SkQ1-induced increases in mH_2O_2. Interestingly, in Late-Stage mice, SkQ1 attenuated Complex I protein content. We therefore normalized mH_2O_2 emissions to complex I protein content in addition to the fiber bundle weight used in the experimental set-up and found only a statistical trend remained such that mH_2O_2 emissions were increased in 80SkQ mice. This suggests that attenuated Complex I protein content can partly explain this SkQ1-induced increase in mH_2O_2 emissions. Moreover, we also found that cancer-induced increases in the phosphorylation status of diaphragm was reversed with SkQ1 treatment in Late-Stage. Therefore, pyruvate entry into the cell is potentially blocked to some effect in 80Veh mice but not 80SkQ. Thus, this theoretically suggests that more pyruvate can enter the cell in the 80SkQ permeabilized muscle fiber bundles compared to 80Veh which could, in turn, lead to more mH_2O_2 emissions. Therefore, both attenuated Complex I protein content in addition to the phosphorylation state of PDH could partially explain how SkQ1 increased mH_2O_2 emissions at Late-Stages.

Nevertheless, it remains unknown as to how SkQ1 could increase mH_2O_2 emissions in Early-Stages mice and future work could evaluate if this is another example of a mitochondrial adaptation to SkQ1.

We also measured 4HNE protein adducts to evaluate if SkQ1 lowered global oxidative stress. We found no cancer-induced increases in 4HNE and therefore no SkQ1-induced reductions in the TA and diaphragm. In fact, we interestingly found a reduction in 4HNE protein adducts in the TA of Late-Stage mice compared to CTRL. To our knowledge, only the Yoshida AH-130 hepatoma tumour bearing rat model has shown increases in 4HNE protein adducts within cancer myopathy[195]. Thus, this could be a reflection of the diversity between cancer cachexia models. Future work should look at more markers of oxidative stress to evaluate a mechanism by which SkQ1 lowers oxidative stress in cancer cachexia.

SkQ1 treatment attenuates mRNA expression of some atrogenes and cytokines

The current investigation identifies that SkQ1 lowers mRNA expression of Atrogin within the TA and IL-6 in addition to TNFα within the diaphragm. A similar relationship has actually been shown with SS-31. Indeed, SS-31 has been previously shown to attenuate C26 cancer-induced increases in mRNA expression of MURF1 within the diaphragm and plasma levels of TNFα[139]. Thus, mitochondrial antioxidants have been previously shown to have anti-inflammatory properties throughout cancer myopathy. Interestingly, however, the current investigation identifies decreases in mRNA expression of Atrogin, but no attenuation in muscle atrophy while SS-31 demonstrates a coupling between attenuated mRNA expression of E3 ligases and skeletal muscle CSA[139]. This could be a reflection of the complexity of metastatic models of cancer cachexia vs ectopic models in the context of muscle mass regulation. This could also suggest other mechanisms in addition to

E3 ligases govern skeletal muscle atrophy within this model of cancer cachexia like autophagy or cell death, as been reported in other cancer models [59,66].

Perspectives and Conclusions

The current investigation demonstrates an improvement in muscle force production within several muscles during cancer myopathy. While exploring the efficacy of SkQ1 as a cancer cachexia therapeutic in an ovarian cancer yielded no improvements in muscle mass or delay to the onset of cachexia, SkQ1 could still potentially be used in combination with exercise to improve muscle health outcomes. Indeed, exercise has been shown to improve patient health-related quality of life[16], improve skeletal muscle health outcomes in preclinical cancer models[17] and even potentially exhibit anti-tumorigenic effects[19]. Thus, if SkQ1 improves skeletal muscle weakness - especially early in cancer-induced skeletal muscle myopathy - then this therapeutic intervention supports further exploration in exercise tolerance and adherence in cancer patients due to potential increased exercise capacity. By improving exercise tolerance and adherence in cancer, this could lead to further improved patient-related quality of life by better maintaining skeletal muscle mass. It should also be emphasized that SkQ1 contains triphenylphosphonium (TPP) conjugated to an antioxidant. Some research groups have utilized a TPP vehicle group to delineate the effects of the mitochondrial antioxidant versus TPP on tumour bearing mice[140]. While this is a necessary control group, these investigations showed marginal effects of TPP alone and therefore have been excluded from the study design[140].

In conclusion, the current investigation is the first to our knowledge to establish a direct link between mitochondria and muscle weakness in cancer-induced myopathy. In addition, this study is also the first to establish a direct link between mitochondrial oxidative stress and atrophy-

independent weakness, at least in the TA. While the precise mechanisms as to how SkQ1 administration improves muscle force production in ovarian cancer remains elusive, improved myoplasmic calcium content is identified as a potential indirect mechanism. This study supports the further exploration of mitochondrial targeted therapeutics in cancer cachexia.

Supplementary Data

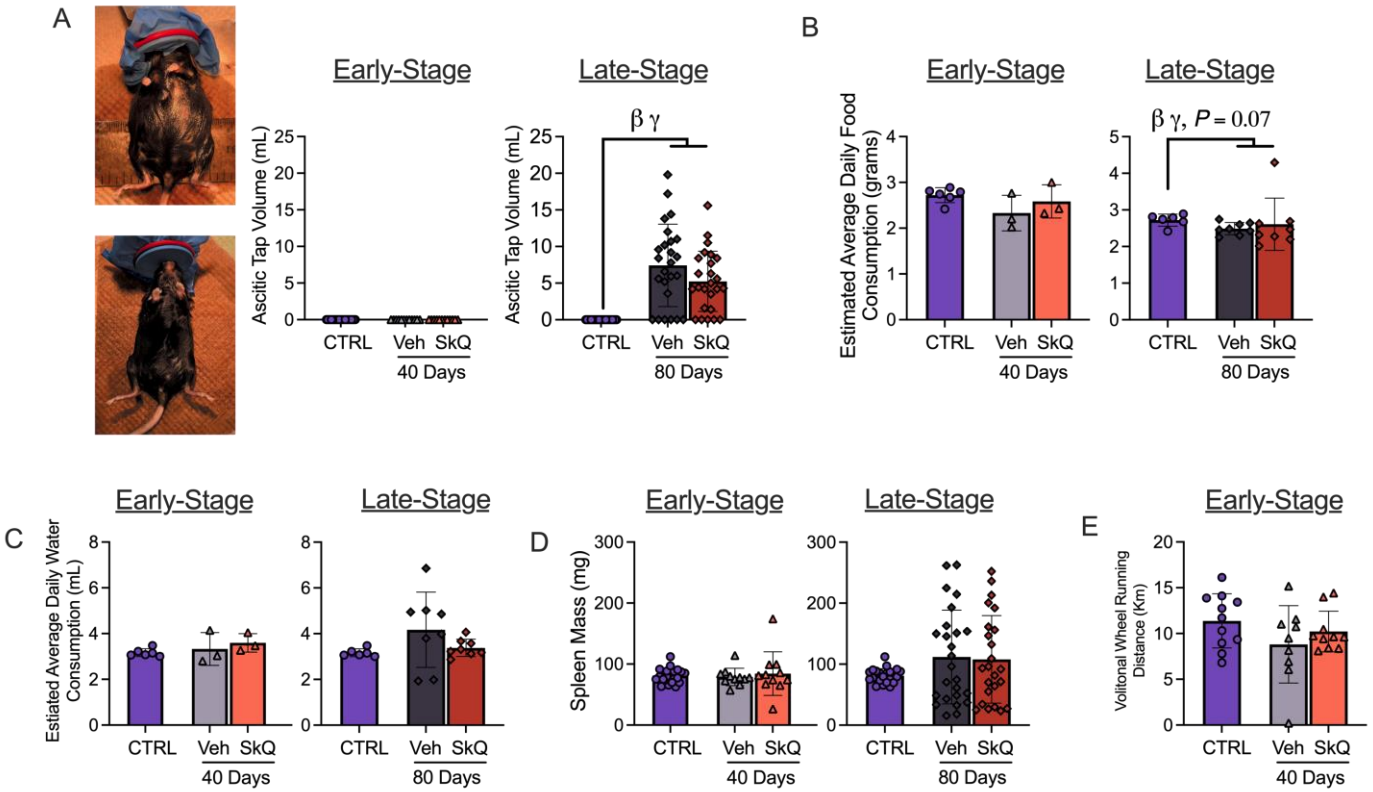

SFigure 6-1. Effects of SkQ1 on ascitic volume, estimated daily food intake, estimated daily water intake, spleen mass and volitional wheel running. Mice were tapped to prolong their survival (A, n=24-25). Daily food intake was estimated as food weights were taken once a week and then divided by the number of mice in the cage and days since last food weight (B, n=3-8). This was repeated for estimated average daily water intake (C, n=3-8). Spleen mass (D, n=12-25) and volitional wheel running after 24 hours of exposure to a running wheel was also analyzed (E, n=9-12). All data was analyzed using a one-way ANOVA and followed by a two-stage step-up method of Benjamini, Krieger and Yukutieli multiple comparisons test. Data that was not normally distributed was analyzed with a Kruskal-Wallis test followed by the same post-hoc analysis. Control (CTRL), Early-Stage Vehicle (40Veh), Early-Stage SkQ1 (40SkQ), Late-Stage Vehicle (80Veh), Late-Stage SkQ1 (80SkQ). Results represent mean ± SD. β P<0.05 CTRL Vs 80Veh; γ P<0.05 CTRL Vs 80SkQ.

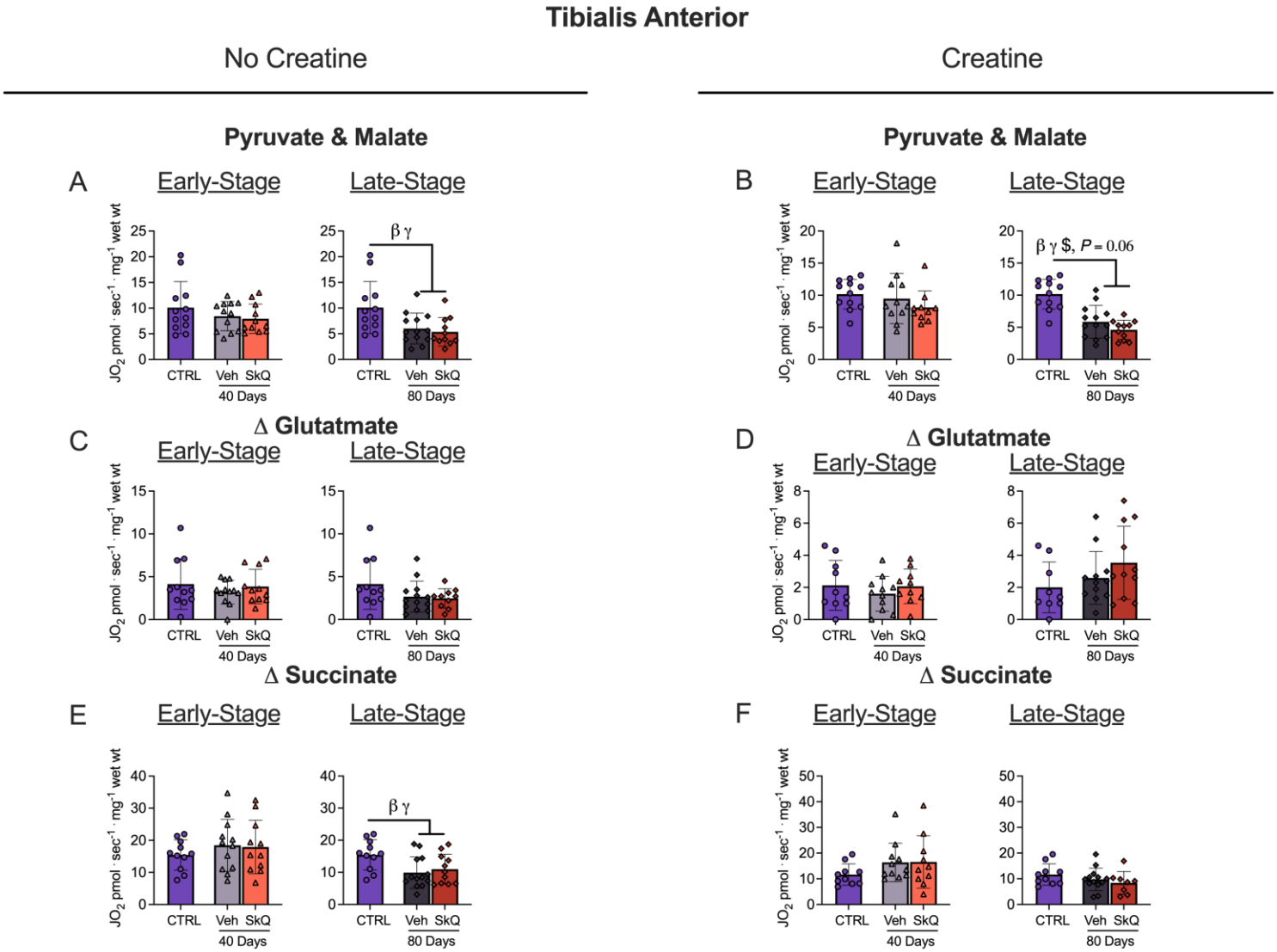

SFigure 6-2. Multiple substrate evaluation of oxygen consumption in tibialis anterior permeabilized muscle fiber bundles. Oxygen consumption was evaluated in the absence of creatine in Early-Stage and Late-Stage mice when stimulated with pyruvate & malate (A), glutamate (C) and Succinate (E). This was repeated in the presence of creatine (B, D, E). All data was analyzed using a one-way ANOVA and followed by a two-stage step-up method of Benjamini, Krieger and Yukutieli multiple comparisons test. Data that was not normally distributed was analyzed with a Kruskal-Wallis test followed by the same post-hoc analysis. Control (CTRL), Early-Stage Vehicle (40Veh), Early-Stage SkQ1 (40SkQ), Late-Stage Vehicle (80Veh), Late-Stage SkQ1 (80SkQ). Results represent mean ± SD. n=10-12. *β* $P<0.05$ CTRL Vs 80Veh; *γ* $P<0.05$ CTRL Vs 80SkQ; $ $P<0.05$ 80Veh Vs 80SkQ.

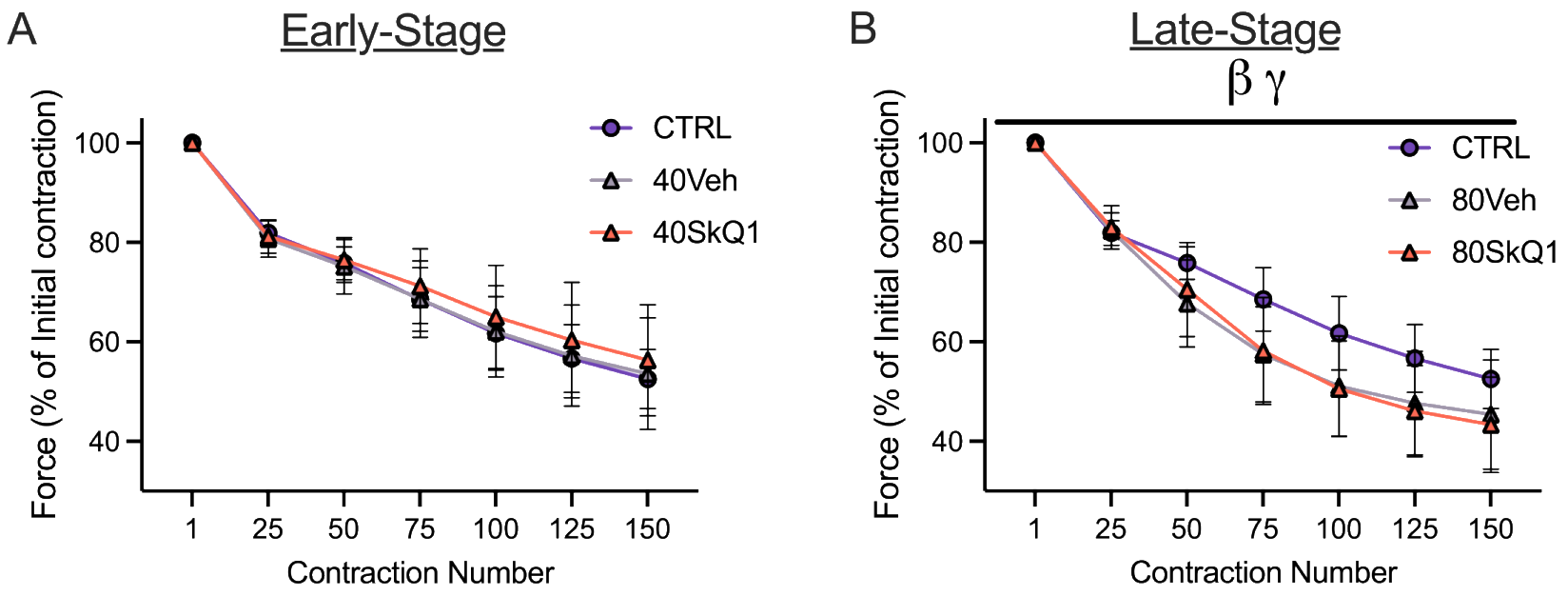

SFigure 6-3. Analysis of force production within the diaphragm during a fatigue protocol. In-Vitro diaphragm fatigue was completed (70Hz for 350ms every 2s for 150 contractions) to assess the effects of SkQ1 on fatiguability in Early-Stage and Late-Stage mice (A, B). All data was analyzed using a two-way ANOVA and followed by a two-stage step-up method of Benjamini, Krieger and Yukutieli multiple comparisons test. Control (CTRL), Early-Stage Vehicle (40Veh), Early-Stage SkQ1 (40SkQ), Late-Stage Vehicle (80Veh), Late-Stage SkQ1 (80SkQ). Results represent mean ± SD. n=8-11. β P<0.05 CTRL Vs 80Veh; γ P<0.05 CTRL Vs 80SkQ.

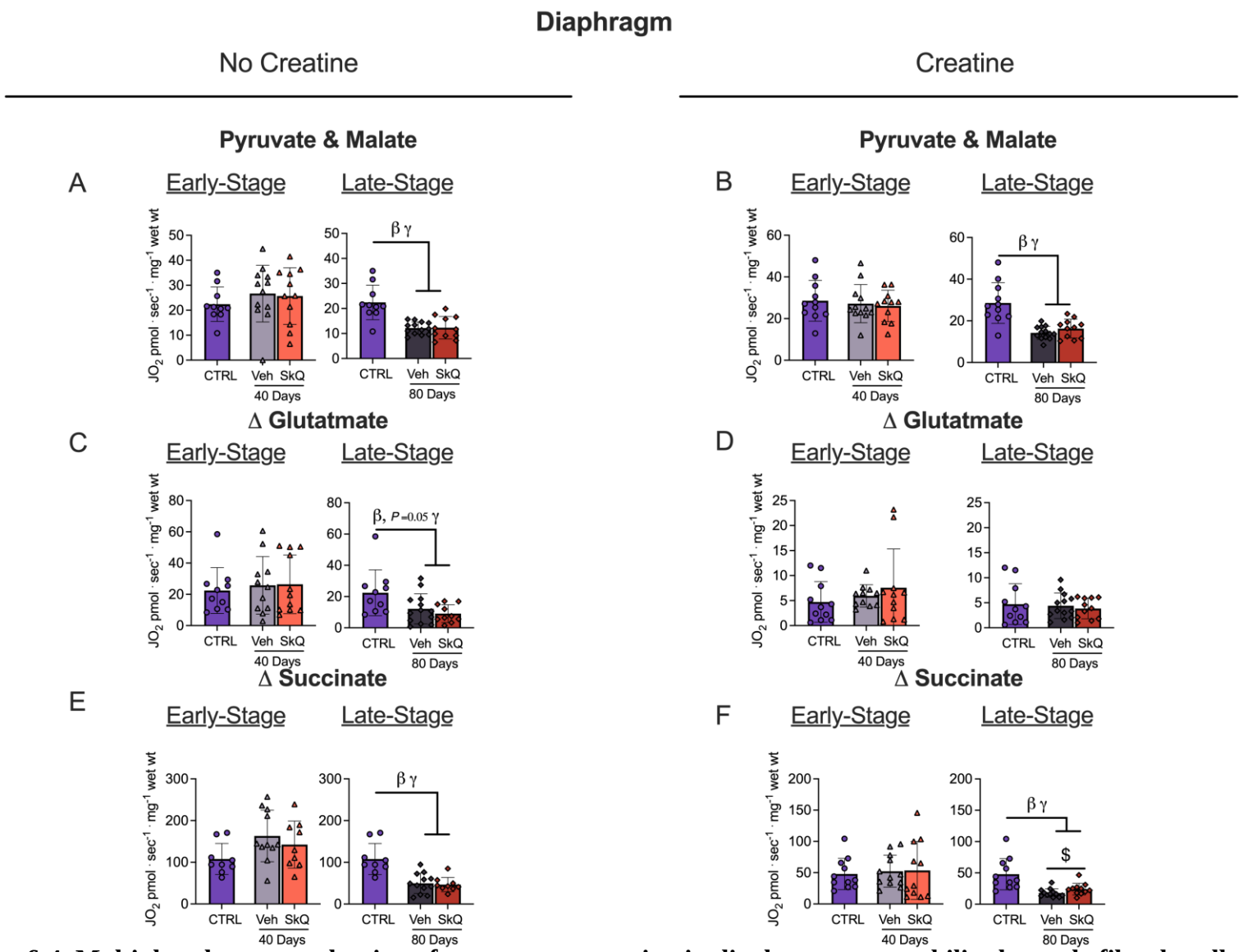

SFigure 6-4. Multiple substrate evaluation of oxygen consumption in diaphragm permeabilized muscle fiber bundles. Oxygen consumption was evaluated in the absence of creatine in Early-Stage and Late-Stage mice when stimulated with pyruvate & malate (A), glutamate (C) and Succinate (E). This was repeated in the presence of creatine (B, D, E). All data was analyzed using a one-way ANOVA and followed by a two-stage step-up method of Benjamini, Krieger and Yukutieli multiple comparisons test. Data that was not normally distributed was analyzed with a Kruskal-Wallis test followed by the same post-hoc analysis. Control (CTRL), Early-Stage Vehicle (40Veh), Early-Stage SkQ1 (40SkQ), Late-Stage Vehicle (80Veh), Late-Stage SkQ1 (80SkQ). Results represent mean ± SD. n=10-12. *β* $P<0.05$ CTRL Vs 80Veh; *γ* $P<0.05$ CTRL Vs 80SkQ; $ $P<0.05$ 80Veh Vs 80SkQ.

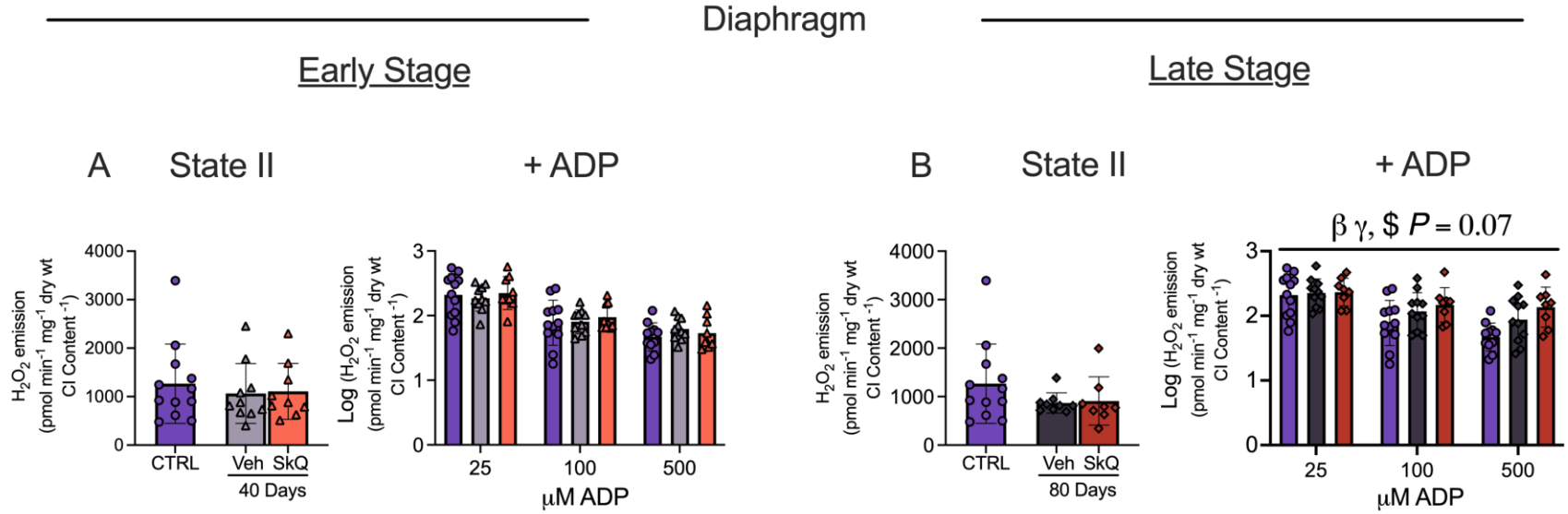

SFigure 6-5. Evaluation of Complex-I stimulated H_2O_2 when normalized to Complex I protein content. Maximal and State III diaphragm mH_2O_2 emissions were normalized to the permeabilized muscle fiber bundle used in the experimental set-up and the ETC Complex I protein content (A,B). Maximal rates were analyzed using a one-way ANOVA and followed by a two-stage step-up method of Benjamini, Krieger and Yukutieli multiple comparisons test. Data that was not normally distributed was analyzed with a Kruskal-Wallis test followed by the same post-hoc analysis. State III values were log transformed as original data was not normally distributed and analyzed with a 2-way ANOVA. control (CTRL), Early-Stage Vehicle (40Veh), Early-Stage SkQ1 (40SkQ), Late-Stage Vehicle (80Veh), Late-Stage SkQ1 (80SkQ). Results represent mean ± SD. n=10-12. β P<0.05 CTRL Vs 80Veh; γ P<0.05 CTRL Vs 80SkQ; \$ P<0.05 80Veh Vs 80SkQ

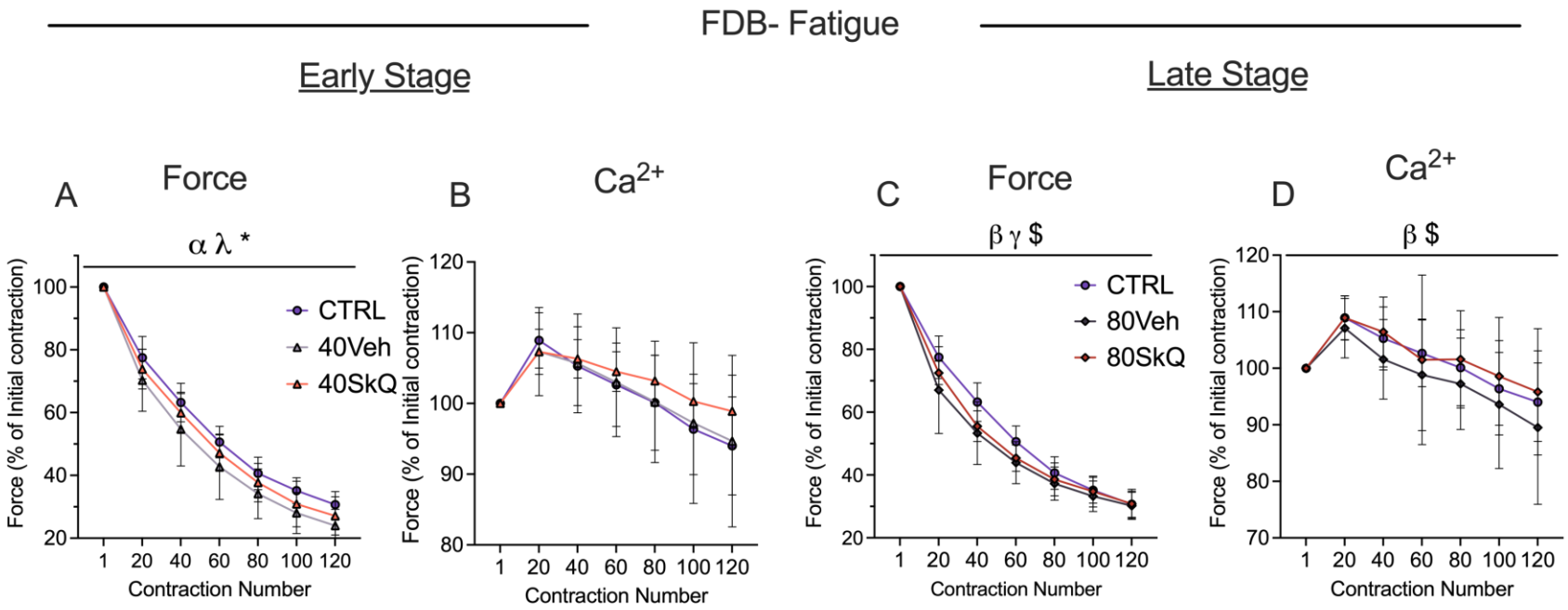

SFigure 6-6. Evaluation force-fatigue and calcium-fatigue relationship in FDB single fibers. In-Vitro FDB fatigue was completed (60Hz for 300ms every second for 120 contractions) to assess the effects of SkQ1 on fatiguability in Early-Stage and Late-Stage mice **(A,C** n=6-10**)**. This was repeated using single fibers for myoplasmic calcium content assessments **(B,D** n=9-12**)**. All data was analyzed using a two-way ANOVA followed by a two-stage step-up method of Benjamini, Krieger and Yukutieli multiple comparisons test. Control (CTRL), Early-Stage Vehicle (40Veh), Early-Stage SkQ1 (40SkQ), Late-Stage Vehicle (80Veh), Late-Stage SkQ1 (80SkQ), flexor digitorum brevis (FDB). Results represent mean ± SD. n=10-12. α P<0.05 CTRL Vs 40Veh; λ P<0.05 CTRL Vs 40SkQ; * P<0.05 40Veh Vs 40SkQ β P<0.05 CTRL Vs 80Veh; γ P<0.05 CTRL Vs 80SkQ $ P<0.05 80Veh Vs 80SkQ.

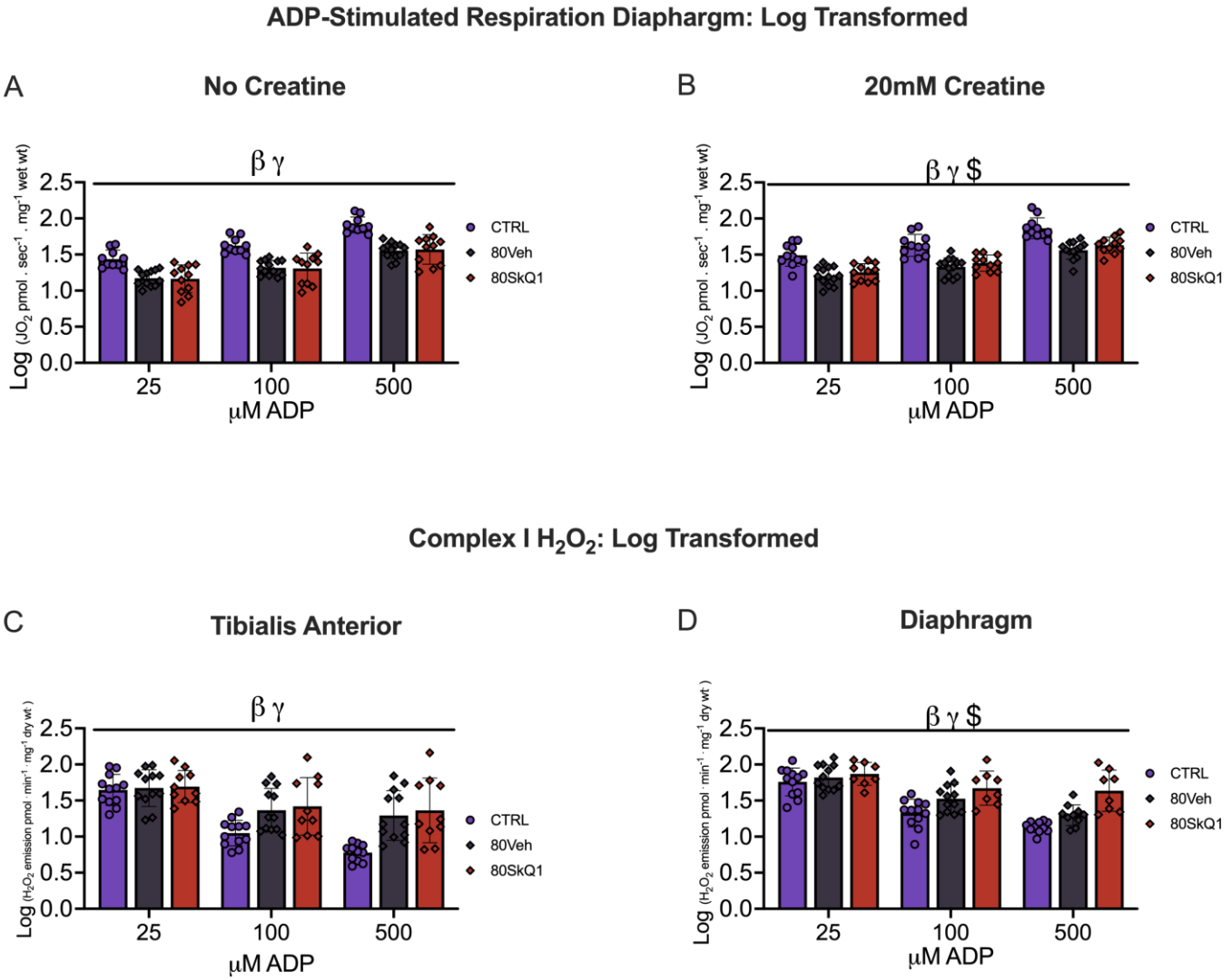

SFigure 6-7. Log transformed data. Data analyzed using a two way ANOVA after log transformation for non-normally distrusted data **(A-D)**. Control (CTRL), Late-Stage Vehicle (80Veh), Late-Stage SkQ1 (80SkQ). Results represent mean ± SD. n=10-12. β P<0.05 CTRL Vs 80Veh; γ P<0.05 CTRL Vs 80SkQ; $ P<0.05 80Veh Vs 80SkQ.

Oligo name	Oligo sequence (5' to 3')
m-actb Fwd	CATTGCTGACAGGATGCAGAAGG
m-actb Rev	TGCTGGAAGGTGGACAGTGAGG
m-TNFa Fw	AGAATGAGGCTGGATAAGAT
m-TNFa Rev	GAGGCAACAAGGTAGAGA
m-IL6 Fw	ACAGAAGGAGTGGCTAAG
m-IL6 Rev	AGAGAACAACATAAGTCAGATAC
m-Murf1 Fw	ACCTGCTGGTGGAAAACATC
m-Murf1 Rev	AGGAGCAAGTAGGCACCTCA
m-Atrogin1 Fw	AGCGCTTCTTGGATGAGAAA
m-Atrogin1 Rev	ACGTCGTAGTTCAGGCTGCT

STable 6-1. List of primers used for qtPCR

7 SUMMARY OF FINDINGS

7.1 General Discussion and Future Directions

Cancer cachexia is a multifactorial syndrome characterized by the ongoing loss ok skeletal muscle mass and function during cancer development[3]. 20%-80% of cancer patients are thought to develop cachexia throughout cancer progression depending on the type and stage of cancer[4]. No approved therapy currently exists for cancer cachexia, leaving cancer patients hopeless upon diagnosis. Given cancer-induced skeletal muscle myopathy can be complex, a successful therapy will likely use a multifactorial approach as is currently being investigated in the ongoing MENAC (Multimodal-Exercise, Nutrition and Anti-inflammatory medication for Cachexia) clinical trial[279]. In addition to more clinical investigations, experts believe more preclinical investigations are also needed but in models that develop tumours orthotopically and demonstrate metastasis[13]. These features are believed to better represent the human disease; thus, usage of these models will improve therapy development and mechanism elucidation[13]. The present dissertation first aimed at comprehensively evaluating the associations between muscle weakness, atrophy and mitochondrial stress across time, multiple muscles and two preclinical models of cancer cachexia (Chapter 4 and 5). Based on these findings, we then used the mitochondrial-targeted antioxidant - SkQ1 - to 1) elucidate the role of mitochondria in muscle weakness and atrophy in an orthotopic model of cancer cachexia and 2) evaluate the efficacy of using a mitochondrial antioxidant as a potential cancer cachexia therapy (Chapter 6). The main findings from this dissertation identifies muscle weakness occurs in the absence of muscle atrophy through multiple muscles and two preclinical models of cancer cachexia. In addition, this dissertation establishes a direct relationship

between mitochondria and muscle weakness in cancer-induced muscle myopathy. This supports the further exploration of mitochondrial targeted therapeutics in cancer cachexia.

Muscle weakness occurs independent of atrophy: How?

Muscle weakness preceding muscle atrophy was one of the main findings from this dissertation, first discovered in the C26-ectopic model (Chapter 4) and further supported in the EOC-orthotopic cachexia model (Chapter 5). While the time-course muscle responses of weakness and atrophy in relation to mitochondrial stress within cancer is novel, muscle weakness occurring independent of atrophy was yet to be explored in the literature until our group. Indeed, muscle weakness has been primarily attributed to muscle wasting, however, the degree to which cancer contributes to muscle weakness independent of wasting has yet to be explored. This dissertation identifies in two models and in multiple muscles that muscle weakness can occur in the absence of muscle atrophy suggesting atrophy independent contributions to weakness exist in cancer.

We demonstrate potential mitochondrial stress associations are linked to atrophy independent weakness like decreases in pyruvate/malate supported mitochondrial respiration and increases in pyruvate/malate stimulated mitochondrial H_2O_2. However, in Chapter 6, using the mitochondrial-targeted antioxidant SkQ1, we establish a direct relationship between mitochondrial ROS emissions and atrophy independent weakness. Indeed, administration of SkQ1 improved force production in tumour bearing mice before the onset of atrophy at early stages and during atrophy without modulating fiber CSA. This suggests that targeting mitochondrial oxidative stress can improve muscle force production but not by protecting muscle mass. Albeit, the direct mechanism of improved force remains unknown. Indeed, it is unlikely that SkQ1 improves force production through improved ATP generating capacity, as was originally hypothesized. Rather, it appears that

a mitochondrial antioxidant can improve force production through a more indirect mechanism like calcium handling.

Within Chapter 6, we demonstrate myoplasmic calcium concentration homeostasis as a potential mechanism of muscle weakness in cancer cachectic muscle. Indeed, at both early and late-stage ovarian cancer tumour development, FDB myoplasmic calcium concentrations were decreased across a range of frequencies. This was coupled to decrease in high-stimulation frequency muscle weakness but only at late stages of tumour development. To our knowledge, only one other study evaluated calcium handling in cancer cachexia, whereby the pCa-force relationship of rectus abdominus single fiber muscle was used to evaluate calcium sensitivity and single fiber force production[283]. Within this study, increases in myofibrillar calcium sensitivity within cancer cachectic muscle were coupled to decreases in force production, which is perplexing given increased calcium sensitivity is suggestive of increased force production[283]. This could propose increases in calcium sensitivity are a compensatory adaptation due to impairments in calcium homeostasis upstream of calcium binding to troponin C to initiate excitation-contraction coupling. While speculative, results from our investigation demonstrate that SR calcium release is decreased in an ovarian preclinical cancer cachexia model. While *Taskin et al. 2014*[283] did not measure intracellular myoplasmic free calcium concentrations during contractions, it is plausible that SR calcium release could also be decreased in human cancer-induced myopathy in single fibers as it was in the EOC model. If so, then increases in calcium sensitivity may be a compensatory response to decreased calcium release to improve force production. Overall, this suggests that calcium handling is relatively plastic in cancer and supports pharmacologically targeting calcium handling to improve force production in this disease. In fact, this has already been explored in ageing models of muscle weakness and has shown positive adaptations to pharmacologically targeting calcium

handling in muscle weakness[284]. Interestingly, however, muscle from non-cachectic cancer patients also exhibit decreases in force production and increases in myofibrillar calcium sensitivity[283]. This suggests non-cachectic cancer patients could exhibit muscle weakness, suggesting decreases in muscle force production could be occurring the absence of atrophy as we have discovered, albeit no measures of atrophy were completed in this study[283]. Nevertheless, this is further supportive of calcium handling contributing to an atrophy-independent mechanism of muscle weakness in cancer cachexia.

While the current dissertation explored peripheral mechanisms of muscle weakness (i.e dysfunctions within skeletal muscle) it is important to note that central mechanisms of muscle weakness exist in cancer cachexia as well. Indeed, while we have focused on the bioenergetic and calcium regulations on skeletal muscle force production, it is possible that cancer myopathy may be a result of motoneuron dysfunction exterior to skeletal muscle fibers. There is some data to suggest that loss of motor unit connectivity also exists in preclinical models of cancer cachexia[172]. However, loss of motor unit connectivity has only been shown to occur concurrently with decreases in muscle wet weights[172]. This is suggestive that muscle weakness due to motoneuron dysfunction is occurring during muscle atrophy, however, muscle wet weights are only suggestive of muscle atrophy. Thus, skeletal muscle histology must be performed to confirm if these central contributions to weakness are atrophy-independent. Therefore, while changes in motor unit number estimations and presynaptic morphology may suggest altered muscle innervation which leads to muscle weakness, it is still unclear if this is an atrophy independent mechanism of weakness[172]. Nevertheless, future work should explore central contributions to muscle weakness in cancer cachexia before the onset of atrophy as a potential mechanism of atrophy-independent weakness in addition to mitochondrial stress and calcium handling.

Cancer-induced skeletal muscle myopathy: Can paralleled results between muscles and models guide clinical insight?

Throughout all three chapters within this dissertation, vast majority of experiments were completed in the same muscles to properly elucidate the mechanisms that govern myopathy in cancer. This is important considering past studies have used different muscles to investigate the same research question which may lead to complex interpretations of fundings. With this approach, we identified both heterogenous and homogenous effects of cancer-induced skeletal muscle myopathy across models.

First, in Chapters 4, 5 and 6 we identify that muscle weakness occurs in early myopathy within the TA, diaphragm and quadriceps in the C26-ectopic and EOC-orthotopic models of cancer cachexia. Considering this conclusion is consistent between both models of cancer cachexia, this is suggestive that early muscle weakness could be a ubiquitous phenomenon across several muscles and other preclinical cancer models not evaluated within this dissertation. If this myopathy also exists in human cancer, this could potentially lead to insight for early cancer diagnosis. Indeed, grip strength has already been identified as a strong predictor of survival in cancer patients among 14,682 cancer patients in China[169]. Thus, it could be possible that muscle weakness (identified via grip strength or other functional measures) could aid in initial cancer diagnosis assuming the relationships observed in this dissertation exist clinically as well. Of course, this discussion does not suggest that muscle weakness is a definitive biomarker for cancer as several pathologies induce muscle weakness like ageing[285] and muscle disuse[286] which could occur concurrently with cancer. Rather, identifications of muscle weakness via grip strength or other functional measures could be used to initiate imaging or other biomarker assessments for cancer diagnosis, especially

considering muscle weakness seems to occur before severe metastasis in the orthotopic EOC mouse model as shown in Chapter 5.

Second, in Chapters 4, 5 and 6 we identify mitochondrial stress as a ubiquitous phenomenon in skeletal muscle cancer-induced myopathy, albeit with muscle-specific and time-dependent responses. While mitochondrial stress is a well understood phenomenon in cancer cachexia[9–12], this dissertation demonstrated that time-dependent and muscle-specific mitochondrial responses can be similar across models. Considering bioenergetic stress occurred early in cancer-induced myopathy, this could represent a tool for predicting cancer progression. While imaging methods already exist to diagnose cancer and thus metastasis - using cancer-induced skeletal muscle myopathy to predict disease progression could help with patient management. For example, if patients are to undergo surgery for the removal of a primary tumour mass, clinicians can dissect skeletal muscle to evaluate mitochondrial bioenergetics. At this time, bioenergetic assessments could be used to predict the progression of cancer, supplemented with cancer imaging for confident assessments for disease progression. While this would require extensive research to identify precise time-course responses to cancer to establish "criteria" of bioenergetic stress, it remains an interesting direction worth future exploration toward improved patient care and management.

Last, we identified an unexpected supercompensation in pyruvate/malate supported mitochondrial respiration in the quadriceps and diaphragm muscle within the C26 model. This phenomenon also existed to some effect within the EOC-orthoptic model in both the diaphragm and TA muscles. Surprisingly, this was coupled to compensatory increases in limb skeletal muscle force production but decoupled to force production in the diaphragm. Considering this has yet to be shown in clinical investigations, this likely demonstrates a unique-rodent specific compensatory response. Indeed, while speculative, delineation in findings between preclinical rodent models and humans

has been observed previously in other diseases. For example, in the dystrophin-deficient *mdx* mouse, regeneration-associated genes were found more activated in mice compared to humans resulting in the identification of new leads for development of Duchenne muscular dystrophy therapies [287]. In the same light, understanding the mechanisms regulating this unique limb-muscle specific adaptation to cancer could identify novel therapies within cancer cachexia. Using RNAseq to identify the gene programs of skeletal muscle with unique compensatory responses compared to those of humans could help identify new therapies for compensation in skeletal muscle. Moreover, the discrepancy between the diaphragm and limb muscle may demonstrate unique insight on muscle functions relevant to cancer-induced myopathy. While speculative, this data could suggest limb muscle - which regulate locomotion - are more plastic in an attempt to maintain functionality. The diaphragm never exhibits such compensations perhaps due to its constant and sustained contraction and relaxation. Indeed, perhaps the diaphragms constant activity disables the ability for beneficial adaptations. While the mechanisms as to why these alterations occur remain incompletely understood, these phenomena provide valuable clinical insight that could potentially be explored in the future.

Cancer-induced myopathy exists before severe metastasis: How does this change conventional cancer cachexia preclinical study designs?

Foundational cancer cachexia literature was primarily completed in rapid-ectopic models within rats and mice[42,128]. While these models were integral for original cancer cachexia myopathy mechanism elucidation, recent criticisms suggest the usage of these models are inadequate for clinical investigations[13]. Indeed, dozens of clinical investigations have been completed in cancer cachexia and none have generated sufficiently positive results to yield an effective treatment for

cancer cachexia patients[5]. It is thus believed that the usage of insufficient models has been partly to blame for failed clinical investigations as the human disease is not well recapitulated in preclinical models due to ectopic tumour growth and absence of metastasis, among other reasons[13]. Therefore, in Chapter 5 we sought out to characterize the development of myopathy of an orthotopic, metastatic model of ovarian cancer induced cachexia. Interestingly, we report similar cancer-induced myopathy across the C26-ectopic and EOC-orthotopic models of cancer cachexia. While two models demonstrating similar phenomenon is highly suggestive of a consistent biological phenomenon, it does raise the question – how does recapitulating metastasis improve current models and should future research groups recapitulate metastasis?

First, recapitulating metastasis in preclinical models is critical for providing clinical context to understand cancer-induced myopathy. It is estimated that up to 66% of cancer deaths are associated with metastasis in those with solid tumours[288]. In ovarian cancer, metastasis is associated with reduced survival rates and severe cachexia[235]. When ovarian cancer is detected early and thus before metastasis, the cure rate is estimated to be as high as 90%[236], in contrast to much lower survival rates once metastasis has occurred. Up to 70% of ovarian cancer cases are diagnosed at late stages and thus during metastasis[235]. Thus, recapitulating this in preclinical models is critical to understanding cancer-induced myopathy before advanced disease progression when the disease becomes untreatable. Identifying mechanisms of dysfunction and evaluating treatment efficacy at a time before severe metastasis thus provides critical clinical insight for patient management. In addition, given cancer cachexia is a multifactorial-induced disease state, recapitulating metastasis can help eliminate potential causes to skeletal muscle myopathy. Indeed, in the current dissertation, we found that muscle weakness and mitochondrial stress occur before the onset of severe metastasis. Considering mitochondrial stress and muscle weakness occurred at the earliest time

point within our study design and before any apparent-metastasis, this suggests that other mechanisms contribute to cancer-induced myopathy independent of metastasis. This is important because it suggests that therapeutic interventions for cancer-induced skeletal muscle myopathy shouldn't consider metastasis as a regulator of dysfunction and thus target other mechanisms.

7.2 Limitations and Perspectives

While all variables were controlled to the best of our ability throughout this dissertation, some limitations must be acknowledged that also uncover interesting perspectives about the current dissertation. First, in all three studies, no investigations were complete using a cancer therapy agent. While chemotherapy is an extremely common anticancer treatment, it is well understood that chemotherapy can induce myopathy independent of cancer (see section 2.1.3.6). As such, the original intention of this dissertation was to explore the therapy-independent contributions of cancer on skeletal muscle myopathy. Considering chemotherapy is used to decrease tumour burden but can induce skeletal muscle myopathy independent of cancer, this could suggest that human cancer myopathy is actually a response to both "diminished" tumour burden (due to the antitumour effects of chemotherapy) and chemotherapy toxicity together. Indeed, in the current dissertation, tumours grew void of any anti-cancer intervention – a situation which is highly unlikely in human cancer cachexia. This represents an important future direction for this dissertation to evaluate cancer-chemotherapy-induced myopathy. An investigation of this magnitude would generate a dissertation in and of itself considering the need for several vehicle-treated control groups. Nevertheless, future studies investigating the mitochondrial relationships between muscle weakness and cancer cachexia would benefit with an anticancer therapy comparison.

Second, in Chapter 4, data was collected from mice which were euthanized at 10-12 weeks of age. Interestingly, this is an age used commonly within the literature [10,12,136] and thus formed the basis of initial methodology within this dissertation. This thus presents a large limitation for the cancer cachexia field as a whole, considering 10-12 weeks of age in mice could be considered "young adult". It's also important to acknowledge age is a risk factor for cancer diagnosis with estimates from the National Cancer Institute that the median age to develop any cancer is 66 years old[289]. Especially considering ageing itself can induce loss of muscle mass and function (sarcopenia) [290], it is increasingly important to model ageing with preclinical models of cancer cachexia. Interestingly, however, one study comparing the effects of age in the C26 model on mice at 11 weeks old vs 12 months old demonstrate very similar skeletal muscle pathology with similar sized tumours, muscle loss and activation of proteolytic pathways[220]. While this study does suggest young adult mice still represents an accurate representation of cancer myopathy, this has only been shown in only one cancer model and it is still unclear how using young adult mice could complicate preclinical therapy development.

Third, the current dissertation does not control for the potential of muscle disuse/inactivity on myopathy in cancer. There is an abundantly clear connection between increased physical activity and increased limb size and strength[291]. In the same regard, it is also well understood that muscle disuse and physical inactivity can induce muscle atrophy[292]. Interestingly, limb immobilization-induced disuse has been shown to induce mitochondrial stress as well[293]. Specifically, decreases in complex-I stimulated mitochondrial respiration can occur in in vastus lateralis muscle as soon as 3 days after disuse [293]. Muscle inactivity is believed to contribute at least partially to cachexia[74,75]. In the C26 ectopic model of cancer cachexia, tumour bearing mice exhibit reduced movement distance and duration compared to PBS controls[136]. It is thus a limitation within this

dissertation and potential future direction to introduce a "muscle disuse control" group within cancer cachectic study designs. Indeed, considering some mitochondrial stress responses can be paralleled in muscle disuse and cancer cachexia, introducing a control group whereby mice are subject to hindlimb suspension or denervation might help delineate between the cancer-induced myopathy and disuse-induced myopathy within cancer models.

Fourth, in Chapter 4, we exclusively investigated the myopathy in tumour bearing male mice. Male cancer patients are shown to exhibit greater weight loss and worse outcomes compared to female cancer patients[294] but data on sex differences in cancer cachexia is limited with some investigations demonstrating distinct transcriptional profiles of males vs females[295]. Few studies have investigated mechanisms underlying sex differences in cancer cachexia as a whole, therefore future work could explore sex differences in both ectopic and orthotopic models.

Last, considering anorexia or reduced food intake is a hallmark of cancer cachexia[3], better estimates of food consumption would be of value. While changes in food take were not measured in Chapter 4, reductions in food intake reported in the C26 model did not contribute to reduced muscle weights, fiber CSA, or muscle force given pair-fed mice retained normal muscle parameters compared to tumour-bearing mice[136,220]. Therefore, we did not have reason to believe food consumption would be different in the C26 model. However, in the EOC model we attempted to estimate food consumption within Chapter 6. While this data yielded no significant differences in food intake between control and tumour bearing mice, mice were group housed to accommodate for large cage expenses. Thus, estimates of food intake were divided equally by 4 mice per cage, introducing variability in our estimates.

7.3 Conclusions

The findings from this dissertation first establish mitochondrial associations between skeletal muscle force production and cancer-induced weakness within the C26-ectopic and EOC-orthotopic preclinical models of cancer cachexia **(Figure 7-1)**. Moreover, administration of the mitochondrial-targeted therapeutic, SkQ1 in EOC mice identifies a direct relationship between mitochondria and skeletal weakness in cancer-induced myopathy **(Figure7-2)**. Partial improvements in cancer-induced muscle weakness with SkQ1 treatment in multiple muscles demonstrate that targeting mitochondrial function can modulate force production, at least in a preclinical setting. Moreover, this dissertation identifies novel mechanisms of muscle weakness in cancer cachexia that are independent of atrophy. While we explored mitochondrial-linked regulations of muscle weakness in cancer-induced myopathy, future research could explore other atrophy independent mechanisms of weakness like calcium handling or innervation. Thus, this dissertation provides a new research direction in cancer-induced muscle weakness and supports the further exploration of mitochondrial therapeutics in cancer-induced cachexia.

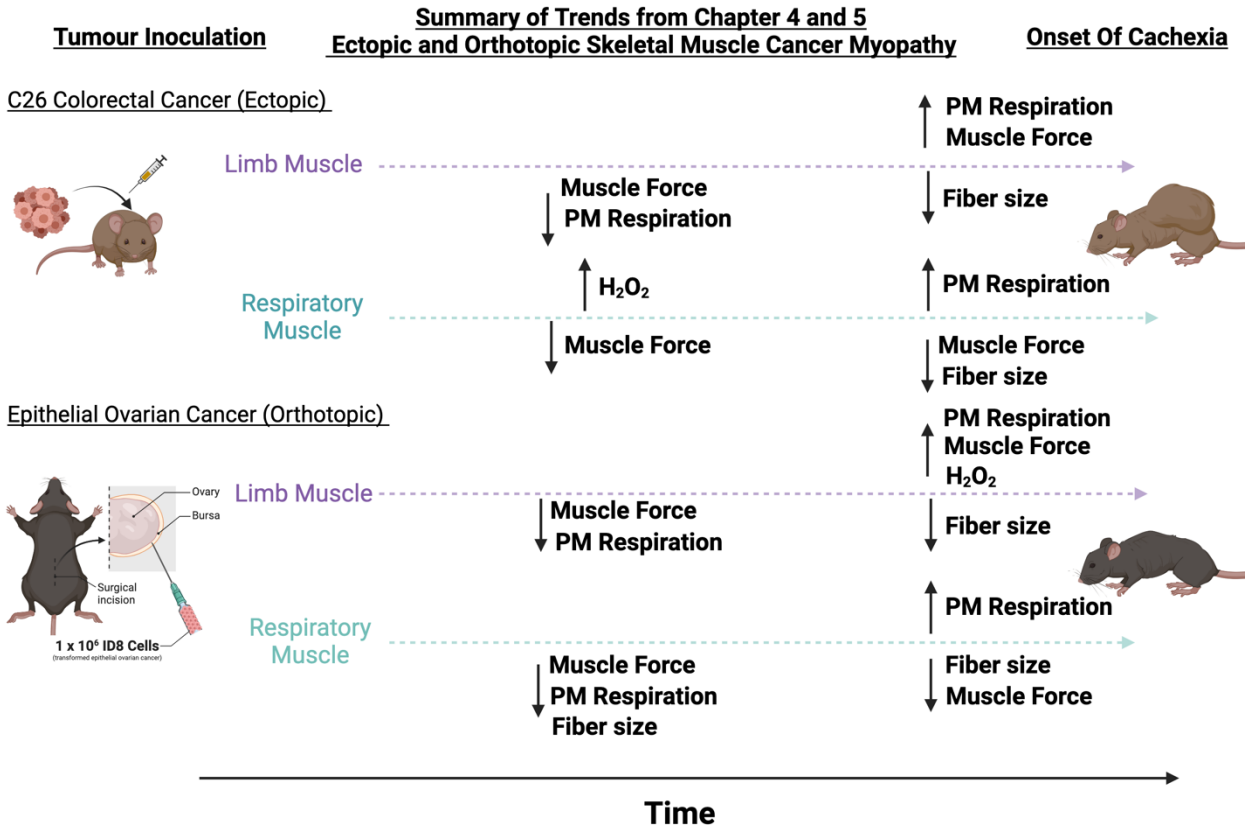

Figure 7-1. Summary of muscle-specific and model-specific alterations in fiber size, force production and mitochondrial bioenergetics throughout cancer progression. General summary of the time course of myopathy across two pre-clinical models of cancer cachexia. Muscle force was measured via direct electrical stimulation while mitochondrial bioenergetics were measured with permeabilized muscle fiber bundles. Muscle atrophy was evaluated with muscle histology. ↓ represents decrease; ↑ represents increase; PM represents pyruvate and malate.

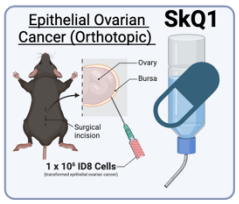

	SkQ1 treatment in **Early-Stage Cancer**		SkQ1 treatment in **Late-Stage Cancer**	
	Limb Muscle	Respiratory Muscle	Limb Muscle	Respiratory Muscle
Muscle Force	↑ TA Only	↑	↑ FDB Only	↑
Total Fiber Size	No effect	No effect	No effect	No effect
Pyruvate Supported - Complex I Respiration	No effect	No effect	↓?	↑?
Pyruvate Supported - Complex I H_2O_2	No effect	↑	↓	↑?
ETC Protein Content	No effect	No effect	No effect	Attenuated Complex I
Intracellular Myoplasmic [Calcium]	No effect	Unknown	↑ FDB Only	Unknown

Figure 7-2. Summary of muscle-specific effects of SkQ1 on skeletal muscle myopathy due to ovarian cancer at Early- and Late-Stage. Direct effects of SkQ1 treatment on skeletal muscle myopathy across two cancer timepoints. ↓ represents decrease; ↑ represents increase; ? represents mixed results

This page has been left intentionally blank.

8 REFRENCES

1. Hanahan D, Weinberg RA. Hallmarks of cancer: The next generation. In: *Cell*. ; 2011. doi:10.1016/j.cell.2011.02.013

2. Lundholm K, Bylund AC, Holm J, Scherstén T. Skeletal muscle metabolism in patients with malignant tumor. *European Journal of Cancer (1965)*. 1976;12(6):465-473. doi:10.1016/0014-2964(76)90036-0

3. Fearon K, Strasser F, Anker SD, et al. Definition and classification of cancer cachexia: An international consensus. *Lancet Oncol*. 2011;12(5):489-495. doi:10.1016/S1470-2045(10)70218-7

4. Tan BHL, Fearon KCH. Cachexia: Prevalence and impact in medicine. *Curr Opin Clin Nutr Metab Care*. 2008;11(4):400-407. doi:10.1097/MCO.0b013e328300ecc1

5. Baracos VE. Clinical trials of cancer cachexia therapy, now and hereafter. *J Clin Oncol*. 2013;31(10):1257-1258. doi:10.1200/JCO.2012.48.3149

6. Baracos VE, Mazurak VC, Bhullar AS. Cancer cachexia is defined by an ongoing loss of skeletal muscle mass. *Annals of Palliative Medicine; Vol 8, No 1 (January 2019): Annals of Palliative Medicine (Update on Cancer Cachexia in Memory of Ken Fearon)*. Published online 2018. https://apm.amegroups.com/article/view/22915

7. Tisdale MJ. Molecular pathways leading to cancer cachexia. *Physiology*. 2005;20:340-348. doi:10.1152/physiol.00019.2005

8. Argilés JM, Busquets S, Stemmler B, López-Soriano FJ. Cancer cachexia: Understanding the molecular basis. *Nat Rev Cancer*. Published online 2014:754-762. doi:10.1038/nrc3829

9. White JP, Baltgalvis KA, Puppa MJ, Sato S, Baynes JW, Carson JA. Muscle oxidative capacity during IL-6-dependent cancer cachexia. *Am J Physiol Regul Integr Comp Physiol*. 2011;300(2):R201-R211. doi:10.1152/ajpregu.00300.2010

10. Neyroud D, Nosacka RL, Judge AR, Hepple RT. Colon 26 adenocarcinoma (C26)-induced cancer cachexia impairs skeletal muscle mitochondrial function and content. *J Muscle Res Cell Motil*. 2019;40(1):59-65. doi:10.1007/s10974-019-09510-4

11. Halle JL, Pena GS, Paez HG, et al. Tissue-specific dysregulation of mitochondrial respiratory capacity and coupling control in colon-26 tumor-induced cachexia. *Am J Physiol Regul Integr Comp Physiol*. 2019;317(1):R68-R82. doi:10.1152/ajpregu.00028.2019

12. Brown JL, Rosa-Caldwell ME, Lee DE, et al. Mitochondrial degeneration precedes the development of muscle atrophy in progression of cancer cachexia in tumour-bearing mice. *J Cachexia Sarcopenia Muscle*. 2017;8(6):926-938. doi:10.1002/jcsm.12232

13. Tomasin R, Martin ACBM, Cominetti MR. Metastasis and cachexia: alongside in clinics, but not so in animal models. *J Cachexia Sarcopenia Muscle*. 2019;10(6):1183-1194. doi:https://doi.org/10.1002/jcsm.12475

14. Penna F, Busquets S, Argilés JM. Experimental cancer cachexia: Evolving strategies for getting closer to the human scenario. *Semin Cell Dev Biol*. 2015;54:20-27. doi:10.1016/j.semcdb.2015.09.002

15. Mueller TC, Bachmann J, Prokopchuk O, Friess H, Martignoni ME. Molecular pathways leading to loss of skeletal muscle mass in cancer cachexia--can findings from animal models be translated to humans? *BMC Cancer*. 2016;16:75. doi:10.1186/s12885-016-2121-8

16. Mishra SI, Scherer RW, Geigle PM, et al. Exercise interventions on health-related quality of life for cancer survivors. *Cochrane Database Syst Rev*. 2012;2012(8):CD007566. doi:10.1002/14651858.CD007566.pub2

17. Tsitkanou S, Murach KA, Washington TA, Greene NP. Exercise Counteracts the Deleterious Effects of Cancer Cachexia. *Cancers (Basel)*. 2022;14(10). doi:10.3390/cancers14102512

18. Leal LG, Lopes MA, Peres SB, Batista ML. Exercise Training as Therapeutic Approach in Cancer Cachexia: A Review of Potential Anti-inflammatory Effect on Muscle Wasting. *Front Physiol*. 2021;11. https://www.frontiersin.org/journals/physiology/articles/10.3389/fphys.2020.570170

19. Kurz E, Hirsch CA, Dalton T, et al. Exercise-induced engagement of the IL-15/IL-15Rα axis promotes anti-tumor immunity in pancreatic cancer. *Cancer Cell*. 2022;40(7):720-737.e5. doi:10.1016/j.ccell.2022.05.006

20. Boston Globe Media's Studio/B. Pfizer Dear Scientist Series. The Boston Globe.

21. Evans WJ, Morley JE, Argilés J, et al. Cachexia: A new definition. *Clinical Nutrition*. 2008;27(6):793-799. doi:10.1016/j.clnu.2008.06.013

22. Butt Z, Rosenbloom SK, Abernethy AP, et al. Fatigue is the most important symptom for advanced cancer patients who have had chemotherapy. *J Natl Compr Canc Netw*. 2008;6(5):448-455. doi:10.6004/jnccn.2008.0036

23. Díaz N, Menjón S, Rolfo C, et al. Patients' perception of cancer-related fatigue: results of a survey to assess the impact on their everyday life. *Clinical and Translational Oncology*. 2008;10(11):753-757. doi:10.1007/s12094-008-0282-x

24. Martin L, Birdsell L, MacDonald N, et al. Cancer Cachexia in the Age of Obesity: Skeletal Muscle Depletion Is a Powerful Prognostic Factor, Independent of Body Mass Index. *Journal of Clinical Oncology*. 2013;31(12):1539-1547. doi:10.1200/JCO.2012.45.2722

25. Moses AWG, Slater C, Preston T, Barber MD, Fearon KCH. Reduced total energy expenditure and physical activity in cachectic patients with pancreatic cancer can be modulated by an energy and protein dense oral supplement enriched with n-3 fatty acids. *Br J Cancer*. 2004;90(5):996-1002. doi:10.1038/sj.bjc.6601620

26. Bachmann J, Heiligensetzer M, Krakowski-Roosen H, Büchler MW, Friess H, Martignoni ME. Cachexia worsens prognosis in patients with resectable pancreatic cancer. *Journal of Gastrointestinal Surgery*. 2008;12(7):1193-1201. doi:10.1007/s11605-008-0505-z

27. Dewys WD, Begg C, Lavin PT, et al. Prognostic effect of weight loss prior tochemotherapy in cancer patients. *Am J Med*. 1980;69(4):491-497. doi:10.1016/S0149-2918(05)80001-3

28. Fukuta A, Saito T, Murata S, et al. Impact of preoperative cachexia on postoperative length of stay in elderly patients with gastrointestinal cancer. *Nutrition*. 2019;58:65-68. doi:https://doi.org/10.1016/j.nut.2018.06.022

29. Antoun S, Baracos VE, Birdsell L, Escudier B, Sawyer MB. Low body mass index and sarcopenia associated with dose-limiting toxicity of sorafenib in patients with renal cell carcinoma. *Ann Oncol*. 2010;21(8):1594-1598. doi:10.1093/annonc/mdp605

30. Prado CMM, Baracos VE, McCargar LJ, et al. Sarcopenia as a determinant of chemotherapy toxicity and time to tumor progression in metastatic breast cancer patients receiving capecitabine treatment. *Clin Cancer Res*. 2009;15(8):2920-2926. doi:10.1158/1078-0432.ccr-08-2242

31. Poisson J, Martinez-Tapia C, Heitz D, et al. Prevalence and prognostic impact of cachexia among older patients with cancer: a nationwide cross-sectional survey (NutriAgeCancer). *J Cachexia Sarcopenia Muscle*. 2021;12(6):1477-1488. doi:10.1002/jcsm.12776

32. Costamagna D, Costelli P, Sampaolesi M, Penna F. Role of Inflammation in Muscle Homeostasis and Myogenesis. Batista ML, ed. *Mediators Inflamm*. 2015;2015:805172. doi:10.1155/2015/805172

33. Tosi MF. Innate immune responses to infection. *J Allergy Clin Immunol*. 2005;116(2):241-249; quiz 250. doi:10.1016/j.jaci.2005.05.036

34. Garcia KC, Teyton L, Wilson IA. Structural basis of T cell recognition. *Annu Rev Immunol*. 1999;17:369-397. doi:10.1146/annurev.immunol.17.1.369

35. Iwasaki A, Medzhitov R. Toll-like receptor control of the adaptive immune responses. *Nat Immunol*. 2004;5(10):987-995. doi:10.1038/ni1112

36. Viola A, Munari F, Sánchez-Rodríguez R, Scolaro T, Castegna A. The Metabolic Signature of Macrophage Responses. *Front Immunol*. 2019;10:1462. doi:10.3389/fimmu.2019.01462

37. Seruga B, Zhang H, Bernstein LJ, Tannock IF. Cytokines and their relationship to the symptoms and outcome of cancer. *Nat Rev Cancer*. 2008;8(11):887-899. doi:10.1038/nrc2507

38. Paval DR, Patton R, McDonald J, Skipworth RJE, Gallagher IJ, Laird BJ. A systematic review examining the relationship between cytokines and cachexia in incurable cancer. *J Cachexia Sarcopenia Muscle*. 2022;13(2):824-838. doi:10.1002/jcsm.12912

39. Todorov P, Cariuk P, McDevitt T, Coles B, Fearon K, Tisdale M. Characterization of a cancer cachectic factor. *Nature*. 1996;379(6567):739-742. doi:10.1038/379739a0

40. Whitehouse AS, Tisdale MJ. Increased expression of the ubiquitin-proteasome pathway in murine myotubes by proteolysis-inducing factor (PIF) is associated with activation of the transcription factor NF-kappaB. *Br J Cancer*. 2003;89(6):1116-1122. doi:10.1038/sj.bjc.6601132

41. Lorite MJ, Smith HJ, Arnold JA, Morris A, Thompson MG, Tisdale MJ. Activation of ATP-ubiquitin-dependent proteolysis in skeletal muscle in vivo and murine myoblasts in vitro by a proteolysis-inducing factor (PIF). *Br J Cancer*. 2001;85(2):297-302. doi:10.1054/bjoc.2001.1879

42. Tisdale MJ. Mechanisms of cancer cachexia. *Physiol Rev*. 2009;89(2):381-410. doi:10.1152/physrev.00016.2008

43. Hasselgren PO, Wray C, Mammen J. Molecular Regulation of Muscle Cachexia: It May Be More Than the Proteasome. *Biochem Biophys Res Commun*. 2002;290(1):1-10. doi:https://doi.org/10.1006/bbrc.2001.5849

44. Baracos VE, DeVivo C, Hoyle DHR, Goldberg AL. Activation of the ATP-ubiquitin-proteasome pathway in skeletal muscle of cachectic rats bearing a hepatoma. *Am J Physiol Endocrinol Metab*. 1995;268(5):E996-E1006. doi:10.1152/ajpendo.1995.268.5.e996

45. Llovera M, Garcia-Martinez C, Agell N, Lopez-Soriano FJ, Argiles JM. Muscle wasting associated with cancer cachexia is linked to an important activation of the atp-dependent ubiquitin-mediated proteolysis. *Int J Cancer*. 1995;61(1):138-141. doi:10.1002/ijc.2910610123

46. Temparis S, Asensi M, Estrela JM, Ferrara M, Larbaud D, Attaix D. Increased ATP-Ubiquitin-dependent Proteolysis in Skeletal Muscles of Tumor-bearing Rats. *Cancer Res*. 1994;54(21):5568-5573.

47. Khal J, Hine A V., Fearon KCH, Dejong CHC, Tisdale MJ. Increased expression of proteasome subunits in skeletal muscle of cancer patients with weight loss. *International Journal of Biochemistry and Cell Biology*. 2005;37(10):2196-2206. doi:10.1016/j.biocel.2004.10.017

48. Martin A, Gallot YS, Freyssenet D. Molecular mechanisms of cancer cachexia-related loss of skeletal muscle mass: data analysis from preclinical and clinical studies. *J Cachexia Sarcopenia Muscle*. 2023;14(3):1150-1167. doi:https://doi.org/10.1002/jcsm.13073

49. Glickman MH, Ciechanover A. The ubiquitin-proteasome proteolytic pathway: Destruction for the sake of construction. *Physiol Rev*. 2002;82(2):373-428. doi:10.1152/physrev.00027.2001

50. Peris-Moreno D, Cussonneau L, Combaret L, Polge C, Taillandier D. Ubiquitin ligases at the heart of skeletal muscle atrophy control. *Molecules*. 2021;26(2):407. doi:10.3390/molecules26020407

51. Neyroud D, Laitano O, Dasgupta A, et al. Blocking muscle wasting via deletion of the muscle-specific E3 ligase MuRF1 impedes pancreatic tumor growth. *Commun Biol*. 2023;6(1):519. doi:10.1038/s42003-023-04902-2

52. Dókus LE, Yousef M, Bánóczi Z. Modulators of calpain activity: inhibitors and activators as potential drugs. *Expert Opin Drug Discov*. 2020;15(4):471-486. doi:10.1080/17460441.2020.1722638

53. Pin F, Minero VG, Penna F, et al. Interference with Ca2+-Dependent Proteolysis Does Not Alter the Course of Muscle Wasting in Experimental Cancer Cachexia. *Front Physiol*. 2017;8. https://www.frontiersin.org/journals/physiology/articles/10.3389/fphys.2017.00213

54. Bonaldo P, Sandri M. Cellular and molecular mechanisms of muscle atrophy. *Dis Model Mech*. 2013;6(1):25-39. doi:10.1242/dmm.010389

55. de Castro GS, Simoes E, Lima JDCC, et al. Human cachexia induces changes in mitochondria, autophagy and apoptosis in the skeletal muscle. *Cancers (Basel)*. 2019;11(9):1264. doi:10.3390/cancers11091264

56. Op den Kamp CM, Langen RC, Snepvangers FJ, et al. Nuclear transcription factor κ B activation and protein turnover adaptations in skeletal muscle of patients with progressive stages of lung cancer cachexia. *Am J Clin Nutr*. 2013;98(3):738-748. doi:10.3945/ajcn.113.058388

57. Pigna E, Berardi E, Aulino P, et al. Aerobic exercise and pharmacological treatments counteract cachexia by modulating autophagy in colon cancer. *Sci Rep*. 2016;6(1). doi:10.1038/srep26991

58. Aversa Z, Pin F, Lucia S, et al. Autophagy is induced in the skeletal muscle of cachectic cancer patients. *Sci Rep*. 2016;6(1). doi:10.1038/srep30340

59. Penna F, Costamagna D, Pin F, et al. Autophagic degradation contributes to muscle wasting in cancer cachexia. *Am J Pathol*. 2013;182(4):1367-1378. doi:10.1016/j.ajpath.2012.12.023

60. Emery PW, Edwards RH, Rennie MJ, Souhami RL, Halliday D. Protein synthesis in muscle measured in vivo in cachectic patients with cancer. *BMJ*. 1984;289(6445):584-586. doi:10.1136/bmj.289.6445.584

61. Galluzzi L, Vitale I, Aaronson SA, et al. Molecular mechanisms of cell death: recommendations of the Nomenclature Committee on Cell Death 2018. *Cell Death Differ*. 2018;25(3):486-541. doi:10.1038/s41418-017-0012-4

62. Elmore S. Apoptosis: A review of programmed cell death. *Toxicol Pathol*. 2007;35(4):495-516. doi:10.1080/01926230701320337

63. Busquets S, Deans C, Figueras M, et al. Apoptosis is present in skeletal muscle of cachectic gastro-intestinal cancer patients. *Clin Nutr*. 2007;26(5):614-618. doi:10.1016/j.clnu.2007.06.005

64. Bossola M, Mirabella M, Ricci E, et al. Skeletal muscle apoptosis is not increased in gastric cancer patients with mild–moderate weight loss. *Int J Biochem Cell Biol*. 2006;38(9):1561-1570. doi:10.1016/j.biocel.2006.03.015

65. Busquets S, Figueras MT, Fuster G, et al. Anticachectic Effects of Formoterol: A Drug for Potential Treatment of Muscle Wasting. *Cancer Res*. 2004;64(18):6725-6731. doi:10.1158/0008-5472.CAN-04-0425

66. Belizário JE, Lorite MJ, Tisdale MJ. Cleavage of caspases-1, -3, -6, -8 and -9 substrates by proteases in skeletal muscles from mice undergoing cancer cachexia. *Br J Cancer*. 2001;84(8):1135-1140. doi:10.1054/bjoc.2001.1700

67. Laviano A, Meguid MM. Nutritional issues in cancer management. *Nutrition*. 1996;12(5):358-371. doi:10.1016/s0899-9007(96)80061-x

68. Argilés JM. Cancer-associated malnutrition. *European Journal of Oncology Nursing*. 2005;9:S39-S50. doi:https://doi.org/10.1016/j.ejon.2005.09.006

69. Rickard KA, Detamore CM, Coates TD, et al. Effect of nutrition staging on treatment delays and outcome in stage IV neuroblastoma. *Cancer*. 1983;52(4):587-598. doi:10.1002/1097-0142(19830815)52:4<587::aid-cncr2820520402>3.0.co;2-t

70. Andreyev HJN, Norman AR, Oates J, Cunningham D. Why do patients with weight loss have a worse outcome when undergoing chemotherapy for gastrointestinal malignancies? *Eur J Cancer*. 1998;34(4):503-509. doi:https://doi.org/10.1016/S0959-8049(97)10090-9

71. Meguid MM, Mughal MM, Debonis D, Meguid V, Terz JJ. Influence of Nutritional Status on the Resumption of Adequate Food Intake in Patients Recovering from Colorectal Cancer Operations. *Surgical Clinics of North America*. 1986;66(6):1167-1176. doi:https://doi.org/10.1016/S0039-6109(16)44080-6

72. Baracos VE. Cancer-associated malnutrition. *Eur J Clin Nutr*. 2018;72(9):1255-1259. doi:10.1038/s41430-018-0245-4

73. de van der Schueren MAE, Laviano A, Blanchard H, Jourdan M, Arends J, Baracos VE. Systematic review and meta-analysis of the evidence for oral nutritional intervention on nutritional and clinical outcomes during chemo(radio)therapy: current evidence and guidance for design of future trials. *Ann Oncol*. 2018;29(5):1141-1153. doi:10.1093/annonc/mdy114

74. Hardee JP, Counts BR, Carson JA. Understanding the Role of Exercise in Cancer Cachexia Therapy. *Am J Lifestyle Med*. 2019;13(1):46-60. doi:10.1177/1559827617725283

75. Peixoto da Silva S, Santos JMO, Costa E Silva MP, Gil da Costa RM, Medeiros R. Cancer cachexia and its pathophysiology: links with sarcopenia, anorexia and asthenia. *J Cachexia Sarcopenia Muscle*. 2020;11(3):619-635. doi:10.1002/jcsm.12528

76. Evans WK, Makuch R, Clamon GH, et al. Limited impact of total parenteral nutrition on nutritional status during treatment for small cell lung cancer. *Cancer Res*. 1985;45(7):3347-3353. https://www.ncbi.nlm.nih.gov/pubmed/2988769

77. Argilés JM, Fontes-Oliveira CC, Toledo M, López-Soriano FJ, Busquets S. Cachexia: a problem of energetic inefficiency. *J Cachexia Sarcopenia Muscle*. 2014;5(4):279-286. doi:10.1007/s13539-014-0154-x

78. Cori CF. The glucose-lactic acid cycle and gluconeogenesis. *Curr Top Cell Regul*. 1981;18:377-387. https://www.ncbi.nlm.nih.gov/pubmed/7273846

79. Zentella A, Manogue K, Cerami A. Cachectin/TNF-mediated lactate production in cultured myocytes is linked to activation of a futile substrate cycle. *Cytokine*. 1993;5(5):436-447. doi:https://doi.org/10.1016/1043-4666(93)90033-2

80. Nicholls DG, Ferguson StuartJ. *Bioenergetics (Fourth Edition)*.; 2013.

81. Krauss S, Zhang CY, Lowell BB. The mitochondrial uncoupling-protein homologues. *Nat Rev Mol Cell Biol*. 2005;6(3):248-261. doi:10.1038/nrm1592

82. Costford S, Gowing A, Harper ME. Mitochondrial uncoupling as a target in the treatment of obesity. *Curr Opin Clin Nutr Metab Care*. 2007;10(6):671-678. doi:10.1097/MCO.0b013e3282f0dbe4

83. Schrauwen P. Skeletal muscle uncoupling protein 3 (UCP3): mitochondrial uncoupling protein in search of a function. *Curr Opin Clin Nutr Metab Care*. 2002;5(3):265-270. doi:10.1097/00075197-200205000-00005

84. Tzika AA, Fontes-Oliveira CC, Shestov AA, et al. Skeletal muscle mitochondrial uncoupling in a murine cancer cachexia model. *Int J Oncol*. 2013;43(3):886-894. doi:10.3892/ijo.2013.1998

85. Bing C, Brown M, King P, Collins P, Tisdale MJ, Williams G. Increased gene expression of brown fat uncoupling protein (UCP)1 and skeletal muscle UCP2 and UCP3 in MAC16-induced cancer cachexia. *Cancer Res*. 2000;60(9):2405-2410. https://www.ncbi.nlm.nih.gov/pubmed/10811117

86. Sanchís D, Busquets S, Alvarez B, Ricquier D, López-Soriano FJ, Argilés JM. Skeletal muscle UCP2 and UCP3 gene expression in a rat cancer cachexia model. *FEBS Lett*. 1998;436(3):415-418. doi:10.1016/s0014-5793(98)01178-8

87. Collins P, Bing C, McCulloch P, Williams G. Muscle UCP-3 mRNA levels are elevated in weight loss associated with gastrointestinal adenocarcinoma in humans. *Br J Cancer*. 2002;86(3):372-375. doi:10.1038/sj.bjc.6600074

88. Kjelstrup S, Barragán D, Bedeaux D. Coefficients for active transport and thermogenesis of Ca2+-ATPase isoforms. *Biophys J*. 2009;96(11):4376-4386. doi:10.1016/j.bpj.2009.02.070

89. Arruda AP, Ketzer LA, Nigro M, Galina A, Carvalho DP, de Meis L. Cold tolerance in hypothyroid rabbits: role of skeletal muscle mitochondria and sarcoplasmic reticulum Ca2+ ATPase isoform 1 heat production. *Endocrinology*. 2008;149(12):6262-6271. doi:10.1210/en.2008-0564

90. Fontes-Oliveira CC, Busquets S, Toledo M, et al. Mitochondrial and sarcoplasmic reticulum abnormalities in cancer cachexia: Altered energetic efficiency? *Biochimica et Biophysica Acta (BBA) - General Subjects*. 2013;1830(3):2770-2778. doi:https://doi.org/10.1016/j.bbagen.2012.11.009

91. Wilson BE, Jacob S, Yap ML, Ferlay J, Bray F, Barton MB. Estimates of global chemotherapy demands and corresponding physician workforce requirements for 2018

and 2040: a population-based study. *Lancet Oncol*. 2019;20(6):769-780. doi:10.1016/S1470-2045(19)30163-9

92. Weiss RB. The anthracyclines: will we ever find a better doxorubicin? *Semin Oncol*. 1992;19(6):670-686. https://www.ncbi.nlm.nih.gov/pubmed/1462166

93. Gilliam LAA, St Clair DK. Chemotherapy-induced weakness and fatigue in skeletal muscle: the role of oxidative stress. *Antioxid Redox Signal*. 2011;15(9):2543-2563. doi:10.1089/ars.2011.3965

94. Cella PS, Matos RLN de, Marinello PC, et al. Doxorubicin causes cachexia, sarcopenia, and frailty characteristics in mice. *PLoS One*. 2024;19(4):e0301379-. https://doi.org/10.1371/journal.pone.0301379

95. Ertunc M, Sara Y, Korkusuz P, Onur R. Differential contractile impairment of fast- and slow-twitch skeletal muscles in a rat model of doxorubicin-induced congestive heart failure. *Pharmacology*. 2009;84(4):240-248. doi:10.1159/000241723

96. Hiensch AE, Bolam KA, Mijwel S, et al. Doxorubicin-induced skeletal muscle atrophy: Elucidating the underlying molecular pathways. *Acta Physiologica*. 2020;229(2):e13400. doi:https://doi.org/10.1111/apha.13400

97. Zhang C, Xu C, Gao X, Yao Q. Platinum-based drugs for cancer therapy and anti-tumor strategies. *Theranostics*. 2022;12(5):2115-2132. doi:10.7150/thno.69424

98. Johnstone TC, Park GY, Lippard SJ. Understanding and improving platinum anticancer drugs--phenanthriplatin. *Anticancer Res*. 2014;34(1):471-476. https://www.ncbi.nlm.nih.gov/pubmed/24403503

99. Conte E, Bresciani E, Rizzi L, et al. Cisplatin-Induced Skeletal Muscle Dysfunction: Mechanisms and Counteracting Therapeutic Strategies. *Int J Mol Sci*. 2020;21(4). doi:10.3390/ijms21041242

100. Sakai H, Sagara A, Arakawa K, et al. Mechanisms of cisplatin-induced muscle atrophy. *Toxicol Appl Pharmacol*. 2014;278(2):190-199. doi:https://doi.org/10.1016/j.taap.2014.05.001

101. Conte E, Camerino GM, Mele A, et al. Growth hormone secretagogues prevent dysregulation of skeletal muscle calcium homeostasis in a rat model of cisplatin-induced cachexia. *J Cachexia Sarcopenia Muscle*. 2017;8(3):386-404. doi:10.1002/jcsm.12185

102. Damrauer JS, Stadler ME, Acharyya S, Baldwin AS, Couch ME, Guttridge DC. Chemotherapy-induced muscle wasting: association with NF-κB and cancer cachexia. *Eur J Transl Myol*. 2018;28(2):7590. doi:10.4081/ejtm.2018.7590

103. Roeland EJ, Bohlke K, Baracos VE, et al. Management of Cancer Cachexia: ASCO Guideline. *Journal of Clinical Oncology*. 2020;38(21):2438-2453. doi:10.1200/JCO.20.00611

104. de van der Schueren MAE, Laviano A, Blanchard H, Jourdan M, Arends J, Baracos VE. Systematic review and meta-analysis of the evidence for oral nutritional intervention on nutritional and clinical outcomes during chemo(radio)therapy: current evidence and guidance for design of future trials. *Ann Oncol*. 2018;29(5):1141-1153. doi:10.1093/annonc/mdy114

105. McGeer AJ, Detsky AS, O'Rourke K. Parenteral nutrition in cancer patients undergoing chemotherapy: a meta-analysis. *Nutrition*. 1990;6(3):233-240. https://www.ncbi.nlm.nih.gov/pubmed/2152097

106. Tobberup R, Thoresen L, Falkmer UG, Yilmaz MK, Solheim TS, Balstad TR. Effects of current parenteral nutrition treatment on health-related quality of life, physical function, nutritional status, survival and adverse events exclusively in patients with advanced cancer: A systematic literature review. *Crit Rev Oncol Hematol*. 2019;139:96-107. doi:10.1016/j.critrevonc.2019.04.014

107. Ruiz Garcia V, López-Briz E, Carbonell Sanchis R, Gonzalvez Perales JL, Bort-Martí S. Megestrol acetate for treatment of anorexia-cachexia syndrome. *Cochrane Database of Systematic Reviews*. 2013;(3). doi:10.1002/14651858.CD004310.pub3

108. Moertel CG, Schutt AJ, Reitemeier RJ, Hahn RG. Corticosteroid therapy of preterminal gastrointestinal cancer. *Cancer*. 1974;33(6):1607-1609. doi:10.1002/1097-0142(197406)33:6<1607::aid-cncr2820330620>3.0.co;2-v

109. Temel JS, Abernethy AP, Currow DC, et al. Anamorelin in patients with non-small-cell lung cancer and cachexia (ROMANA 1 and ROMANA 2): results from two randomised, double-blind, phase 3 trials. *Lancet Oncol*. 2016;17(4):519-531. doi:10.1016/S1470-2045(15)00558-6

110. Currow D, Temel JS, Abernethy A, Milanowski J, Friend J, Fearon KC. ROMANA 3: a phase 3 safety extension study of anamorelin in advanced non-small-cell lung cancer (NSCLC) patients with cachexia. *Ann Oncol*. 2017;28(8):1949-1956. doi:10.1093/annonc/mdx192

111. Bai Y, Hu Y, Zhao Y, et al. Anamorelin for cancer anorexia-cachexia syndrome: a systematic review and meta-analysis. *Supportive Care in Cancer*. 2017;25(5):1651-1659. doi:10.1007/s00520-016-3560-0

112. Wakabayashi H, Arai H, Inui A. The regulatory approval of anamorelin for treatment of cachexia in patients with non-small cell lung cancer, gastric cancer, pancreatic cancer, and colorectal cancer in Japan: facts and numbers. *J Cachexia Sarcopenia Muscle*. 2020;12(1):14-16. doi:10.1002/jcsm.12675

113. Reid J, Hughes CM, Murray LJ, Parsons C, Cantwell MM. Non-steroidal anti-inflammatory drugs for the treatment of cancer cachexia: a systematic review. *Palliat Med*. 2012;27(4):295-303. doi:10.1177/0269216312441382

114. Costelli P, Muscaritoli M, Bonetto A, et al. Muscle myostatin signalling is enhanced in experimental cancer cachexia. *Eur J Clin Invest*. 2008;38(7):531-538. doi:10.1111/j.1365-2362.2008.01970.x

115. Aversa Z, Bonetto A, Penna F, et al. Changes in myostatin signaling in non-weight-losing cancer patients. *Ann Surg Oncol*. 2011;19(4):1350-1356. doi:10.1245/s10434-011-1720-5

116. Ling T, Zhang J, Ding F, Ma L. Role of growth differentiation factor 15 in cancer cachexia (Review). *Oncol Lett*. 2023;26(5):462. doi:10.3892/ol.2023.14049

117. Smith RC, Cramer MS, Mitchell PJ, et al. Myostatin Neutralization Results in Preservation of Muscle Mass and Strength in Preclinical Models of Tumor-Induced Muscle Wasting. *Mol Cancer Ther*. 2015;14(7):1661-1670. doi:10.1158/1535-7163.MCT-14-0681

118. Kim-Muller JY, Song L, LaCarubba Paulhus B, et al. GDF15 neutralization restores muscle function and physical performance in a mouse model of cancer cachexia. *Cell Rep*. 2023;42(1):111947. doi:10.1016/j.celrep.2022.111947

119. Solheim TS, Laird BJA, Balstad TR, et al. A randomized phase II feasibility trial of a multimodal intervention for the management of cachexia in lung and pancreatic cancer. *J Cachexia Sarcopenia Muscle*. 2017;8(5):778-788. doi:10.1002/jcsm.12201

120. Grande AJ, Silva V, Sawaris Neto L, Teixeira Basmage JP, Peccin MS, Maddocks M. Exercise for cancer cachexia in adults. *Cochrane Database Syst Rev*. 2021;3(3):CD010804. doi:10.1002/14651858.CD010804.pub3

121. Hardee JP, Fix DK, Koh HJ, Wang X, Goldsmith EC, Carson JA. Repeated eccentric contractions positively regulate muscle oxidative metabolism and protein synthesis during cancer cachexia in mice. *J Appl Physiol (1985)*. 2020;128(6):1666-1676. doi:10.1152/japplphysiol.00908.2019

122. Pigna E, Berardi E, Aulino P, et al. Aerobic Exercise and Pharmacological Treatments Counteract Cachexia by Modulating Autophagy in Colon Cancer. *Sci Rep*. 2016;6:26991. doi:10.1038/srep26991

123. Shalamzari SA, Agha-Alinejad H, Alizadeh S, et al. The effect of exercise training on the level of tissue IL-6 and vascular endothelial growth factor in breast cancer bearing mice. *Iran J Basic Med Sci*. 2014;17(4):231-258. https://www.ncbi.nlm.nih.gov/pubmed/24904714

124. McLean JB, Moylan JS, Andrade FH. Mitochondria dysfunction in lung cancer-induced muscle wasting in C2C12 myotubes. *Front Physiol*. 2014;5(503):1-8. doi:10.3389/fphys.2014.00503

125. Ubachs J, van de Worp WRPH, Vaes RDW, et al. Ovarian cancer ascites induces skeletal muscle wasting in vitro and reflects sarcopenia in patients. *J Cachexia Sarcopenia Muscle*. 2022;13(1):311-324. doi:10.1002/jcsm.12885

126. Calore F, Londhe P, Fadda P, et al. The TLR7/8/9 Antagonist IMO-8503 Inhibits Cancer-Induced Cachexia. *Cancer Res*. 2018;78(23):6680-6690. doi:10.1158/0008-5472.CAN-17-3878

127. Smith HJ, Lorite MJ, Tisdale MJ. Effect of a cancer cachectic factor on protein synthesis/degradation in murine C2C12 myoblasts: Modulation by eicosapentaenoic acid. *Cancer Res*. 1999;59:5507-5513.

128. Ballarò R, Costelli P, Penna F. Animal models for cancer cachexia. *Curr Opin Support Palliat Care*. 2016;10(2):281-287. doi:10.1097/SPC.0000000000000233

129. Talbert EE, Cuitiño MC, Ladner KJ, et al. Modeling Human Cancer-induced Cachexia. *Cell Rep*. 2019;28(6):1612-1622.e4. doi:10.1016/j.celrep.2019.07.016

130. Luan Y, Zhang Y, Yu SY, et al. Development of ovarian tumour causes significant loss of muscle and adipose tissue: a novel mouse model for cancer cachexia study. *J Cachexia Sarcopenia Muscle*. 2022;13(2):1289-1301. doi:10.1002/jcsm.12864

131. Spadafora V, Pryce BR, Oles A, et al. Optimization of a mouse model of pancreatic cancer to simulate the human phenotypes of metastasis and cachexia. *BMC Cancer*. 2024;24(1):414. doi:10.1186/s12885-024-12104-0

132. Nosacka RL, Delitto AE, Delitto D, et al. Distinct cachexia profiles in response to human pancreatic tumours in mouse limb and respiratory muscle. *J Cachexia Sarcopenia Muscle*. 2020;11(3):820-837. doi:https://doi.org/10.1002/jcsm.12550

133. Go KL, Delitto D, Judge SM, et al. Orthotopic Patient-Derived Pancreatic Cancer Xenografts Engraft Into the Pancreatic Parenchyma, Metastasize, and Induce Muscle Wasting to Recapitulate the Human Disease. *Pancreas*. 2017;46(6):813-819. doi:10.1097/MPA.0000000000000843

134. Ledford H. Cocktails for cancer with a measure of immunotherapy. *Nature*. 2016;532(7598):162-164. doi:10.1038/532162a

135. Bonetto A, Rupert JE, Barreto R, Zimmers TA. The Colon-26 Carcinoma Tumor-bearing Mouse as a Model for the Study of Cancer Cachexia. *J Vis Exp*. 2016;(117):54893. doi:10.3791/54893

136. Murphy KT, Chee A, Trieu J, Naim T, Lynch GS. Importance of functional and metabolic impairments in the characterization of the C-26 murine model of cancer cachexia. *DMM Disease Models and Mechanisms*. 2012;5:533-545. doi:10.1242/dmm.008839

137. Graves E, Hitt A, Pariza MW, Cook ME, McCarthy DO. Conjugated linoleic acid preserves gastrocnemius muscle mass in mice bearing the colon-26 adenocarcinoma. *Res Nurs Health*. 2005;28(1):48-55. doi:10.1002/nur.20052

138. Khamoui A V, Park BS, Kim DH, et al. Aerobic and resistance training dependent skeletal muscle plasticity in the colon-26 murine model of cancer cachexia. *Metabolism*. 2016;65(5):685-698. doi:10.1016/j.metabol.2016.01.014

139. Smuder AJ, Roberts BM, Wiggs MP, et al. Pharmacological targeting of mitochondrial function and reactive oxygen species production prevents colon 26 cancer-induced cardiorespiratory muscle weakness. *Oncotarget*. 2020;11(38):3502-3514. doi:10.18632/oncotarget.27748

140. Pin F, Huot JR, Bonetto A. The Mitochondria-Targeting Agent MitoQ Improves Muscle Atrophy, Weakness and Oxidative Metabolism in C26 Tumor-Bearing Mice. *Front Cell Dev Biol*. 2022;10(March):1-13. doi:10.3389/fcell.2022.861622

141. Ballarò R, Lopalco P, Audrito V, et al. Targeting Mitochondria by SS-31 Ameliorates the Whole Body Energy Status in Cancer- and Chemotherapy-Induced Cachexia. *Cancers (Basel)*. 2021;13(4):850. doi:10.3390/cancers13040850

142. Moser AR, Pitot HC, Dove WF. A dominant mutation that predisposes to multiple intestinal neoplasia in the mouse. *Science (1979)*. 1990;247(4940):322-324. doi:10.1126/science.2296722

143. Su LK, Kinzler KW, Vogelstein B, et al. Multiple intestinal neoplasia caused by a mutation in the murine homolog of the APC gene. *Science (1979)*. 1992;256(5057):668-670. doi:10.1126/science.1350108

144. VanderVeen BN, Hardee JP, Fix DK, Carson JA. Skeletal muscle function during the progression of cancer cachexia in the male Apc(Min/+) mouse. *J Appl Physiol (1985)*. 2017;124(3):684-695. doi:10.1152/japplphysiol.00897.2017

145. Narsale AA, Puppa MJ, Hardee JP, et al. Short-term pyrrolidine dithiocarbamate administration attenuates cachexia-induced alterations to muscle and liver in ApcMin/+ mice. *Oncotarget*. 2016;7(37):59482-59502. doi:10.18632/oncotarget.10699

146. Velázquez KT, Enos RT, Narsale AA, et al. Quercetin supplementation attenuates the progression of cancer cachexia in ApcMin/+ mice. *J Nutr*. 2014;144(6):868-875. doi:10.3945/jn.113.188367

147. Bray F, Ferlay J, Soerjomataram I, Siegel RL, Torre LA, Jemal A. Global cancer statistics 2018: GLOBOCAN estimates of incidence and mortality worldwide for 36 cancers in 185 countries. *CA Cancer J Clin*. 2018;68(6):394-424. doi:10.3322/caac.21492

148. Pin F, Barreto R, Kitase Y, et al. Growth of ovarian cancer xenografts causes loss of muscle and bone mass: a new model for the study of cancer cachexia. *J Cachexia Sarcopenia Muscle*. 2018;9(4):685-700. doi:10.1002/jcsm.12311

149. Straughn AR, Kelm NQ, Kakar SS. Withaferin A and Ovarian Cancer Antagonistically Regulate Skeletal Muscle Mass. *Front Cell Dev Biol*. 2021;9:636498. doi:10.3389/fcell.2021.636498

150. Johns N, Hatakeyama S, Stephens NA, et al. Clinical classification of cancer cachexia: phenotypic correlates in human skeletal muscle. *PLoS One*. 2014;9(1):e83618. doi:10.1371/journal.pone.0083618

151. Zhang Y, Wang J, Wang X, et al. The autophagic-lysosomal and ubiquitin proteasome systems are simultaneously activated in the skeletal muscle of gastric cancer patients with cachexia. *Am J Clin Nutr*. 2020;111(3):570-579. doi:10.1093/ajcn/nqz347

152. Op den Kamp CM, Langen RC, Snepvangers FJ, et al. Nuclear transcription factor κ B activation and protein turnover adaptations in skeletal muscle of patients with progressive stages of lung cancer cachexia1234. *Am J Clin Nutr*. 2013;98(3):738-748. doi:https://doi.org/10.3945/ajcn.113.058388

153. Dolly A, Dumas JF, Servais S. Cancer cachexia and skeletal muscle atrophy in clinical studies: what do we really know? *J Cachexia Sarcopenia Muscle*. 2020;11(6):1413-1428. doi:10.1002/jcsm.12633

154. Op den Kamp CM, Gosker HR, Lagarde S, et al. Preserved muscle oxidative metabolic phenotype in newly diagnosed non-small cell lung cancer cachexia. *J Cachexia Sarcopenia Muscle*. 2015;6(2):164-173. doi:10.1002/jcsm.12007

155. Judge SM, Nosacka RL, Delitto D, et al. Skeletal Muscle Fibrosis in Pancreatic Cancer Patients with Respect to Survival. *JNCI Cancer Spectr*. 2018;2(3):ky043. doi:10.1093/jncics/pky043

156. Stephens NA, Skipworth RJE, Macdonald AJ, Greig CA, Ross JA, Fearon KCH. Intramyocellular lipid droplets increase with progression of cachexia in cancer patients. *J Cachexia Sarcopenia Muscle*. 2011;2(2):111-117. doi:10.1007/s13539-011-0030-x

157. Acharyya S, Butchbach MER, Sahenk Z, et al. Dystrophin glycoprotein complex dysfunction: a regulatory link between muscular dystrophy and cancer cachexia. *Cancer Cell*. 2005;8(5):421-432. doi:10.1016/j.ccr.2005.10.004

158. Roberts BM, Ahn B, Smuder AJ, et al. Diaphragm and ventilatory dysfunction during cancer cachexia. *FASEB J*. 2013;27(7):2600-2610. doi:10.1096/fj.12-222844

159. Hardee JP, Mangum JE, Gao S, et al. Eccentric contraction-induced myofiber growth in tumor-bearing mice. *J Appl Physiol (1985)*. 2015;120(1):29-37. doi:10.1152/japplphysiol.00416.2015

160. Murphy KT, Struk A, Malcontenti-Wilson C, Christophi C, Lynch GS. Physiological characterization of a mouse model of cachexia in colorectal liver metastases. *American Journal of Physiology-Regulatory, Integrative and Comparative Physiology*. 2013;304(10):R854-R864. doi:10.1152/ajpregu.00057.2013

161. Washington TA, Schrems ER, Haynie WS, et al. Development of skeletal muscle fibrosis in a rodent model of cancer cachexia. *Cell Biochem Funct*. 2023;41(4):478-489. doi:10.1002/cbf.3797

162. Alves MJ, Figuerêdo RG, Azevedo FF, et al. Adipose tissue fibrosis in human cancer cachexia: the role of TGFβ pathway. *BMC Cancer*. 2017;17(1):190. doi:10.1186/s12885-017-3178-8

163. Frontera WR, Ochala J. Skeletal Muscle: A Brief Review of Structure and Function. *Calcif Tissue Int*. 2015;96(3):183-195. doi:10.1007/s00223-014-9915-y

164. Calderón JC, Bolaños P, Caputo C. The excitation-contraction coupling mechanism in skeletal muscle. *Biophys Rev*. 2014;6(1):133-160. doi:10.1007/s12551-013-0135-x

165. Galińska-Rakoczy A, Engel P, Xu C, et al. Structural basis for the regulation of muscle contraction by troponin and tropomyosin. *J Mol Biol*. 2008;379(5):929-935. doi:10.1016/j.jmb.2008.04.062

166. Bellissimo C, Perry C. Regulation of Skeletal Muscle Reactive Oxygen Species During Exercise. In: *The Routledge Handbook on Biochemistry of Exercise*. 1st ed. Taylor & Francis Group; 2020:1-20.

167. Anderson LJ, Lee J, Mallen MC, et al. Evaluation of physical function and its association with body composition, quality of life and biomarkers in cancer cachexia patients. *Clin Nutr*. 2020;40(3):978-986. doi:10.1016/j.clnu.2020.07.001

168. Gale N, Wasley D, Roberts S, et al. A longitudinal study of muscle strength and function in patients with cancer cachexia. *Supportive Care in Cancer*. 2019;27(1):131-137. doi:10.1007/s00520-018-4297-8

169. Xie H, Ruan G, Wei L, et al. Hand grip strength-based cachexia index as a predictor of cancer cachexia and prognosis in patients with cancer. *J Cachexia Sarcopenia Muscle*. 2023;14(1):382-390. doi:https://doi.org/10.1002/jcsm.13139

170. Springer J, Jové Q, de Lima Junior EA, et al. Effects of S-pindolol in mouse pancreatic and lung cancer cachexia models. *J Cachexia Sarcopenia Muscle*. 2023;14(3):1244-1248. doi:10.1002/jcsm.13249

171. Roberts BM, Frye GS, Ahn B, Ferreira LF, Judge AR. Cancer cachexia decreases specific force and accelerates fatigue in limb muscle. *Biochem Biophys Res Commun*. 2013;435(3):488-492. doi:10.1016/j.bbrc.2013.05.018

172. Huot JR, Pin F, Bonetto A. Muscle weakness caused by cancer and chemotherapy is associated with loss of motor unit connectivity. *Am J Cancer Res*. 2021;11(6):2990-3001. https://www.ncbi.nlm.nih.gov/pubmed/34249440

173. Mitchell P. Coupling of phosphorylation to electron and hydrogen transfer by a chemi-osmotic type of mechanism. *Nature*. 1961;191:144-148. doi:10.1038/191144a0

174. Nelson DL, Cox MM. *Lehninger Principles of Biochemistry, Sixth Edition.*; 2013. doi:10.1017/CBO9781107415324.004

175. Sies H, Jones DP. Reactive oxygen species (ROS) as pleiotropic physiological signalling agents. *Nat Rev Mol Cell Biol*. 2020;21(7):363-383. doi:10.1038/s41580-020-0230-3

176. Covarrubias L, Hernández-García D, Schnabel D, Salas-Vidal E, Castro-Obregón S. Function of reactive oxygen species during animal development: Passive or active? *Dev Biol*. 2008;320(1):1-11. doi:10.1016/j.ydbio.2008.04.041

177. Brand MD. The sites and topology of mitochondrial superoxide production. *Exp Gerontol*. 2010;45(7-8):466-472. doi:10.1016/j.exger.2010.01.003

178. Brand MD. Mitochondrial generation of superoxide and hydrogen peroxide as the source of mitochondrial redox signaling. *Free Radic Biol Med*. 2016;100:14-31. doi:https://doi.org/10.1016/j.freeradbiomed.2016.04.001

179. Colombini M. VDAC: The channel at the interface between mitochondria and the cytosol. *Mol Cell Biochem*. 2004;256(1/2):107-115. doi:10.1023/b:mcbi.0000009862.17396.8d

180. Meyer RA, Sweeney HL, Kushmerick MJ. A simple analysis of the “phosphocreatine shuttle”. *Am J Physiol*. 1984;246(5 Pt 1):C365-77. doi:10.1152/ajpcell.1984.246.5.C365

181. Schlattner U, Tokarska-Schlattner M, Wallimann T. Mitochondrial creatine kinase in human health and disease. *Biochim Biophys Acta Mol Basis Dis*. 2006;1762:164-180. doi:10.1016/j.bbadis.2005.09.004

182. Houston ME. *Biochemistry Primer for Exercise Science*. Third.; 2006. doi:10.1097/00005768-199604000-00022

183. Guzun R, Gonzalez-Granillo M, Karu-Varikmaa M, et al. Regulation of respiration in muscle cells in vivo by VDAC through interaction with the cytoskeleton and MtCK within Mitochondrial Interactosome. *Biochimica et Biophysica Acta (BBA) - Biomembranes*. 2012;1818(6):1545-1554. doi:https://doi.org/10.1016/j.bbamem.2011.12.034

184. Wallimann T, Tokarska-Schlattner M, Schlattner U. The creatine kinase system and pleiotropic effects of creatine. *Amino Acids*. 2011;40(5):1271-1296. doi:10.1007/s00726-011-0877-3

185. Aliev M, Guzun R, Karu-Varikmaa M, Kaambre T, Wallimann T, Saks V. Molecular system bioenergics of the heart: experimental studies of metabolic compartmentation and energy fluxes versus computer modeling. *Int J Mol Sci*. 2011;12(12):9296-9331. doi:10.3390/ijms12129296

186. Halliwell B. Antioxidants: The Basics-what they are and how to Evaluate them. In: Sies H, ed. *Advances in Pharmacology*. Vol 38. Academic Press; 1996:3-20. doi:https://doi.org/10.1016/S1054-3589(08)60976-X

187. Sheu SS, Nauduri D, Anders MW. Targeting antioxidants to mitochondria: A new therapeutic direction. *Biochimica et Biophysica Acta (BBA) - Molecular Basis of Disease*. 2006;1762(2):256-265. doi:https://doi.org/10.1016/j.bbadis.2005.10.007

188. Murphy MP. Targeting lipophilic cations to mitochondria. *Biochimica et Biophysica Acta (BBA) - Bioenergetics*. 2008;1777(7):1028-1031. doi:https://doi.org/10.1016/j.bbabio.2008.03.029

189. Severin FF, Severina II, Antonenko YN, et al. Penetrating cation/fatty acid anion pair as a mitochondria-targeted protonophore. *Proceedings of the National Academy of Sciences*. 2010;107(2):663-668. doi:10.1073/pnas.0910216107

190. Zhao K, Zhao GM, Wu D, et al. Cell-permeable Peptide Antioxidants Targeted to Inner Mitochondrial Membrane inhibit Mitochondrial Swelling, Oxidative Cell Death, and Reperfusion Injury *. *Journal of Biological Chemistry*. 2004;279(33):34682-34690. doi:10.1074/jbc.M402999200

191. Brand MD, Nicholls DG. Assessing mitochondrial dysfunction in cells. *Biochem J*. 2011;435(2):297-312. doi:10.1042/BJ20110162

192. Julienne CM, Dumas JF, Goupille C, et al. Cancer cachexia is associated with a decrease in skeletal muscle mitochondrial oxidative capacities without alteration of ATP production efficiency. *J Cachexia Sarcopenia Muscle*. 2012;3(4):265-275. doi:10.1007/s13539-012-0071-9

193. Dolly A, Lecomte T, Tabchouri N, et al. Pectoralis major muscle atrophy is associated with mitochondrial energy wasting in cachectic patients with gastrointestinal cancer. *J Cachexia Sarcopenia Muscle*. 2022;13(3):1837-1849. doi:10.1002/jcsm.12984

194. Davies MJ. Protein oxidation and peroxidation. *Biochem J*. 2016;473(7):805-825. doi:10.1042/BJ20151227

195. Barreiro E, de la Puente B, Busquets S, López-Soriano FJ, Gea J, Argilés JM. Both oxidative and nitrosative stress are associated with muscle wasting in tumour-bearing rats. *FEBS Lett*. 2005;579(7):1646-1652. doi:10.1016/j.febslet.2005.02.017

196. Fukawa T, Yan-Jiang BC, Min-Wen JC, et al. Excessive fatty acid oxidation induces muscle atrophy in cancer cachexia. *Nat Med*. 2016;22(6):666-671. doi:10.1038/nm.4093

197. Kanvah S, Joseph J, Schuster GB, Barnett RN, Cleveland CL, Landman U. Oxidation of DNA: damage to nucleobases. *Acc Chem Res*. 2010;43(2):280-287. doi:10.1021/ar900175a

198. Horvath SE, Daum G. Lipids of mitochondria. *Prog Lipid Res*. 2013;52(4):590-614. doi:10.1016/j.plipres.2013.07.002

199. Smith RAJ, Murphy MP. Animal and human studies with the mitochondria-targeted antioxidant MitoQ. *Ann N Y Acad Sci*. 2010;1201:96-103. doi:10.1111/j.1749-6632.2010.05627.x

200. Petrov A, Perekhvatova N, Skulachev M, Stein L, Ousler G. SkQ1 Ophthalmic Solution for Dry Eye Treatment: Results of a Phase 2 Safety and Efficacy Clinical Study in the Environment and During Challenge in the Controlled Adverse Environment Model. *Adv Ther*. 2016;33(1):96-115. doi:10.1007/s12325-015-0274-5

201. Kasvis P, Vigano M, Vigano A. Health-related quality of life across cancer cachexia stages. *Ann Palliat Med*. 2019;8(1):33-42. doi:10.21037/apm.2018.08.04

202. Arthur ST, Van Doren BA, Roy D, Noone JM, Zacherle E, Blanchette CM. Cachexia among US cancer patients. *J Med Econ*. 2016;19(9):874-880. doi:10.1080/13696998.2016.1181640

203. Toyama EQ, Herzig S, Courchet J, et al. AMP-activated protein kinase mediates mitochondrial fission in response to energy stress. *Science*. 2016;351(6270):275-281. doi:10.1126/science.aab4138

204. Hancock CR, Han DH, Chen M, et al. High-fat diets cause insulin resistance despite an increase in muscle mitochondria. *Proceedings of the National Academy of Sciences*. 2008;105(22):7815 LP - 7820. doi:10.1073/pnas.0802057105

205. Hughes MC, Ramos S V, Turnbull PC, et al. Impairments in left ventricular mitochondrial bioenergetics precede overt cardiac dysfunction and remodelling in Duchenne muscular dystrophy. *J Physiol*. 2020;598(7):1377-1392. doi:10.1113/JP277306

206. Hughes MC, Ramos S V., Turnbull PC, et al. Early myopathy in Duchenne muscular dystrophy is associated with elevated mitochondrial H2O2 emission during impaired oxidative phosphorylation. *J Cachexia Sarcopenia Muscle*. 2019;10(3):643-661. doi:10.1002/jcsm.12405

207. Ramos S V, Hughes MC, Delfinis LJ, Bellissimo CA, Perry CGR. Mitochondrial bioenergetic dysfunction in the D2.mdx model of Duchenne muscular dystrophy is associated with microtubule disorganization in skeletal muscle. *PLoS One*. 2020;15(10):e0237138. doi:10.1371/journal.pone.0237138

208. Turnbull PC, Hughes MC, Perry CGR. The fatty acid derivative palmitoylcarnitine abrogates colorectal cancer cell survival by depleting glutathione. *Am J Physiol Cell Physiol*. 2019;317(6):C1278-C1288. doi:10.1152/ajpcell.00319.2019

209. Kuznetsov A V, Tiivel T, Sikk P, et al. Striking differences between the kinetics of regulation of respiration by ADP in slow-twitch and fast-twitch muscles in vivo. *Eur J Biochem*. 1996;241(3):909-915. doi:10.1111/j.1432-1033.1996.00909.x

210. Schlattner U, Kay L, Tokarska-Schlattner M. Mitochondrial Proteolipid Complexes of Creatine Kinase. *Subcell Biochem*. 2018;87:365-408. doi:10.1007/978-981-10-7757-9_13

211. Rosa-Caldwell ME, Benson CA, Lee DE, et al. Mitochondrial Function and Protein Turnover in the Diaphragm are Altered in LLC Tumor Model of Cancer Cachexia. *Int J Mol Sci*. 2020;21(21):7841. doi:10.3390/ijms21217841

212. Jones DP. Radical-free biology of oxidative stress. *Am J Physiol Cell Physiol*. 2008;295(4):C849-68. doi:10.1152/ajpcell.00283.2008

213. Go YM, Jones DP. Redox control systems in the nucleus: mechanisms and functions. *Antioxid Redox Signal*. 2010;13(4):489-509. doi:10.1089/ars.2009.3021

214. Jackson MJ. Redox regulation of skeletal muscle. *IUBMB Life*. 2008;60(8):497-501. doi:https://doi.org/10.1002/iub.72

215. Ørtenblad N, Stephenson DG. Rapid Report. *J Physiol*. 2003;548(1):139-145. doi:https://doi.org/10.1111/j..2003.t01-1-00139.x

216. Matsumoto C, Sekine H, Nahata M, et al. Role of Mitochondrial Dysfunction in the Pathogenesis of Cisplatin-Induced Myotube Atrophy. *Biol Pharm Bull*. 2022;45(6):780-792. doi:10.1248/bpb.b22-00171

217. Steinberg GR, Kemp BE. AMPK in Health and Disease. *Physiol Rev*. 2009;89(3):1025-1078. doi:10.1152/physrev.00011.2008

218. Hargreaves M, Spriet LL. Skeletal muscle energy metabolism during exercise. *Nat Metab*. 2020;2(9):817-828. doi:10.1038/s42255-020-0251-4

219. Mina DS, Langelier D, Adams SC, et al. Exercise as part of routine cancer care. *Lancet Oncol*. 2018;19(9):e433-e436. doi:10.1016/S1470-2045(18)30599-0

220. Talbert EE, Metzger GA, He WA, Guttridge DC. Modeling human cancer cachexia in colon 26 tumor-bearing adult mice. *J Cachexia Sarcopenia Muscle*. 2014;5(4):321-328. doi:10.1007/s13539-014-0141-2

221. Pratt SJP, Lovering RM. A stepwise procedure to test contractility and susceptibility to injury for the rodent quadriceps muscle. *J Biol Methods*. 2014;1(2):e8. doi:10.14440/jbm.2014.34

222. Fajardo VA, Smith IC, Bombardier E, Chambers PJ, Quadrilatero J, Tupling AR. Diaphragm assessment in mice overexpressing phospholamban in slow-twitch type I muscle fibers. *Brain Behav*. 2016;6(6):e00470. doi:10.1002/brb3.470

223. Perry CGR, Kane DA, Lin C Te, et al. Inhibiting myosin-ATPase reveals a dynamic range of mitochondrial respiratory control in skeletal muscle. *Biochemical Journal*. 2011;437(2):215-222. doi:10.1042/BJ20110366

224. Walsh B, Tonkonogi M, Söderlund K, Hultman E, Saks V, Sahlin K. The role of phosphorylcreatine and creatine in the regulation of mitochondrial respiration in human skeletal muscle. *J Physiol*. 2001;537(3):971-978. doi:https://doi.org/10.1111/j.1469-7793.2001.00971.x

225. Perry CGR, Heigenhauser GJF, Bonen A, Spriet LL. High-intensity aerobic interval training increases fat and carbohydrate metabolic capacities in human skeletal muscle. *Appl Physiol Nutr Metab*. 2008;33(6):1112-1123. doi:10.1139/H08-097

226. Chen ZP, Stephens TJ, Murthy S, et al. Effect of Exercise Intensity on Skeletal Muscle AMPK Signaling in Humans. *Diabetes*. 2003;52(9):2205 LP - 2212. doi:10.2337/diabetes.52.9.2205

227. Jubrias SA, Crowther GJ, Shankland EG, Gronka RK, Conley KE. Acidosis inhibits oxidative phosphorylation in contracting human skeletal muscle in vivo. *J Physiol*. 2003;553(2):589-599. doi:https://doi.org/10.1113/jphysiol.2003.045872

228. Wackerhage H, Hoffmann U, Essfeld D, Leyk D, Mueller K, Zange J. Recovery of free ADP, Pi, and free energy of ATP hydrolysis in human skeletal muscle. *J Appl Physiol*. 1998;85(6):2140-2145. doi:10.1152/jappl.1998.85.6.2140

229. Hughes MC, Ramos S V, Turnbull PC, et al. Mitochondrial Bioenergetics and Fiber Type Assessments in Microbiopsy vs. Bergstrom Percutaneous Sampling of Human Skeletal Muscle. *Front Physiol*. 2015;6:360. doi:10.3389/fphys.2015.00360

230. Houde VP, Donzelli S, Sacconi A, et al. AMPK β1 reduces tumor progression and improves survival in p53 null mice. *Mol Oncol*. 2017;11(9):1143-1155. doi:10.1002/1878-0261.12079

231. Bloemberg D, Quadrilatero J. Rapid determination of myosin heavy chain expression in rat, mouse, and human skeletal muscle using multicolor immunofluorescence analysis. *PLoS One*. 2012;7(4):e35273. doi:10.1371/journal.pone.0035273

232. Greene NP, Lee DE, Brown JL, et al. Mitochondrial quality control, promoted by PGC-1α, is dysregulated by Western diet-induced obesity and partially restored by moderate physical activity in mice. *Physiol Rep*. 2015;3(7). doi:10.14814/phy2.12470

233. Glickman ME, Rao SR, Schultz MR. False discovery rate control is a recommended alternative to Bonferroni-type adjustments in health studies. *J Clin Epidemiol*. 2014;67(8):850-857. doi:https://doi.org/10.1016/j.jclinepi.2014.03.012

234. Sajjad H, Imtiaz S, Noor T, Siddiqui YH, Sajjad A, Zia M. Cancer models in preclinical research: A chronicle review of advancement in effective cancer research. *Animal Model Exp Med*. 2021;4(2):87-103. doi:10.1002/ame2.12165

235. Yeung TL, Leung CS, Yip KP, Au Yeung CL, Wong STC, Mok SC. Cellular and molecular processes in ovarian cancer metastasis. A Review in the Theme: Cell and Molecular Processes in Cancer Metastasis. *Am J Physiol Cell Physiol*. 2015;309(7):C444-56. doi:10.1152/ajpcell.00188.2015

236. Bast RCJ, Hennessy B, Mills GB. The biology of ovarian cancer: new opportunities for translation. *Nat Rev Cancer*. 2009;9(6):415-428. doi:10.1038/nrc2644

237. Delfinis LJ, Bellissimo CA, Gandhi S, et al. Muscle weakness precedes atrophy during cancer cachexia and is linked to muscle-specific mitochondrial stress. *JCI Insight*. 2022;7(24). doi:10.1172/jci.insight.155147

238. Berkenblit A, Cannistra SA. Advances in the management of epithelial ovarian cancer. *J Reprod Med*. 2005;50(6):426-438.

239. LI LI, WANG L, ZHANG WEI, et al. Correlation of Serum VEGF Levels with Clinical Stage, Therapy Efficacy, Tumor Metastasis and Patient Survival in Ovarian Cancer. *Anticancer Res*. 2004;24(3B):1973 LP - 1979. http://ar.iiarjournals.org/content/24/3B/1973.abstract

240. Greenaway J, Henkin J, Lawler J, Moorehead R, Petrik J. ABT-510 induces tumor cell apoptosis and inhibits ovarian tumor growth in an orthotopic, syngeneic model of epithelial ovarian cancer. *Mol Cancer Ther*. 2009;8(1):64-74. doi:10.1158/1535-7163.MCT-08-0864

241. Greenaway J, Moorehead R, Shaw P, Petrik J. Epithelial-stromal interaction increases cell proliferation, survival and tumorigenicity in a mouse model of human epithelial ovarian cancer. *Gynecol Oncol*. 2008;108(2):385-394. doi:10.1016/j.ygyno.2007.10.035

242. Matuszewska K, Santry LA, van Vloten JP, et al. Combining Vascular Normalization with an Oncolytic Virus Enhances Immunotherapy in a Preclinical Model of Advanced-Stage Ovarian Cancer. *Clinical Cancer Research*. 2019;25(5):1624-1638. doi:10.1158/1078-0432.CCR-18-0220

243. Russell S, Duquette M, Liu J, Drapkin R, Lawler J, Petrik J. Combined therapy with thrombospondin-1 type I repeats (3TSR) and chemotherapy induces regression and significantly improves survival in a preclinical model of advanced stage epithelial ovarian cancer. *FASEB J*. 2015;29(2):576-588. doi:10.1096/fj.14-261636

244. Greenaway JB, Virtanen C, Osz K, et al. Ovarian tumour growth is characterized by mevalonate pathway gene signature in an orthotopic, syngeneic model of epithelial ovarian cancer. *Oncotarget*. 2016;7(30):47343-47365. doi:10.18632/oncotarget.10121

245. Krause MP, Moradi J, Nissar AA, Riddell MC, Hawke TJ. Inhibition of plasminogen activator inhibitor-1 restores skeletal muscle regeneration in untreated type 1 diabetic mice. *Diabetes*. 2011;60(7):1964-1972. doi:10.2337/db11-0007

246. Dellorusso C, Crawford RW, Chamberlain JS, Brooks S V. Tibialis anterior muscles in mdx mice are highly susceptible to contraction-induced injury. *J Muscle Res Cell Motil*. 2001;22(5):467-475. doi:10.1023/a:1014587918367

247. Tamayo T, Eno E, Madrigal C, Heydemann A, García K, García J. Functional in situ assessment of muscle contraction in wild-type and mdx mice. *Muscle Nerve*. 2016;53(2):260-268. doi:10.1002/mus.24714

248. Bellissimo CA, Delfinis LJ, Hughes MC, et al. Mitochondrial creatine sensitivity is lost in the D2.mdx model of Duchenne muscular dystrophy and rescued by the mitochondrial-enhancing compound Olesoxime. *Am J Physiol Cell Physiol*. 2023;324(5):C1141-C1157. doi:10.1152/ajpcell.00377.2022

249. Bellissimo CA, Gandhi S, Castellani LN, et al. The slow-release adiponectin analogue ALY688-SR modifies early-stage disease development in the D2.mdx mouse model of Duchenne muscular dystrophy. *American Journal of Physiology-Cell Physiology*. Published online December 25, 2023. doi:10.1152/ajpcell.00638.2023

250. Pesta D, Gnaiger E. High-resolution respirometry: OXPHOS protocols for human cells and permeabilized fibers from small biopsies of human muscle. *Methods in Molecular Biology*. 2012;810:25-28. doi:10.1007/978-1-61779-382-0_3

251. Perry CGR, Kane DA, Lanza IR, Neufer PD. Methods for assessing mitochondrial function in diabetes. *Diabetes*. 2013;62(4):1041-1053. doi:10.2337/db12-1219

252. Lambert AJ, Brand MD. Inhibitors of the quinone-binding site allow rapid superoxide production from mitochondrial NADH:ubiquinone oxidoreductase (complex I). *J Biol Chem*. 2004;279(38):39414-39420. doi:10.1074/jbc.M406576200

253. Dobin A, Davis CA, Schlesinger F, et al. STAR: ultrafast universal RNA-seq aligner. *Bioinformatics*. 2013;29(1):15-21. doi:10.1093/bioinformatics/bts635

254. Ritchie ME, Phipson B, Wu D, et al. limma powers differential expression analyses for RNA-sequencing and microarray studies. *Nucleic Acids Res*. 2015;43(7):e47. doi:10.1093/nar/gkv007

255. Ydfors M, Hughes MC, Laham R, Schlattner U, Norrbom J, Perry CGR. Modelling in vivo creatine/phosphocreatine in vitro reveals divergent adaptations in human muscle mitochondrial respiratory control by ADP after acute and chronic exercise. *J Physiol*. 2016;594(11):3127-3140. doi:10.1113/JP271259

256. Cadenas E, Boveris A, Ragan CI, Stoppani AOM. Production of superoxide radicals and hydrogen peroxide by NADH-ubiquinone reductase and ubiquinol-cytochrome c reductase from beef-heart mitochondria. *Arch Biochem Biophys*. 1977;180(2):248-257. doi:https://doi.org/10.1016/0003-9861(77)90035-2

257. Robb EL, Hall AR, Prime TA, et al. Control of mitochondrial superoxide production by reverse electron transport at complex I. *Journal of Biological Chemistry*. 2018;293(25):9869-9879. doi:https://doi.org/10.1074/jbc.RA118.003647

258. Hinkle PC, Butow RA, Racker E, Chance B. Partial Resolution of the Enzymes Catalyzing Oxidative Phosphorylation: XV. REVERSE ELECTRON TRANSFER IN THE FLAVIN-CYTOCHROME b REGION OF THE RESPIRATORY CHAIN OF BEEF HEART SUBMITOCHONDRIAL PARTICLES. *Journal of Biological Chemistry*. 1967;242(22):5169-5173. doi:https://doi.org/10.1016/S0021-9258(18)99410-X

259. St-Pierre J, Buckingham JA, Roebuck SJ, Brand MD. Topology of Superoxide Production from Different Sites in the Mitochondrial Electron Transport Chain*. *Journal of Biological Chemistry*. 2002;277(47):44784-44790. doi:https://doi.org/10.1074/jbc.M207217200

260. Pin F, Novinger LJ, Huot JR, et al. PDK4 drives metabolic alterations and muscle atrophy in cancer cachexia. *FASEB J*. 2019;33(6):7778-7790. doi:10.1096/fj.201802799R

261. Huch S, Nissan T. Interrelations between translation and general mRNA degradation in yeast. *Wiley Interdiscip Rev RNA*. 2014;5(6):747-763. doi:10.1002/wrna.1244

262. Bellissimo CA, Garibotti MC, Perry CGR. Mitochondrial stress responses in Duchenne muscular dystrophy: metabolic dysfunction or adaptive reprogramming? *Am J Physiol Cell Physiol*. 2022;323(3):C718-C730. doi:10.1152/ajpcell.00249.2022

263. Cheng AJ, Hwee DT, Kim LH, et al. Fast skeletal muscle troponin activator CK-2066260 increases fatigue resistance by reducing the energetic cost of muscle contraction. *J Physiol*. 2019;597(17):4615-4625. doi:10.1113/JP278235

264. Baltgalvis KA, Berger FG, Pena MMO, Davis JM, Muga SJ, Carson JA. Interleukin-6 and cachexia in ApcMin/+ mice. *Am J Physiol Regul Integr Comp Physiol*. 2008;294(2):R393-401. doi:10.1152/ajpregu.00716.2007

265. Arter ZL, Desmond D, Berenberg JL, Killeen JL, Bunch K, Merritt MA. Epithelial ovarian cancer survival by race and ethnicity in an equal-access healthcare population. *Br J Cancer*. 2024;130(1):108-113. doi:10.1038/s41416-023-02471-z

266. Curry SJ, Byers T, Hewitt M, eds. *Fulfilling the Potential of Cancer Prevention and Early Detection*.; 2003. doi:10.17226/10263

267. Peterson CM, Johannsen DL, Ravussin E. Skeletal muscle mitochondria and aging: a review. *J Aging Res*. 2012;2012:194821. doi:10.1155/2012/194821

268. Hyatt H, Deminice R, Yoshihara T, Powers SK. Mitochondrial dysfunction induces muscle atrophy during prolonged inactivity: A review of the causes and effects. *Arch Biochem Biophys*. 2019;662:49-60. doi:10.1016/j.abb.2018.11.005

269. Jiang X, Deng W, Tao S, et al. A RIPK3-independent role of MLKL in suppressing parthanatos promotes immune evasion in hepatocellular carcinoma. *Cell Discov*. 2023;9(1):7. doi:10.1038/s41421-022-00504-0

270. Agarwal R, Kaye SB. Ovarian cancer: strategies for overcoming resistance to chemotherapy. *Nat Rev Cancer*. 2003;3(7):502-516. doi:10.1038/nrc1123

271. Campbell NE, Greenaway J, Henkin J, Moorehead RA, Petrik J. The thrombospondin-1 mimetic ABT-510 increases the uptake and effectiveness of cisplatin and paclitaxel in a mouse model of epithelial ovarian cancer. *Neoplasia*. 2010;12(3):275-283. doi:10.1593/neo.91880

272. Dewys WD, Begg C, Lavin PT, et al. Prognostic effect of weight loss prior to chemotherapy in cancer patients. Eastern Cooperative Oncology Group. *Am J Med*. 1980;69(4):491-497. doi:10.1016/s0149-2918(05)80001-3

273. Delfinis LJ, Ogilvie LM, Khajehzadehshoushtar S, et al. Muscle weakness and mitochondrial stress occur before metastasis in a novel mouse model of ovarian cancer cachexia. *bioRxiv*. Published online 2024.

274. Anisimov VN, Egorov M V, Krasilshchikova MS, et al. Effects of the mitochondria-targeted antioxidant SkQ1 on lifespan of rodents. *Aging (Albany NY)*. 2011;3(11):1110-1119. doi:10.18632/aging.100404

275. Gineste C, Youhanna S, Vorrink SU, et al. Enzymatically dissociated muscle fibers display rapid dedifferentiation and impaired mitochondrial calcium control. *iScience*. 2022;25(12):105654. doi:10.1016/j.isci.2022.105654

276. Cheng AJ, Westerblad H. Mechanical isolation, and measurement of force and myoplasmic free [Ca(2+)] in fully intact single skeletal muscle fibers. *Nat Protoc*. 2017;12(9):1763-1776. doi:10.1038/nprot.2017.056

277. Cheng AJ, Allodi I, Chaillou T, et al. Intact single muscle fibres from SOD1(G93A) amyotrophic lateral sclerosis mice display preserved specific force, fatigue resistance and training-like adaptations. *J Physiol*. 2019;597(12):3133-3146. doi:10.1113/JP277456

278. Cheng AJ, Bruton J, Lanner JT, Westerblad H. Antioxidant treatments do not improve force recovery after fatiguing stimulation of mouse skeletal muscle fibres. *J Physiol*. 2014;593(2):457-472. doi:10.1113/jphysiol.2014.279398

279. Solheim TS, Laird BJA, Balstad TR, et al. Cancer cachexia: rationale for the MENAC (Multimodal-Exercise, Nutrition and Anti-inflammatory medication for Cachexia) trial. *BMJ Support Palliat Care*. 2018;8(3):258-265. doi:10.1136/bmjspcare-2017-001440

280. Cheng AJ, Bruton JD, Lanner JT, Westerblad H. Antioxidant treatments do not improve force recovery after fatiguing stimulation of mouse skeletal muscle fibres. *J Physiol*. 2015;593(2):457-472. doi:https://doi.org/10.1113/jphysiol.2014.279398

281. Umanskaya A, Santulli G, Xie W, Andersson DC, Reiken SR, Marks AR. Genetically enhancing mitochondrial antioxidant activity improves muscle function in aging. *Proc Natl Acad Sci U S A*. 2014;111(42):15250-15255. doi:10.1073/pnas.1412754111

282. Skulachev VP, Antonenko YN, Cherepanov DA, et al. Prevention of cardiolipin oxidation and fatty acid cycling as two antioxidant mechanisms of cationic derivatives of plastoquinone (SkQs). *Biochimica et Biophysica Acta (BBA) - Bioenergetics*. 2010;1797(6):878-889. doi:https://doi.org/10.1016/j.bbabio.2010.03.015

283. Taskin S, Stumpf VI, Bachmann J, Weber C, Martignoni ME, Friedrich O. Motor protein function in skeletal abdominal muscle of cachectic cancer patients. *J Cell Mol Med*. 2013;18(1):69-79. doi:10.1111/jcmm.12165

284. Andersson DC, Betzenhauser MJ, Reiken S, et al. Ryanodine receptor oxidation causes intracellular calcium leak and muscle weakness in aging. *Cell Metab*. 2011;14(2):196-207. doi:10.1016/j.cmet.2011.05.014

285. Delmonico MJ, Harris TB, Visser M, et al. Longitudinal study of muscle strength, quality, and adipose tissue infiltration. *Am J Clin Nutr*. 2009;90(6):1579-1585. doi:10.3945/ajcn.2009.28047

286. Abadi A, Glover EI, Isfort RJ, et al. Limb Immobilization Induces a Coordinate Down-Regulation of Mitochondrial and Other Metabolic Pathways in Men and Women. *PLoS One*. 2009;4(8):e6518. https://doi.org/10.1371/journal.pone.0006518

287. Turk R, Sterrenburg E, de Meijer EJ, van Ommen GJB, den Dunnen JT, 't Hoen PAC. Muscle regeneration in dystrophin-deficient mdx mice studied by gene expression profiling. *BMC Genomics*. 2005;6:98. doi:10.1186/1471-2164-6-98

288. Dillekås H, Rogers MS, Straume O. Are 90% of deaths from cancer caused by metastases? *Cancer Med*. 2019;8(12):5574-5576. doi:10.1002/cam4.2474

289. National Cancer Institute. Age and Cancer Risk. National Institutes of Health.

290. Santilli V, Bernetti A, Mangone M, Paoloni M. Clinical definition of sarcopenia. *Clin Cases Miner Bone Metab*. 2014;11(3):177-180. https://www.ncbi.nlm.nih.gov/pubmed/25568649

291. Rostron ZP, Green RA, Kingsley M, Zacharias A. Associations Between Measures of Physical Activity and Muscle Size and Strength: A Systematic Review. *Arch Rehabil Res Clin Transl*. 2021;3(2):100124. doi:10.1016/j.arrct.2021.100124

292. Nunes EA, Stokes T, McKendry J, Currier BS, Phillips SM. Disuse-induced skeletal muscle atrophy in disease and nondisease states in humans: mechanisms, prevention, and recovery strategies. *Am J Physiol Cell Physiol*. 2022;322(6):C1068-C1084. doi:10.1152/ajpcell.00425.2021

293. Miotto PM, Mcglory C, Bahniwal R, Kamal M, Phillips SM, Holloway GP. Supplementation with dietary ω-3 mitigates immobilization-induced reductions in skeletal muscle mitochondrial respiration in young women. *The FASEB Journal*. 2019;33(7):8232-8240. doi:https://doi.org/10.1096/fj.201900095R

294. Zhong X, Zimmers TA. Sex Differences in Cancer Cachexia. *Curr Osteoporos Rep*. 2020;18(6):646-654. doi:10.1007/s11914-020-00628-w

295. Morena da Silva F, Lim S, Cabrera AR, et al. The time-course of cancer cachexia onset reveals biphasic transcriptional disruptions in female skeletal muscle distinct from males. *BMC Genomics*. 2023;24(1):374. doi:10.1186/s12864-023-09462-7

Appendix A: Additional Contributions

The following work encompasses the additional contributions made throughout my PhD that are not included in my dissertation.

Co-Author: Published

1. Ogilvie LM, **Delfinis LJ,** Coyle-Asbil B, Vudatha V, Alshamali R, Garlisi B, Pereira M, Matuszewska K, Garibotti MC, Gandhi S, Brunt KR, Trevino JG, Perry CGR, Petrik J, Simpson JA. Cardiac atrophy, dysfunction and metabolic impairments: a cancer-induced heart failure phenotype. *Am J Pathol,* Accepted June 20 2024.

2. Bellissimo CA, **Delfinis LJ**, Hughes MC, Turnbull PC, Gandhi S, DiBenedetto SN, Rahman FA, Tadi P, Amaral C, Dehghani A, Cobley JN, Quadrilatero J, Schlattner U, Perry CGR. Mitochondrial creatine sensitivity is lost in the D2.mdx model of Duchenne muscular dystrophy and rescued by the mitochondrial-enhancing compound Olesoxime. *Am J Physiol Cell Physiol*, 2023; 324(5):C1141-C1157. PMID: 36689672

3. Bellissimo CA, Gandhi S, Castellani LN, Murugathasan M, **Delfinis LJ**, Thuhan A, Garibotti MC, Seo Y, Rebalka IA, Hsu HH, Sweeney G, Hawke TJ, Abdul-Sater AA, Perry CGR. The slow-release adiponectin analog ALY688-SR modifies early-stage disease development in the D2.*mdx* mouse model of Duchenne muscular dystrophy. *Am J Physiol Cell Physiol*, 2024; 326(4):C1011-C1026. PMID: 38145301

4. Ferguson EJ, Bureau J, Stokes T, Nyman D, Seigel J, Gandhi S, **Delfinis LJ**, Gurd BJ, Perry CGR, McGlory C. Quantifying variability associated with high-resolution respirometry in human permeabilized skeletal muscle fibres. *Advanced Exercise and Health Science,* Accepted May 30 2024

First Author: In Progress

1. **Delfinis LJ**, Khajehzadehshoushtar S, and Perry CGR. Understanding mitochondrial function vs dysfunction in non-disease- and disease-induced muscle disuse/inactivity. Invited review, *J Phyiol*.

Co-Author: In Progress

1. Gandhi S, **Delfinis LJ,** Bhatt PD, Garibotti MC, Bellissimo C, Goli AN, Morris BA, Brahmbhatt AN, Castellani LN, Yakobov S, Backx PH, Edgett BA, Simpson JA, Sweeney G, Hsu HH, Perry CGR. Robust right ventricular fibrosis in a mouse model of Duchenne muscular dystrophy is prevented by the anti-inflammatory adiponectin receptor agonist ALY688.

2. Khajehzadehshoushtar S, **Delfinis LJ**, Garibotti MC, Gandhi S, Brahmbhatt AN, Morris BA, Garlisi B, Lauks S, Aitken C, Petrik J, Perry CGR. Exploring the relationship between mitochondrial-linked cell death and muscle atrophy during ovarian cancer progression.

3. Garibotti MC, Thuhan AT, **Delfinis LJ**, Khajehzadehshoushtar S, Abdul-Sater AA, Perry CGR. An examination of relationships between mitochondrial stress and muscle health in a modified mouse model of experimental autoimmune myositis.

4. Coyle-Asbil B, Ogilvie LM, Pereira M, Matuszewska M, **Delfinis LJ,** Brunt KR, Perry CGR, Petrik J, Simpson JA. The progression of changes in cardiac structure and function in mice with epithelial ovarian cancer.

5. Lesinki M, Mikhail A, Rishi S, Rebalka IA, **Delfinis LJ,** Perry CGR, Hawke TJ, Ljubicic V. AMPK is required for skeletal muscle mass maintenance in cancer cachexia through the regulation of mitochondrial dynamics and fibrosis.

6. Tsitkanou S, Morena da Dilva F, Cabrera AR, Schrems ER, Muhyudin. R, Koopmans P, Khadgi S, Lim S, **Delfinis LJ**, Washington TA, Murach KA, Pery CGR, Greene NP. Mitochondrial antioxidant SkQ1 attenuates cancer-induced muscle wasting in males and muscle weakness in females.

7. Collaboration with Dr. Jim Dowling at University of Toronto evaluating mitochondrial function in Pik3c2b KO cells.

Appendix B: Detailed Experimental Methods

B.1 C26- Inoculation

Tumour Inoculation – SOP: LD
Updated September 2020

Growing and implanting C26 cells: **NEED TO GROW CELLS 4/5 DAYS PRIOR TO INJECTION FOR PROPER CONFLUENCY AND VOLUME ON INJECTION DAY**

1) Warm all C26 growth media (10%FBS, 1% P/S) to 37^{o} in a waterbath
2) Thaw frozen vial of C26 cells in waterbath and follow "cell thawing technique" (See SOP)
3) Pipette all cells (should be ~1.5x10^6 cells, depends how much was frozen down) into flask and tilt to spread cells evenly.
4) Place in incubator and check ~2 hours later that cells are beginning to adhere.
5) Replace media every 2 days until Injection day (Cells should be growing for 4-5 days and flask should be ~70%-90% confluency)

Injection Day:

6) Remove media and rinse flask with PBS twice.
7) Add trypsin (1mL for T75)
8) Incubate ~5 min
9) Gently tap plate.
10) Add at least 2ml of culture media to plate and pipet around plate to dislodge cells.
11) Collect media+cells in 15mL tube.
    (1) Add 20 uL of cell cocktail to 180 uL of tryban blue. Flick tube to mix
    (2) Count the cells by loading 10uL on hematocytometer with coverglass on top.
12) Spin down at 1000RPM (200g) for 5min.
13) Remove supernatant without disturbing the pellet.
14) Add ~5mL PBS to cell pellet and mix by gentle pipetting.
15) Repeat steps 12-15 2x. (2 Spin downs with PBS in total).
16) Re-suspend pellet in 5 x 10^6 cells/mL
    (1) Keep cells on ice and inject within 3 hours.
17) Inject
    a) Anesthetize in isoflurane box and place prone in nose cone.
        i) Shave both flanks near hindlimb
        ii) Sterilize the skin surface
        iii) Draw up 140uL of cell suspension (5x10^5 cells).
        iv) Remove needle, dispose and insert new sterile needle with cell suspension in syringe.
            (1) Note:140uL was drawn initially to ACCOUNT for volume lost when changing needle tips (data in Luca Delfinis Lab book MSc2/PhD1)
        v) Insert needle subcutaneously so that bevel is visible through surface of the skin.

vi) Slowly inject cells so that a symmetrical bubble arises from the flank.
    (1) Do not remove needle immediately but rather wait ~15 seconds and withdraw very slowly to prevent cells from coming out of injection site.
    (2) Pinch needle ever so slightly while removing so cells do not grow around injection site
vii) Tumor development should become obvious around 2 weeks post injection

B.2 In-Situ Quadriceps Force

In Situ Quad Force Production Protocol
Edited LD December 2020

See attached paper for step up procedure with videos (1).

A good rule of thumb is to have practiced this surgery at least 10-15 times and be able to get consistent data with previous literature. If you are doing a new model establish your own normal values in a pilot data set.

Set-Up

1. Once mouse is under Isoflurane, apply nair on right leg and leave for 10 minutes
2. Wipe all hair off and make a very small cut at the skin over the patellar tendon
3. Use your forceps to stab underneath the patellar tendon and feed suture thread through with a loop already tied (ask experienced lab members for guidance if confused)
4. Tie **3 knots** at the patellar tendon to ensure knot does not slip during force protocol
5. Cut the tendon underneath the knot
6. Hook suture thread to force transducer and turn all Aurora equipment on

Protocol

1. Create a folder to save files for each animal - Setup: Autosave Folder, open folder you created; click "current folder"
2. Setup: Instant Stim
    a. Pulse Frequency: 1Hz
    b. Pulse Width: 0.2ms
    c. Number of Pulses: 1
    d. Train Frequency: 0.1Hz
    e. Run Time: 1 second
    ** I have a train frequency that does 3 twitches with a delay between that I find most useful for optimizing current
3. Open Live Data monitor and set time to 10 minutes
4. Optimize Resting Length
    a. Before officially setting optimal length, you will need to toggle the thread from the quad to the hook with forceps- this will reduce any basal tension in the line
    b. Increase/decrease length of quad until maximal twitch force is achieved, wait about 30 seconds in between twitches to avoid fatigue
    c. Time and keep basal tension about constant in the study
5. Optimize Current
    a. Range:10mA -100mA (if you can get the right placement this can go to 10mA, but if you struggle can go to 10% of 100mA- still 10mA)
    b. Run instant stim
    c. Adjust range to ensure all muscle fibres are being recruited – obtain 3 twitches in a row where force does not increase (run instant stim and increase current between twitches (wait about 30 seconds in between twitches)
    d. Set supramaximal current by increasing current by 15%

Once optimal current and length have been set, protocol is ready to begin

6. Load **"Quad In Situ Force Frequency"** sequence
    a. Frequencies of 40Hz, 60Hz, 80Hz, 100Hz, 120Hz, 140Hz, 160Hz,180Hz, 200Hz, 220Hz
        i. Initial Delay: 0.2ms
        ii. Pulse Frequency: ____Hz (above frequency)
        iii. Pulse Width: 0.2ms
        iv. Duration: 300ms
    b. 45 seconds in between (can extend up to 1 min)
7. Allow 5 minutes of recovery
8. Load the tetanic protocol at the frequency that produced the highest force during step 6
9. Perform Pre Fatigue Max Force Test – make sure to save this file!
10. Allow 2 minutes recovery
11. Load "**Quad In Situ Fatigue"** sequence for your study (Fatigue protocols are varied in the literature- find one that works for your study
    a. 60 Hz, stim every second for 120 seconds (2mins)
    b. 60Hz, stim every 1.5 seconds for 120 contractions (3mins)
12. Allow 5-minute recovery from fatigue
13. Perform a second max force test at the same frequency used in step 8 – this assesses recovery from fatigue- label as **5min-post-fatigue**
14. Allow 5 minute recovery; perform another max force-label as **10min-post-fatigue**
15. Allow 5 minutes recovery; perform last max force-label as **15min-post-fatigue**
16. Harvest muscle and before freezing **MAKE SURE TO RECORD MUSCLE WEIGHT**

Data will be normalized muscle weight

B.3 In-Situ TA Force

In Situ TA Force Production Protocol
MG and LD

A good rule of thumb is to have practiced this surgery at least 10-15 times and be able to get consistent data with previous literature. If you are doing a new model establish your own normal values in a pilot data set.

Protocol

1. Create a folder to save files for each animal - Setup: Autosave Folder, open folder you created; click "current folder"
2. Setup: Instant Stim
    a. Pulse Frequency: 1Hz
    b. Pulse Width: 0.2ms
    c. Number of Pulses: 1
    d. Train Frequency: 0.1Hz
    e. Run Time: 1 second
    ** I have a train frequency that does 3 twitches with a delay between that I find most useful for optimizing current
3. Open Live Data monitor and set time to 10 minutes
4. Once TA has been sutured at the distal tendon and tied to force transducer, insert needle electrodes in the fascia underneath the TA. Note: do not insert needles directly into muscle belly.
5. Optimize Current
    a. **Range:10mA -100mA (if you can get the right placement this can go to 10mA, but if you struggle can go to 10% of 100mA). If you placed the electrodes well you will be able to stimulate the sciatic nerve with very little current (20% of 10mA).**
    b. Run instant stim
    c. Adjust range to ensure all muscle fibres are being recruited – obtain 3 twitches in a row where force does not increase (run instant stim and increase current between twitches (wait about 30 seconds in between twitches)
    d. Set supramaximal current by increasing current by 15%
6. Optimize Resting Length
    a. Increase/decrease length until maximal twitch force is achieved, wait about 30 seconds in between twitches to avoid twitch potentiation.
    b. On average ~10week old female mice have ~10 baseline tension for reference. This can change with age, sex, breed, and disease.

Once optimal current and length have been set, record muscle length and protocol is ready to begin. This step is crucial as the in-situ set-up can have human variability in how high you cut the TA. Recording length ensures consistency.

7. Load **"TA In Situ Force Frequency"** sequence

a. Frequencies of 1Hz, 10Hz, 20Hz, 30Hz, 40Hz, 50Hz, 60Hz, 80Hz, 100Hz, 120Hz, 200Hz
    i. Initial Delay: 0.2ms
    ii. Pulse Frequency: ____Hz (above frequency)
    iii. Pulse Width: 0.2ms
    iv. Duration: 300ms
b. 1 minute in between

8. Harvest muscle and before freezing **MAKE SURE TO RECORD MUSCLE WEIGHT**

Data will be normalized muscle CSA.

B.4 In-Vitro Diaphragm Force

In Vitro Diaphragm Force Production Protocol

Updated: June 2020 CAB

***Protocol based on (1)

See attached paper for set-up procedure with videos (2). Practice of the dissection is crucial for this technique as changes in force development could be a result of technical skill of experimenter, before a study make sure you can consistently produce normal forces. When performing dissection, do so under dissection microscope in cold Tyrodes (also called Ringers) buffer on an ice pack, pining muscle when necessary. Use surgeons' knots to tie off central tendon and loop before attaching to force transducer.

Ensure you bath is filled with Tyrodes solution and oxygenated for 30mins with attached 95% O_2/ 5% CO_2 tank, with water circulator turned on and maintained at 25°C prior to start of surgery. This ensures the bath and muscle has enough oxygen since we are relying on diffusion of oxygen into the muscle and not perfusion through blood supply. CO_2 provides necessary buffering of pH during contraction. Limit strip width to 2mm (maximum 4mm) as wider strips have difficulties with diffusion limitations of O_2. 25°C is used over 37°C as oxygen has poor solubility at higher temperatures.

If you were previously doing in-vivo force

In vitro force is measured in force production (mN) not moment of Force (mN-m)—this is TORQUE

To change units: setup→ Channel set up→ force in device→ select mN

repeat with length (should appear in mm)

setup→ Channel set up →length in → select mm

Have Bath temperature to 25°C- this is to ensure oxygen stays dissolved in the bath

Protocol:

1. Create folder to save files for each animal→ File→ set up autosave folder→ open folder created→click "current folder"
2. Set up Instant Stim→ this will be used for length optimization and stim optimization
    a. Pulse Frequency : 1Hz (this is a single twitch; can increase if you want to provide tetanus stimulus)
    b. Pulse width: 0.2ms (how long the stimulus is given)
    c. Number of pulses: 3 (again giving single twitch)
    d. Train Frequency: 0.1Hz (If you are using multiple twitches this gives 10s of rest between stimuli)
    e. Run time: 1 second (amount of time of data collection)
    ** currently I have a better instant stimulation for optimizing current saved (the settings are saved in a photo on force computer)

3. Open live data monitor (File→ open live data monitor); Instant stim orange button will be available for use.
    a. Set time to 10mins (can see protocol or optimization) (screen will automatically scroll)

4. Let diaphragm strip acclimatize for 20-30mins with some tension applied (will appear at 0mm on length in monitor at the end of acclimatization)
    a. This will allow resting tension in the muscle to relax and will reduce background tension; I typically have it resting with some tension on it (6-10mm) and will give it a tetanus stimulus to fully relax the fibres before optimizing length for full data collection.

5. Optimize the current
    a. Range: **1A (50-70%)** (in vitro force stimulation requires a much higher amperage or voltage than in-situ or in-vivo force stimulation since this is a field stimulation- don't be afraid to have it at a high amperage)
    b. Run Instant Stim and check force development
    c. Increase range to ensure all fibres are recruited- if you see an increase in force development then more fibres have been recruited and you are not at a supramaximal current. Use 3 twitches in a row with increasing current (30s rest between) where force does not increase.
    d. Set supramaximal current by increasing current by 15% (this will ensure you have all fibres being activated in the muscle strip).

6. Optimize the length (necessary to make sure maximal amount of cross bridges are forming)
   YOU NEED TO RECORD THIS LENGTH AT THE END OF DATA COLLECTION
    a. Gradually increase length of diaphragm strip and apply instant stim. Provide 30s of rest to avoid fatigue.
    b. Continue to increase length of diaphragm until you obtain maximal twitch force.
    c. You will need to increase the length of the diaphragm quite considerably compared to an upright bath since this bath is flat- but be careful of drastic changes in length this will increase basal tension of diaphragm strip. Use ¼ turns of fine adjustment knob and use gross only when necessary.
    d. If you want to collect this data load a single twitch protocol in DMC software and enable autosave- this is optional but for training purposes would be beneficial to look at the shape of the twitch. Can also do this with tetanus to
    e. Measure the length of the diaphragm and record, this is L_o and can be input on the main DMC screen and will be used for analysis
        i. Setup normalization- enter the reference length in mm

f. Allow some time (approx. 5min) for muscle to rest before starting force frequency curve

7. Optimal current and length have now been set, protocol is ready to begin.

8. Load "Diaphragm in-vitro force frequency" sequence
    a. Frequencies of 1 Hz, 10Hz, 20Hz, 40Hz, 80Hz, 100 Hz, 120Hz, 140Hz,160Hz & 200Hz
        i. Initial delay : 0.2ms (this is the rest period prior to stim)
        ii. Pulse Frequency: the above frequencies
        iii. Pulse Width: length of stimulus
        iv. Duration: **400ms** (inputted in s in protocol editor) *might consider increasing this but 400ms provides tension to return to baseline recording following contraction (Tupling lab uses a 1 sec- 600-800ms might be sufficient).
    b. 60s rest in between; avoids fatigue

9. Allow 5 mins recovery for the muscle to avoid fatigue in max force test
10. Load tetanic protocol at the frequency that produces the highest force during force frequency test (label this as pre-fatigue max force test)
11. Perform Pre-Fatigue Max-Force Test
12. Allow 2 mins recovery
13. Load "**Diaphragm In Vitro Fatigue**" sequence
    a. 70Hz (350ms stim, 0.2ms pulse width) every 2 seconds for 5 mins
14. Allow 5 minutes recovery from fatigue
15. Perform a second max force test at the same frequency used in Prefatigue max force test- this assesses recovery from fatigue and can be labelled as **5-min-post-fatigue max** force test.
16. Allow 5 minutes recovery
17. Perform third max force test; label as **10min-post-fatigue-max**
18. Allow 5 minutes recovery
19. Perform Fourth max Recovery test label as **15min-post-fatigue-max**
20. MAKE SURE YOU HAVE RECORDED LENGTH!!!
21. Remove muscle from bath and remove from central tendon and ribs before weighing. Obtain weight in mg.
22. Data will be normalized to Cross sectional area : mass X length X density
    a. Mammalian skeletal muscle density =1.06g/cm^3 (Mendez and key, 1960); this is commonly used in the field as it. CSA in short allows you to compare differing muscle weights and lengths of muscle. Normalizing to CSA is a way of controlling for sarcomeres in parallel and normalizing to muscle length during

shortening contractions is a way of controlling for the number of sarcomeres in series.

b. “If you need a visual -think of a rope. How strong is a single rope- now cut it in half so you have 2 shorter ropes. Lay them beside each other and glue them together. You now effectively have a new stronger rope with twice the CSA of the first rope, but it weighs the exact same (wait... forget the glue... the rope just really sticky for some reason). Cut the rope again and stick the two pieces together again. Repeat as many times as you want. You now have a rope which has a much larger CSA than the original rope, and it can handle much more load than the original rope but weighs the same and is much shorter. Replace rope with contracting muscle fibres and you probably get the idea. “- Ian Smith 2018

B.5 Bioenergetics Buffer Detailed Descriptions and Compositions

BIOPS BUFFER (Extracellular)

Chemical	Stock Solution	Molecular Weight	Final Concentration	Addition to *2 Litre* Final Volume
CaK_2EGTA*	100mM		2.77mM	55.4mL
K_2EGTA*	100mM		7.23mM	144.6mL
Na_2ATP		605.3	5.77mM	6.99g
$MgCl_2 \cdot 6H_2O$		203.3	6.56mM	2.67g
Taurine		125.1	20mM	5.02g
Na_2Phosphocreatine		327.14	15mM	9.81g
Imidazole		68.1	20mM	2.72g
Dithiothreitol (DTT)		154.2	0.5mM	0.154g
MES Hydrate		195.2	50mM	19.52g

*__ALWAYS__ double check molecular weights for supplier-specific chemicals (n=m/M.W.)

BIOPS contains the following ion concentrations		**EXTRACELLULAR RANGE**
Ca^{2+} free	0.1uM	Rat: 7.6mM Mouse: 1.3mM
Mg^{2+} free	1mM	
Na^+	41mM	Human: 133-143mM
K^+	20mM	Human: 4.5mM
Cl^-	13mM	Rat: 160mM Mouse: 95-120mM
MgATP	5mM	
Ionic Strength	160mM	
Osmolality	295 mOsm	

*Ionic strength is the sum of all ions
*Buffers do not perfectly reflect extracellular conditions
*Species-specific extracellular ranges exist
*Ranges are expressed as mmol/L (refer to ion concentration summary chart)

CaK_2EGTA: Dissolve 2.002g of $CaCO_3$ in 100mM hot (80°C) solution of EGTA (7.608g of EGTA in 200mL ddH_2O). Add 2.3g of KOH and adjust pH to 7.0 using KOH. Freeze unused portions.

K_2EGTA: Dissolve 7.608g EGTA and 2.3g KOH into 200mL ddH_2O. Adjust pH to 7.0 using KOH. Freeze unused portions.

To make BIOPS:

1. Add approximately 1500mL of ddH_2O to 2000mL beaker
2. While constantly stirring add stock solutions of CaK_2EGTA and K_2EGTA
3. Weigh and add all powder chemicals
4. Adjust pH to 7.2 using KOH pellets
5. Using graduated cylinder, bring total volume to 2000mL
6. Filter and then aliquot into 50mL falcon tubes
7. Freeze falcon tubes

MiRO BUFFER (Intracellular)

Chemical	Stock Solution	Molecular Weight	Final Concentration	Addition to *2 Litre* Final Volume
EGTA		380.4	0.5mM	0.38g
$MgCl_2 \cdot 6H_2O$		203.3	3mM	1.22g
K-Lactobionate*	0.5M	358.3 free acid	60mM	240mL
Taurine		125.1	20mM	5.02g
KH_2PO_4		136.1	10mM	2.72g
HEPES		238.3	20mM	9.54g
Sucrose		342.3	110mM	75.3g
BSA		154.2	1g/L	2.0g

*__ALWAYS__ double check molecular weights for supplier-specific chemicals (n=m/M.W.)

MiRO contains the following ion concentrations		**INTRACELLUAR RANGE**
Ca^{2+} free	0.0uM	Human: 30nM – 60nM SR: 5.7-20mmol/L Free Ca^{2+} in SR 0.2-0.5mM Rat: 7.76-11.11 ueq/g dry wt
Mg^{2+} free	2.1mM	
Na^+	0.0mM	Human: 6-13mM Rat: 7.10-21.9mmol/L
K^+	90mM	Human: 130 – 164mmol/L Rat: 117 – 149mmol/L
Cl^-	6mM	Rat: 4.97-16.57mmol/L
PO_4^{3-}	10mM	
EGTA free	0.46mM	
Ionic Strength	95mM	
Osmolality	330 mOsm	

*Ionic strength is the sum of all ions
*Buffers do not perfectly reflect extracellular conditions
*Species-specific intracellular ranges exist

*Ranges are expressed as mmol/L (refer to ion concentration summary chart)

K-Lactobionate: Dissolve 71.6g lactobionic acid in 300mL ddH_2O, adjust pH to 7.0, adjust final volume to 400mL with ddH_2O

To make MiRO:

1. Add approximately 1500mL of ddH_2O to 2000mL beaker
2. While constantly stirring add stock solution of K-Lactobionate
3. Weigh and add all powder chemicals
4. Adjust pH to 7.2 using KOH pellets
5. Using graduated cylinder, bring total volume to 2000mL
6. Filter and then aliquot into 50mL falcon tubes
7. Freeze falcon tubes

BUFFER Z (Intracellular)

Chemical	Molecular Weight	Final Concentration	Addition to *500mL* Final Volume
K-MES	233.33	105mM	12.26g
KCl	74.55	30mM	1.12g
KH_2PO_4	136.08	10mM	0.7g
$MgCl_2 \cdot 6H_2O$	203.3	5mM	0.51g
EGTA	380.35	1mM	0.19g
BSA		5mg/mL	2.5g

*__ALWAYS__ double check molecular weights for supplier-specific chemicals (n=m/M.W.)

Buffer Z contains the following ion concentrations		**INTRACELLULAR RANGE**
Ca^{2+}	0.0uM	Human: 30nM – 60nM SR: 5.7-20mmol/L Free Ca^{2+} in SR 0.2-0.5mM Rat: 7.76-11.11 ueq/g dry wt
Mg^{2+} (total, not free)	5mM	
Na^+	0.0mM	Human: 6-13mM Rat: 7.10-21.9mmol/L
K^+	145mM	Human: 130 – 164mmol/L Rat: 117 – 149mmol/L
Cl^-	40mM	Rat: 4.97-16.57mmol/L
PO_4^{3-}	10mM	
EGTA free	1mM	

*Buffers do not perfectly reflect extracellular conditions
*Species-specific intracellular ranges exist
*Ranges are expressed as mmol/L (refer to ion concentration summary chart)

To make Buffer Z:

1. Add approximately 400mL of ddH_2O to 1000mL beaker
2. Weigh and add all powder chemicals
3. Adjust pH to 7.2 using KOH pellets
4. Using graduated cylinder, bring total volume to 500mL
5. Filter and then aliquot into 50mL falcon tubes

6. Freeze falcon tubes

I. BIOPS BUFFER

- BIOPS is designed to mimic the extracellular environment
- BIOPS should be a relaxing media to prevent basal sodium/potassium flux that stimulates electrical signals in muscle - this is the purpose of having high K^+ (K^+ counteracts action potentials)
- BIOPS prevents cell shrinkage or swelling
  - ➔ Keep Ca^{2+} low and ATP available
  - ➔ Keep it cold
- Saponin removes cell membrane ~ 15mins into permeabilization

<u>CaK_2EGTA</u>

- ❖ Need some Ca^{2+}, but too much kills cell (calpain and caspase activation, mitochondrial swelling)
- If you do not have enough Ca^{2+}, you cannot prime all dehydrogenases and ETC (keep them active)
- PDH requires Ca^{2+} as an example to be activated ← Ca^{2+} binds PDP (pyruvate dehydrogenase phosphatase), not PDH itself
- SR may have lost their normal regulation, so we need EGTA to maintain low Ca^{2+}
- ❖ K^+ relaxes the fibres so they stay flaccid while you are separating (prevent spontaneous depolarization)
- ❖ EGTA is a cationic non-specific chelater – it can chelate Ca^{2+} and Mg^{2+}; binds divalent cations (that is why it cannot chelate Na^+ or K^+); EGTA has a higher affinity for chelating Ca^{2+} (prevents Ca^{2+} from going too high)
- EGTA buffers Ca^{2+} and keeps Free Ca^{2+} super low
- Mito can swell over time if you do not have EGTA to buffer Ca^{2+}
- Amount of Ca^{2+} and amount of EGTA determines Free Ca^{2+} (refer to sample calculation e.g. McGuigan et al. *Can. J. Physiol. Pharmacol.* 69:1733 – 1749, 1991)

<u>Na_2ATP</u>

- Na^+ is exchanged with Mg^{2+} from $MgCl_2$ (ATP naturally binds to Mg^{2+} creating Mg•ATP in the buffer)
- ATP relaxes fiber in buffer – therefore, it relaxes myosin with ATP
- ATP supports metabolism while separating fibers in BIOPS
- BIOPS contains 41mM of Na^{2+}, which is less than the known extracellular ion concentration of 133-143mM – this may be to ensure that fibres are not excessively activated (remain somewhat relaxed) – see ion concentration chart in separate file

<u>$MgCl_2$</u>

- Mg^{2+} is needed for metabolism because it is required in the ETC for ATP production (cofactor for ATP synthase)
- Any enzyme that hydrolyzes or makes ATP needs Mg^{2+}
- EDTA preferentially chelates Mg^{2+} over Ca^{2+} (this is why EDTA is <u>NOT</u> added)

<u>Taurine</u>

- Sulphur-based, inert compound used to balance osmolarity; could be an antioxidant
- Cation chelater (keeps Ca^{2+} and Mg^{2+} in balance)

<u>PCr</u>

- Need it for energy production and phosphate shuttling mechanism between mitochondria and cytoplasm; keeps energy exchange higher
- PCr loss likely occurs during permeabilization, which requires addition to buffer

Imidazole ** might do many things

- Preservative and antioxidant that prevents bacterial growth in BIOPS and might inhibit contraction
- Potentially causes hyperpolarization of mitochondrial membrane

Dithiothreitol (DTT)

- Two thiols groups → very common antioxidant; if you do not have antioxidants, a lot of enzymes can form disulfide bonds and become inactivated by ROS
- Therefore, it must be at very low concentrations

2-(N-Morpholino) ethanesulfonic acid (MES) Hydrate

- Buffers protons and is a substitute for the natural in vivo bicarbonate buffer
- "S" refers to sulfonic acid, which buffer protons
- Acids exist in equilibrium as negative and positive. Therefore, sulfonic acids will buffer H+ as a natural part of their equilibrium
  MES effective pH range: 5.5-6.7
  HEPES pH range: 6.8-8.2 ← this may be more ideal

Cytoplasmic Ca^{2+} low, Mg^{2+} high

- This prevents Ca^{2+} induced mitochondrial swelling and ensures high Mg^{2+} for ATP synthase and ATPases throughout cell given Mg^{2+} is a cofactor for ATP
- Therefore, EGTA is used, not EDTA, to keep Ca^{2+} low and Mg^{2+} high (EGTA is a strong Ca^{2+} chelater and a weak Mg^{2+} chelater) – EDTA is the opposite
- Must prevent mitochondrial swelling (keep low Ca^{2+} so it does not die and need Mg^{2+} for metabolism while you are separating and permeabilizing fibres)
- Free Mg^{2+} is a calculation of what is left from $MgCl_2$ after being bound to ATP that was added to the buffer and chelated weakly by EGTA
- The same is true of Free Ca^{2+} and EGTA

Importance of total osmolarity

- Do not want to swell or shrink the cytoplasm and mitochondria while you are separating (osmolarity is anything that draws water)
- Calculated based on concentration of every component of the buffer – every component is water soluble (contributes to osmolarity), not just the salts
- Extracellular osmolarity is 295 mOsm, just like BIOPS buffer

Importance of total ionic strength

- Maintaining protein shapes throughout cell through ionic bonds
- Ionic strength is total ions in a cell

II. MiRO BUFFER

Lactobionate/Taurine
- Osmotic regulators (hold onto water); prevent shrinking or swelling of mitochondria by maintaining osmolarity
- Cells have higher mOsm than extracellular (MiRO and Z need to be saltier than BIOPS – that is what mitochondria are accustomed to)
- They are also weak antioxidants

K-Lactobionate
- Main source of K^+ in MiRO buffer

HEPES
- buffer (effective range @ pH 6.8-8.2)

Sucrose
- Membrane stabilizer
- Antioxidant

KH_2PO_4
- Provides inorganic phosphate for ATP synthesis

BSA
- Osmolarity, Antioxidant, Buffer

Cytoplasmic Ca^{2+} low, Mg^{2+} high (same as BIOPS, but ALSO)
- This prevents Ca^{2+}-induced mitochondrial swelling and ensures high Mg^{2+} for ATP synthase and ATPases throughout cell given Mg^{2+} is a cofactor for ATP
- Therefore, EGTA is used, not EDTA, to keep Ca^{2+} low and Mg^{2+} high (EGTA is a strong Ca^{2+} chelater and a weak Mg^{2+} chelater) – EDTA is the opposite
- Not only do you need high Mg^{2+} to drive ATP synthase but also to maintain steady state respiration by supporting ATPases (potentially other pathways that use ATP) throughout the cell that regenerate ADP for the mitochondria
- Without Mg^{2+} in the buffer, ATP would not be synthesized or utilized, and respiration would not be steady state

III. BUFFER Z (alternative to MiRO)

Special notes:
- principles listed above for BIOPS and/or MiRO are the same for Buffer Z, regarding $MgCl_2$, EGTA, BSA, KH_2PO_4 and MES
- Buffer Z is used for H_2O_2 emission because it does not contain any antioxidants or sucrose

BSA benefits:
1. Buffers protons;
2. Buffers FFA;
3. Buffers ROS (it is loaded with cysteines and histidines which can react with ROS to buffer it);
4. Contributes to osmolarity of cell

Special note: Potassium source

- BUFFER Z uses K-MES, not K-Lactobionate (as in MiRO)

Special note: Chloride (from KCl)

- Intracellular Cl^- is supraphysiological; this does not seem to affect respiration (see figure 1A of Perry and Kane et al. *Diabetes* 2013. Note Mitomed is similar to MiRO in figure)
- Cl^- above 30mM can cause mtCK to dissociate from inner membrane space according to Oroboros blue book. However, our lab still obtains good respiration and H_2O_2 with Cr compared to without

B.6 Permeabilized Muscle Fiber Bundles and using the Oroboros-O2K

Permeabilized Fibre Preparation

Pre-surgery

1. For every fibre bundle you are going to make you will need one 0.5mL tube for wet weights one 1.5mL eppendorf tube for permeabilization and one 1.5mL tube for wash

* Keep all tubes and buffers on ice

2. In a 5mL tube, make 10mg/mL Saponin solution by dissolving a small amount of saponin in distilled water
    a. Vortex gently and place on rocker until ready for use
3. Fill all permeabilization tubes with 1.5mL of freshly thawed BIOPS (or BIOPS from fridge with fresh EGTA…see "Other Things to Consider") and *40ug/mL saponin (6uL in 1.5mL BIOPS).
    a. * different saponin concentrations may be used depending on species/tissue type but 40ug/mL is standard for rodent
4. Fill all wash tubes with 1.5mL freshly thawed MiRO (or from fridge…same as above)
5. Fill all 0.5mL tubes with 500uL of BIOPS
6. Using a 50mL falcon tube, weigh out ~ 0.05g of creatine (this number will change based on the number of chambers you need with creatine), add the correct amount of MiRO to make a 20mM Creatine MiRO Solution
    a. Place on rocker as creatine takes some time to dissolve
7. Label and fill a 5mL tube with 3.5mL BIOPS for every muscle that will be harvested during surgery
8. Proceed to "O2k Setup" Section, after O2k's are setup you are ready for surgery

Post-Surgery

1. Separate fibres in BIOPS as quickly and carefully as possible
    a. Remember to change ice block/ice pack frequently as buffer should never be allowed to warm up
2. Place separated fibres in corresponding 0.5mL tube with BIOPS and proceed to wet weight procedure

Bundle Wet Weights

1. Fill a 1.5mL tube with BIOPS until a dome of liquid covers the top
2. Place tube in holder on scale and tare the scale
3. With fine forceps remove first bundle from eppendorf and using a kim wipe, blot the bundle to remove excess liquid
    a. Try to blot no more than 3 times and try to turn the bundle the same way each time to get consistent blotting
4. Very carefully place bundle in liquid on scale, making sure the forceps to not draw up any liquid
5. Wait for scale to stabilize and record weight
6. Until accuracy is proven, do duplicates of each weight and take average if within 0.2mg, repeat weighing if weights are more variable

7. When done weighing, place back in 0.5mL eppendorf tube until all bundles have been weighed

Permeabilization

1. Once all bundles are weighed, switch bundles to permeabilization tubes (the ones that have saponin) using forceps or a gel loading pipette tip
2. Place on nutator in the fridge for 30 minutes
    a. Make sure all eppendorfs have the liquid mixing by ensuring that the air bubble is moving
    b. If air bubble appears stuck, invert eppendorf 1-2 times to allow for movement and place back on nutator
3. After 30 minutes, transfer bundles to corresponding wash tubes using gel loading pipette tip
4. Place bundles in wash back on nutator in the fridge for 15 minutes
    a. Permeabilized bundles can remain in fridge in wash for up to 2 hours but will start to lose viability after that point so use bundles ASAP
5. After 15 minute wash proceed to "Running an Experiment"

O2k Setup

1. Using the switch on the back of the machine, turn machine on
2. Open up DatLab and a connection box should pop up
    a. For O2k 1 and O2k 2
        i. O2k 1 – USB: E-0085
        ii. O2k 2 – Com 3: C-0024
    b. When connection box pops up ensure the top blue bar says E-0.0085

    c. If it does not, click the configuration tab, click "select communication port" and select USB
    d. Click the control tab and click "Connect to Oxygraph-2k"
    e. A screen will pop up asking you to change the file name, save file in location of choice
    f. An "Edit Experiment" screen will appear, click "Save"
    g. After O2k 1 is connected, open DatLab again and an error screen will appear, change the serial port to "Com 3" and click ok

    h. Follow steps d-f for O2k 2

    i. For O2k 3 and O2k 4
        i. O2k 3 – Com 3: D-0008
        ii. O2k 4 – Com 4: D-0098
    j. Follow steps b-g for O2k 3 and O2k 4

3. Remove stoppers and place with top down on top of the O2k

4. Turn on the aspirator and remove ethanol from chambers…keep aspirator AWAY from membrane inside the chamber
    a. the best way to ensure this is to only touch the bottom of the chamber on the wide opposite the membrane to avoid contact
5. Fill chambers with water and aspirate out water
    a. When cleaning chambers be sure to not let chambers stay dry for very long, always replace liquid immediately
6. Repeat rinse with ethanol
7. Finish with 3 rounds of water rinses and leave spinning in water until ready to load buffers
   * If this is the first experiment of the day do Volume Calibration before loading buffers
8. Load chambers with 2.1mL Creatine MiRO (or just regular MiRO if no creatine is wanted)
9. Push stoppers down and adjust height with the plastic wrench so both stoppers are at the same height
10. Wait for both O_2 Concentration and O_2 Slope to reach steady state and then proceed with "Air Calibration"

Volume Calibration

1. Volume calibrate chambers at the start of each day but it is not necessary to do in-between rounds of experiments
2. Add 2.1mL of water to each chamber
3. Using the allen wrench found in the O2k Accessory kit loosen the collar on the stopper and push it all the way to the top
4. Slowly lower stopper into chamber until the first bit of liquid comes out the top of the capillary in the stopper
5. Push the collar all the way to the bottom and tighten with allen wrench

Air Calibration

1. When a steady state has been achieved, click on the blue Y_1 box in the top right corner of chamber A
2. Holding down the shift button, use your mouse, click down and drag across the steady O_2 concentration line to create a "mark"
3. Click "F5." (Air cal should be at 180-200. If not probably problem with the membrane. Check solubility factor)
4. Select 01 in the "Select Mark" box for the "Air Calibration" line

Running an Experiment

1. When fibres are done washing and chambers have been air phased, remove stoppers and place on top of O2k
2. Add 5uM BLEB and stop the stir bar pressing F11 for Chamber A and F12 for Chamber B
3. Add fibre and loosely place stopper in chamber (do not push down at all)
4. Turn stir bar back on by clicking F11 and F12
5. Add a very small amount of O_2 with syringe through capillary in stopper

6. Wait until O_2 concentration reaches ~350 and remove stopper, O_2 concentration will continue to rise, when the levels begin to fall push stopper in all the way so there is a tight seal between the chamber and stopper
7. Ensure there is no air bubble in the chamber
8. If no air bubble, press F10 to shut off lights
9. If there is an air bubble, remove stopper, add more buffer and repeat steps 5-8
10. Wait for background to reach a steady state…this usually takes 10+ minutes (see "Important Considerations, proceed with following protocol (remember to always achieve a steady state after the addition of a substrate)
    a. See "Important Considerations" for important tips on setting up syringes/beakers and substrates
11. In order to record when you add each substrate, by clicking "Control" and Left Clicking your mouse on the spot on the graph that you added a substrate you can make an event
    a. A screen will pop up allowing you to name your event and you can pick whether it is for Chamber A, Chamber B or both
    b. Do this after the addition of each substrate
12. At the end of the experiment, turn lights on clicking F10 and stop stir bars
13. Remove tissue if being saved and place in labeled eppendorf
14. Turn stir bars back on and proceed with cleaning
    a. 2 water washes
    b. 2 ethanol washes
    c. 1 water wash
    d. Add 70% ethanol and leave in chamber
    e. Rinse stoppers in sink with water and ethanol
    f. Place stoppers loosely in chamber with caps on and turn off machine

Analyzing Data

1. Open file you wish to analyze and click "F3"
2. In the box labeled "background correction" click "Copy from File"
3. Select the O2k file that contains your most recent background curve for that machine (See "Background Curve" section)
    a. Note you can also manually enter the slope and y-intercepts from your background curve in each file
4. Click save
5. In the top right corner of Chamber A, click on Y_2 so the red box is highlighted
6. Using the technique to "make a mark" like you did for air calibration, make marks for each of your steady states following a substrate addition as well as your background steady state
    a. If you make a mark and wish to delete it, hold shift and right click your mouse and drag over the mark you wish to delete, then let go and the mark will disappear
7. Once all marks are made, click "layout" at the top of the screen and select "05 Flux per Volume Corrected"
    a. Your data is not corrected using the background curve you imported
8. Click F2 and select copy to clipboard, your data can now be pasted into excel
9. Repeat steps 5-8 for Chamber B

a. Note that while clicking F2 and pasting will export both Chamber A and Chamber B data…the data is not accurate unless you see the "X" beside that chamber in the pasted data (glitch in the system)

POS Service and Membrane Mounting

** Membranes should be changed and electrode should be cleaned when data appears excessively noisy or air calibration curves have dropped below normal**
** See O2k Manual for detailed instructions and pictures

POS Service

1. IMORTANT: make sure to touch somewhere on the sides of the O2K to de-static yourself before removing the sensors
2. Pull back the blue sheath and slowly remove sensor from inside the system
3. Unplug the wire from the port on the O2K (should be plugged in to the port labeled O_2)
4. Remove the black cap from the sensor and keep in safe place as this may be reused
5. Using the black "membrane mounting tool" use the open end of the smaller piece to squeeze and remove the membrane ring off the sensor head
6. Using clean forceps remove the membrane from the top of the sensor and discard
7. Using distilled water, rinse sensor 1-2 times with water but covering sensor until dome of water appears and then dump water off
8. If gold cathode looks dirty (not shiny, dark grey colour) it must be cleaned with extreme care
    a. Using the "O2K Polishing Cloth" that is in the O2K accessory kit, add a small amount of "polishing powder" to the top of the cloth and wet with distilled water
    b. Place the top of the centre face down on the cloth and very gently make small circles using the cloth and powder to clean the cathode, continue until cathode appears gold and shiny again
9. Rinse sensor with distilled water 1-2 times
10. The anode also becomes oxidized over time changing it from a cream colour to a dark grey colour, when this happens it must be cleaned with 25% ammonia
11. Under fume hood, cover sensor with 25% ammonia until a dome appears, leave for 10 minutes
12. Repeat 1-2 times until grey colour disappears, if anode is very dark it may require overnight treatment with ammonia and/or a higher percentage solution of ammonia
13. If leaving overnight in ammonia seal ammonia in with membrane (see below) and make sure sensor is protected from light
14. After cleaning, rinse 1-2 times with water to make sure all traces of ammonia are removed

Membrane Mounting

1. If this is the first time mounting a membrane, fill "electrolyte solution" up to the 10mL mark with distilled water
    a. This is simply 1M KCl (you can also dissolve 1.49g KCl in 20mL water)
2. Cover sensor with electrolyte until dome appears

3. With forceps, remove a membrane from the membrane box avoiding contact with skin and making sure to remove the paper on either side of the membrane
4. Using the wider piece of "membrane mounting tool", place membrane flat on the ledge inside the tool
5. Pull down sheath on blue POS connector and place membrane mounting tool on top of sensor, letting go of sheath so it locks in place with the membrane lying flat on top of the electrolyte solution
6. Place membrane ring around circle on the end of the smaller piece of the membrane mounting tool
7. Using a good amount of force, going straight up and down push the smaller piece of the membrane mounting tool straight down on top of the membrane so the membrane ring locks in place
8. Remove both pieces of the membrane mounting tool (pull back sheath to remove bigger piece)
9. Check for air bubbles under the membrane, if there are considerable air bubbles you must restart at step 2 with a new membrane
10. Once membrane is mounted with no air bubbles, cover the sensor with the black rubber cap and make sure the entire gold cathode is visible
11. Plug connector wire into O_2 port, pull back sheath on POS and place sensor back in place in the O2k
12. Let Datlab run with the machine on for 24 hours to allow new membrane to equilibrate
    a. File will start off very noisy but by the end of 24 hours it should be a flat line, if file is still noisy, remove sensor and check membrane

* over time the black caps get looser, if you notice the chamber leaking after replacing the membrane, replace the black cap so there is a tighter seal

Background Curves

1. Set up O2k as you would for normal experiment (see "O2k Setup") loading chambers with 2.1mL of MiRO Buffer
2. When a steady state is achieved for the air phase, complete air calibration (see "Air Calibration")
3. Add O_2 to chambers until O_2 levels reach ~350(hyper-oxygenate), remove stoppers to ensure no air is trapped in stoppers
4. When O_2 levels start to drop, push stoppers in all the way and make sure there is no air bubble within the chamber
5. Allow for a background steady state to be achieved
6. Using the "zeroing powder" (dithionite) in the O2k accessory kit, mix a few grains of dithionite with distilled water and vortex
7. Add 1uL of dithionite solution to each chamber once a steady state is achieved
    a. It is impossible to know how much dithionite to add, you want the oxygen concentration to drop 30-40 units with each addition so with your first addition add 1uL, see how much it drops and add more if necessary
    b. Dithionite **degrades over the course of the experiment** so towards the end of the titration you will need a larger volume to get the same decrease in oxygen
8. after each addition wait for a steady state to be achieved, continue with dithionite additions until O_2 concentration reaches ~0. **When O_2 looks to be reaching zero add a large amount of dithionite (~20uL) to ensure O_2 levels are at 0.**
9. Once O_2 has reached zero, create a mark measuring O_2 concentration at the zero level in the same way you would make your air calibration mark
10. Click F5 and insert "02" in the zero calibration "select mark" box
    a. Note, "01" should already be inserted in the "air calibration" select mark box"
11. Click "Calibrate and Copy to Clipboard"
12. Click on the red Y_2 box in the upper right corner of each chamber to switch to "respiration mode", using the method for making marks (see "Air Calibration"), make marks for each steady state that occurs after a dithionite addition (including the background steady state)
13. With Chamber A highlighted (click anywhere on the chamber A box), select "F2" and then select "copy to clipboard"
14. In excel paste the data you have just copied from DatLab
15. Using the "O_2 Concentration (A)" and "O_2 Slope uncorr. (A)" data, create a graph with concentration on the y-axis and slope on the x-axis
    a. By having 7-10 points to use, you can drop outliers that do not fit the straight line model
16. Repeat steps 13-15 for chamber B
17. Record the slope and y intercept for each chamber
18. Back in your DatLab file click "F3" In the section that says "background correction" insert your y intercept for each chamber in the a° boxes and the slopes in the b° boxes and click save

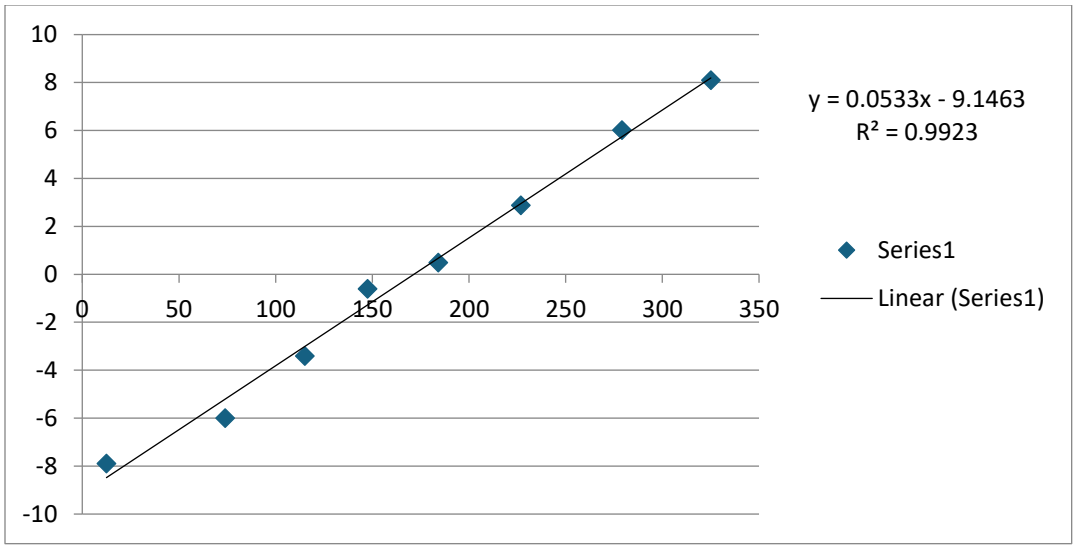
10
8
6
4
2
0
-2
-4
-6
-8
-10
0
50
100
150
200
250
300
350
y = 0.0533x - 9.1463
R² = 0.9923
Series1
Linear (Series1)

Important Considerations

Buffers

Buffers must be thawed fresh each day for actual data collection. When thawed, write the date of thawing on the tube and place any left over in the fridge. For practice, buffers in the fridge can be reused…if it was thawed <2 days prior, it is fine to use as is. If it was thawed 3 days prior or more (up to 1 week….throw out buffers that are more than a week old) it must be topped up with EGTA. To do this, pour buffer into graduated cylinder to get accurate volume. Thaw a 0.5M EGTA from the freezer and add corresponding volume to get the following final concentrations:
BIOPS: 10mM
MiRO: 0.5mM
Buffer Z: 1mM

Substrates

When making substrates, pH to 7.1 and aliquot into small volumes, enough for 6 chambers for 1 protocol. When running experiments, thawed substrates cannot be put back in the freezer, they must be placed in fridge and can be used for up to 1 week after thawing (except for FCCP, Oligomyocin and Rotenone, see below).
** ADP must be thawed fresh each day, do not reuse for actual data collection (ok for practice)
Pyruvate must be made fresh each day, make 2M solution in a 1.5mL eppendorf by combining power and water, throw out pyruvate at the end of each day.

Syringes and Beakers

Each protocol being followed should have it's own separate syringe and beaker filled with water. Syringes should be rinsed with water prior to use and should be wiped with a kim wipe after being put in the chamber to remove residual buffer. When switching substrates, syringes should be rinsed thoroughly with water.
IMPORTANT: FCCP, Oligomyocin and Rotenone have THEIR OWN SYRINGES AND BEAKERS. Beakers should be filled with ethanol and these inhibitors should never be near other syringes. Only use these labeled syringes for their specific chemical and keep beakers labeled and separate from other beakers being used. Additionally, these inhibitors can be placed back in the freezer after use as they are dissolved in Ethanol

Rotenone/Oligomyocin

Rotenone (complex I inhibitor) and Oligomyocin stick to the chambers even after multiple water/ethanol washes. It is necessary to use yeast to remove all residual chemicals. After your experiment, rinse chambers with 2 water washes and 2 99% ethanol washes. Then add a small scoop of yeast to each chamber and fill chamber with water. Allow yeast to spin for 10 minutes. Aspirate out yeast solution using aspirator (if yeast clumps in tip use pipette tip to loosen). Repeat yeast wash 2 more times for a total of 30 minutes in yeast. Rinse chambers with water 2-3 times or until there is no residual yeast left. Complete 2 more 99% ethanol washes and leave in 70% ethanol over night.

Steady States

It is very important to make sure a steady state is achieved before each addition in order to get accurate data. When waiting for background steady state (after adding fibre but before adding

any substrates) wait until respiration has leveled out ABOVE zero. If the background is below zero respiration will be a negative and all data will be corrected for a negative rate. This may take 10+ minutes to achieve proper steady state.
After adding Glutamate/Pyruvate/Malate respiration often tends to slowly increase, again, make sure you have an accurate steady state so you do not end up over estimating this rate and getting a lower rate with your first substrate addition (may need to way 5+ minutes).
If data is very noisy, make a large mark over steady state as opposed to trying to find a small flat line. Taking a larger area average will give a more accurate reading.

Oxygen Levels

Do not let oxygen levels drop below 150. If oxygen is below 200, make next addition and wait for steady state, once respiration has achieved steady state, loosen stopper and re-oxygenate up to 350. Push stopper back in and wait for steady state. Often when reoxygenating, respiration rates steady state higher than before reoxygenation, if this happens, take an average of the rate before reoxygenation and after reoxygenation and then proceed with adding next addition.

B.7 Mitochondrial H_2O_2 Buffer, Collection and Analysis

Amplex Ultra Red – Preparation

Total volume per experiment: 1000ul in Hellma 109.004F fluorescent cell
Total volume per black tube: 1030ul (recommend 1050 next time)

Stock A and B ingredients required:

5mM Amplex Ultra-Red (Invitrogen A36006)
5000 IU/ml Cu/Zn Superoxide dismutase (SOD1; Sigma S9697)
10mM Blebbistatin (BLEB; Cayman)
0.5M EGTA (aliquots in freezer)

Stock B additional ingredients:

20mM Creatine anhydrous

Final concentrations for both AUR Stock A and AUR Stock B:

10uM AUR
5uM BLEB
25U/ml Cu/Zn SOD1
1mM EGTA

Work fairly quickly given AUR and BLEB should not be stored on ice. Best to prepare with lights out in lab as AUR and BLEB are light sensitive.

Preparation of AUR Stock A (No Creatine):

Step 1: Prepare 5mM AUR. Add 666.6ul of DMSO to 1mg AUR. Vortex gently. Prepare in black tube but do not place on ice (DMSO will freeze).

Step 2: Prepare 10mM BLEB. Add 1.71 ml DMSO to 5mg bottle of BLEB. Prepare in black tube but do not place on ice.

Step 3: Prepare 5000IU/mL SOD1 from 30KU/mL stock. Add 3 mL to sigma bottle, mix well and move to 15mL falcon tube. Add 3 more mL to sigma bottle again and move this to 15mL falcon tube (6mL altogether). pH this to ~7. **MAKE SURE YOU USE 1M KOH TO BRING pH UP, TITRATE THIS INCREMENTALLY (1uL at a time).** Prepare in 850uL aliquots and keep in freezer labelled with date, name and "5000IU/ml SOD1."

Step 3: Prepare 10uM AUR stock. Mix the following:

- 160.6 ml of Buffer Z. Note: sucrose buffers lower oxidant emission.
- 325ul of 5mM AUR
- 812.5ul of 5000 IU/ml SOD1
- 80.3ul of 10mM BLEB

- 325ul of 0.5M EGTA

Aliquot 1.030 ul in black tubes. Store @ -80˚C.
(recommend 1050 ul next time)

Preparation of AUR Stock B (20mM Creatine):

Prepare 10uM AUR stock as in Stock A but with 20mM creatine anhydrous. Mix the following:

- 160.6 ml of Buffer Z.
- 421.19 mg creatine anhydrous
- 325ul of 5mM AUR
- 812.5ul of 5000 IU/ml SOD1
- 80.3ul of 10mM BLEB
- 325ul of 0.5M EGTA

Aliquot 1.025 ul in black tubes. Store @ -80˚C.
(recommend 1050ul next time)

mH_2O_2 Collection-Standard Curve

1. H2O2 dilution (serial dilution)
   - H2O2 is light sensitive. Keep in dark when possible.
   - Use H2O2 purchased within last 6 months (stored in fridge, wrapped in foil).
   - One standard curve per batch is acceptable, but re-make curve if batch approaches 6 months of age. Discard if curve no longer consistent with original curve.
   - Good in -20C freezer up to 6 months or so.
   - Use stock 3% w/w H2O2 : 3 g H2O2 / 100 mL solution (1 mol H2O2 / 34.01 g) = 0.0882 mol H2O2 / .100 L = .882 mol H2O2 / 1 L = 0.882 M H2O2
     1. 4310ul ddH2O + 100ul 3% w/w H2O2 >>>> 20mM H2O2. Use in dilution step 2.
     2. 3980ul ddH2O + 20ul of 20mM H2O2 >>>>>> 100uM H2O2. Use in dilution step 3 for 20uM.
     3. 3200ul ddH2O + 800ul 100uM H2O2 >>>>> 20uM H2O2. Use in table below.
     4. 2000ul ddH2O + 2000ul 20uM H2O2 >>>>>> 10uM H2O2. Use in table below.
     5. 2000ul ddH2O + 2000ul 10uM H2O2 >>>>>> 5uM H2O2. Use in table below.

NOTE:
- H2O2 is light sensitive.
- Prepare large volumes to minimize pipetting/dilution errors.
- Do not vortex – H2O2 is unstable and dismutates spontaneously to H2O2 over time. Agitation may worsen. Flip tube in hand several times.
- Make this right before you are about to start standard curve

2. Add your Amplex UltraRed, HRP, (oligomycin) and other substrates (G/M/S/G-3-P……) into the cuvette as per your protocol.

NOTE:
- You only need to pick one protocol (ie substrate combination, succinate or P&M) to perform background on. Sofhia Ramos performed experiment to show that each substrate combination does not change background fluorescence that much
- Make sure you add total volume of ADP to the titrate as well- does not matter what concentration you use

3. H2O2 titration. NOTE: [final H2O2] depends on the final volume in the cuvette, which will vary depending on your protocol.

BACKGROUND COLLECTION: collect for 3 mins at minimum
(VERIFY LAST 30S OF BACKGROUND LOOKS LINEAR)

Make sure to clean the pipette tip by pipetting up and down in a beaker of ddH2O after each addition, and wipe pipette tip with kim wipe. This avoids excess additions of H2O2 as you progress.

If for 1000 ul Titrate very fast, 45-60 sec		**If for 600ul** Titrate very fast, 45-60 sec	
[H2O2] (µM)	Add (µl))	[H2O2] (µM)	Add (µl))
5	3.33	5	2.0
5	3.33	5	2.0
10	3.33	10	2.0
10	5	10	3
20	5	20	3
20	5	20	3
20	10	20	6

4. Repeat 3 times. Average all 3 standard curves to make one equation for analyses in excel if values are consistent. See next page for acceptable ranges of values and general considerations…

NOTE: Prepare a standard curve for project- make sure you save some Amplex red buffer for any redos for standard curve you need to do.

General Considerations:

- **In general, collect background of 3 mins and collect 45s-60s for each H_2O_2 titration.**
- You will have 8 points in the Standard Curve. Consult experienced personnel on judgement for quantifying steady state fluorescence.
- During analyses, it can be common to drop points if the standard curve begins to form a curvilinear response. Check curve closely following analyses. Aim for at least 4 data points in the final curve.
- Finally, the accuracy of dilutions as an enormous effect on the lowest H_2O_2 points of the standard curve. It is not uncommon for new trainees to see scattered points at the low end. The stocks must be re-made with new curves prepared if this is the case.
- APRIL 2020: we compared normalizing each titration of H_2O_2 to its own drift calculation and it gives the same results as normalizing each H_2O_2 titration to the drift calculation from the background. In drift calculation use the last 30s of 3 min background for drift calculation so long as it is linear- this can change to less points if only last 10-15s are linear in the background.

RANGES:

A. **SLOPE: LOW 1millon- LOW 2millon (**newer bulbs will give you closer to low 2 million)**

- Bulb should be changed if slopes are seeing less than 1millon- always check bulb usage hours if you are getting lower slope maximum bulb usage time is 400 hours. **Always check bulb usage hours before you start a study**

  If you get a very high slope (ie 2.5 million) it might be a new bulb but re-run standard curve to be sure it was not an H2O2 dilution error.

B. **Y-INTERCEPT: do not go above 5 000 if slope is around 1 million, 8 000 if slope is closer to 2 million (subject to change based on group discussions)**

- **You need positive value- needs to be as close to 0 as possible**
- If all y-intercepts are positive, then go to the values as closest to 0 (and are below cutoffs listed above) and average these intercepts. **Use your judgement**
- If all y-intercept are negative, then redo standard curves. But negatives that are close to 0 might be acceptable as well **(subject to group discussion) -use your judgement**

H_2O_2 Collection-Protocols

Treatment in Saponin Solution	In Cuvette Prior to Experiment	Volume to Add	Substrate added to induce H_2O_2	Volume to add
NONE	Amplex Red 1U/mL HRP	1mL 2uL of 500U/ml	10mM Succinate	5uL of 2M
35uM CDNB (5uL of 10.5mM Stock)	Amplex Red 1U/mL HRP	1mL 2uL of 500U/ml	10mM Pyruvate 2mM Malate	5uL of 2M 2uL of 1M
35uM CDNB (5uL of 10.5mM Stock)	Amplex Red 1U/mL HRP	1mL 2uL of 500U/ml	20mM Glycerol-3-Phosphate	20uL of 1M
35uM CDNB (5uL of 10.5mM Stock)	Amplex Red 1U/mL HRP **0.5uM Rotenone****	1mL 2uL of 500U/ml **2uL of 250uM**	10mM Pyruvate	5uL of 2M
NONE	Amplex Red 1U/mL HRP	1mL 2uL of 500U/ml	2.5uM Antimycin A	5uL of 0.5mM
NONE	Amplex Red 1U/mL HRP	1mL 2uL of 500U/ml	250uM Tyramine	5uL of 50mM

****Use Green Tape Cuvettes for Rotenone as it sticks to glass**

ADP Titration for:

1. Succinate
2. Pyruvate + Malate
3. G3P

Addition 1: 25uM ADP – 5uL of 5mM
* Open lid prior to addition, wait 2 minutes before next addition

Addition 2: 100uM ADP – 1.5uL of 50mM
* Open lid prior to addition, wait 2 minutes before next addition

Addition 3: 500uM ADP – 0.8uL of 500mM
* Open lid prior to addition, wait 2 minutes before next addition

mH_2O_2 Analysis

Phase 1: Export Traces

1. Go to the lab computer where H_2O_2 experiments were completed and open felix software
2. Open H_2O_2 file, right click protocol and click "export trace." Save all files in a folder and use a USB to transfer data over to a personal computer and back up data on One Drive (or any other location where you keep your data)
3. Once data is on personal computer where you wish to analyze, right click file you wish to analyze and click "export with excel.
4. Highlight first 4 rows and click delete.
5. All that should be remaining in the file is data in column A and column B. Column A will contain time data (independent variable) while column B will contain fluorescence intensity data (dependent variable), in other words the index of H_2O_2 emission. Copy all column A and column B data and paste it into the H_2O_2 analysis template

Phase 2: Setting up and understanding template sheet

1. Open H_2O_2 analysis template provided by a lab member and ensure the following criteria are met:

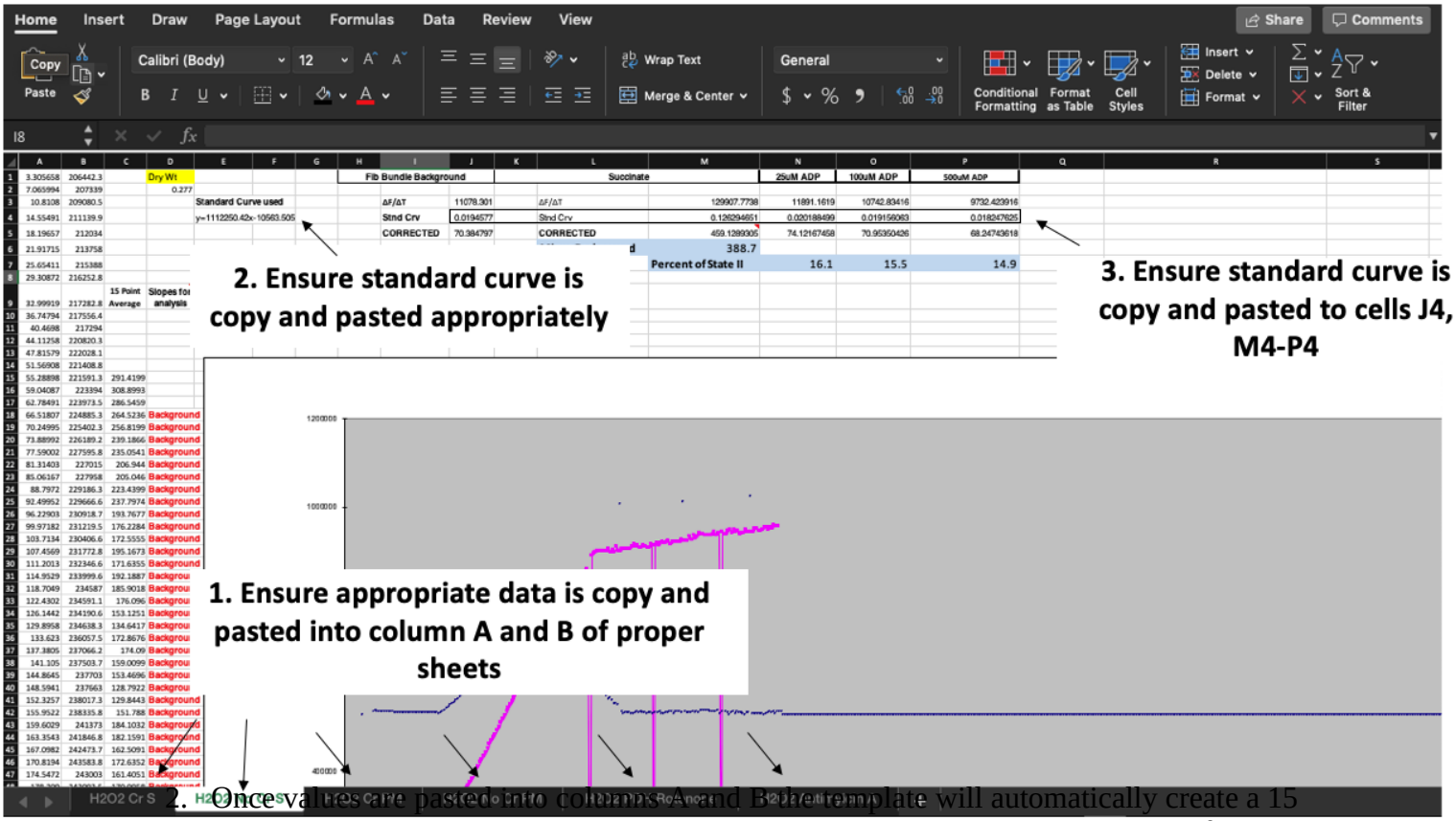

2. Once values are pasted into columns A and B, template will automatically create a 15 point or 10 point slope calculation in column C and generate a graph. See below for interpretation of data.

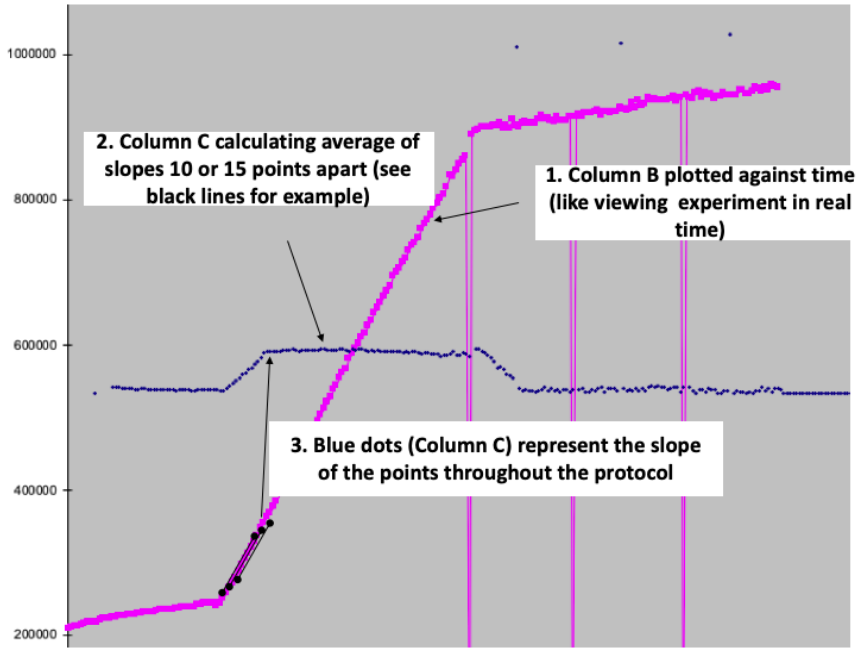

Phase 3: Analyze H_2O_2 Traces

Every protocol has slightly different patterns of H_2O_2 emission and therefore slightly different regions to be analyzed. Although different regions will be selected per protocol, the fundamental premise remains – **take large averages of max substrate emissions.** Some protocols can be a "judgment call" but this SOP will attempt to walk the reader through the best choices.

Succinate

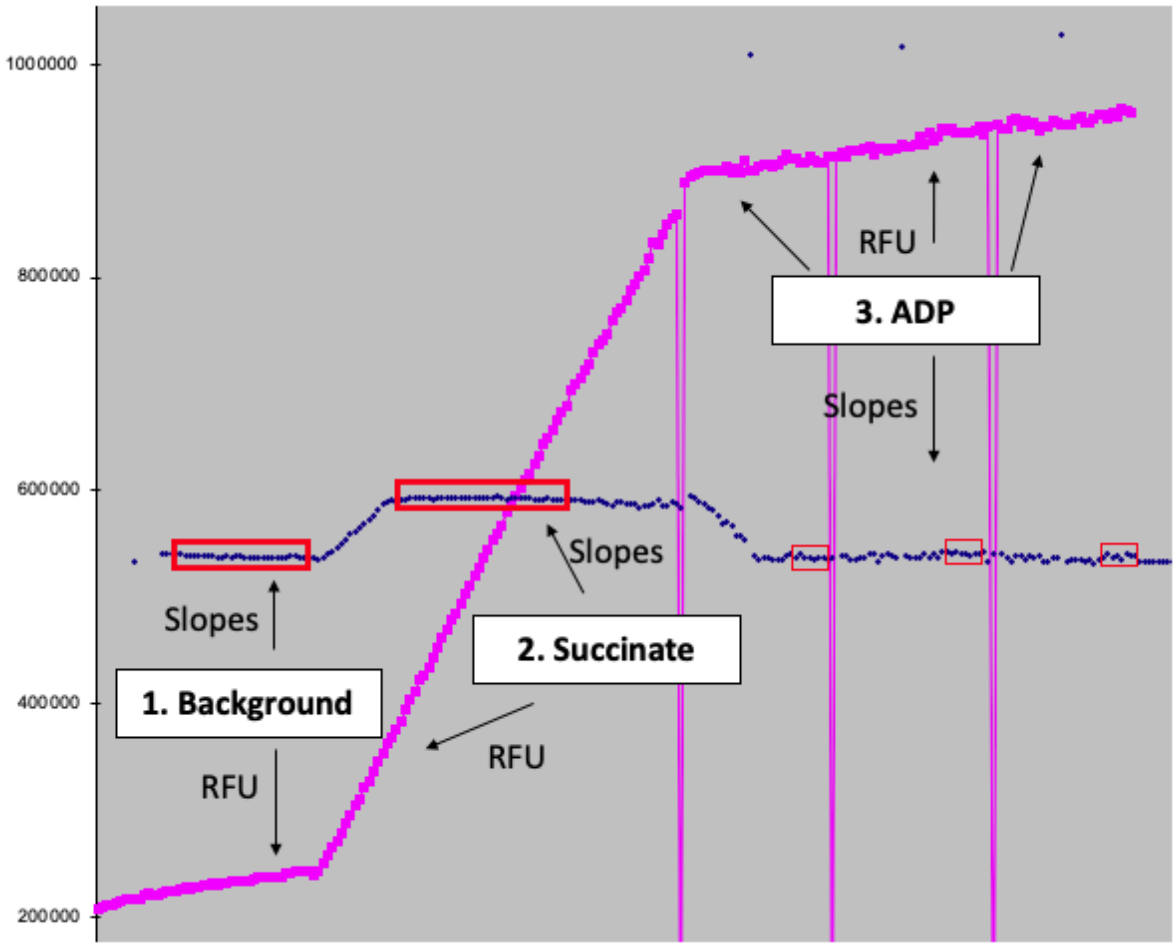

1. Background should be 2-3 minutes, succinate 5 minutes, ADP 2 minutes each
2. Make sure you are referencing column C to ensure you are measuring correct slopes calculated from RFU data (column B). **Be extra careful you are NOT averaging slopes of recording data from a previous titration.**
3. Data copied are in cells J5-P5 (corrected rates).

Pyruvate Malate

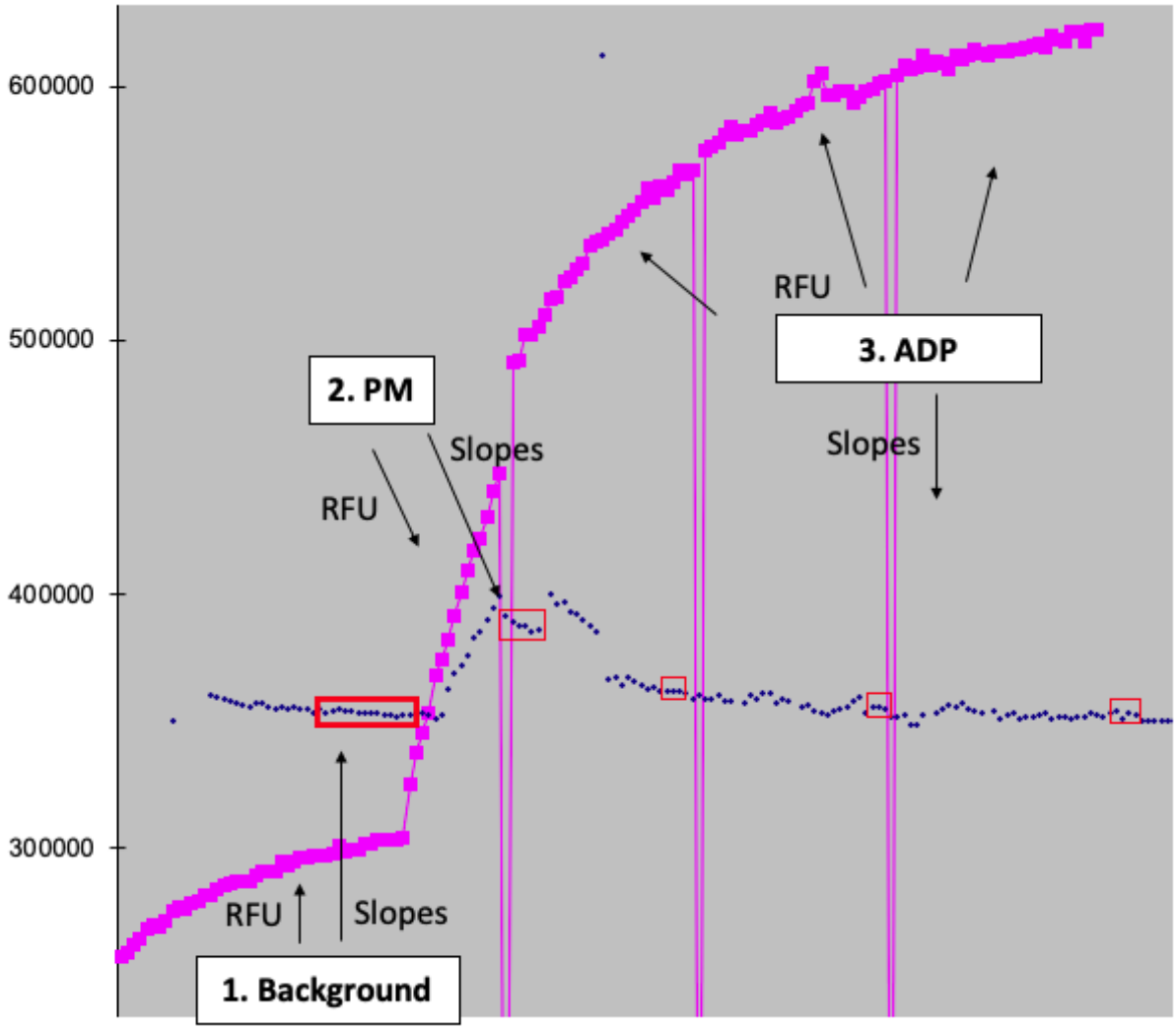

1. Background should be 2-3 minutes, PM 1 minute, ADP 2 minutes each
2. NOTE: PM is increasingly difficult because PM generates so much H_2O_2 that the longer the protocol runs, the more the fiber could be dying due to cell damage. This protocol requires a 1-minute titration and a narrow window to select for averages compared to succinate. **Be extra careful you are NOT averaging slopes of recording data from a previous titration.**
3. Data copied are in cells J5-P5 (corrected rates).

PDH Rotenone Inhibitor

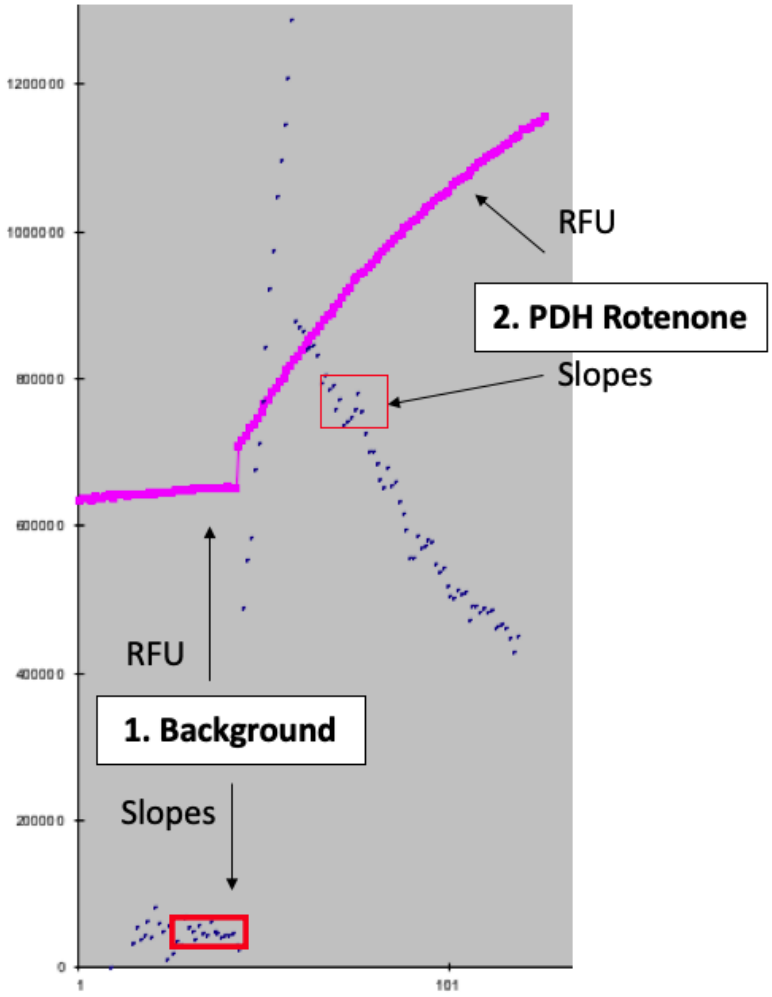

1. Rotenone should be titrated in the cuvette and the cuvette should sit in the fluorometer for 10 minutes. Then 3 minute background and 5 minute pyruvate.
2. PDH is challenging to identify the max rate as the blue dots seem to gradually descend. To pick the appropriate slopes, average the slopes where there is a very quick plateau in about the middle of the reaction (red box). **Be extra careful you are NOT averaging slopes of recording data from a previous titration.**
3. Data copied are in cells M5 (corrected rates).

Antimycin A

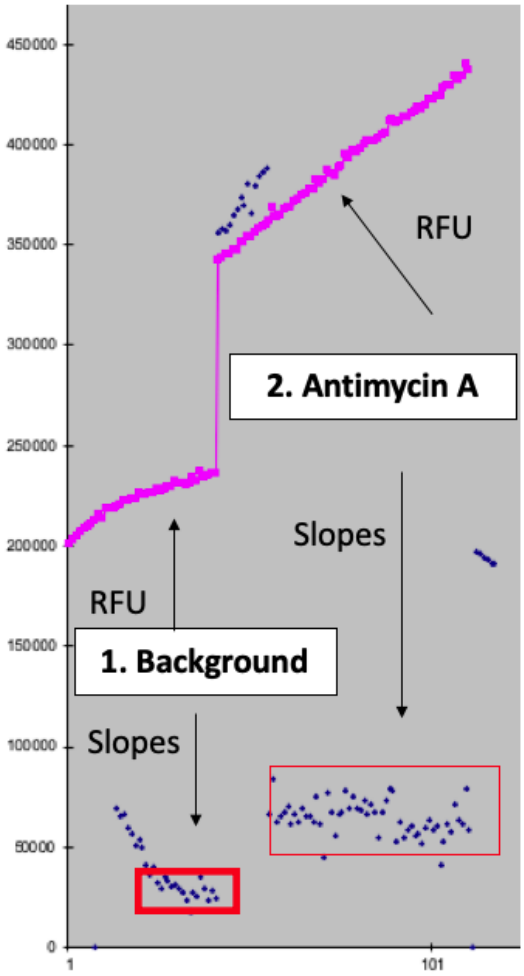

1. When Antimycin A is titrated, there consistently seems to be some autofluorescence that initiates a large increase in RFU. Ignore the values comparing background to Antimycin A as they are irrelevant.
2. **Be extra careful you are NOT averaging slopes of recording data from a previous titration.**
3. Data copied are in cells M5 (corrected rates).

NOTE: All graphs were generated using control mice from Luca's Cancer Cachexia thesis. All protocols may not look identical but general trend should be similar.

B.8 MHC Fiber Typing Immunofluorescence

Immunofluorescence Fiber Typing Procedure – LD Edit 2020

All section/slide incubations for this procedure are done at room temperature (RT), on the shaker (~~220rpm~~), and with 50-100µL of solution (only large sections/areas require 100µL). Make sure slides are as flat/level as possible when they are in the incubation container. Also, when blotting slides, even though it is important to remove as much of the solution as possible, the Kimwipes will leave fabric fibers on the sections which show up very brightly blue on the microscope. So, avoid touching the pap pen area with the Kimwipe. Finally, make up antibody dilutions immediately before they are applied.

Set Up:

1. Container
    a. Put wet paper towel on top of lid covered by parafilm held up by tape (this ensures slides will not get dried out)
2. PBS
    a. 1 tablet/100mL of ddH_2O
    b. Filter and keep at room temperature

3. Blocking
    a. 10% Goat Serum kept in freezer – 400uL aliquots
        i. **If staining cocktail** - 1mL of blocker per slide
            1. 900uL PBS and 100uL goat Serum

4. Primary (make immediately before using)
    a. **Primary Cocktail** (leave on rocker away from light for 2 hours)
        i. MHCl (BA-F8) @ 1:25 – IgG2b: blue
        ii. MHClla (SC-71) @ 1:500 – IgG1: green
        iii. MHCllb (BF-F3) @ 1:50 – IgM: red
        iv. ~~MHCllx (6H1) @ 1:100 – IgM: red~~ → This will not be done so it will be black
        v. NOTE: these dilutions are for hybridomas at ~50ug/uL

5. Secondary (make immediately before using)
    a. **Secondary Cocktail** (leave on rocker away from light for 1 hour)
        i. Alexa Fluor 350 IgG_{2b} 1:1000 (blue)
        ii. Alexa Fluor 488 IgG_1 1:1000 (green)
        iii. Alexa Fluor 568 IgM 1:1000 (red)

Procedure:

1. Air dry slides for 10 minutes at room temperature and outline sections in pap pen (optional).
2. Incubate sections for 1 hour in blocking solution

3. Blot dry slides. Incubate section in 1˚ antibodies appropriately diluted in blocking solution (see above). Give the stock antibody tubes a quick shake/inversion before pipetting out of them. – leave away from light, on rocker for 2 hours.
4. Wash slides 3 x 5 minutes in a Columbia jar with 1 x PBS.
5. Blot dry slides. Incubate sections in appropriate 2˚ antibodies appropriately diluted in blocking solution for 1 hour at room temperature in the dark. (Note: precipitate forms in the stock tubes which show up as bright spots on the microscope; centrifuge for 15 seconds before pipetting out of stock tubes. Ensure as little light as possible makes contact with the 2˚ antibodies and sections from this point.)
6. Wash slides 3 x 5 minutes in a Columbia jar with PBS. Take the mounting medium, nail polish and coverslips.
7. Apply 15µL of Prolong to each slide and mount with a number 1 coverslip. (Perform this step in the microscope room in almost total darkness.) The coverslip can be pressed gently to remove bubbles, but do not apply pressure direction above sections, they will squish.
8. Tack the corners of the coverslip down with nail polish and place in a labeled, light-proof slide box.
9. Slides can be imaged after the nail polish has dried (5 to 10 minutes), but next day imaging seems to work better as the Prolong is allowed to set. Slides should be imaged no longer than 2 days after staining.

B.9 eMHC immunofluorescence

eMHC/WGA Costain Protocol on Frozen Mouse Muscle

Day 1 (Approx. 3 hours)

1. Air dry sections for 20 min
2. Fix sections in 10% formalin for 5 min @ 4°C.
3. Wash 3 x 2 min PBS
4. Block for 1 hour @ RT (10% NGS + 1.5% BSA + 0.3% Triton X-100)
5. Wash 3 x 2 min PBS
6. M.O.M. IgG Block for 1 hour @ RT (1 drop M.O.M IgG reagent in 1.25 ml PBS)
7. Wash 3 x 2 min PBS
8. M.O.M. Diluent for 5 min @ RT (40 µl of protein concentrate in 500 ml PBS)
9. Tap off excess diluent
10. Primary anti-eMHC (15ug/mL) O/N @ 4°C

Day 2 (Approx. 5 hours excluding imaging)

11. Wash 5 x 2 min PBS
12. Secondary Alexa Fluor 647 IgG (donkey anti mouse ab150107; 1:1000 in PBS) for 2 hours @ 4^{o}C
13. Wash 5 x 2 min PBS-T ***DARK**
14. Block for 40 min @ RT (10% NGS + 1.5% BSA + 0.3% Triton X-100) ***DARK**
15. Preconjugated WGA (1:1000 in PBS) for 1 hour @ RT ***DARK**
16. Wash 5 x 2 min PBS-T ***DARK**
17. Dry, DAPI mounting media, coverslip
18. Store @ 4°C

NOTES

- All washes should be done in coplin jars (to ensure a cleaner, more comprehensive wash)
- After applying secondary antibody, keep DARK (i.e., place a box on top)

BLOCKS, ANTIBODIES, KITS

- **Vector M.O.M. Kit**
  MJS BioLynx (BMK-2202, stored at 4°C)

- **Anti-eMHC 1˚**
  DSHB (F1.652, supernatant, stored at -20°C in glycerol - add 500uL to 1mL stock. Final Concentration should be ~15ug/mL)
  Mouse Monoclonal
  Isotype: IgG1

- **Alexa 647 Donkey Anti-Mouse IgG**
  Abcam (ab150107, stored at 4°C)

- **Wheat Germ Agglutinin (WGA) 488 Conjugate**
  Thermofisher/Life Technologies W11262

- **DAPI mounting media 408 Conjugate**
  Abcam104139 (20mL)

Preparation:

M.O.M IgG Block
- 1 drop M.O.M IgG reagent in 1.25 ml PBS

M.O.M Diluent
- 40 µl of protein concentrate in 500 ml PBS

PBS-T (0.02%)
- Add 100 ul Tween-20 to 500 ml 1X PBS

B.10 Western Blotting

WESTERN PROTOCOL – UPDATED 2021 LD

Chemical solutions needed for this experiment – CHECK TO SEE IF ALL OF THESE ARE MADE BEFORE STARTING WESTERN

---

10 X Running Buffer:

	500 ml	**1 L**	**2 L**
Tris Base	15 g	30 g	60 g
Glycine	72 g	144 g	288 g
SDS	5 g	10 g	20 g

1 X Running Buffer: 10 X Running buffer 100 ml
dH_2O 900 ml

Trans-Blot Turbo 1x Transfer Buffer (Bio-Rad) 1L:

	1 L
5x Transfer Buffer	200mL
ddH_2O	600mL
Ethanol	200mL

---

10 X TBS (Tris Buffered Saline):

	500 ml	**1 L**
Tris Base	12.1 g	24.2 g
NaCl	40 g	80 g
Adjust to pH 7.6 with HCl		

1 X TBST:

	1 L	**2 L**
10 X TBS	100 ml	200 ml
ddH_2O	900 ml	1800 ml
Tween 20	1ml	2 ml

Note: Ensure solution is stirring when adding Tween

1.5M Tris-Base pH 8.8

	1 L
Tris-Base	g
ddH_2O	1000mL

Add KOH pellets or HCl to adjust pH as needed

1M Tris-Base pH 6.8

	1 L
Tris-Base	g
ddH_2O	1000 mL

Add KOH pellets or HCl to adjust pH as needed

10% SDS

	1 mL
SDS	100 mg
ddH_2O	1000 uL

10% APS (need to make fresh every experiment)

	1 mL
APS (Ammonium Persulfate)	100 mg
ddH_2O	1000 uL

Amido Black De-stain

	1 L
Isopropanol	250 mL
ddH_2O	650 mL
Acetic Acid	100 mL

Amido Black 1x

	50 mL
Amido Black Staining Solution (2x)	25 mL
ddH_2O	25 mL

	Stacking	**Running**				
		5%	**6%**	**8%**	**10%**	**12%**
dH_2O	6.8 ml	11.4	10.6 ml	9.4 ml	8 ml	6.7 ml
1.5M Tris-Base, pH 8.8	***	5 ml	5 ml	5 ml	5 ml	5 ml
1M Tris-Base, pH 6.8	1.25 ml	***	***	***	***	***
30 % Acrylamide (in fridge)	1.70 ml	3.4 ml	4 ml	5.3 ml	6.7 ml	8 ml
10 % SDS	100 µl	200 µl	200 µl	200 µl	200 µl	200 µl
10 % APS	100 µl	200 µl	200 µl	200 µl	200 µl	200 µl
Temed	**20 µl**	**20 µl**	**20 µl**	**20 µl**	**20 µl**	**20 µl**

Blocking Buffer

- 20mL LiCOR Blocking solution

Primary

- Blocking Buffer (typically 7mL)
- Primary antibody (typically 1:1000 – 7uL)
- .1% Tween (typically 7uL)
- .01% SDS (typically 7uL)

Secondary

- Blocking Buffer (typically 20mL)
- Secondary antibody (typically 1:20,000 – 1 uL)
- .1% Tween (typically 20 uL)
- .01% SDS (typically 20 uL)

1. In 50mL falcon tubes make running gel and stacking gel (1 column makes 2 gels) ***DO NOT ADD TEMED UNTIL READY TO LOAD***
2. Take 1 short plate and one spacer plate and clean both sides of glass with methanol and kimwipe
3. Place clean short plate on top of spacer place and place both in mounting apparatus, ensuring the edge of the plates are lined up against the bench top
4. Place plates in apparatus on foam piece in gel stand
5. Place 3 transfer pipettes and falcon tube with methanol close to gel stand
6. Add TEMED to running gel and invert falcon tube 1-2 times
7. Using transfer pipette, fill space between glass plates with running gel until solution reaches the top of the green doors
1. Using new transfer pipette add methanol to top of plate to create an even line along the top of the gel removing any bubbles
2. Let sit until remaining running gel has hardened in the falcon tube
3. Once gel has set, invert gel to remove any excess methanol
4. Add TEMED to stacking gel and invert 1-2 times
5. Using transfer pipette, add stacking gel to top of glass plates, use methanol transfer pipette to remove any bubbles
6. Add comb to top of gel and allow to set

7. Prepare diluted samples by combining sample, water and Laemmeli's buffer + 2-mercaptoehtanol (100 µl 2-mer: 900 µl Lam)
    a. **Example of dilution to load 50µg protein at a concentration of 1µg/ µl**

Sample	Corr Prot (ug/ul)	Aliquot (ug)	Sample (ul)	H20	4X Laem (1:9 2-Mercap)	Vol for 1 Well
C7.5-A	**4.599**	50	**10.9**	26.6	12.5	50

8. Boil samples at 95 °C for 5 minutes
9. Spin down samples for 5 seconds
10. Make 1X running buffer in 1000mL graduated cylinder
11. Remove combs from gels and place gels in gasket
12. Place gasket with gels in tank and add 1X running buffer until it fills the top of gasket and tank
13. Load wells with desired concentration of samples
14. Run for desired time (40-75 minutes) at 160mV (or desired voltage)

15. Fill 2 plastic "biorad" dishes, one with methanol and one with transfer buffer
16. Place 2 transfer packs in dish of transfer buffer and place membrane in dish of methanol
17. After 2-3 minutes place first transfer pack on bottom of transfer case
18. Place membrane in transfer buffer for 10-15 seconds
19. Place membrane on top of transfer pack ensuring no air bubbles
20. Remove short plate from gel and place gel face down on membrane
21. Place second transfer pack on top of membrane

22. Using roller, roll from one side of transfer pack to the other to remove air bubbles
23. Hold firmly down in the middle of the transfer pack and remove excess liquid
24. Put lid on transfer case and run transfer (standard setting is 1.5mm gel for 10 minutes)

25. Following transfer remove membrane and place in dish with blocking buffer (50% Odyssey Blocking Buffer, 50% TBS) for 1 hour, rocking at room temperature
26. After 1 hour pour blocking buffer back into falcon tube (it can be resused) and add primary antibody
27. Place membrane in primary in fridge overnight, rocking
28. In the morning remove primary and pour back into falcon tube (can be resued)
29. Add TBST to dish and complete 3x5 minute TBST washes rocking at room temperature.
30. Add secondary antibody and leave rocking at room temperature for 1 hour
31. Remove secondary and place back in falcon tube (can be resused)
32. Complete 3 more 3x5 minute TBST washes
33. Detect using LiCOR Infrared Imager
34. Once imaging is complete, place membrane in biorad dish and shake for 3 minutes with Amido Black
35. Put amido black back in aluminum foil falcon tube and fill biorad dish with amido black destain and shake for 30 minutes.
36. Once membrane is dried, scan membrane for total protein.

TROUBLESHOOTING TIPS

White non-specific bands (LD)

- Ensure your blocking is fresh and NOT diluted (sometimes we dilute blocking 50:50 with PBS)
- Your secondary antibody concentration may be too high – try diluting. 1:40 000 is the highest you should probably go
- Do **NOT** include SDS in your primary (unsure why, but AMPK and PAMPK blots come out with little/no white bands when we used no SDS in primary)

Blot not running straight (LD)

- Likely a leak in the electrode cassette. To avoid this be very diligent in refilling the electrode while the gel is running (every 5 minutes for the first 20 minutes). This issue never happens with 4 gels but tends to happen with 2.
- Make sure the wire is clean. There may be build-up of salts

B.11 RNA Extraction for qt-PCR

1. Add 1mL of Trizol to 2mL Eppendorf tubes provided in Aurum Extraction kit (Trizol maintains RNA integrity while disrupting cells and dissolving cellular components).
2. Add sample and homogenize 10 seconds at speed 3 or until fully liquefied.
3. Centrifuge samples at 12, 000xg for 10 minutes at 4^{o}C
4. Transfer supernatant to new 2mL tubes (from kit) and incubate for 5 minutes at room temp.
5. Add 200uL of **chloroform** to each tube and vortex for 15 seconds. Samples will become cloudy. Incubate for 15 minutes. (Phase separation - chloroform extracts proteins and makes RNA aqueous)
6. Centrifuge samples at 12, 000xg for 15 minutes at 4^{o}C. Samples should separate into 3 layers.
7. Transfer ONLY THE CLEAR UPPER PHASE to a new 2mL Eppendorf tube
8. Add 600uL **isopropanol** into each tube and mix by hand (invert 15 times). Wait 10 minutes. Mix again before starting step 9. (Precipitate - isopropanol precipitates RNA)
9. Transfer 700uL of each sample into an RNA binding column and centrifuge at 12, 000xg for 1 minute. (Columns are made of silica which bind to the nucleic acids of RNA)
10. Discard flow through, transfer any remaining sample into the binding column and centrifuge again at 12, 000xg for 1 minute. Discard flow through and tap column dry.
11. Add 700uL of **low stringency wash solution** from Aurum RNA isolation kit to each RNA binding column (dissolves salts but not RNA to purify the RNA).
12. Centrifuge for 30s at 12, 000xg and discard flow through.
13. Mix 5uL of **reconstituted DNAse I** with 75 uL of **DNAse dilution solution** in a 1.5mL Eppendorf tube (cleaves DNA to ensure this is a pure RNA extraction and no DNA is in samples).
14. Add 80uL of diluted DNAse I solution to membrane stack of each column and incubate for 25 minutes at room temperature.
15. Add 700uL of **high stringency wash solution** to each RNA binding column and centrifuge for 30 seconds at 12, 000xg. Discard flow through. (dissolves salts but not RNA to purify the RNA).
16. Add 700uL of **low stringency wash solution** to each RNA binding column and centrifuge for 30 seconds at 12, 000xg. Discard flow through. (dissolves salts but not RNA to purify the RNA).
17. Centrifuge again for 2 minutes at 12, 000xg to remove residual wash solution and discard flow through.
18. Transfer RNA binding column to a new 1.5mL capped Eppendorf tube.
19. Add 25uL of heated elution buffer (75 degrees) to each RNA binding column and let sit for 1 minute.
20. Centrifuge for 2 minutes at 12, 000xg. Keep flow through.

B.12 Glutathione

Buffer:

- **TRIS-BSA:** homogenization buffer with Trizma Base + Boric Acid/Serine/Acivicin to inhibit γ-glutamyltranspeptidase from metabolizing GSH/GSSG.
    - 200mL HPLC grade water
    - 50mM Trizma Base: 1.212g -- (MW=121.14g)
    - 20mM Boric Acid: 0.248g – (MW=61.83g)
    - 2mM L-serine: 0.042g – (MW=105.69g)
    - 20uM Acivicin: (MW=178.57)
    - Acivicin inhibits y-glutamyltranspeptidase, a protein bound to the cell membrane which catabolizes glutathione upon contact
    - pH to 8 with HCL
- DAY OF:
    - Add 25ul 0.2M NEM for every 1ml TRIS-BSA fresh day of use (some suggest NEM is light sensitive, freeze sensitive, not sure if this is true or not, but adding it same day allows for to decide whether you would want to or not add NEM, only time you wouldn't add NEM is if you wanted to measure total glutathione)
    - NEM irreversibly binds to GSH creating a GS-NEM conjugate and inhibits glutathione reductase preventing the auto-oxidation GSH to GSSG

Making Mobile phase solvents

- **GSH mobile phase**
    - Solvent A: 0.25% Glacial Acetic Acid in HPLC grade water
        - 2.5mL glacial acetic acid into 997.5mL water
            - Or 1.25ml glacial acetic acid into 498.75mL water
        - pH to 3.1 by adding in a couple drops of 2M NaOH to bring pH up or glacial acetic acid to bring pH down
        - **Prepare fresh every day**
    - Solvent B: 100% Acetonitrile
- **GSSG mobile phase**
- Solvent A: 25mM Na_2HPO_4 in HPLC grade water
    - Make 425ml
        - pH to 6.0 using phosphoric acid
    - Add 75ml MeOH to get final 15% methanol mobile phase

Sample preparation:

- Make up 6 tubes:
    - Tube1 for homogenate/lysis
    - Tube2 for protein assay
        - 5ul homogenate into 45ul buffer/RIPA buffer for cells
        - Poke hole in top of tube
    - Tube3 with TCA
        - 7ul TCA into tube
    - Tube4 PCA
        - 70ul PCA into tube
    - Tube5 labeled GSH
        - Poke hole in top of tube

    - Tube6 labeled GSSG
        - 500ul 0.5M NaOH
- <u>For muscle:</u>
    - Homogenize tissue in TRIS-BSAN at a 1mg-10ul ratio, leave on ice until all samples (I usually do about 10 samples at a time, do samples in random order).
        - Try and get at least 145ul final volume, otherwise need to adjust volumes of TCA and PCA
    - Spin samples at 800g for 10 minutes at 4 degrees
    - Add supernatant to tube 1
- <u>For Cells:</u>
    - Wash cells in PBS-NEM (PBS with 0.5mM NEM – 25ul 0.2M NEM into 10ml PBS)
    - Trypsinize cells, re-suspend in media-NEM (2mM NEM in media)
    - spin at ~1000g for 5 minutes at 4^{o}C
    - Wash cells with PBS-NEM
    - spin at ~1000g for 5 minutes at 4^{o}C
    - aspirate off PBS-NEM carefully, re-suspend in ~155ul TRIS-BSAN
    - Add to tube 1
- Now have cells or muscle homogenate in tube 1
- Take from tube 1:
    - 5ul tube 1 -> tube 2 (protein tube)
        - Freeze in liquid nitrogen
    - 70ul tube 1 -> tube 3 (TCA tube, for GSH)
        - Put onto rocker
    - 70ul tube 1 -> tube 4 (PCA tube, for GSSG)
        - Put onto rocker
    - Vortex tubes 3 and 4
- Spin TCA and PCA tubes at 20,000g for 5minutes at 4^{o}C
- Carefully take tubes out of centrifuge, be careful not to dislodge pellet
- From tube 3: Take off supernatant, and transfer to tube 5 (GSH tube)
- From tube 4: take 100ul of tube 4 -> tube 6 (GSSG tube)
- Freeze

Determine protein from samples using tube 2 (protein tube)

GSH determination (UV)

- GSH flow rate at 1.25 ml/min (new HPLC down to 1.05ml/min)
- Sample detected using VWD (UV detector) detector (on HPLC stack) at 265nm
- 94% Mobile phase A, 6% acetonitrile
    - Protocol name on HPLC is TurnbullGSH
- Take GSH tube, transfer total volume into HPLC vial.
- Have machine insert 10ul of sample into machine
    - GSH elutes as two peaks right before NEM spike
        - No idea why is elutes as two peaks, cant find answer (yet) but is reported as common – I think it is likely due to some of the amino acid residues being chimeric (maybe?)

        - Found answer: it is because the configuration of GSH (3 amino acids) can be built in two ways depending on the specific amino acid configuration, I always use 2nd peak because 1st peak is sometimes influenced by other compounds depending on the tissue being analyzed
- **GSH Standard**
    - Every day, run a 4 point standard
    - 250uM GSH, 62.5uM GSH, 31.25uM GSH, 15.6uM GSH
    - Step 1: Make 50mM GSH in TRIS-BSAN
    - Step 2: Dilute 50mM GSH -> 5mM GSH in TRIS-BSAN
    - Step 3: Dilute 5mM GSH -> 0.5mM GSH in TRIS-BSAN
    - Step 4: Do serial dilutions from 0.5mM (500uM GSH)
        - 500uM GSH -> 250uM GSH -> 125uM GSH -> 62.5uM GSH -> 31.25uM GSH -> 15.6uM GSH
    - Take 70ul of 250uM GSH, 62.5uM GSH, 31.25uM GSH, 15.6uM GSH tubes, and transfer to new tubes with 7ul TCA
    - Transfer GSH-TCA tube to HPLC vial, ready to load

GSSG determination (fluorescent)

- Excitation/Emission 350/420nm
- Flow rate at 0.5 ml/min
- Sample elutes as a single peak
- Injection volume: 50ul
- Protocol is set up as TurnbullGSSG
- Take tube 6 out of freezer
- When thawed, add in 37.5ul of 0.1% OPA (our fluorophore, which is stored in -20^{o}C freezer)
- Incubate samples in the dark for at least 15 minutes
- After incubation, transfer to HPLC vial, ready for run.
- **GSSG Standard**
    - Every day, run a 4 point standard
    - 10uM GSH, 2.5uM GSH, 1.25uM GSH, 0.625uM GSH
    - Step 1: Make up 20mM GSSG in TRIS-BSAN
    - Step 2: Dilute 20mM GSSG -> 2mM GSSG in TRIS-BSAN
    - Step 3: Dilute 2mM GSSG -> 0.2mM GSSG in TRIS-BSAN
    - Step 4: Dilute 0.2mM GSSG -> 20uM GSSG in TRIS-BSAN
    - Step 5: Do serial dilutions starting from 20uM GSSG
        - 20uM GSSG -> 10uM GSSG -> 5uM GSSG -> 2.5uM GSSG -> 1.25uM GSSG -> 0.625uM GSSG.
    - Take 100uL from GSSG standards and transfer to new tube with 500ul 0.5M NaOH
    - Add in 37.5ul of 0.1% OPA-MeOH (our fluorophore, which is stored in -20^{o}C freezer)
    - Incubate standards in the dark for at least 15 minutes
    - After incubation, transfer to HPLC vial, ready for run.

Day of checklist:

- Make up TRIS-BSAN
    - Thaw 0.2M NEM stock from freezer, add 25ul NEM per 1ml TRIS-BSA
- Make up mobile phase
- Make up standard curve
- For GSH:
    - Transfer tubes into HPLC Vials
- For GSSG:
    - Incubate with OPA for 15 minutes before transfer tubes to HPLC vials